UNIVERSITÉ DU LUXEMBOURG

PhD-FSTM-2022-155
The Faculty of Science, Technology and Medicine

DISSERTATION

Presented on 15/12/2022 in Esch-sur-alzette

to obtain the degree of

DOCTEUR DE L'UNIVERSITÉ DU LUXEMBOURG

EN PHYSIQUE

by

Damilola ADELEYE
Born in Ilorin, (Nigeria)

DESIGN OF A THREE-STAGE PROCESS, PHOTOLUMINESCENCE AND DEFECT SPECTROSCOPY OF $Cu(In,Ga)S_2$

Dissertation defence committee

Dr. Susanne Siebentritt, Dissertation supervisor
Professor, Université du Luxembourg

Dr. Levent Gütay
Group leader, Carl von Ossietzky University of Oldenburg

Dr. Alex Redinger, Chairman
Professor, Université du Luxembourg

Dr. Nicolas Barreau
Professor, University of Nantes

Dr. Emmanuel Defay, Vice Chairman
Head of unit, Luxembourg Institute of Science and Technology

To my guiding light,

my parents,

Emmanuel Adewale and Margaret Kehinde,

my sister,

Oluwaseun Toyin

Contents

Abstract

$Cu(In,Ga)S_2$ is a chalcopyrite material suitable as the higher bandgap top cell in tandem applications in next generation multi-junction solar cells. This owes primarily to the tunability of its bandgap from 1.5 eV in $CuInS_2$ to 2.45 eV in $CuGaS_2$, and its relative stability over time. Currently, a major hinderance to the potential use of $Cu(In,Ga)S_2$ in tandem capacity remains a deficient single-junction device performance in the form of low open-circuit voltage (V_{OC}) and low efficiency. Aside interfacial recombination which leads to losses in the completed $Cu(In,Ga)S_2$ solar cell, deficiencies stems from a low optoelectronic quality of the $Cu(In,Ga)S_2$ absorber quantified by the quasi-Fermi level splitting (QFLS) and which serves as the upper limit of V_{OC} achievable by a solar cell device. In this thesis, the QFLS is compared with the theoretical V_{OC} (V_{OC}^{SQ}) in the radiative limit, and "V_{OC}^{SQ} deficit" is defined to compare the difference between V_{OC}^{SQ} and QFLS as a comparable measure of the optoelectronic deficiency in the absorber material. In contrast to the counterpart $Cu(In,Ga)Se_2$ absorber which has produced highly efficient solar cell devices, the $Cu(In,Ga)S_2$ absorber still suffers from a high V_{OC}^{SQ} deficit. However, V_{OC}^{SQ} deficit in $Cu(In,Ga)S_2$ can be reduced by growing the absorbers under Cu-deficient conditions.

For the effective use of $Cu(In,Ga)S_2$ as the top cell in tandem with Si or $Cu(In,Ga)Se_2$ as the bottom cell, an optimum bandgap of 1.6-1.7 eV is required, and this is realized in absorbers with Ga content up to [Ga]/([Ga]+[In]) ratio of 0.30-0.35. However, the increase of Ga in Cu-poor $Cu(In,Ga)S_2$ poses a challenge to the structural and optoelectronic quality of the absorber, resulting from the formation of segregated Ga phases with steep Ga/bandgap gradient which constitutes a limitation to the quality of the $Cu(In,Ga)S_2$ absorber layer with a high V_{OC}^{SQ} deficit and low open-circuit voltage and overall poor performance of the finalized solar cell.

In this work, the phase segregation in $Cu(In,Ga)S_2$ has been circumvented by using different first stage substrate temperatures and adapting the Ga flux during the first-stage of deposition when growing the $Cu(In,Ga)S_2$ absorbers. A more homogenous $Cu(In,Ga)S_2$ phase and improved Ga/bandgap gradient is achieved by optimizing the Ga flux at higher first stage substrate temperature to obtain a $Cu(In,Ga)S_2$ absorber with high optoelectronic quality and low V_{OC}^{SQ} deficit. Additionally, the variation of the Cu-rich phase when growing the $Cu(In,Ga)S_2$ absorber layers

was found to not only alter the notch profile and bandgap minimum of the absorbers, but also influence the optoelectronic quality of the absorber. Shorter Cu-rich phase in the absorbers led to narrower notch profile and higher bandgap. Ultimately, several steps in the three-stage deposition method used for processing the $Cu(In,Ga)S_2$ absorbers were revised to enhanced the overall quality of the absorbers. Consequently, the V_{OC}^{SQ} deficit in high bandgap $Cu(In,Ga)S_2$ absorbers is significantly reduced, leading to excellent device performance.

This thesis also examines the temperature- and compositional-related optoelectronic improvement in pure Cu-rich $CuInS_2$ absorbers without Ga, where improvement in QFLS were initially linked to a reduction of nonradiative recombination channels with higher deposition temperatures and increase in Cu content. Findings through photoluminescence decay measurements show that the origin of the improved QFLS in $CuInS_2$ is rather linked to changes in doping levels with variations of deposition temperature and Cu content.

Finally, in order to understand and gain insight into the influence of Ga in $Cu(In,Ga)S_2$, the electronic structure of $CuGaS_2$ absorbers was investigated in dependence of excitation intensity and temperature by low temperature photoluminescence measurements. A shallow donor level and three acceptor levels were detected. It was found that similar acceptor levels in $CuInSe_2$ and $CuGaSe_2$ which are otherwise shallow become deeper in $CuGaS_2$. These deep defects serve as nonradiative recombination channels and their appearance in the Ga-containing compound will be detrimental to the optoelectronic quality of $Cu(In,Ga)S_2$ absorbers when Ga content is increased, therefore, limiting the optimum performance of $Cu(In,Ga)S_2$ devices.

Chapter 1

Introduction

The major weather and climate occurrences of the past few years are full of unprecedented natural disasters [1]. These events, which include record-breaking temperatures, droughts and desertification, rapidly melting ice caps, catastrophic flooding events, landslides, widespread wildfires, just to name a few, are the devastating impacts of climate change. These calamitous events are catalysts for humanitarian crises, which no place on earth has escaped the dreadful impact [2]. Still with a sense of impending doom, at the time of writing this thesis, various countries in Europe are bracing for a looming energy crises particularly during the coming winter months [3], when these countries will have to survive at least three dark cold months without gas supply from a particularly hostile country (which they have long depended on for gas supply) [4-6]. Concurrently the global economy is gripped by a food crisis exacerbated by the effect of climate change and hyperinflation which has been blamed on many factors including the aftermath of the global pandemic caused by 'SARS-CoV-2' [7], which is still not over, and actions of the hostile country. Nevertheless, all is not as "doom and gloom" as it may seem, since there is nearly a unilateral agreement that a collective action is needed to tackle the climate crises [8]. New policies with concrete plans are being enacted to shift towards sustainable energy and to reduce greenhouse emissions.

Photovoltaics (PV) has been at the forefront in the drive towards renewable energy with world installation capacity of ~ 834 GW [9]. The drastically reduced price of PV modules from about 106 $/W in 1976 to around 0.38 $/W in 2019 [10], has accelerated its adoption and consequently increased PV module production. The demand for PV installation is projected to increase in the coming years, which means it is necessary to keep the cost low. The cost of PV modules is currently at their lowest, with the components accounting for most of the cost, as such, improvement of efficiency is the key to keeping the cost even lower with the projected demand. The PV market is mostly dominated by the more advanced mono crystalline and multicrystalline silicon technology occupying about 95 % of the PV market share. The leading thin film

technologies, which include cadmium telluride (CdTe) and copper indium gallium di-selenide (CIGSe) occupy a far smaller market share. Research efforts in thin film technologies have expedited, which has yielded lab efficiencies of ~ 23.4 % in CIGSe [11], 21.0 % in CdTe and 23.7 % in Perovskite [12].

Efficiency is a very important parameter in PV technology, and the leading PV technology, particularly Si is close to its practical peak efficiencies [13, 14]. However, the need for improved efficiency calls for advanced technological concepts to increase the efficiency and payback time of PV modules. One of such advanced concepts is multi-junction or tandem solar cells, which reduces the losses incurred in single junction solar cells [15]. Fig. 1.1a is a schematic depiction of a single junction solar cell with a single bandgap. With such a bandgap, losses incurred in such a solar cell in dominated by absorption and thermalization losses. Absorption loss is when photons with energies lower than the solar cell bandgap are not absorbed while thermalization losses occurs when photons of energies higher than the bandgap are absorbed, but the excess energies are loss to the thermal lattice.

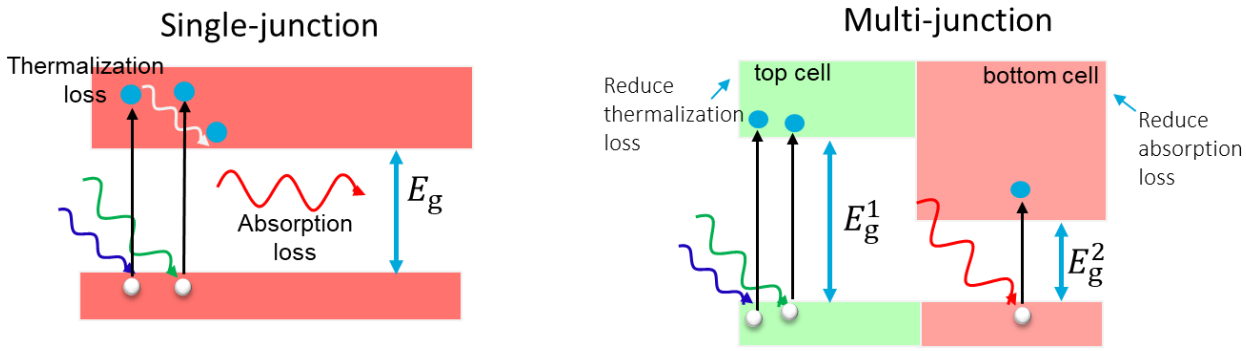

Figure 1.1: (a) Illustration of absorption and thermalization losses in a single junction solar cell, and (b) mitigation of the losses in a multi-junction solar cell.

To mitigate absorption and thermalization losses, the concept of tandem solar cell as illustrated in Fig. 1.1b makes use of two or more solar cells, with different bandgaps stacked on top of the other. By using different optimum bandgaps, the losses which would otherwise be incurred in single junction solar cells are mitigated, that is, thermalization losses reduced by a high bandgap top cell and absorption losses reduced by a low bandgap bottom cell. Theoretically, efficiencies up to 46 % can be achieved with different tandem configurations [16, 17].

Si and CIGSe with bandgap around 1.1 eV and having achieved greater than 23 % fit the criteria for bottom cells. Their use as bottom cells have already been demonstrated with perovskite as top cell and efficiencies of 29.3 % and 24.2 % have been achieved in perovskite-silicon and perovskite-CIGSe configurations respectively [15, 18, 19]. Even though these results are promising, perovskite solar cells are limited by stability issues [20] and it is necessary to seek alternative materials for top cell in such tandem configuration.

Copper indium gallium disulfide, $Cu(In,Ga)S_2$, is a chalcopyrite material which has not received as much attention as its well-researched counterpart, $Cu(In,Ga)Se_2$. The possibility of tuning its bandgap from ~ 1.55 eV in $CuInS_2$ [21] to ~ 2.45 eV in $CuGaS_2$ [21] not only provides suitable bandgap values which makes it useful as a single-junction solar cell but also as a top cell in tandem applications [22, 23]. Unlike perovskite which has stability issues, $Cu(In,Ga)S_2$ has a chalcopyrite phase which is stable even when compositions deviate from stoichiometry. As a single junction solar cell, the highest certified efficiency for $Cu(In,Ga)S_2$ is 15.5 % [24], which was realized on Cu-deficient absorbers grown at high temperature. This efficiency is much lower than those recorded in CIGSe and perovskite solar cells for examples, moreover, there is still a high open-circuit voltage (V_{OC}) deficit in comparison to the selenide counterpart $Cu(In,Ga)Se_2$ [24, 25]. In pure $CuInS_2$ investigated by Lomuscio et al. [26, 27], the optoelectronic quality of Cu-poor absorbers was bad, although the optoelectronic quality was better translated to V_{OC} than in Cu-rich absorbers. Nevertheless, better optoelectronic quality was achieved in the Cu-rich $CuInS_2$ through high deposition temperatures.

The use of $Cu(In,Ga)S_2$ absorbers as a top cell in tandem applications requires that high efficiencies be achieved in its use as a single junction solar cell, and this has been the main motivation in various research on $Cu(In,Ga)S_2$. An efficiency of 16 % has recently been reported by Barreau et al. [28], although the bandgap of the absorber was 1.55 eV, which is lower than the optimum bandgap of 1.6-1.7 eV needed for a top cell in tandem applications. Given the similarity between the chalcopyrite structure of $Cu(In,Ga)S_2$ and the well-established CIGSe, it can be appealing to assume that the procedures which allows high performance to be achieved in CIGSe absorbers and devices translates to $Cu(In,Ga)S_2$, the contrary has actually been reported by Barreau et al [29-31]. This contradiction shows a need for better understanding of the $Cu(In,Ga)S_2$ system and alternate means of achieving high performance in $Cu(In,Ga)S_2$

Structure of the thesis

Chapter 2 present an overview of the chalcopyrite structure. First, the chalcopyrite crystal structure and the phase diagram of CuS-Ga_2S_3 system and pseudo-binary phase system of $CuGaS_2$-In. Intrinsic point defects of $CuGaS_2$ and a literature review of defects in $CuGaS_2$ are presented.

Chapter 3 introduces the structure of the Cu(In,Ga)S_2 devices and the recombination losses in a typical solar cell. Next, the benefits of bandgap-grading in solar cells are briefly discussed. After, the physical vapour deposition system used to grow the investigated absorbers is introduced. Following this, the deposition steps for a single-stage co-evaporation process used for growing CuGaS2 films is described. Then, the two-stage and the three-stage deposition methods used for achieving Cu-rich and Cu-poor compositions are explained.

In Chapter 4, time-resolved photoluminescence measurements were performed on several Cu-rich $CuInS_2$ absorbers. The $CuInS_2$ absorbers have been reported to show improved quasi-Fermi level splitting (QFLS) with increased deposition temperature and copper content. The lifetimes were correlated with the doping level to investigate the origin of the improved QFLS.

Chapter 5 presents investigations of the electronic structure of $CuGaS_2$ absorbers. Defect spectroscopy by photoluminescence analyses (PL) was performed using excitation and temperature dependent measurements to investigate defect levels. Full characterization of shallow defect levels were performed on Cu-rich $CuGaS_2$ absorbers. Lastly, a novel solar cell is completed on Cu-rich $CuGaS_2$ absorber.

Chapter 6 contains several deposition processes for improving the quality of Cu(In,Ga)S_2 absorber to obtain highly efficient devices. By PL analyses, the origin of bulk recombination limiting the optoelectronic quality of Cu-rich Cu(In,Ga)S_2 absorbers were investigated. Then, the influences of front surface gallium on the optical bandgap and how it can improve the QFLS of the absorbers, but hinder device performance are presented. Subsequently, the optimum surface gallium for improved performance of Cu(In,Ga)S_2 devices is obtained. The last parts of the same Chapter 6 are devoted to the back gallium gradient. Different analytical techniques were used to investigate the challenges of phase-segregation limiting the optimum quality of high gallium Cu(In,Ga)S_2 absorbers and devices, then various deposition procedures were used to mitigate the phase-

segregation. These deposition procedures include the thermal cracking of larger sulfur molecules to obtain smaller species, the use of first stage substrate temperature to mitigate phase-segregation, the influence of substrate temperature ramping rate on notch width, and the influence of Cu excess on $Cu(In,Ga)S_2$ absorber and devices.

The summary of the results and outcomes discussed in the thesis and the outlook for future experiments are presented in Chapter 7.

Contributions to the thesis

In Chapter 4, I performed lifetime analyses and estimated doping concentration on all the Cu-rich $CuInS_2$ absorbers. The growth and optoelectronic characterization of the absorbers were performed by Dr. Alberto Lomuscio. Dr. Michele Melchiorre carried out the compositional characterization on the absorbers by energy dispersive x-ray (EDX) spectroscopy and performed KCN-etching to remove the secondary Cu-excess phases on the absorbers. Dr. Mohit Sood performed capacitance-voltage (CV) measurements to complement the doping concentration.

For the absorbers presented in Chapter 5, I prepared all the $CuGaS_2$ absorbers in the then newly commissioned physical vapour deposition system (S-PVD). Defect spectroscopy through low temperature photoluminescence measurement and analyses was performed by me. Dr. Michele Melchiorre and I characterized the composition of the absorbers by EDX. The KCN etching performed on the absorbers and acquisition of the cross-sectional micrographs using scanning electron microscope were by Dr. Michele Melchiorre. The Raman measurement in carried out by Dr. Mael Guennou and the XRD measurement was performed by me. Dr. Mohit Sood fabricated the device on the novel on $CuGaS_2$ solar cell and performed electrical characterization on it.

In Chapter 6, all the $Cu(In,Ga)S_2$ absorbers were prepared by me, with the exception of Section 6.1 where four select absorbers were processed by Dr. Sudhanshu Shukla. I performed energy dispersive X-Ray (EDX), X-Ray dispersion (XRD) and all optical measurements, characterization and analyses on the $Cu(In,Ga)S_2$ absorbers. Dr Michele Melchiorre acquired all the SEM cross-sectional images and did EDX mapping on the absorbers in Section 6.3. Dr. Mohit Sood and Dr Michele Melchiorre completed solar cells on the $Cu(In,Ga)S_2$ absorbers. Electrical analyses on the $Cu(In,Ga)S_2$ solar in Section 6.2.2 and Section 6.3 were performed by me, while Dr. Mohit Sood

carried out the electrical characterization and analyses on the solar cells presented in Section 6.4. Aline Vanderhaegen performed the PL decay measurements on absorbers in Section 6.4. All Secondary-ion mass spectrometry (SIMS) depth analyses performed on the absorber layers were by Dr. Nathalie Valle and Dr. Brahime El Adib at Luxembourg Institute of Science and Technology (LIST). All the cathodoluminescence measurements on the samples were implemented at the Cambridge Centre for Gallium Nitride at Cambridge university by Dr. Gunnar Kusch and Benson Chun Pang Law.

Chapter 2

Fundamentals and literature review

In this chapter, the characteristic properties of the chalcopyrite structure which the $Cu(In,Ga)S_2$ and its parent compounds belong to are discussed. First, Section 2.1 describes the chalcopyrite crystal structure, the phase diagrams of $CuGaS_2$ and $Cu(In,Ga)S_2$, as well as the classification of intrinsic defects inherent to crystals. Section 2.2 discusses charge-transfer, which is essential for the functionality of semiconductors along with the generation of charge carriers. Section 2.3 will discuss the different radiative transitions observed in a photoluminescence experiment. Afterwards, the methods used in evaluating the photoluminescence emission to determine the quasi-Fermi level splitting of an absorber is described. A review of the transition energies detected in $CuGaS_2$ from various reports is presented in Section 2.4. Lastly, in Section 2.5 a description of the set-up used for the photoluminescence measurements in this thesis is described.

2.1 Chalcopyrite structure

$Cu(In,Ga)S_2$ is a direct bandgap quaternary semiconductor obtained by alloying $CuInS_2$ and $CuGaS_2$; both ternary compounds belonging to the $A^{I}B^{III}C_2^{VI}$ chalcopyrite family. This compound is much like $Cu(In,Ga)Se_2$, obtained from $CuInSe_2$ and $CuGaSe_2$. The description of the phase diagram will focus on $CuGaS_2$, except otherwise stated. However, the description still applies to the $Cu(In,Ga)S_2$ quaternary compound with minor changes which will be indicated.

2.1.1 Crystal structure

$Cu(In,Ga)S_2$ crystallizes into a tetragonal chalcopyrite structure. The chalcopyrite structure derives its name from the naturally occurring $CuFeS_2$ [32]. This is a lattice structure derived from the sphalerite structure found in the binary zincblende crystal, e.g., ZnS, which is in turn a derivation of the diamond or cubic lattice structure of group IV atoms, such as silicon and germanium. Fig.

2.1 shows the relation of the chalcopyrite structure to the cubic structure. The cubic structure possesses a bond of one atom to four valence electrons ratio. The zincblende structure is a face-centered cubic structure formed by substituting the group IV atom of the cubic structure by one of each atom of group II and group VI as found in ZnS, CdTe and CdS, etc., or by one of each atom of group III and group V as in GaAs, InSb and InP, as illustrated in Fig. 2.1.

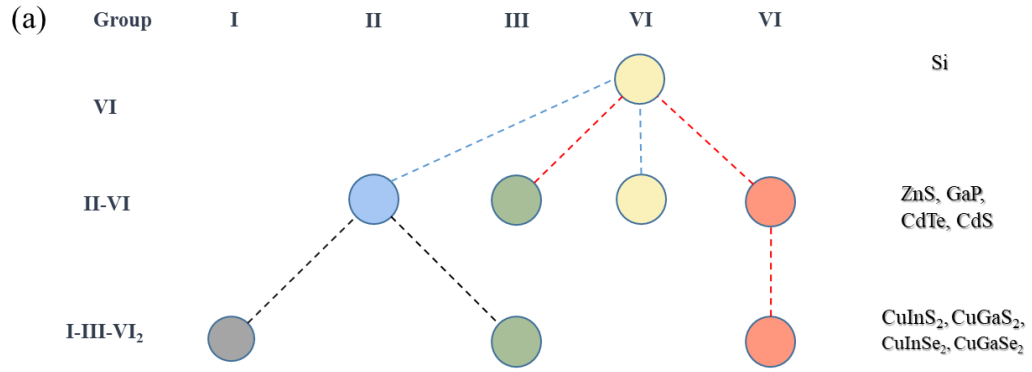

Figure 2.1: Derivation of the chalcopyrite lattice structure from the zincblende structure and the cubic lattice structure of the group IV atom.

Further disintegrating the sphalerite zincblende structure, by the substitution of two group II atoms for one group I and one of group III atom, the result is a chalcopyrite structure. As such, the chalcopyrite structure comprising the joint I-III-VI_2 group atoms is a superlattice of two-unit-cell of the zincblende structure of II-VI or III-V group atoms or eight atoms of the diamond structure. Fig. 2.2a and Fig. 2.2b show the lattice structure of the zincblende and the chalcopyrite structures. In both Fig. 2.2a and Fig. 2.2b, every group I and group III atom is tetrahedrally bonded to four group VI atoms and every group VI atom is tetrahedrally bonded to two group I atoms and two group III atoms. The group VI atom is referred to as the anion, while the group I and group III atoms are referred to as cations. Owing to the different sizes of the atoms, the substitution of group II atom with group I and group III atoms in the chalcopyrite leads to a dislocation of the anion from its ideal position, and the bond lengths between the cations and anions which creates a structural difference between the zincblende superlattice and the actual chalcopyrite unit cell. This different bond length results in bond length mismatch, anion displacement and tetragonal distortion in the chalcopyrite structure [33]. For instance, there is a different bond length between Cu-S and

In/Ga-S. The lattice constants, a and c are functions of the bond length as shown in Fig. 2.2. In essence, the tetragonal distortion or splitting, given by the quantity $\eta = c/a$, is a measure of the tetragonal distortion or a deviation from the ideal zincblende superlattice, in which case, the ratio between the lattice constants will be 2. A measure of the anion dislocation is given by u, a quantity defined by the equation:

$$u = \frac{1}{4} + \frac{R_{AC}^2 + R_{BC}^2}{a^2} \tag{2.1}$$

where R_{AC} and R_{BC} are the bond lengths between the C anion and the A and B cation respectively.

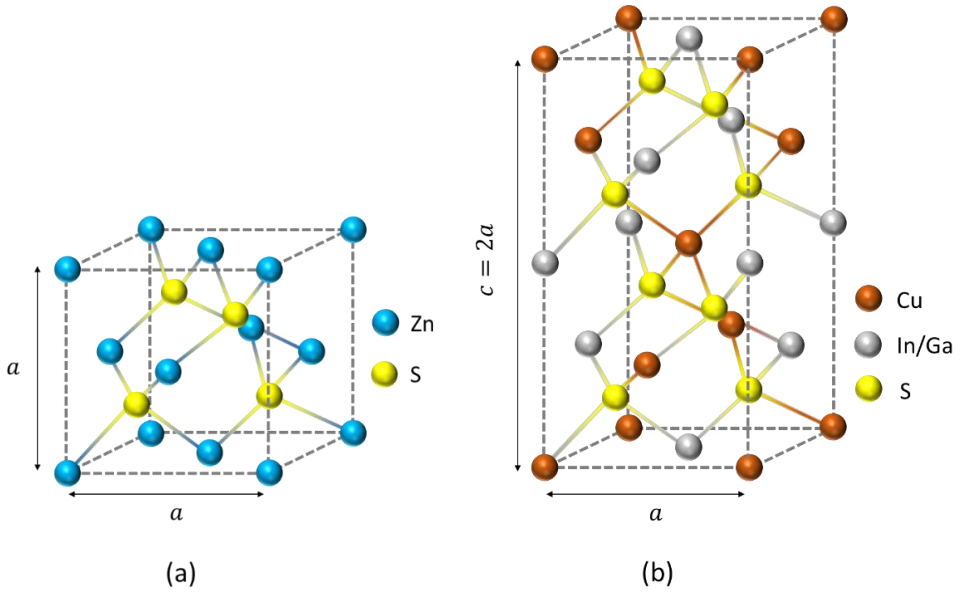

Figure 2.2: (a) A unit cell of the zincblende sphalerite structure, with ZnS for example. (b) Unit cell of the chalcopyrite structure.

The bond length mismatch is represented by $\alpha = R_{AC}^2 - R_{BC}^2$. When there is no bond length mismatch, and there is no tetragonal distortion, as is the case of the zincblende structure, $u = \frac{1}{4}$. The values of the lattice constants taken from the works of Abrahams and Bernstein for $CuInS_2$ are $a = 5.523$ Å and $c = 11.13$ Å while the values for $CuGaS_2$ are $a = 5.347$ Å and $c = 10.47$ Å, putting the tetragonal distortion at 2.016 and 1.959 for $CuInS_2$ and $CuGaS_2$ respectively. The influence of η deviating from 2 can be seen when X-ray diffraction is performed on the

chalcopyrite compounds by a splitting of a reflection peak; this will be discussed in Chapter 5. It should be mentioned that in $Cu(In,Ga)Se_2$, gallium content does influence tetragonal distortion, as Abou-Ras et al. has shown that η is less than 2 for $x > 0.23$ and greater than 2 for $x < 0.23$ [34]. An isovalent substitution of an atom in a ternary compound, that is, fractional exchange of indium in $CuGaS_2$ or gallium in $CuInS_2$, forms the quaternary compound $CuIn_{1-x}Ga_xS_2$ with $0 \leq x \leq 1$. Hence, the band gap of the quaternary $CuIn_{1-x}Ga_xS_2$ compound can be tuned from 1.55 eV in $CuInS_2$ ($x = 0$), to 2.53 eV in $CuGaS_2$ ($x = 1$) at 2 °K [21]. The overall ratio of Ga in the compound is expressed by [Ga]/([Ga]+[In]) (GGI) ratio. When the GGI ratio is 0, the compound contains no gallium and the ternary compound $CuInS_2$ is formed, while when the GGI ratio is 1, the ternary compound $CuGaS_2$ is formed. The dependence of the bandgap of the quaternary $Cu(In,Ga)S_2$ on gallium content is given by:

$$E_G^{CIGS} = E_G^{CIS}(1-x) + E_G^{CGS}x - bx(1-x) \tag{2.2}$$

with E_G^{CIS}, E_G^{CGS} and E_G^{CIGS} being the bandgap of the $CuInS_2$, $CuGaS_2$ and the $CuIn_{1-x}Ga_xS_2$ alloy, while *b* is referred to as the bowing factor. Using the bowing factor of 0.2 eV, taken from the report of Bodnar et al. [35], the bandgap of the quaternary compound $CuIn_{1-x}Ga_xS_2$ in dependence of Ga-content or GGI ratio is illustrated in Fig. 2.3. The room temperature bandgap of the $CuIn_{1-x}Ga_xS_2$ compounds studied in this thesis is between 1.5 eV and 2.45 eV.

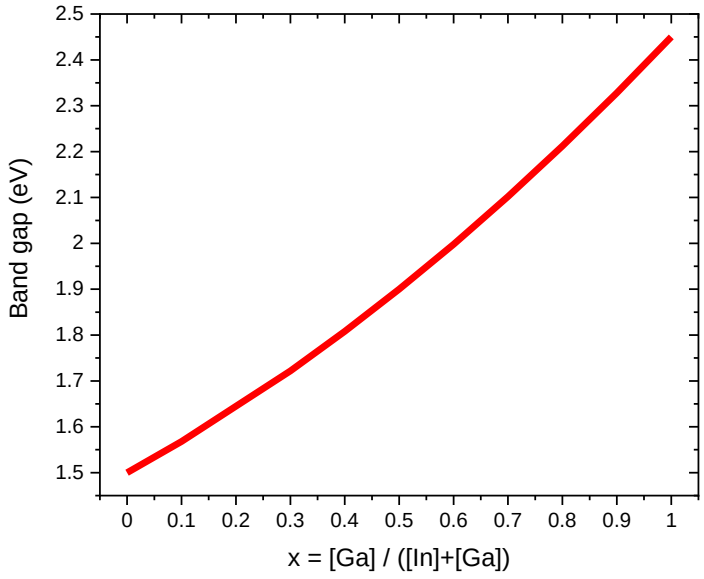

Figure 2.3: Room temperature bandgap of $CuIn_{1-x}Ga_xS_2$ in dependence on Ga-content.

2.1.2 Phase diagram

Several phases can form along with the chalcopyrite phases during the growth of a $CuIn_{1-x}Ga_xS_2$ absorber, since factors such as temperature and the availability of constituent elements can influence the phases formed during the growth of the absorber. The temperature-dependent liquid phases formed along the Cu_2S-Ga_2S_3 pseudo-binary system has been researched by Kokta et al. [36], and later by Maeda et al. [37, 38]. The pseudo-binary phase diagram taken from the work of Kokta et al. [36] is present in Fig. 2.4a with minor modifications. For the $CuGaS_2$ system in Fig. 2.4a, the stoichiometric composition of $CuGaS_2$ exist at 50 mol % Ga_2S_3 [36].

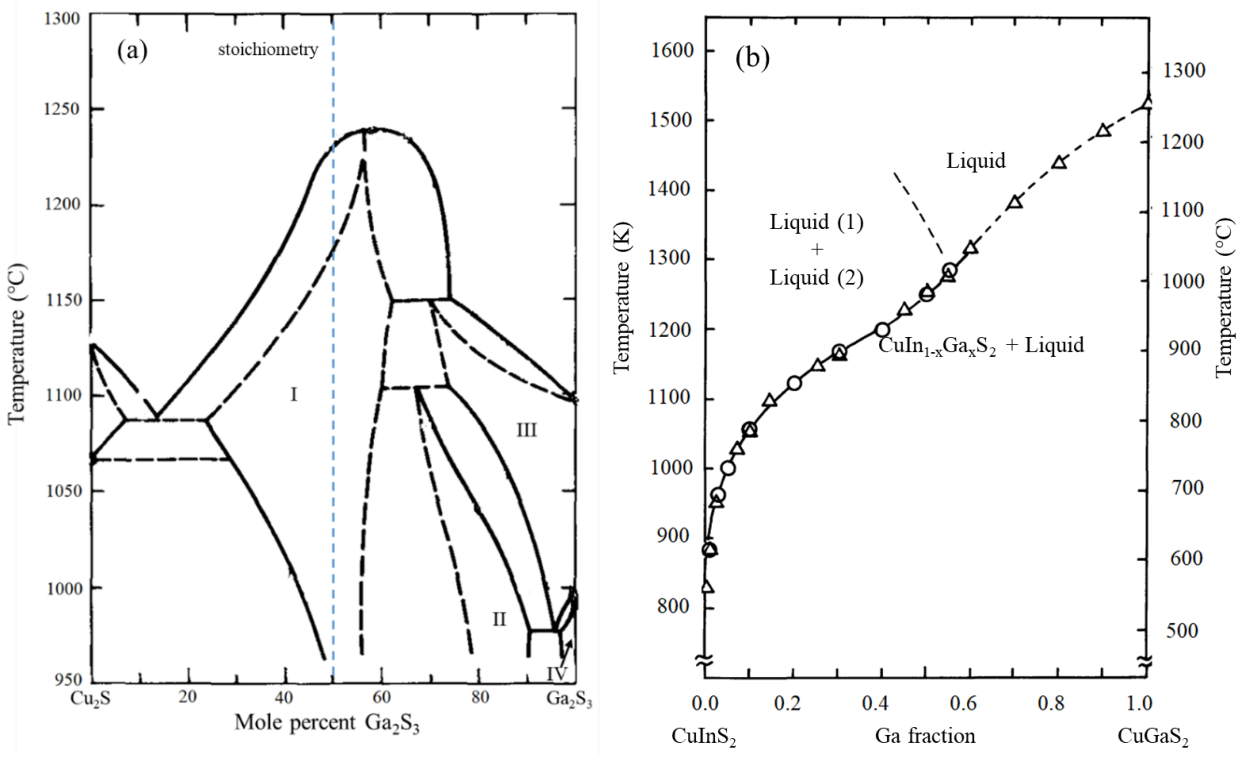

Figure 2.4: (a) Pseudo-binary phase diagram of the Cu_2S-Ga_2S_3 system as a function of mol % Ga_2S_3 and temperature. Region I represents the main chalcopyrite phase [36]. (b) $CuGaS_2$-In pseudo-binary phase diagram with the liquid immiscibility region indicated by liquid (1) + liquid (2). Liquid (1) is S-excess In solution, while liquid (2) is S-deficient In solution [39]. The diagrams are excerpts from Ref. [36] and [39] with minor modifications.

At room temperature, the chalcopyrite structure represented by Region I in Fig. 2.4a exists from 50 mol % to 55 mol % Ga_2S_3, while a stannite-type $CuGa_5S_8$ exist at ~70-90 mol % Ga_2S_3 in Region II [36-38]. At 60 mol % ≤ Ga_2S_3 ≤ 75 mol % in Region III, a mixture of chalcopyrite-type and stannite-type phases were identified through X-ray diffraction by Maeda et al. [37]. From Fig. 2.4a, the chalcopyrite phase has a maximum melting temperature of 1240 °C with no high-temperature phases existing outside this region [36]. The stannite-type $CuGa_5S_8$ is an ordered defect compound (ODC) with a wide existence range which is unstable at temperatures higher than 1150 °C, as it decomposes. The bandgap of the stannite $CuGa_5S_8$ is approximately 2.66 eV, which is wider than the bandgap of chalcopyrite $CuGaS_2$ at 2.45 eV [37]. The other regions of the phase diagram in Fig. 2.4a are not well known, however, the regions were reported to likely exhibit ODC phases [36].

The pseudo-binary phase diagram in the Cu_2S-In_2S_3 system has been studied by Binsma et al. [40]. The chalcopyrite phase exists between 37-70 mol % In_2S_3 and, although the melting point of the ternary $CuInS_2$ compound is at 1090 °C, the chalcopyrite phase is only stable up to 980 °C, after which there is a transition to a sphalerite phase. Beyond 1045 °C, the phase is transformed to a wurtzite-type phase. Above 83 mol % In_2S_3, the compound is $CuIn_5S_8$ with a thiospinel phase up to 1085 °C at which it melts.

To understand the behaviour of indium incorporation in $CuGaS_2$, Miyake et al. studied the phase diagram of the $CuGaS_2$-In pseudo-binary system in which indium solution is saturated by stoichiometric $CuGaS_2$ [39]. The curve presented in Fig. 2.4b shows the liquidus temperature plotted against the mole fraction of indium in stoichiometric $CuGaS_2$. From Fig. 2.4b, it can be observed that the liquidus temperature decreases with the increase of In-content in the $CuGaS_2$-In solute. In the study, the crystals obtained were investigated by X-ray powder diffraction and energy-dispersive X-ray microanalysis. As depicted in Fig. 2.4b, at temperatures below 1020 °C, it was reported that there is a miscibility gap at which the indium solution saturated with stoichiometric $CuGaS_2$ separates into two liquid phases which comprise S-excess and S-deficient indium solutions.

More recently, crystallographic analysis of the Cu_2S-In_2S_3-Ga_2S_3 pseudo-ternary system by Thomere et al. produced the phase diagram shown in Fig. 2.5. The $Cu(In,Ga)S_2$ pseudo-ternary phase system was shown to be more complex and possess some dissimilarity from the

$Cu(In,Ga)Se_2$ system [31]. They reported that, for $Cu(In,Ga)S_2$, the chalcopyrite structure is not as adaptable as in $Cu(In,Ga)Se_2$, because indium is less adaptable to the chalcopyrite structure under Cu deficiency conditions [31, 41]. As seen on the phase diagram in Fig. 2.5, when Cu is introduced into the $(In,Ga)_2S_3$ precursor and the Cu-content in the compound increases, two different phases - trigonal and cubic - are formed in the Cu-deficient phase. It was reported that these two phases do not mix, rather they remain segregated in the prepared absorber. These segregated phases present compositional plateaus, particularly in the Cu-deficient $Cu(In,Ga)S_2$ absorber [29, 30]. Another revelation from the phase diagram in Fig. 2.5 is that, near stoichiometric compositions, there is a narrow existence range for the chalcopyrite phase in $Cu(In,Ga)S_2$.

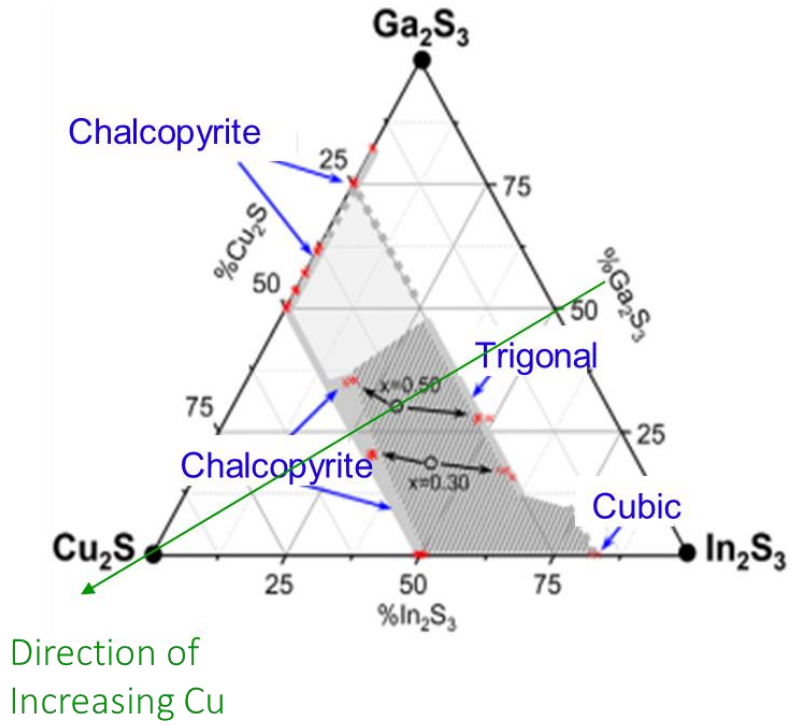

Figure: 2.5: The Cu_2S-In_2S_3-Ga_2S_3 pseudo-ternary diagram as studied by Thomere et al. [31]. The diagram is taken from Ref. [31] with minor modifications.

2.1.3 Intrinsic point defects

By the law of thermodynamics and kinetics of defects, perfect semiconductors do not exist since defects are inherent in semiconductors. The existence of intrinsic defects is implicit in the complex

chalcopyrite structure, more so in $CuIn_{1-x}Ga_xS_2$ which is composed of many elements. The fact that the $CuIn_{1-x}Ga_xS_2$ compound can be intentionally modified during growth by controlled amounts of impurities or defects contribute to the usefulness of $CuIn_{1-x}Ga_xS_2$, although defects can also be detrimental. Generally, the types of defects can be classified as follows [42]:

- **Misalignment** of atoms in the crystal which causes line defects or dislocation.
- **Planar defects** formed by arrays of dislocations.
- **Voids** are volume defects where several atoms are either missing or replaced by another solid.
- **Point defect** occurs at single lattice points when an atom is displaced from its site in the crystal. Such defect can either be intrinsic of extrinsic.

In chalcopyrite compounds, intrinsic point defects are essential since they are critical to the doping of the compounds [43, 44]. The different elements which constitute the ternary compound mean that there are several prospective intrinsic point defects which could occur in $Cu(In,Ga)S_2$. The possible types of defects are as follows:

- **Vacancies** are caused by atoms displaced or missing from their ideal position in the crystal lattice. They could be V_{Cu}, V_{In}, V_{Ga}, V_S.
- **Interstitials** occur when atoms occupy usually vacant positions between the crystal structure. These can be Cu_i, In_i Ga_i S_i.
- **Antisites** develop when atoms occupy wrong positions belonging to another atom. These are Cu_{In} Cu_{Ga} In_{Cu} Ga_{Cu}.
- **Complexes** form when two or more of the defects combine to form a new electronic state, such as $2V_{Cu}$-In_{Cu}, In_{Cu}-V_{Cu}, Ga_{Cu}-V_{Cu}, Cu_i-Cu_{In}, Cu_i-V_{In}, Cu_i-$2V_{Cu}$, etc.

2.2 Generation and recombination in semiconductors

A vital aspect of a semiconductor is the transport of charge carriers and electrical currents. The carriers can be either electrons or holes, as such, carrier concentration is an important characteristic in the operation of a semiconductor device. Information in this section is available in semiconductor textbooks. However, in this thesis, the background information on semiconductor

is assimilated from the references in [42, 45-47]. The periodic structure of the semiconductor result in a split energy level that form energy bands of allowed and forbidden energy, referred to as bandgap. In the ideal intrinsic semiconductor, at $T = 0\ K$, all the energy states in the valence band, that is, the band below the forbidden energy are occupied by electrons while the states in the conduction band, that is, above the forbidden gap, are empty. As the temperature increases and the crystal lattice vibrates, electrons gain enough energy and are liberated into the conduction band, leaving behind holes in the valence band. As such, in an intrinsic semiconductor, the concentration of holes (p_0) in the valence band and concentration of electrons (n_0) in the conduction band are equal, and both concentrations can be designated $n_i = n_0 = p_0$.

2.2.1 Carrier concentrations in semiconductors

The concentration of charge carrier is given by the integration of the density of states function, g(E), which describes the number of allowed states per unit volume and energy, and the Fermi-Dirac distribution function, $f(E)$, which describes the occupation probability, that is, the ratio of states filled with electrons to the total allowed states. For a non-degenerate semiconductor and in thermal equilibrium, the solutions expressing the concentration of electrons (n_0) and holes (p_0) are given by,

$$n_0 = N_C \exp\left(-\frac{E_C - E_F}{k_B T}\right) \tag{2.3}$$

$$p_0 = N_V \exp\left(-\frac{E_F - E_V}{k_B T}\right) \tag{2.4}$$

Where N_C and N_V are the effective density of states of the conduction band and the valence band respectively, E_F is the Fermi energy, E_C and E_V are the conduction band-edge and valence band-edge respectively, k_B is the Boltzmann constant and T is the temperature. Equation (2.3) and equation (2.4) are true if Boltzmann approximation is applicable, that is, if the Fermi energy lies more than $3k_BT$ away from the band-edges. In the intrinsic semiconductor, that is, without impurities, the concentration of excited electrons and holes are equal, and the Fermi energy level is midgap, then the intrinsic carrier concentration is

$$n_0 p_0 = n_i^2 = N_C N_V \exp\left(-\frac{E_C - E_V}{k_B T}\right) \tag{2.5}$$

$E_C - E_V = E_g$, is the bandgap. The equation (2.5) shows that carrier concentration in an intrinsic semiconductor is strongly temperature dependent. Since there is no Fermi level in equation (2.5), it is valid for doped semiconductor as well as the intrinsic semiconductor.

In many semiconductor applications, a high charge carrier concentration is desired, and the intrinsic semiconductor might not be applicable for such semiconductor devices, since a very high temperature would be necessary for high carrier concentrations. As such, for many semiconductor applications, extrinsic semiconductors are more suitable; these are semiconductors that have been manipulated by doping with controlled amounts of impurities or defects. The dopants contribute additional charge carriers which boosts the net carrier concentration in the semiconductor. A semiconductor is p-type (doped) if the majority charge carriers are holes and the minority charge carriers are electrons, while it is n-type (doped) if the majority charge carriers are electrons, and the minority charge carriers are holes. When the semiconductor is in a state of non-equilibrium through illumination, for example, more charge carriers are generated, and the concentration of electrons (n) and holes (p) strongly increases above the equilibrium carrier concentration. The excited carriers rapidly thermalize with the crystal lattice and if the carriers have a long enough lifetime, a quasi-equilibrium state is formed. The Fermi energy can no longer be described by a single Fermi level, rather the Fermi level splits in an electron quasi-Fermi level, which describes the concentration of electrons, and a hole quasi-Fermi level which describes the concentration of holes. The density of electrons can be described by

$$n = N_C \exp\left(-\frac{E_C - E_{FC}}{k_B T}\right) \tag{2.6}$$

and the density of holes described by

$$p = N_V \exp\left(-\frac{E_{FV} - E_V}{k_B T}\right) \tag{2.7}$$

Hence, the product of the carrier concentrations under non-equilibrium conditions is such that,

$$np = n_i^2 \exp\left(\frac{\Delta E_F}{k_B T}\right) \tag{2.8}$$

$E_{FC} - E_{FV} = \Delta E_F$ is the quasi-Fermi level splitting (QFLS). The equation (2.8) shows that, under non-equilibrium conditions, the product of charge carrier concentrations exponentially depends on the quasi-Fermi level splitting. The QFLS is a figure of merit of a semiconductor, and it describes the maximum open-circuit voltage achievable. How the QFLS of an absorber is evaluated will be described in Subsection 2.3.2.

2.2.2 Charge carrier generation

The section has been taken from the textbook [48], readers are advised to consult the book for further background reading. When an external source, such as an external voltage source or illumination, is applied to a semiconductor, it is no longer in a state of equilibrium. In the case of illumination by a steady-state source, such as a continuous-wave laser, after any reflection loss (R), the photon flux density $\phi(x)$ inside the semiconductor is described by the Beer-Lambert law:

$$\phi(x) = \phi_0(1 - R)\mathrm{e}^{-\alpha x} \tag{2.9}$$

ϕ_0 is the photon flux density impinging on the semiconductor and x is an arbitrary position in the absorber [48]. The absorption of the incident photon flux by the semiconductor material depends on its absorption coefficient α. After absorption of the excitation photons, and excess carriers are generated and the quasi-Fermi level splits, depending on the carrier lifetime, the excess carriers remain in the quasi-equilibrium state until they recombine. However, because of the continuous generation of excess carriers by the steady-state excitation source, after some time, equilibrium between generation $G(x)$ and recombination $R(x)$ is established. The rate of generation follows as

$$G(x) = R(x) = -\frac{\partial \phi(x)}{\partial x} = \alpha \phi_0(1 - R)e^{-\alpha x} \tag{2.10}$$

With a pulsed excitation, where the excitation source is not continuous but as a train of short pulses, the generation of excess carriers occurs per pulse. For both excitation sources, if the laser parameters and output properties of the laser are known, the photon flux density ϕ_0 can be estimated.

2.3 Photoluminescence spectroscopy

Photoluminescence is the emission of photons by electrons which have been excited from a state of thermal equilibrium (valence band) into a higher energy state (conduction band) through the absorption of excitation photons. The emission occurs when the electrons in a higher energy state recombine with holes in the valence band by releasing the absorbed photons. The photons emitted is a spectrum which bears a signature of the semiconductor characteristics and can give insights into the properties and electronic structure of the semiconductor. The observable transitions in a photoluminescence experiment will be discussed in the following section. The textbooks [49, 50] have been used for references.

2.3.1 Observable transitions in a photoluminescence experiment

The observable transitions in a photoluminescence experiment are illustrated in Fig. 2.6.

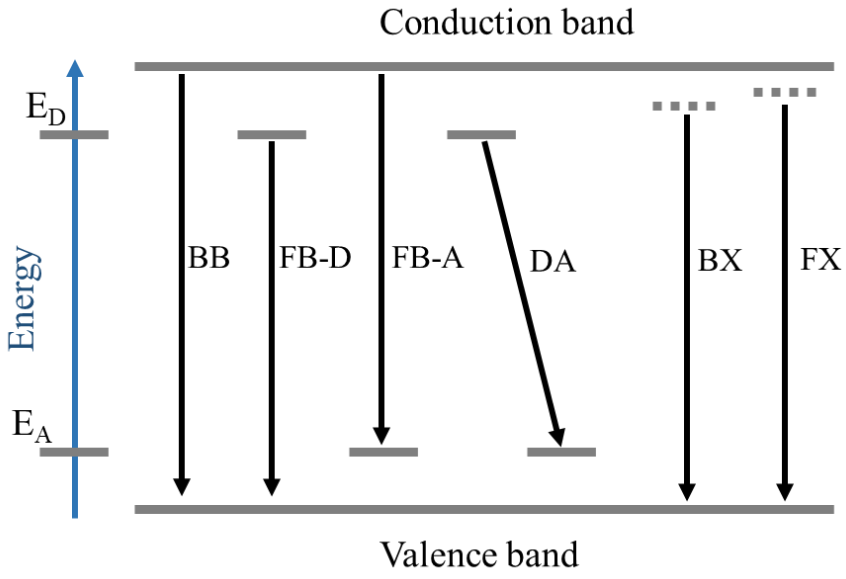

Figure 2.6: Illustration of observed optical transitions in a photoluminescence experiment. The transitions presented are band-to-band (BB), free-to-bound associated with a donor (FB-D), free-to-bound associated with an acceptor (FB-A), donor-acceptor pair (DA), bound-exciton (BX), and free-exciton (FX) transitions.

Band-to-band transition

At room temperature, there is an abundance of free carriers in the band-edges because excitons dissociate due to thermal ionization and shallow defects are emptied as charge carriers are re-emitted to the band-edges. The net recombination rate (R) is the sum of radiative (R_{rad}) and non-radiative (R_{nrad}) recombination rates. The radiative recombination rate is proportional to the free electron (n) and the free hole (p) concentrations. Radiative band-to-band transition becomes unavoidable since electrons in the conduction band minimum recombine with holes in the valence band maximum by the spontaneous emission of photons. In photoluminescence measurements, deviations from the thermal equilibrium are of interest, as such, the net radiative recombination rate is

$$R_{rad}^{net} = B(np - n_0 p_0) \tag{2.11}$$

where p_0 and n_0 are the electron and hole carrier concentrations at thermal equilibrium respectively and B is the radiative recombination coefficient. Substituting the non-equilibrium carrier concentrations in equations (2.6) and (2.7) into equation (2.11), the relationship between the net radiative recombination rate and the quasi-Fermi levels is derived as

$$R_{rad}^{net} = B n_i^2 (\exp\left(\frac{\Delta E_F}{k_B T}\right) - 1) \tag{2.12}$$

Equation (2.12) shows that in a semiconductor, the net radiative (band-to-band) recombination rate is exponentially proportional to the quasi-Fermi level splitting. The analyses of the quasi-Fermi level splitting followed in this work will be presented in Subsection 2.3.2.

Free-to-bound transition

The introduction of defects into the crystal lattice of a semiconductor gives rise to localized states within the mid-gap of the semiconductor. If the localized states lie close to the band-edges, a shallow defect level is formed, i. e., shallow acceptor level if close to the valence band or shallow donor level if close to the conduction band. The weak bond of holes or electrons to shallow defects means that when thermally excited, charge carriers are contributed to the semiconductor, thereby boosting electrical conductivity. The energy required to break the bond is referred to as ionization

or binding energy ($E_{A/D}$). The recombination of free electrons (or holes) in the conduction (or valence) band with holes (or electrons) in a shallow acceptor (or donor) level is called free-to-bound transition. The equation describing the free-to-bound transition is given by

$$h\omega_{FB} \approx \left[E - (E_g - E_{A/D})\right]^{1/2} \exp\left(-\frac{E - (E_g - E_{A/D})}{k_B T}\right) \tag{2.13}$$

Donor-to-acceptor transition

In a compensated semiconductor where both acceptors (A) and donors (D) are present, the recombination of electrons from the neutral donor level with holes from the neutral acceptor level is called donor-to-acceptor (DA) pair transition. The DA transition leave oppositely charged defects with effective Coulomb attraction. The energy of the emitted photon ($h\omega_{DA}$) in a DA pair transition is

$$h\omega_{DA} = E_g - (E_A + E_D) + \frac{q^2}{4\pi\varepsilon_r\varepsilon_0 R_{DA}} \tag{2.14}$$

E_A and E_D are the energy levels corresponding to the acceptor level and donor levels, respectively. The last term describes the additional Coulomb interaction between the donor and acceptor levels with q being the elementary charge, ε_0 is vacuum permittivity, ε_r is relative permittivity and R_{DA} is the spatial distance between the donor and acceptor.

2.3.2 Quasi-Fermi level splitting analyses

When the semiconductor is not in equilibrium, there is a splitting of the quasi-Fermi energy levels, and the concentration of the electrons and holes is described by the hole and electron Fermi levels, respectively [51]. The quasi-Fermi level splitting (QFLS) is a quality factor for the optoelectronic attribute of an absorber since it is a measure of radiative recombination, and it predicts the maximum open-circuit voltage achievable by a photovoltaic device before the complexities of completing the absorber in a device. QFLS can be evaluated from an intensity-calibrated photoluminescence (PL) measurements at room temperature; an intensity-calibration is performed to equate incident photon flux (Φ_{inc}) to the AM1.5 photon flux density, to determine the absolute PL yield of the semiconductor material. After the calibrated PL measurements, in this work, two

methods are used to evaluate the QFLS on the Cu(In,Ga)S_2 absorbers [52]: The first approach is a direct fit of the Planck's generalized law [51, 53] to the absolute photon flux density of the absorber. The Planck's generalized law, which describes the emission of photon flux density per energy $\Phi_{PL}(E)$ from a semiconductor [53], is given by

$$\Phi_{PL}(E) = \frac{1}{4\pi^2\hbar^3c^2}\frac{A(E)E^2}{\exp\left(\frac{E-\Delta E_F}{k_BT}\right)-1} \tag{2.15}$$

where the absorptivity $A(E)$ is expressed by $A(E) = (1-R(E))\left(1-e^{-\alpha(E)d}\right)$, with R representing the energy-dependent surface reflectivity, and d the absorber thickness. The deposition of the absorbers on non-transparent back contact imposes some limitations on the measurement of measurement of absorptance spectrum of the absorbers, therefore, on the high energy end of the emission spectrum at adequately high energies (E_{min}) above the emission peak (E_{PL}), that is, $E_{min} > E_{PL} + 0.1$ eV, absorptivity can be assumed to be unity, $A(E) \approx 1$. This assumption is mostly valid for sufficiently thick homogenous absorbers, additionally, it has been shown that absorptivity is not always unity for graded absorbers [54]. By Boltzmann approximation, the exponential term in the denominator is much greater than 1, since at room temperature $E - \Delta E_F \gg 3k_BT$. Therefore, rearranging the equation (2.15) with consideration of Boltzmann approximation gives

$$\ln\frac{\Phi_{PL}(E)h^3c^2}{2\pi E^2} = -\frac{1}{k_BT}E + \frac{1}{k_BT}\Delta E_F \tag{2.16}$$

This is a linear relation with the slope given by $1/k_BT$ and the intercept by $\Delta E_F/kT$.

The second approach draws the relationship between the open-circuit voltage in the radiative limit (qV_{OC}^{rad}), where every absorbed photon generates an electron-pair which recombines radiatively, and the actual open-circuit voltage (qV_{OC}) or QFLS of the absorber as described by Shockley and Queisser [13]. The relation can be expressed as [55],

$$qV_{OC}^{rad} = qV_{OC} + qV_{OC}^{nrad} = qV_{OC} - k_BT\ln(ERE) \tag{2.17}$$

where qV_{OC}^{nrad} describes the non-radiative voltage losses and ERE is the external radiative efficiency of the absorber. ERE is defined as [56],

$$ERE = \frac{\Phi_{PL}}{\Phi_{inc}} \tag{2.18}$$

where Φ_{PL} is the integrated photon flux density from the absorber and Φ_{inc} is the incident photon flux density. Assuming that qV_{OC}^{rad} is equal to the theoretically predicted open-circuit voltage by Shockley and Queisser (qV_{OC}^{SQ}) [13], the relation becomes

$$V_{OC}^{SQ} = QFLS - k_B T \ln(ERE) \tag{2.19}$$

Apart from evaluating the ERE, the requirement for determining the QFLS by this method is a knowledge of the bandgap of the absorber, which is used to determine the corresponding V_{OC}^{SQ} value.

2.4 Review of photoluminescence transitions and defects in $CuGaS_2$

Early studies on various properties of I-III-VI_2 compounds such as $CuGaS_2$ and $CuInS_2$ were by Tell et al. in 1971 [21, 57]. $CuGaS_2$ semiconductors were grown by slow cooling stoichiometric melts, and of p-type conductivity by annealing under maximum sulfur pressure, although with limitations on its n-type conductivity. The low-temperature bandgap was estimated as 2.53 eV from an exciton binding energy of 28 meV [21, 32]. Years later in 1985, studies of $CuGaS_2$ under different sulfur overpressure by Masse et al. through various photoluminescence (PL) studies including time-resolved PL, excitation and temperature dependent studies show that the green luminescence of $CuGaS_2$ single crystals at 2.40 eV originates from a donor-acceptor (DA) pair with lattice phonon interaction [58, 59]. This provided understandings into the energy and defect levels and it was determined that a donor level exists at ~ 50 meV while an acceptor level exists at ~ 130 meV [58]. Annealing studies on a broadband red emission ~1.8 eV, attributed the emission to S vacancies. By 1993, Yagi et al. provided more insight into the aforementioned broad red emission from studies on thin film $CuGaS_2$ grown on GaAs and GaP substrates through vapour phase epitaxy (VPE), and crystals grown by iodine transport [60]. The broad red emission was shown to involve two transitions, around 1.7 eV and 1.85 eV, and these transitions are attributed to chalcogen deficiency during the growth process. The more intense 1.85 eV transition was credited to DA transition involving S vacancy as proposed by Masse et al. [58, 60]. Another

emission at approximately 1.40 eV was attributed to V_{Cu} [60]. Thorough studies of band-edge transitions on $CuGaS_2$ crystals grown by iodine transport were performed by Shirakata et al., they reported the occurrence of free exciton transition at 2.504 eV and bound exciton transitions at 2.501 eV (donor-bound), 2.495 eV and 2.493 eV (acceptor bound) [61]. Soon after, in addition to a broad emission, a strong phonon assisted transition with zero phonon line at 2.29 eV was observed in $CuGaS_2$ single crystals grown by iodine transport [62]. Shirakata and Chichibu studied MOVPE-grown $CuGaS_2$ films on GaP and GaAs substrates, where nearly stoichiometric epilayers exhibited strong exciton-related PL at 2.489 eV and 2.477 eV [63]. In addition, a free-to-bound (FB) transition was observed at 2.43 eV, and by excitation-dependent analyses, the ionization energy is estimated as 90 meV. While Cu-rich layers were dominated by broad band-edge luminescence, Ga-rich epilayers were found to be dominated by a DA transition at 2.39 eV which involved a donor at 46 meV and an acceptor at 100 meV. The donor level was attributed to V_S and Ga_{Cu} related defects, while the acceptor was related to V_{Cu}. Broad band luminescence centered at 2.1 eV and 1.65 eV were reportedly dominant at 200 K and room temperature respectively [63, 64]. Photoluminescence studies conducted by Botha et al. on co-evaporated $CuGaS_2$ deposited on GaAs showed the dominance of ~ 2.4 eV transition for Ga-rich absorbers, and the dominance of ~ 2.3 eV for Cu-rich absorbers, which involved a DA transition. A shallow donor level with a binding energy of ~53 meV and acceptor level at ~210 meV were implicated in the DA transition. From 2002 to 2004, Metzner et al. and Eberhardt et al. studied epitaxial $CuGaS_2$ grown on silicon substrates. Stoichiometric and Cu-rich absorbers were characterized by excitonic luminescence. A transition at 2.4 eV and broad deep defect at 2.1 eV were present in all the absorbers, however, the 2.4 eV transition was even more prominent and broader in Ga-rich $CuGaS_2$ epilayers, while the 2.1 eV was more composition related as it was red-shifted with the ratio of Cu to Ga [65-67]. Subsequently, further photoluminescence analyses performed on the same epilayers by Metzner et al. found, in addition to excitonic transitions two FB at 2.415 eV and 2.435 eV, and two DA transitions at 2.39 eV and 2.41 eV. These transitions were reported to involve a common shallow donor at ~ 25 meV due to a V_S and two acceptor levels as 89 meV and 109 meV, both related to V_{Cu} and V_{Ga}. From 2003 to 2007 Botha et al. and Branch et al. did several PL studies on MOVPE-grown $CuGaS_2$ including the influence of composition on PL transitions [68-75]. The transition at ~2.4 eV was only observed in near-stochiometric to somewhat Cu-rich absorbers. Its thermal activation energy was ~ 30 meV and was tentatively assigned a shallow donor level as it compares

with earlier reports. For near-stoichiometric to Ga-rich absorbers, a broad peak remained between 2.24–2.25 eV, but is shifted below 2 eV in Cu-rich absorbers [74].

The summary of this review of the photoluminescence transitions of $CuGaS_2$ from literature has been summarized in Fig. 2.7. The transitions around 2.5 eV have been identified as either free-exciton or bound-exciton. Around 2.4 eV, transitions have been identified as donor-to-acceptor (DA) transition or free-to-bound transitions. Transitions around 2.3 eV and 2.1 eV which were initially labeled deep-level defects have been identified DA transitions. The nature of the transition around 1.8 eV is not well known, however recent studies have identified it as DA transitions. There are still deep level transitions below 1.7 eV which are yet to categorized.

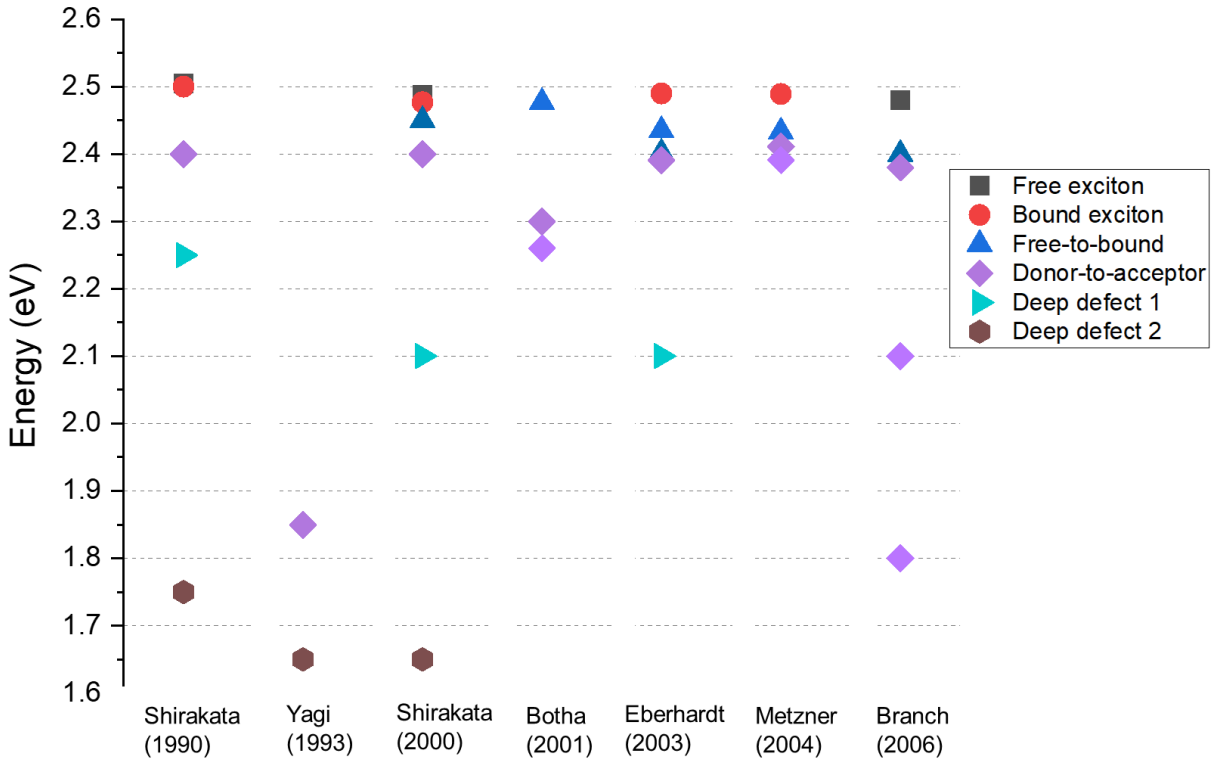

Figure 2.7: Overview of transition energies of $CuGaS_2$ identified from some preview studies.

2.5 Photoluminescence experiment set-up

All the photoluminescence (PL) measurements in this thesis were performed in the home-built set-up which is illustrated in Fig. 2.8. The excitation source is a continuous-wave diode laser with the

wavelength of 405 nm or 660 nm (depending on the optical bandgap of the absorber), the 532 nm diode laser was not used in this thesis. In front of each laser, a band-pass filter centered at its wavelength is used to block unwanted beam modes from the laser. In the laser beam path is a filter wheel with several neutral density filters, from optical density (OD) 1 to 4, to attenuate the laser power. Also on the beam path is a converging lens which reduces the spot size up to three orders of magnitude, and therefore increases the excitation intensity by several orders of magnitude. As depicted in Fig. 2.8, the laser beam goes through the aperture of the off-axis parabolic mirror 1 (OAPM1) to the sample. Afterwards, the emitted PL from the samples is acquired by OAPM1, collimated, and reflected into OAPM2. The emission is refocused by OAPM2 into a multimode fiber into a spectrograph. Unwanted laser beam is filtered by appropriate high quality long pass filters. The spectrograph has two gratings, one with a grating density of 100 lines/mm and another with 300 lines/mm.

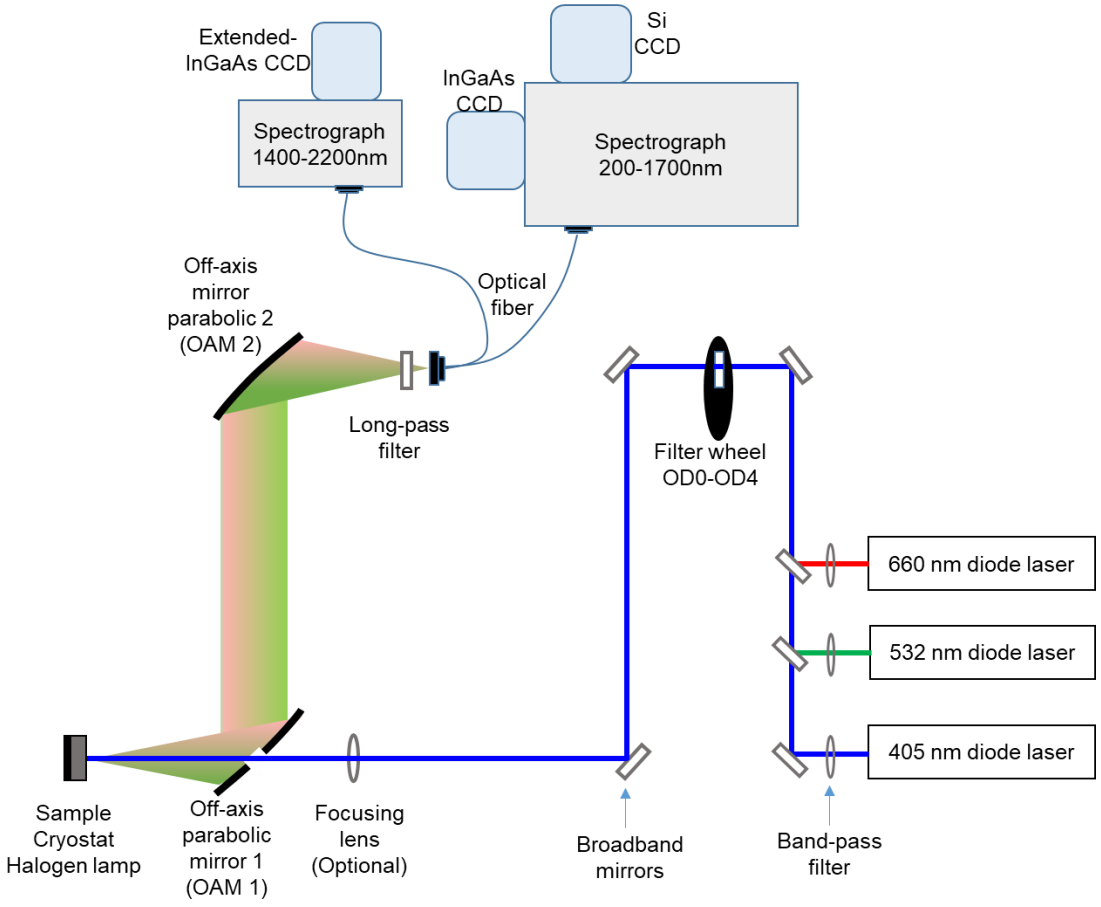

Figure 2.8: Sketch of the home-built experimental setup where all the photoluminescence experiments in this thesis were performed.

The beam is dispersed to the detector which is either as a Si-CCD, for a spectral range of 300-1100 nm, or an InGaAs-array for the spectral range of 900-1700 nm. The set-up is also equipped with an extended InGaAs-array detector which measures the spectral range of 1400-2200 nm. Subsequently, the raw PL data is spectral- and intensity-corrected. The spectral correction is with a commercial calibrated halogen lamp. The raw PL data are spectrally corrected to; (i) account of the sensitivities of optical components pertaining to the collection of the raw data, such as cameras/detectors, lens, mirrors, filters, optical fibers et cetera, (ii) convert each pixel to wavelength and assign units to the y-axis. To generate the correction function ($\xi(\lambda)$), known spectrum of the halogen lamp ($\varphi_{HL}^{ck}(\lambda)$) is divided by its spectrum measured in the PL set-up ($\varphi_{HL}^{meas}(\lambda)$), that is, $\xi(\lambda) = \varphi_{HL}^{cor}(\lambda)/\varphi_{HL}^{meas}(\lambda)$. The actual PL spectrum of an absorber ($\Phi_{PL}^{cor}(\lambda)$) after correction is,

$$\Phi_{PL}^{cor}(\lambda) = \xi(\lambda) \times \Phi_{PL}^{meas}(\lambda) \tag{2.20}$$

where $\Phi_{PL}^{meas}(\lambda)$ is the measured PL spectrum. Upon application of the correction function and using Jacobian transformation on the raw data, the corrected spectrum has the same unit as the calibrated lamp spectrum, the y-axis is transformed to the units of photons/(cm^2·nm·s) and each spectrum is transformed into the energy space [76].

The purpose of the absolute intensity calibration is to quantify the photon flux of the laser, and associate it with the measured PL signal of the sample. This is particularly important for intensity calibrated measurement to determine the QFLS. The quantification of the laser beam requires that the laser beam radius (w) and its power at the sample be known (P_0); both properties are measured with CCD camera and a photodiode power meter, respectively. The laser wavelength (λ) is made known by the manufacturer. The photon flux density (Φ_0) can be calculated from the knowledge of beam radius, power, and wavelength of the laser by the equation,

$$\Phi_0(\text{photons/s/cm}^2) = \frac{2P_0\lambda}{\pi w^2 hc} \tag{2.21}$$

It is important to measure the laser properties at the sample position because, depending on which laser is used, about 50 % of the laser power is lost on the optical path by reflection and scattering. The spectrum of the laser is also measured at the sample position by reflecting the laser beam on

a spectralon into the PL set-up. The signal collected by the optical fiber is limited by its (fiber) diameter, as such, only the photons at the peak of the laser beam are collected. It is possible to correlate the photon flux of the laser with the spectrum/relative flux of the laser measured in the PL set-up. A ratio of the calculated laser photon flux to the spectrum/relative flux gives the calibration factor. Multiplying the calibration factor with the measured PL spectrum of an absorber gives the actual photon flux from the absorber.

For low-temperature photoluminescence (PL) experiments, the samples are housed in a helium-flow cryostat. The laser beam is focused on the absorber, with the PL emission collected by the two off-axis parabolic mirrors. The PL emission is focused into either a 200-μm or a 105-μm collection fiber, then spectrally resolved by the monochromator and detected by the silicon charge-coupled-device (CCD). The thinner fiber is used for better resolution of the sharp peaks near the band-edge. For excitation intensity-dependent measurements, the laser power is varied, and several neutral density filters are used to achieve different orders of magnitude. Temperature-dependent measurements are also performed between 10 K to 300 K.

Chapter 3

Thin film solar cell devices

In this chapter, an overview of the $Cu(In,Ga)S_2$ thin film solar cell is introduced. First in the Section 3.1, the basic principle of p-n junction on which a $Cu(In,Ga)S_2$ solar cell works will be discussed. The details and physics of p-n junction can be found in any good textbook on the principles of solar cell, however, this section is referenced from the textbooks in Refs. [45, 51, 77]. The different layers that make up a $Cu(In,Ga)S_2$ solar cell stack and the respective functions are shown in Section 3.2. The band diagram of the complex solar cell stack and various recombination channels that can occur in the completed solar cell are presented in Section 3.3. In chalcogenide solar cells, the double bandgap gradient has become a characteristic feature of the solar cells which has led to high efficiencies, as such, in Section 3.4, a review of some advantages of graded-bandgap in $Cu(In,Ga)S_2$ solar cell will be presented. The most important parameters used to characterize a solar cell device under operation will be introduced in Section 3.5. All the absorbers presented in this thesis were grown by physical vapour deposition, accordingly, Section 3.6 describes the PVD system, and the section covers the preparation method of the absorbers by co-evaporation technique. Specific descriptions are given for the one-stage and the more complex two-stage and three-stage deposition processes.

3.1 The p-n junction in solar cells

$Cu(In,Ga)S_2$ devices work by the principle of p-n junctions. In the heterojunction configuration, two differently doped semiconductors are brought into contact, hence a formation of the junction. Simplified illustrations showing the band diagram of an n-type and p-type materials in isolation are presented in Fig. 3.1a. As a single entity, charge-neutrality is maintained in each of the materials since in the p-type semiconductor, the negatively charged acceptor atoms balances the positively charged holes and the positively charged atoms of the n-type semiconductor compensates the negatively charged electrons. In each of the semiconductor, at thermal

equilibrium, the Fermi energy level (E_F) which describes the occupation of the valence band with holes and the conduction band with electrons, as in Equations (2.3) and (2.4), thus the Fermi level is closer to the valence band in the p-type semiconductor and closer to the conduction band in the n-type semiconductor. When both materials are brought into contact as illustrated in Fig. 3.1b, a metallurgic junction is formed and there is a net flow of free carriers across the interface in both directions, which leaves the regions close to the junction depleted of charge carriers, thereby exposing the oppositely charged ionized atoms in the respective semiconductors.

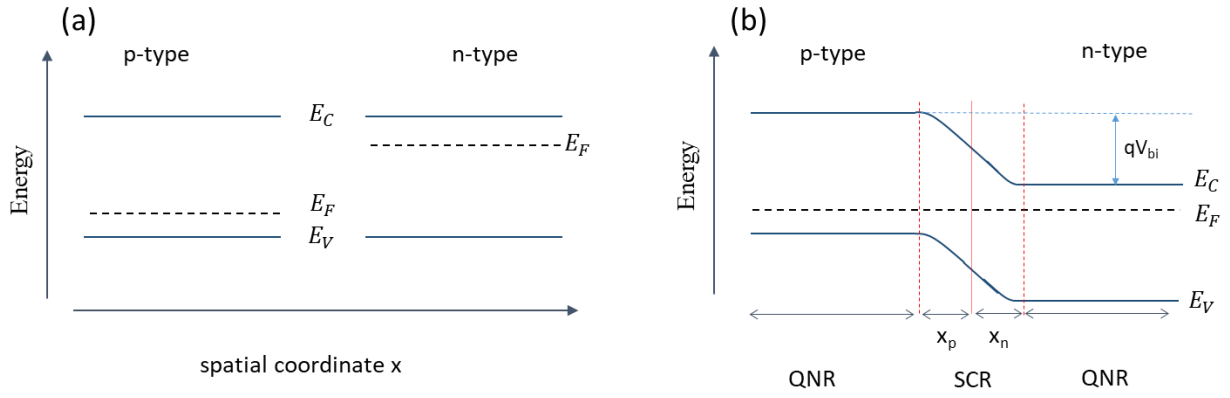

Figure 3.1: (a) Depiction of energy band diagram of p-type and n-type doped semiconductors in an equilibrium state. E_C and E_V are the energies corresponding to the conduction band and valence band-edges, respectively. (b) Illustration of the formation of the p-n junction by the two semiconductors when in contact. The built-in potential is denoted by V_{bi}, while x_p and x_n represent the proportions of the SCR extending into the p-type and n-type sides of the semiconductor, respectively.

The regions with the exposed positively and negatively charged atoms, which are no longer compensated, is referred to as the space charge region (SCR) or depletion region. The region outside this SCR is referred to as the quasi-neutral region (QNR). The opposite charges of the ionized atoms in the SCR induce an internal electric field, V_{bi}, which is opposite to the diffusion force acting on the charge carriers. With no external voltage applied, the internal electric field counterbalances the diffusion force. As the p-n junction is in thermal equilibrium, the position of

the Fermi energy stays constant all over the combined system, however, since the energy of the Fermi level relative to the bands does not change in the QNR, the bands bend in the SCR due to the electric field to compensate for the changes in the electrostatic potential across the SCR as depicted in Fig. 3.1b. As a result, there is no flow of current and the charge carriers remain in the QNR, with holes in the p-type side and electrons in the n-type side.

The total width of the SCR (w) is given by the summation of x_p and x_n which represent the proportion of the SCR extending into the p-type and n-type sides of the semiconductor, respectively. This is expressed as

$$w = x_p + x_n = \sqrt{\frac{2\varepsilon_0\varepsilon_r}{q}\left(\frac{1}{N_A} + \frac{1}{N_D}\right)(V_{bi} - V)} \tag{3.1}$$

where ε_0 is the vacuum permittivity, ε_r is the dielectric constant, q is the elementary charge, V is the applied external voltage, N_A and N_D are the doping concentrations in the p-type semiconductors, respectively. Equation (3.1) shows that the width of the SCR can be varied by an applied voltage or illumination. In chalcopyrite solar cells such as $Cu(In,Ga)S_2$, the n-type semiconductor is highly doped in comparison to the p-type absorber, that is $N_D \gg N_A$, thus the SCR is only in the p-type absorber [77]. Equation (3.1) becomes,

$$w = x_p = \sqrt{\frac{2\varepsilon_0\varepsilon_r}{qN_A}(V_{bi} - V)} \tag{3.2}$$

Since V_{bi} is negative in the p-type region with reference to the n-type region, as shown in Fig. 3.1b, when the applied voltage is negative, the potential difference across the p-n junction increases resulting in a wider SCR. This negative voltage is referred to as reverse bias voltage. When the p-n junction is no longer under equilibrium condition, the Fermi energy level splits, and the quasi-Fermi levels which describes the concentration of holes and electrons is established. On the contrary, when the external voltage is positive, in the case of a forward bias voltage, the potential difference across the p-n junction decreases and the SCR becomes narrower. As the potential barrier reduces, the electric field across the p-n junction reduces since the concentration gradient of charge carriers also changes, that is, the balance between drift and diffusion, that exists in equilibrium, will be perturbed. There is an injection of minority carriers as holes from the p-type

material diffuse into the n-type material and electrons from the n-type material diffuse into the p-type material. Due to the diffusion, minority carriers from one semiconductor recombine with its majority carriers in the bulk giving rise to a recombination current.

If no external voltage is applied to the p-n junction, that is V = 0, there is balance between drift force and diffusion force, resulting in zero force and thus no driving force for a current. The generation current is determined by the availability of thermally generated minority carriers. Meanwhile, recombination current increases with the Boltzmann factor under moderate forward-bias voltage. The net current density is expressed by

$$J(V) = J_0 \left(\exp\left(\frac{qV}{Ak_BT}\right) - 1 \right) \tag{3.3}$$

where k_B is the Boltzmann constant, T is the temperature, and J_0 is the saturation current density of the p-n junction, which is the current density under reverse bias and A is the ideality factor.

Alternatively, under illumination, there are additional photogenerated carriers as electron-hole pairs are created by impinging photons with energies greater than the bandgap of the semiconductor. In turn, there is a significant increase in minority carrier concentrations. The flow of photogenerated carriers produces photocurrent in addition to the thermally generated current. Without external load on the device, it is in short-circuit conditions, that is, no voltage difference between the contacts. Rather, there is a net current density referred to as short-circuit current J_{SC}. Under illumination, the relationship between the photocurrent density and applied voltage is described by

$$J(V) = J_0 \left(\exp\left(\frac{qV}{Ak_BT}\right) - 1 \right) - J_{ph} \tag{3.4}$$

where J_{ph} is the photocurrent density. The minus sign before J_{ph} indicates that the photogenerated current flows in opposite direction to the dark diode current. If no voltage is applied, the total photocurrent density is the short-circuit current, which is the J_{SC}. If applied, the voltage at which the total current density equals zero is referred to as the open-circuit voltage (V_{OC}). Under the assumption that $qV_{OC} \gg Ak_BT$ the equation (3.4) is approximated as

$$V_{OC} = \frac{Ak_BT}{q} \ln\left(\frac{J_{ph}}{J_0}\right) \tag{3.5}$$

Under illumination with the carriers in a steady state, the built-up voltage at the contacts is the difference between the electron quasi-Fermi level at the electron contact and the hole quasi-Fermi level at the hole contact, hence the measurement of quasi-Fermi level splitting (QFLS) is under open-circuit condition and serves as the upper limit of open-circuit voltage achievable.

3.2 Cu(In,Ga)S_2 absorber layer and device structure

The typical assembly of layers constituting the $CuIn_{1-x}Ga_xS_2$ device structure, from the top layer to the bottom layer, will be discussed in this subchapter. Being that Cu(In,Ga)Se_2 is a closely associated compound which is years ahead in research, some ideas and knowledge already established from Cu(In,Ga)Se_2 will also be used to discuss and describe the structure of Cu(In,Ga)S_2 device. A depiction of Cu(In,Ga)S_2 device structure is illustrated in Fig. 3.2.

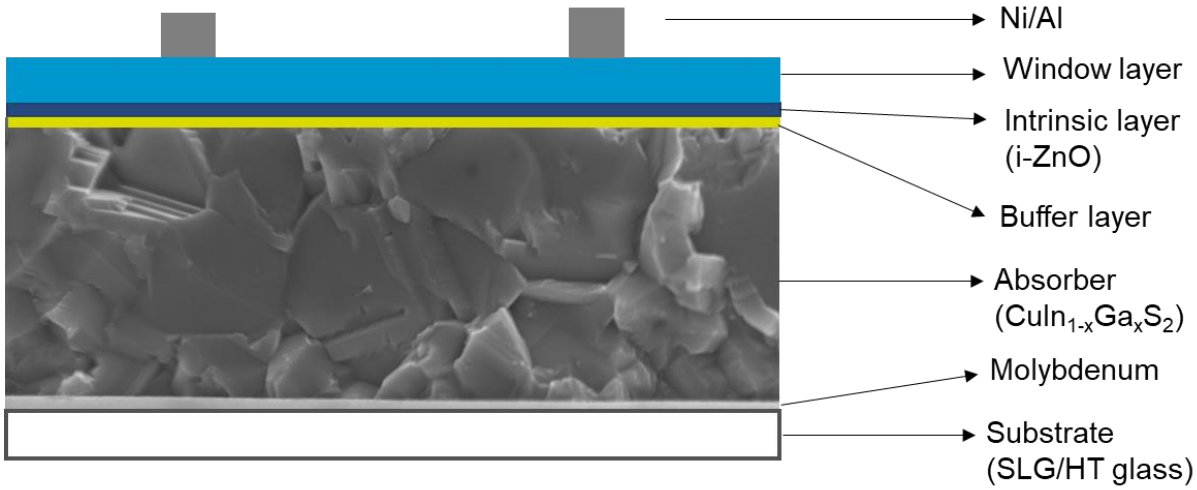

Figure 3.2: Illustration of the different layers constituting the $CuIn_{1-x}Ga_xS_2$ device structure.

Substrate: Unlike silicon, which is self-containing, the thin film requires a structural support for which the substrate is responsible for. The substrate is an inactive component of the structure which

holds the whole device stack. The substrate can either be flexible and lightweight, such as polyimide foil, which is often used in low-temperature processes [78-80], or rigid, such as glass [81]. The glass of choice in $Cu(In,Ga)(S,Se)_2$ research is the soda-lime glass (SLG), having replaced alumina and Corning glass, due to the discovery of the advantageous impact of sodium (Na) in $Cu(In,Ga)Se_2$ by Hedstrom et al. in 1993 [82]. SLG has the benefit of unintentionally supplying Na, which diffuses into the absorber during the absorber deposition due to SLG containing 12-16 % Na_2O [83]. SLG is also preferred for its low cost, thermal and mechanical stability, and similar thermal expansion as the CIGS thin film [84]. In this thesis report, the SLG and a high thermal resistant (HT) glass with much lower Na content were used.

Back-contact: The back-contact is required to be highly conductive and particularly be a good ohmic contact for the majority carrier, i.e., holes in p-type $Cu(In,Ga)S_2$ absorbers, and required to have a low recombination for minority carriers. Thin layer of molybdenum (~ 500 nm) is the most widely used back contact in $Cu(In,Ga)(S,Se)_2$. Due to its high melting point of ~ 2700 °C, it is inactive during the absorber deposition process, it also has a low sheet resistance and allows the diffusion of Na into the absorber [81]. However, Mo is a highly recombinative layer for minority carriers, as such, bandgap-grading is used to mitigate the high recombination at the back-contact. Bandgap-grading is discussed in Section 3.4. In the selenides, it has been shown that a thin ohmic contact layer of $MoSe_2$ forms between the molybdenum layer and the back surface of the absorber [85, 86]. Detailed analysis on a similar formation of MoS_2 in the sulfides is missing, however, Brus et al. have shown that the electrical contact at the Mo-$CuInS_2$ interface is ohmic [87].

Absorber: As the name suggests, the absorption of photons occurs in the absorber. It consists of evaporated elements deposited on the Mo-sputtered SLG, from which the arbitrary nucleation of condensing species form the thin film [88]. An absorber is expected to have a high absorption coefficient. The $Cu(In,Ga)S_2$ absorber with a tunable band gap of 1.5 eV to 2.45 eV is the subject of investigation in this thesis and Chapter 4 to Chapter 6 will be dedicated to discussing the results and observations of these investigations.

Buffer layer: The buffer layer is an n-type semiconductor with a wide bandgap which allows the favourable band alignment at the absorber-buffer interface [77]. The buffer layer also prevents damages to the absorber surface during the sputtering of transparent front contacts. Cadmium sulfide, (CdS) zinc-oxy-sulfide (Zn(O,S)) and zinc-tin-oxide (Zn,Sn)O are buffer layers that have

been used in this thesis. Although CdS is the most widely used buffer layer in chalcopyrite solar cells, it has an unfavorable band alignment with $Cu(In,Ga)S_2$ absorbers. Zn(O,S) has been shown to have a better band alignment with $Cu(In,Ga)S_2$ [89, 90].

i-layer and window layer: The trio of buffer layer, i-layer and window layer have high bandgaps and are transparent for illuminating photons to reach the absorber. The intrinsic layer is a highly resistive layer which also serves as a protective layer covering spots and holes uncovered by the buffer layer, which neutralizes and minimize shunting paths in the completed device [91]. The cell structure is completed with an n-type transparent conductive layer. The intrinsic layer used is zinc oxide layer (i-ZnO) and a highly doped n-type aluminium doped zinc oxide (Al:ZnO) [92].

3.3 Recombination mechanisms in solar cells

This section is a summary of the most compelling recombination pathways occurring in completed heterostructure device such as a solar cell as presented by Scheer and Schock [77]. Detailed analyses on recombination mechanisms in solar cells are presented in textbooks, such as [77, 93], to which interested readers are referred to for further reading.

A schematic band diagram of a model illuminated solar cell such as the $Cu(In,Ga)S_2$ device is illustrated in Fig. 3.2. The possible recombination paths, which will be briefly described below, have also been highlighted.

After illumination of the solar cell by light source which the window layers are transparent to, if the energy of the photon is higher than the bandgap of the absorber, the photon is absorbed and there is a generation of electron-hole pair in the absorber. The electron, having acquired energy higher than the bandgap, is excited to the conduction band, releases the excess energy to the crystal lattice and thermalizes to the band-edges within picoseconds of excitation. The energy lost in this process, referred to as thermalization loss (1), is the difference between the absorbed photon energy and the bandgap of the absorber. This is a principal loss in single junction solar cells which can be mitigated by next generation photovoltaic devices such as multi-junction solar cells [17, 94]. Due to the finite lifetime of a carrier in an excited state, the electron recombines radiatively or non-radiatively. A recombination with the majority charge carriers in which the absorbed photons are

spontaneously emitted is a radiative recombination (2) and this is the most desired process in the solar cell. After excitation and thermalization, it is important that the photogenerated carriers have long enough lifetime to establish a quasi-equilibrium state before they recombine.

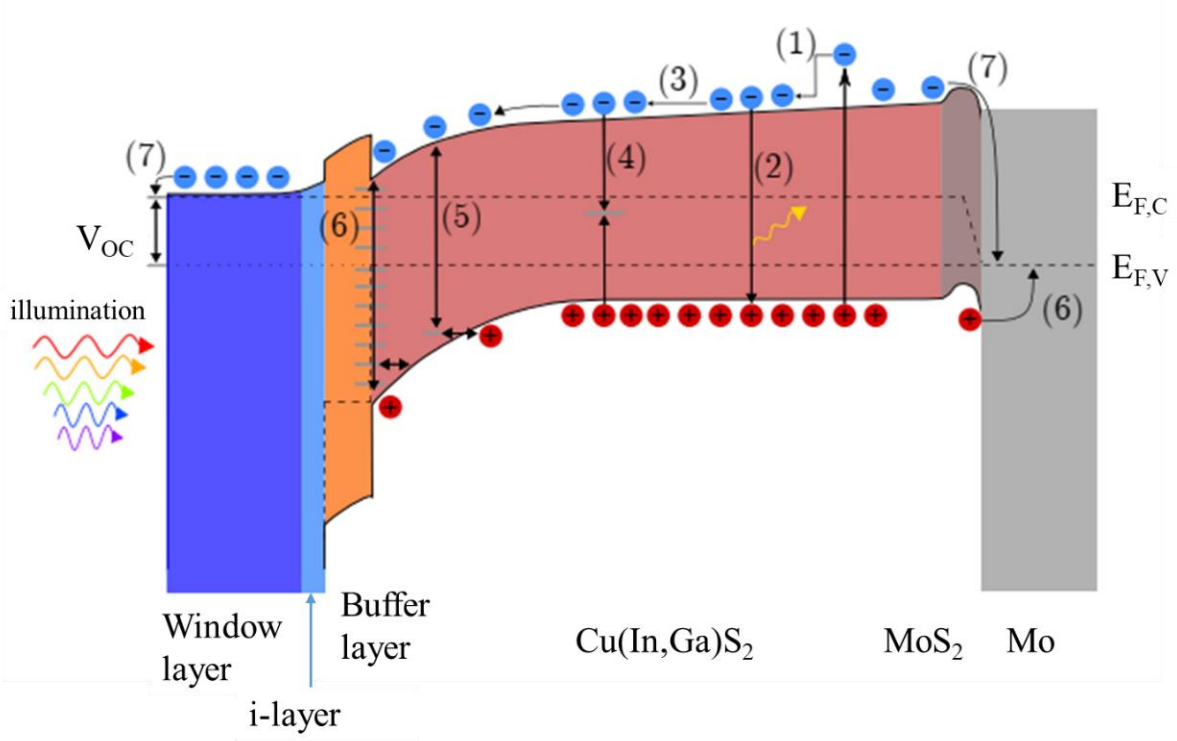

Figure 3.3: Depiction of the band alignment of a typical solar cell (e.g. Cu(In,Ga)S_2 device) under illumination and open-circuit condition. The recombination mechanisms and losses portrayed are (1) thermalization loss, (2) radiative recombination (3) transport losses (4) defect recombination, (5) tunnel recombination, (6) interface recombination, and (7) contact recombination. The image has been taken from the doctoral dissertation of Finn Babbe [95].

If the minority carrier and diffusivity are low, this leads to transport loss (3) and low photogenerated carrier collection. The recombination path (4) and (5) are non-radiative recombination as this recombination occurs through deep defects. The recombination at such mid-gap states is described by Shockley-Read-Hall recombination, which particularly limits the performance of photovoltaic devices. The recombination path (5) is additionally increased by tunnelling of carriers into defect states. The recombination path at (6) is specific to heterojunction solar cells at the interface between absorber and buffer layer, as lattice mismatch or segregation

facilitates interface defect states. At the molybdenum-absorber interface, the back contact recombination (7) is particularly prominent in absorbers without back-gradient. The recombination can be mitigated by adopting graded bandgap.

3.4 Bandgap grading in $Cu(In,Ga)S_2$

The record-breaking $Cu(In,Ga)(S,Se)_2$ solar cells are based on graded bandgap in which the bandgap is varied throughout the bulk of the absorber. The bandgap is increased towards the front and back surfaces of the absorber from a point of the lowest bandgap referred to as the notch. The origin of the gradient is typically a varied concentration of Ga in the absorber since in the selenides, it is known that Ga increases the conduction band minimum [96], consequently, this has also been demonstrated in the sulfides [97, 98]. It should be mentioned that the bandgap can also be varied by a by S-Se substitution [99]. This thesis is limited to the variation of Ga content for bandgap gradient. The increase of Ga or bandgap towards the front surface of the absorber aims to reduce high surface recombination at the absorber-buffer interface. Ideally, the impact of the front surface gradient can be twofold, on one hand, an increase of bandgap in areas of high recombination can increase the open-circuit voltage (V_{OC}) while still preserving the short-circuit current (J_{SC}) [77]. On the other hand, it has been shown experimentally and theoretically that a strong front grading can result in a barrier for photogenerated electrons which leads to reduced J_{SC} [79, 93].

The increase of the bandgap towards the absorber-Mo interface not only reduces the back surface recombination but also creates a gradient which acts as a driving force for photogenerated carriers. The effect is similar to the back surface field (BSF) in silicon solar cells [100]. The high bandgap at the back of the absorber reduces the diffusion of electrons to the back contact, as such, a reduced back-surface recombination. The reduced back-surface recombination together with the bandgap-gradient improves charge carrier collection at the notch [77, 100-102].

Bandgap-gradient is typically achieved by taking advantage of the different diffusion rates of gallium and indium during absorber growth. In practice, bandgap-gradient can be achieved by various methods [103, 104] which includes the multi-stage deposition methods described in Section 3.6.

3.5 Solar cell operation: current-voltage characteristics

The working principle of solar cells is well described in references [48, 51]. The standard parameters used to characterize the performance of a solar cell are conversion efficiency (η), short circuit current (J_{SC}), open-circuit voltage (V_{OC}) and fill factor (FF). The parameters are highlighted in Fig 3.4. The parameters are extracted from current-voltage (I-V) measurements with characteristics as shown in Fig 3.4, considering the ideal characteristics of the solar cell in the dark (without illumination) and under illumination. The solar simulator in the IV setup is set to emit approximately the AM1.5 solar spectrum which is equivalent to incident power of 1000 W/m^2.

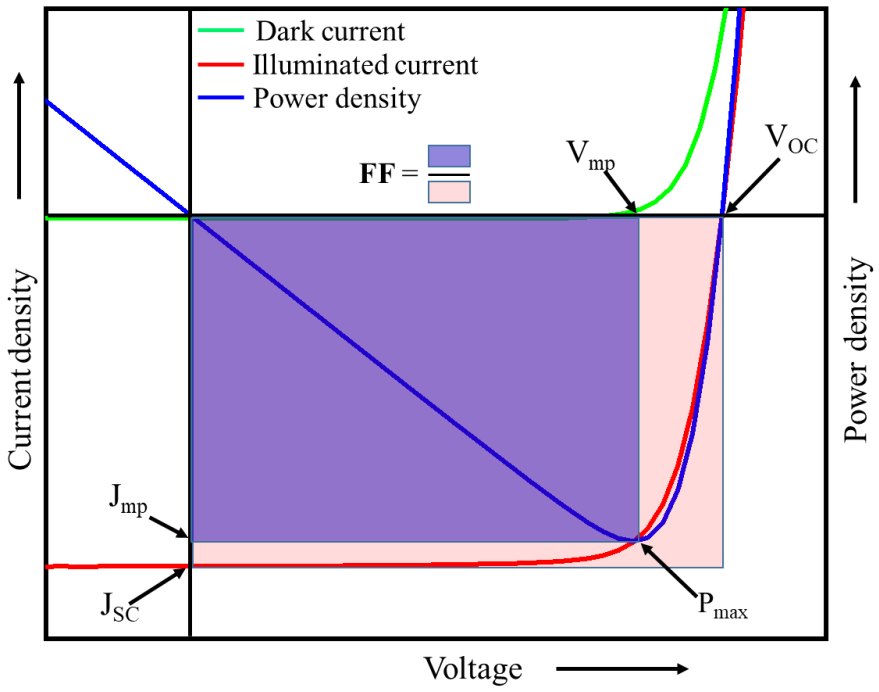

Figure 3.4: Example of a current-voltage (I-V) curve under dark and under AM1.5 illumination.

The efficiency (η) of the solar cell is the fraction of the maximum power density (P_{max}) generated by the solar cell to the incident power density (P_{in}). P_{max} is the product the current density (J_{mp}) voltage (V_{mp}) at the maximum power point as depicted in Fig. 3.4. The fill factor is the ratio of the

maximum power density, that is, $P_{max} = J_{mp} \times V_{mp}$, to the product of product of V_{OC} with J_{SC}. In essence FF can be visualized as a measure of the squareness of the I-V curve as shown in Fig. 3.4. The relationship between the efficiency and the other parameters used to characterize the solar cell is given by

$$\eta = \frac{P_{max}}{P_{in}} = \frac{J_{mp} \times V_{mp}}{P_{in}} = \frac{V_{OC} \times J_{SC} \times FF}{P_{in}} \tag{3.6}$$

3.6 Deposition of Cu(In,Ga)S_2 absorbers

This section describes the physical vapour deposition (PVD) system and procedures used in growing the polycrystalline absorbers investigated in this thesis. The $CuInS_2$ absorbers which are investigated in Chapter 4 were grown by Alberto Lomuscio using either the one-stage or the two-stage deposition process in a different PVD system (colloquially referred to as Calimero in the LPV). The detailed description of the machine and how the absorbers were grown can be found in the doctoral dissertation of Alberto Lomuscio [26]. For all the $CuGaS_2$ and Cu(In,Ga)S_2 samples, they were grown in a new PVD system, referred to as (sulfur) S-PVD which will be briefly described in this section 3.6.1. The $CuGaS_2$ absorbers were grown solely by the one-stage deposition method; a two- or three-stage growth of this material will require a dedicated optimization procedure which was not within the scope of this research. Lastly, the Cu(In,Ga)S_2 samples were processed by either of the one-, two- or three-stage deposition methods.

The deposition processes will be described with respect to the growth of $CuGaS_2$ and Cu(In,Ga)S_2 absorbers. However, the descriptions should be applicable to $CuInS_2$ absorbers or any other type of absorbers to be processed in this system, albeit with minor modifications. The substrate on which the Cu(In,Ga)S_2 absorbers were deposited is the SLG while the $CuGaS_2$ absorbers were rather deposited on high thermal resistant glass, which will be referred to as HT-glass.

Section 3.6.1 describes the S-PVD in which the absorbers were synthesized. The growth process of $CuGaS_2$ and Cu(In,Ga)S_2 absorbers are specifically presented in Section 3.6.2 and Section 3.6.3 respectively.

3.6.1 The physical vapour deposition system (S-PVD)

The background on physical vapour deposition processes described here follows the textbooks by Mattox [105] and Harsha [106], and interested readers are referred to the books for further reading. Physical vapour deposition (PVD) procedures are depositions of atomic proportions in which substances, such as liquid or solid sources, are vaporized in atomic or molecular form and then transported through vacuum or low pressure atmosphere to a substrate where they condense [105]. The thermal evaporation is usually executed by means of thermally heated sources like cermanic crucibles with tungsten wire coils or by high energy electron beam, while the substrates are mounted at a considerable distance from the evaporation source to lessen the effect of radiant heating of the substrate by the vaporization source [105].

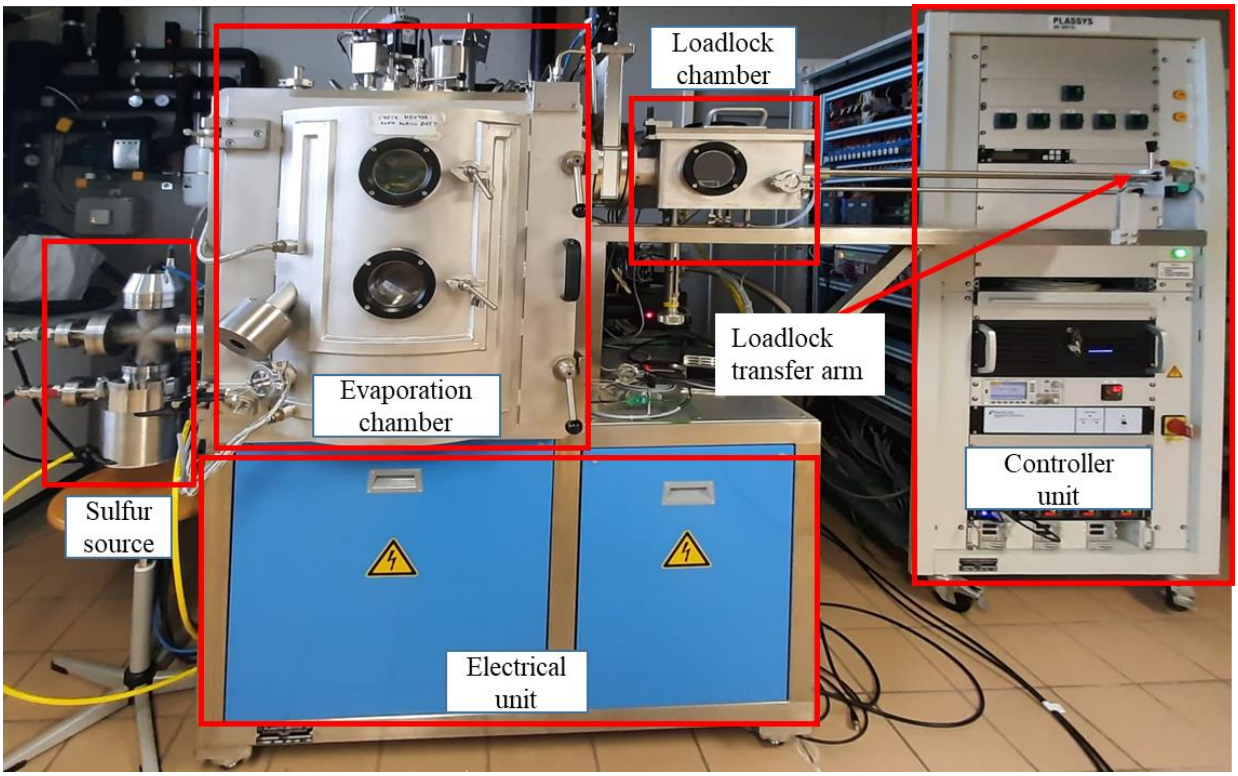

Figure 3.5: Picture (front view) of the physical vapour deposition system used for growing the absorbers investigated in this thesis. The pumps, cold trap and cooling system are at the back.

A picture showing the front parts of the (sulfur) physical vapour deposition system (S-PVD) used to grow some of the absorbers investigated in this thesis is shown in Fig. 3.5. There are other machineries behind which are not shown in the picture. The S-PVD was developed by Plassys Bestek with parts such as the sulfur source by Nano4energy and Gencoa. The principal component of the PVD is the evaporation chamber where the deposition processes occur. The chamber also houses the evaporating thermal sources, the substrates and heater, several sensors, detectors and gauges to monitor the absorber growth processes and conditions of the chamber.

Before viewing the interior of the S-PVD chamber, it is worth mentioning other supporting modules which make up the S-PVD system.

As seen in Fig. 3.5, the **sulfur source** is externally mounted on the side of the chamber. It consists of a heating element which heats the sulfur containing crucible. The sulfur vapour is fed into the main evaporation chamber via an injector through a quartz tube. The control of the sulfur flux is by a ball valve which can be regulated by a chamber pressure or sulfur sensor feedback loop. There is also an injector fitted with a thermal cracker which can thermally crack large sulfur molecules into smaller sulfur species.

The **loadlock** is a small chamber which can be brought under vacuum within a short period. It is used for temporarily storing and transferring substrates from the atmospheric pressure into the evaporation chamber without breaking the chamber pressure.

The **Pumps and cold trap**, not seen in the picture, are used to purge the evaporation chamber of gases and maintain the evaporation chamber under low pressure or vaccum. The base pressure in the evaporation chamber reaches approximately 1.0×10^{-7} mbar. The evaporation chamber is directly connected to a cold trap, which is brought to low temperatures by a cooling unit that can maintain low temperature between -36 °C to -40 °C, then to the turbo pump and finally the rough pump. The cold trap is necessary to capture evaporants, mostly sulfur, which did not condense on the water-cooled walls of the evaporation chamber.

The **controller unit** is the frame hosting all the controllers for the components used to bring the S-PVD into operation. The components include the substrate heaters, evaporation sources, sulfur sources (crucible, valve, injector) and so on.

Fig. 3.6 shows the interior of the evaporation chamber of the S-PVD system. There are shields lining the walls of the chamber. At the top of the chamber is the support around the substrate heater, which is made of Pyrolytic Boron Nitride (PBN). The temperature of the heater can be increased up to a set temperature of ~ 800 °C. Beneath the heater is the sample holder held by a rotating substrate holder and a substrate shutter to prevent deposition of evaporants on the substrates when not needed. The substrate holder can be rotated to improve homogeneity during the deposition process.

The equilibrium vapour pressure of a substance is its vapour pressure when it is in equilibrium with the solid or liquid surface in a closed vessel. At equilibrium, the number of atoms leaving the surface is the same as the number of atoms returning. With the vessel at a constant temperature, the elements outflowing through the opening depend on the pressure differential. As the environment outside the opening is vacuum, and the rate of elements leaving the substance is known, the equilibrium vapor pressure of the substance in the vessel can be calculated. Different materials have different vapour pressures and since the vapour pressure exerted by each evaporating substance is important, it is important to monitor the chamber conditions during absorber deposition. The flux of the evaporated source is monitored by electron impact emission spectroscopy (EIES) and quartz crystal microbalance (QCM). The QCM, not pictured in Fig. 3.6, is a piezoelectric device based on a quartz crystal which oscillates at a resonant frequency. It is surface-sensitive and detects changes in mass deposits by changes in the resonance frequency, which is in turn correlated with the deposition rate. It is used to quantify the deposition rate of copper, indium and gallium. The EIES is also used for measuring the vapour flux density of each element by measuring the distinctive photon emission of the evaporated copper, indium and gallium.

The S-PVD is also equipped with a beam flux monitor (BFM) which can measure the partial pressure from the sources and the chamber pressure, however; the BFM was not used at the time of these investigations. BFM is an ionizing gauge in which electrons emitted from the cathode accelerate towards an anode, as such, positive ions are formed when the electrons collide with atoms. The ionization rate is proportional to molecular density, hence the pressure.

The chamber pressure was measured with Pirani and Penning gauges. The Pirani gauge is a thermal conductivity gauge used to measure high pressures, while the Penning gauge is also an ionization

or cold cathode gauge used to measure low pressure. The sulfur vapour pressure is measured by a lambda sensor from Gencoa which has been adapted to sense group six elements. Lambda sensors have been typically used with catalytic converter as an oxygen sensor in a vacuum and in cars. The device has a Zirconium-dioxide sensing element that is enclosed in a steel shell which is connected to a platinum electrode. The top of the lambda sensor is introduced into the evaporation chamber, as sulfur molecules in the chamber contact the sensing component, oxygen flowing in through the tail-end outside the chamber are heated to generate ions. The difference in concentration between the sulfur molecule detected by the sensing element and the oxygen generates a potential difference, which is then be translated as the sulfur vapour pressure.

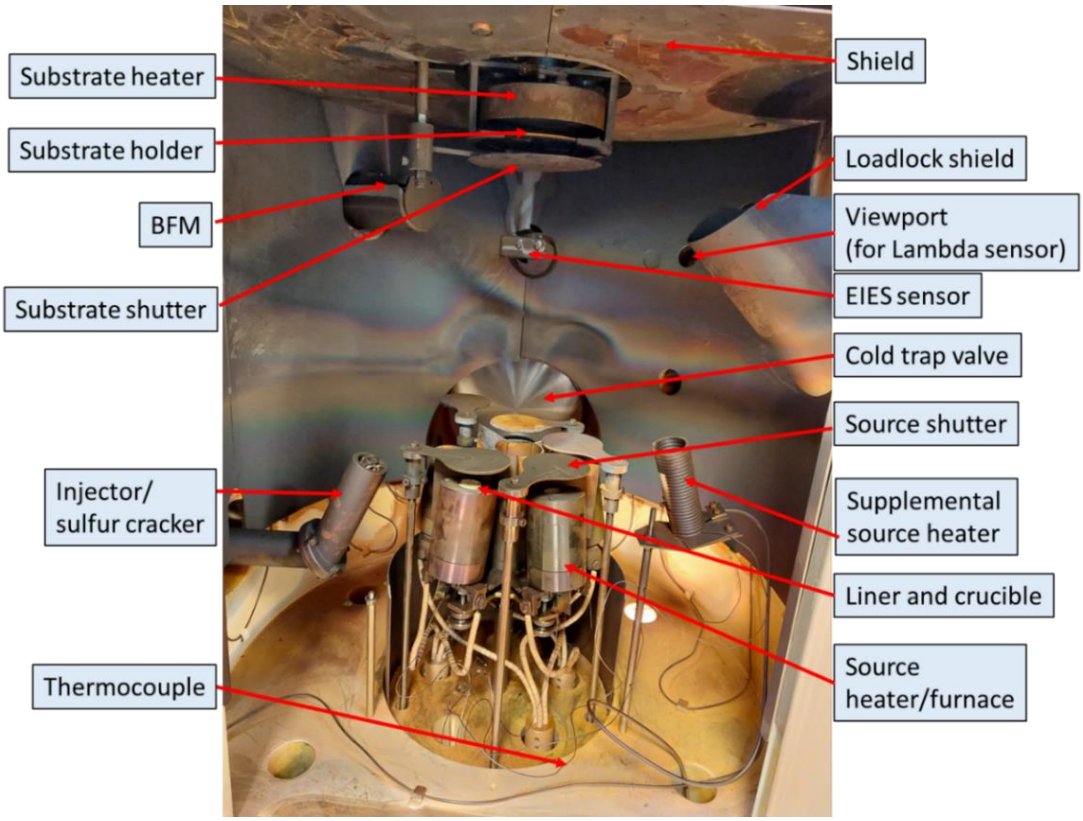

Figure 3.6: Picture of the interior of the S-PVD system.

A pyrometer is used to measure the surface temperature of the absorber during the deposition process. It works by detecting the energy radiated from the absorber surface. The pyrometer was

used to monitor the evolution of phases during the absorber growth. The use of the pyrometer in this capacity will be further discussed in section 3.6.3.

At the bottom of the chamber are five thermal vapourization sources (crucible containers) with their respective shutters. The crucible containers may hold large quantities of liquified evaporants although the distribution of the vapour flux will change as the level of the liquified substance also changes. Metallic containers have the drawback that they are often wetted by the liquefied substance which can spread to unwanted areas. To prevent wetting, a liner can be used along a crucible. Liners are generally made from pyrolytic graphite, pyrolytic boron nitride, BN/TiB_2, BeO, Al_2O_3, etc. and have poor thermal conductivity. The heating is by RADAK and OLED furnaces and can reach temperatures of 1400 °C. Each thermal source is equipped with alumina crucible and with a PBN liner, together with thermocouples at the bottom of the crucibles.

The injector which encases the quartz pipe connected to the sulfur source acts as the sulfur outlet. It has heating elements which can be heated to 850 °C and used to thermally crack/break sulfur molecules. A supplemental sulfur source heater has also been installed in the PVD chamber. It is limited by size and the ability to control the sulfur flux by only the heating temperature.

3.6.2 Co-evaporation of $CuGaS_2$ (single-stage deposition)

The $CuGaS_2$ absorbers investigated were all processed by the single-stage deposition process in which, at constant fluxes, all the individual elements are simultaneously evaporated during the absorber deposition. The single-stage deposition profile is simply illustrated in Fig. 3.7. The depiction shows both the source temperatures and elemental fluxes in dependence of deposition time, however the most important factor controlling the desired compositional ratio of the final absorber are the elemental fluxes during the growth process, and the fluxes are dependent on the source temperature. The phase evolution during the growth of the absorber in the one-stage deposition does not require monitoring, as the final composition is dictated by the elemental fluxes set during the deposition process. The desired fluxes are determined before the deposition by calibrating the elemental fluxes to source temperature using the EIES. The maximum of four Mo-

covered HT-glass substrates are placed on the molybdenum or pyrolytic quartz sample holder and loaded unto the substrate holder in the PVD through the transfer loadlock.

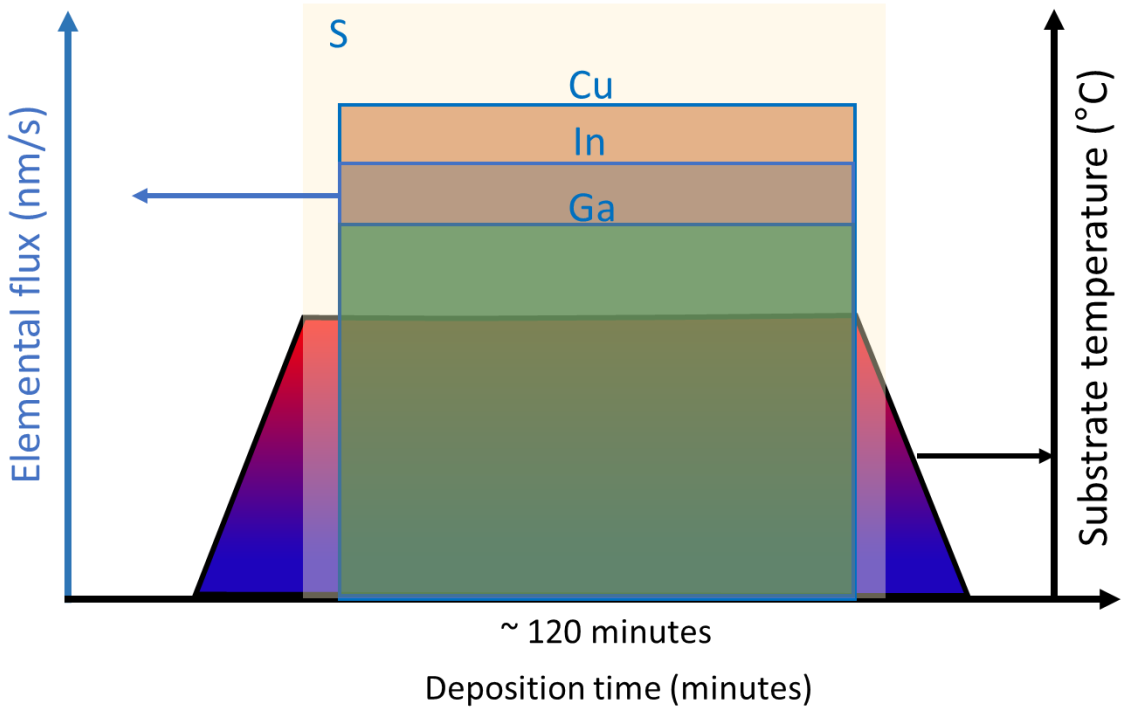

Figure 3.7: Schematic representation the temperature and flux profile used in the single stage deposition process in the growth of Cu(In,Ga)S_2 absorbers. For the deposition of $CuGaS_2$ absorbers, indium is not evaporated, similarly for the deposition of pure $CuInS_2$ absorbers, gallium is not evaporated.

The substrate shutter is closed to prevent residual surfactants during the degassing and heating of both substrate and thermal sources. To improve the homogeneity of the absorbers during the growth process, the rotation of the substrate holder is immediately initialized to rotate at 4-8 revolutions per minute (rpm).

The substrate heater temperature is ramped up at 20-30 °C/minute to the set temperature of 600 °C, and held at this temperature for 30 minutes to clean and to degas the surface of the substrate. The actual substrate temperature corresponding to this set temperature can be found in the

Appendix 2. The influence of substrate temperature on $CuGaS_2$ will be presented in Chapter 5. Concurrently, the temperatures of the thermal sources are also ramped up during this time. Due to the volatility of sulfur, the temperature of the sulfur source is increased in steps of 15-20 °C to approximately 90-120 °C. If not already done, the fluxes of copper and gallium may be measured or calibrated since the level of the molten source in the crucible influences temperature-dependent flux. After the substrate-cleaning period, the deposition process begins with a pre-deposition sulfurization process by opening of the valve of the sulfur source and the substrate shutter while the shutter of copper and gallium remain closed. The pre-deposition sulfurization process enables the formation of an ohmic contact of a thin MoS_2 layer between Mo and the $CuGaS_2$ at the back of the absorber. To minimise pressure fluctuation in the chamber, the sulfur vapour pressure during sulfurization is the same as that which will be used during the absorber deposition. Generally, the temperatures of the Cu and Ga thermal sources are lowered by about 200 °C during the sulfurization period to prevent the evaporation of Cu and Ga when not required, but this also ensures that the Cu and Ga fluxes do not drastically change from the beginning to the end of the deposition period. Towards the end of the sulfurization period, the temperature of the Cu and Ga thermal sources are increased to the temperature matching the desired fluxes earlier calibrated. Thereafter, the copper and gallium shutters are opened under the sulfur atmosphere for the growth of the $CuGaS_2$ absorber layer. For the duration of the deposition process, all the sources' temperatures are kept constant. The chamber pressure is kept constant by the close-feedback loop which adjusts the sulfur flux to maintain a stable chamber pressure. The duration of deposition is approximately two hours and results in the absorber thickness of ~ 2-2.5 µm. The absorber deposition is terminated by closing the shutters and initiating the cooling down of both copper and gallium thermal sources. The cooling down of the substrate heater is also set between 20-30 °C/minutes while the sulfur vapour pressure is kept at the same level as during the absorber growth until the substrate is cooled down to about 200 °C. Since a high chalcogen vapour pressure is needed to grow $CuGaS_2$ absorber layer, a high sulfur vapour is maintained to avert sulfur re-evaporation from the grown absorber during the cooling down process [107, 108]. Additionally, a high sulfur vapour pressure during cool down is important for absorbers processed under copper excess condition because it enables the transformation of Cu_2S to CuS, otherwise, the unavailability of surface sulfur in the absorber for the formation of a secondary phase enhances

the formation of surface defects [109]. The flow of sulfur is stopped after 300 °C and cooling of the samples continues until 200 °C, after which they are removed from the evaporation chamber.

3.6.3 Co-evaporation of $Cu(In,Ga)S_2$ (two-stage and three-stage deposition)

Almost all $Cu(In,Ga)S_2$ absorbers investigated were processed by either the two-stage or three-stage deposition process. The exception is in section 6.1 where some absorbers were deposited by the single-stage method. The description for the growth of such absorbers will not be repeated here as it can be found in Ref [110], however, for a single stage deposition of $Cu(In,Ga)S_2$, the procedure follows the one-stage deposition procedure described above with the simultaneous evaporation of Cu, In and Ga under the sulfur atmosphere.

Additional points to note are that the more intricate three-stage deposition method is a continuation of the two-stage deposition method, hence, the two-stage deposition method will not be exclusively described, rather the explanation of the three-stage deposition method will be presented, however, an explanation of the termination of the two-stage deposition will be given. Furthermore, it will be shown in section 6.2 that for high Ga containing $Cu(In,Ga)S_2$ absorbers, the evaporation of Ga at the third stage of deposition requires some precautions.

The substrates, which in this case are Mo-sputtered SLG, are loaded onto the substrate holders and into the PVD as described in the one-stage deposition above. Fig. 3.8 depicts the three-stage deposition profile followed in part or wholly. The deposition process begins with the degassing and ridding of the Mo-surface of residual surfactants at a set temperature of 450 °C, higher than the first stage deposition temperature. This initial high temperature was not necessary in the one-stage deposition process, since the substrate temperature is high enough to remove adsorbents from the Mo-surface. After about 30 minutes of the cleaning phase, the substrate temperature is reduced as illustration in Fig. 3.8 to the set temperature for the first-stage deposition. In the entirety of this work, different first stage set substrate temperatures between 180-350 °C which corresponds to actual temperatures of ~ 260-435°C have been used (see Appendix 2). Next, the pre-deposition sulfurization step is performed for about 30 minutes under the sulfur vapour pressure to be used in the first stage deposition step. The absorber growth begins when the indium and gallium shutters are opened along with sulfur, which is already flowing into the evaporation chamber. In the first

stage, the $(In_xGa_{1-x})_2S_3$ precursor layer makes up approximately 90 percent of the indium and gallium content in the final $Cu(In,Ga)S_2$ absorber. The thickness of ~ 1.7 um is targeted in this stage after about 60 minutes of deposition. To end the first stage deposition step, the indium and gallium shutters are closed, and the Cu shutter is opened as the substrate set temperature is ramped up to 490 °C at rates between 20-40 °C/minutes; thus, marking the beginning of the second stage deposition step. The influence of different heat ramping rates is discussed in Section 6.4.4.

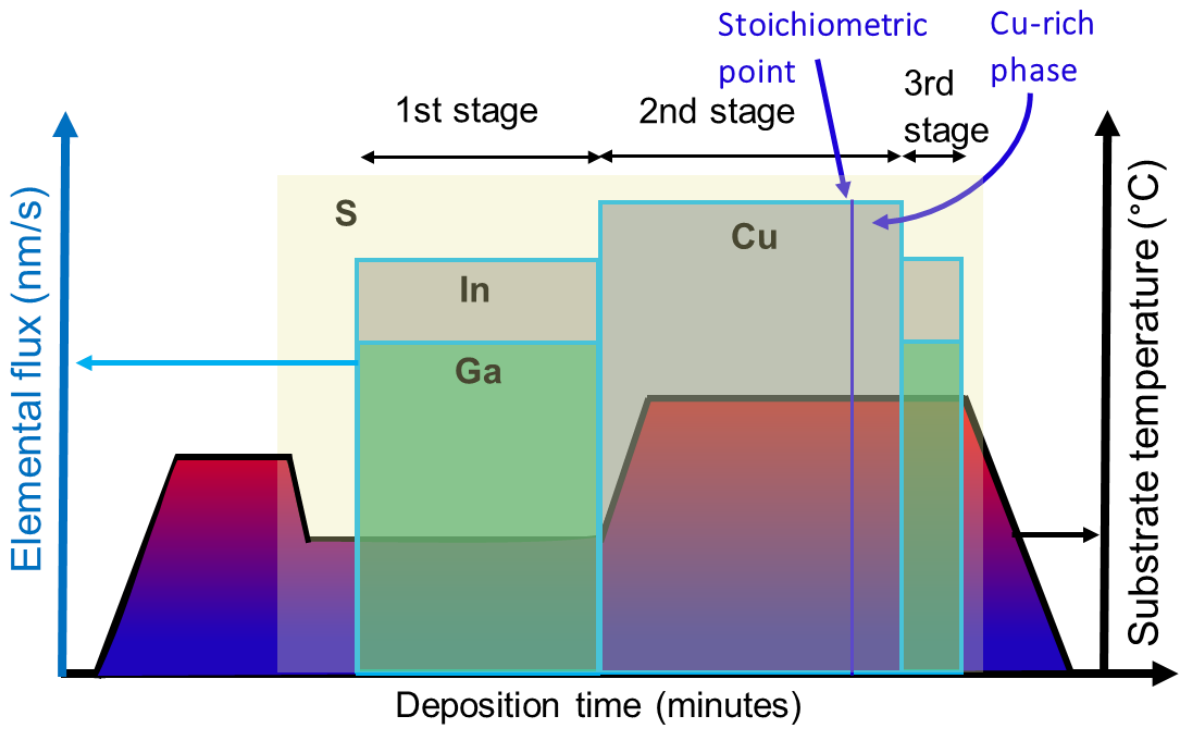

Figure 3.8: Depiction of the deposition profile followed in the three-stage growth process of $Cu(In,Ga)S_2$ absorber layers. The two-stage deposition process is without the third stage. The time is arbitrary and changes with the desired absorber thickness, desired compositional ratio and many more factors.

In the second stage, Cu reacts and diffuses through the $(In_xGa_{1-x})_2S_3$ precursor layer as the Cu-content in the gradually evolving $CuIn_{1-x}Ga_xS_2$ phase progresses. The most important point during the second stage of deposition is the first stoichiometric composition point at which the [Cu]/[III] ratio is approximately 1, after which the Cu-rich regime begins with the formation of secondary

Cu_xS phase. This is marked by an increase in the emissivity of the surface which is being detected by the pyrometer [111]. The metallic nature of the secondary Cu_xS phase means that the surface emissivity of the absorber increases, which leads to higher heat dissipation from the surface of the absorber. This higher emissivity is also reflected in the output power of the substrate heater since it increases to maintain the constant temperature of the substrate heater. For a two-stage deposition process, the duration or amount of the excess Cu deposited after this first stoichiometric point will determine the final [Cu]/([Ga] + [In]) ratio of the $Cu(In,Ga)S_2$ absorber. Cu-excess deposition times up to 15 minutes have been explored in this study. Shutting off the Cu shutter to stop the Cu flux completes the end of the second stage deposition or the two-stage deposition process.

In the case of a three-stage process, indium and gallium are deposited again after the Cu excess deposition, during which there is a recrystallization of the excess Cu by In and Ga. Since the surface emissivity of the absorber reduces, the pyrometer "temperature readout" reduces, as does the output power of the substrate heater. The influence of the Cu excess before the third-stage deposition has also been investigated in this thesis. At the end of Cu recrystallization, a second stoichiometric point is crossed. The continual deposition of In and Ga after this second stoichiometric point determines the final [Cu]/[III] composition. After the desired deposition time, the indium and gallium fluxes are halted, and the absorbers are cooled at the rate of 20 °C/minutes under sulfur atmosphere to 200 °C in a similar manner as described in subsection 3.6.2.

Chapter 4

Why does the QFLS of $CuInS_2$ absorbers improve with temperature and composition?

This Chapter 4 is already published [112] and is taken verbatim with minor modifications. This is highlighted by a report of this chapter in a different text font.

4.1 Effect of deposition temperature and composition on QLFS of $CuInS_2$

In comparison to its selenide counterpart, $Cu(In,Ga)S_2$ still suffers from a high open-circuit voltage deficit, that is, voltage loss relative to bandgap, ~ 600 mV compared to ~ 360 mV in $Cu(In,Ga)Se_2$ [25, 113]. However, Hiroi et al. have achieved a high efficiency $Cu(In,Ga)S_2$ solar cell with absorbers processed at high temperature deposition [24, 113]. To understand the influence of the deposition temperature, previously, we have shown, for $CuInS_2$ (without Ga), that the main enhancement from a higher deposition temperature stem from reduced non-radiative recombination in the absorber, because we observed an increased quasi-Fermi level splitting with higher deposition temperature (QFLS) [27, 114]. Additionally, we have shown that for a set deposition temperature, there is an increase in QFLS with higher Cu-excess, i.e., integral composition of [Cu]/[In] > 1. [27, 114] We could show that the higher QFLS goes along with the reduction of a deep defect [27]. Therefore, it was assumed that the QLFS improvement is due to the reduced density of recombination centers, which will increase the minority carrier lifetime. QFLS gives insight into the quality of the absorber without and before the intricacies of completing the device. As such, it serves as an upper limit for the open-circuit voltage in solar cell devices [51, 115].

The minority carrier lifetime is one of the essential parameters used for characterizing doped semiconductor materials for solar cell [116]. It is a measure of device quality by quantifying the rate of recombination and it is directly related to device efficiency [117-119]. $Cu(In,Ga)S_2$ features very short lifetimes of hundred picoseconds [120] when compared to $Cu(In,Ga)Se_2$ where lifetime can range from tens to hundreds of nanoseconds [118, 119, 121]. Shorter minority carrier lifetimes indicate a higher concentration of minority carriers and thus a higher electron Fermi level $E_{F,C}$, which in turn increases the QFLS.

The dependence of many device properties and performance on doping concentration makes it an important material property. Established techniques of obtaining the dopant concentration in thin-film solar cells include capacitance–voltage (CV) measurements or Hall measurements [47, 122, 123]. Doping concentration has a strong influence on the QFLS of an absorber. In a p-type $CuInS_2$ absorber, with a higher number of acceptors than donors, any changes in doping concentration will change the position of the hole Fermi level ($E_{F,V}$), thereby changing the QFLS.

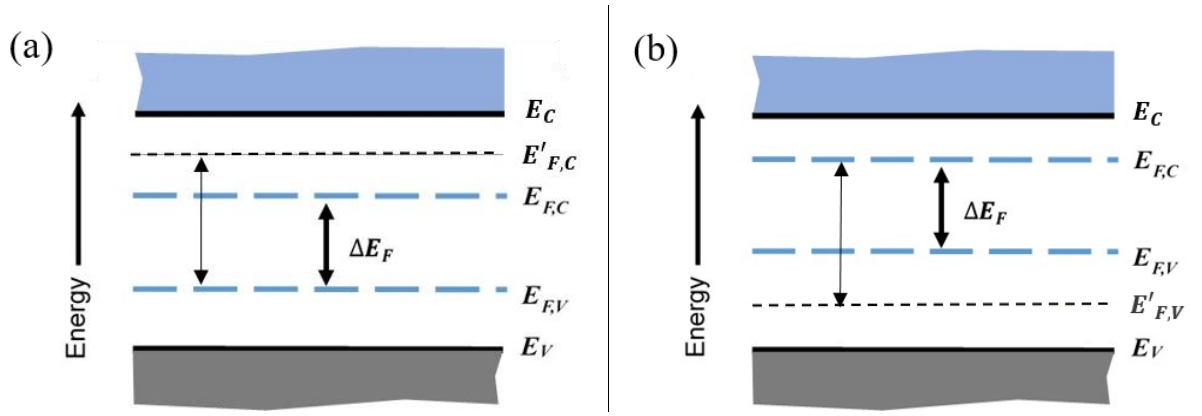

Figure 4.1: Illustration of the positions of the Fermi energy levels with respect to: (a) a reduction of recombination centers (higher electron Fermi level) (b) higher doping concentration (lower hole Fermi level).

The effect of changes in Fermi levels with changes in the density if recombination centers or doping level, which in turn results in changes in QFLS, are illustrated in Fig. 4.1. Fig. 4.1a shows the case of a reduced density of recombination centers: with the quasi-Fermi levels

split, the position of the electron Fermi level $E_{F,C}$ will shift higher to $E'_{F,C}$ as s—own here - and it is assumed that everything else remain unchanged. This shift of $E_{F,C}$ will in turn increase the QFLS. Rather, as shown in Fig. 4.1b, as the doping concentration increases and no change in the density of recombination centers, the hole Fermi level ($E_{F,V}$) moves closer to the valence band, which in turn increases the QFLS.

In this report, the cause of the improvement in QFLS with growth temperature and Cu content for Cu-rich $CuInS_2$ absorbers by means of photoluminescence measurements is probed [115, 124]. By using information derived from time-resolved and calibrated photoluminescence (PL) measurements, which yield the effective minority carrier lifetime and QFLS respectively, we investigate if the improved QFLS is due to less recombination or higher doping concentration. All PL measurements are excited by a laser that is absorbed within the first nm of the μm thick films, thus an influence of differences in the absorptivity can be excluded.

4.2 Preparation of samples and details of experimental procedures

The absorber layers studied were deposited by co-evaporation under Cu excess condition i.e, integral composition of [Cu]/[In] > 1, denoted as Cu-rich. The absorbers form stoichiometric $CuInS_2$ with Cu/In ratio ≈ 1, and copper sulfide (Cu_xS) secondary phases. [125] The Cu_xS phase was removed by potassium cyanide (KCN) etching leaving an almost stoichiometric absorber. [125] Details of the deposition process can be found in reports by Lomuscio et al [27, 114]. Unlike the selenides, e.g. $CuInSe_2$, the absorbers do not degrade in air and did not require cadmium sulfide (CdS) coating to prevent degradation [27, 126]. In time-resolved photoluminescence (TRPL) measurement, a laser pulse excites electron-hole pairs in the absorber and the photoluminescence is recorded in time. The TRPL measurements were performed by time-correlated single photon counting (TCSPC) [127]. Excitation was supplied by an 85 ps pulsed laser of 638 nm wavelength at a repetition rate

(f_{rep}) of 20 MHz. The diameter of the focused beam was ~ 45 μm. The PL emission was detected with a high-speed photomultiplier with an integrated amplifier. As illustrated in Fig. 4.2a, all measurements were at the PL emission peak ~ 820 nm, with the integrated monochromator bandwidth of 45 nm to accumulate an adequate number of photons for all the samples at the same measurement condition. The number of excess minority carriers was approximately 7.6×10^{16} cm^{-3}. This is determined by calculating the number of photons per pulse, assuming that all the photons are absorbed and generate excess carrier pairs, which are then evenly distributed over the absorption length. That is, $\Delta n = \alpha \cdot P_0/(f_{rep} * A_{beam} * E_{photon})$, where Δn, α, P_0, f_{rep}, A_{beam} and E_{photon} are the excess minority carriers, absorption coefficient, average laser power, repetition rate, beam area and photon energy respectively. The absorption coefficient of $CuInS_2$ at the wavelength of the pulsed laser, was estimated as 6.5×10^4 cm^{-1} [77]. We aim at low injection conditions, where the excess carrier concentration (Δn) is less than the equilibrium hole density (p_0), i.e. $\Delta n \ll p_0$, because in this case the PL decay time is solely determined by the minority carrier lifetime [128]. On the other hand, in a high injection condition $\Delta n \gg p_0$ and the PL decay time is determined by both, minority and majority carrier lifetimes [128, 129]. In this work, the excess carrier density is close to the low-injection condition, lower than the typical doping concentration of ~ 10^{17} cm^{-3} for Cu-rich $CuInS_2$ [130, 131]. Excitations at lower injection levels were not possible due to the weak luminescence of the absorbers, which led to a low signal to noise ratio. To account for uncertainty in TCSPC, we also measure the instrument response function (IRF) of the set-up. The measured decay curve, $M(t)$ is a convolution in time t of the luminescence decay $D(t)$ and the $IRF(t)$, i.e., $M(t) = \int_0^t IRF(t')D(t-t')\mathrm{d}t'$ [130]. The luminescence decay $D(t)$ is recovered and fitted using a commercial software from Edinburgh Instruments.

The luminescence decay for an ideal semiconductor is characterized by a single exponential decay [116]. However, CIGS absorbers often feature a multi-exponential decay which can be described as an overlay of several decay times [119]. In this work, background signal from the dark count is subtracted, after which the effective lifetime is extracted from the luminescence decay curve by a triple-exponential fit

$$I_{PL}(t) = \sum_i A_i \exp\left(-\frac{t}{\tau_i}\right) \tag{4.1}$$

where $I_{PL}(t)$ is the intensity at a time t after the laser pulse, A_i decay amplitude and τ_i the decay times for each $i = 1, 2, 3$. The effective lifetime is then a weighted-average τ_{amp} defined as, $\tau_{amp} = \sum_i A_i \tau_i / \sum_i A_i$ [132]. The weighted-average method takes does not give information of the different decay channels, but it allows for a comparison of samples.

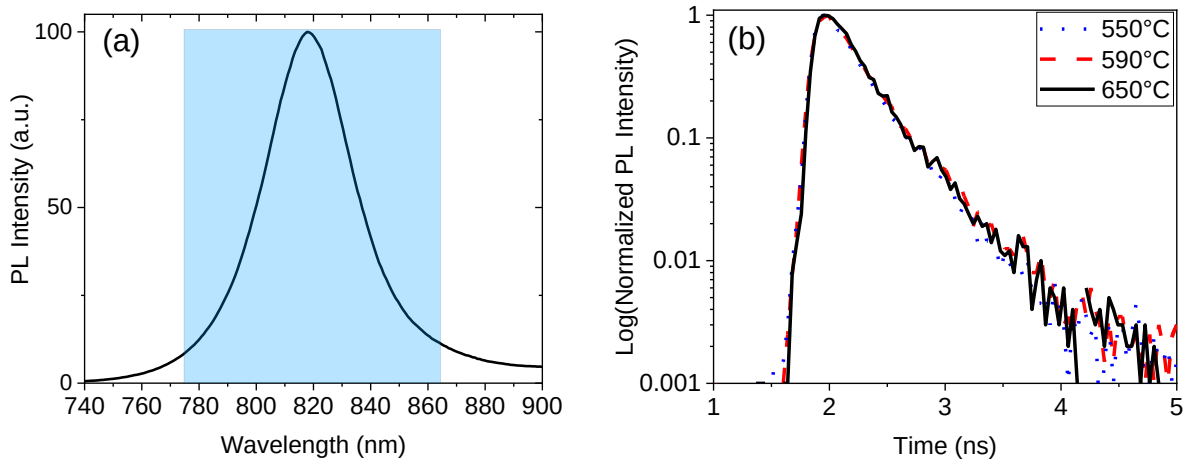

Figure 4.2: Exemplary photoluminescence curves. (a) Spectrum of a Cu-rich CIS showing the range accounted for by the monochromator bandwidth. (b) Normalized measured time-resolved decays on absorbers with growth temperature of 550° C (dotted line), 590 °C (dashed line) and 650 °C (solid line).

For a calibrated measurement to determine the QFLS, the PL experiment is performed using a 660 nm continuous-wave (CW) laser for optical excitation. Two corrections, namely spectral and intensity, are applied to the raw PL data measured by a steady state excitation. The spectral correction is applied with a commercial calibrated halogen lamp. The intensity correction entails the measurement of the laser beam diameter with a charged-couple device (CCD) camera and the laser power by a photodiode power meter. The incident photon flux is then calculated and adapted to twice the AM 1.5 solar spectrum photon flux above the bandgap. The room-temperature bandgap for the samples was ~ 1.51 eV.

An equivalent illumination of “1 sun” is used on the samples. The corrected (and now calibrated) spectra are transformed to the energy domain and evaluated using Planck’s generalized law [53], which describes the energy dependence of the PL yield as a function of absorptivity, temperature, and QFLS. The QFLS is extracted from a fit of the sufficiently high-energy wing of the PL spectra where absorptivity is assumed to be unity [133], More details on QFLS evaluation can be found in the supplemental detail reported by Babbe et al. [134].

4.3 Influence of growth properties on optoelectronic quality and lifetime of $CuInS_2$

The influence of the integral composition and growth temperature on quasi-Fermi level splitting of Cu-rich CIS absorbers have been reported by Lomuscio et al. [114]. The results of the different growth parameters and composition on lifetime are presented and discussed here.

4.3.1. Effect of growth temperature on the QFLS and effective lifetime of $CuInS_2$

To investigate the impact of growth temperature on the rate of recombination, lifetime measurements were carried out on three absorbers with similar Cu/In ratio of 1.8, but different growth temperatures of 550 °C, 590 °C and 650°C. The decay curves are shown in Fig. 4.2b. It can be seen that, there is no change in the decay curves for the three absorbers. Upon evaluation, the extracted lifetime is about 200 ps. This is an indication of a faster rate of recombination in the CIS absorbers compared to the selenides. Nonetheless, the similarity in the effective lifetime shows that the difference in growth temperature has no significant influence on the rate of recombination of minority carriers in the different absorbers. Details

of the QFLS and lifetime of the absorbers are presented in Table 4.1 from which it is seen that there is a clear increase in QFLS with increasing growth temperature, but the lifetime does not change. The dependence of QFLS on Cu/In has also been reported by Lomuscio et al. [114]. It was shown that there is an increase in QFLS with higher Cu-excess. Here, the Cu-rich absorbers with a Cu/In ratio from about 1.1 to 1.8 are investigated. In Fig. 4.3a, the QFLS and the effective lifetimes are plotted against the corresponding Cu/In ratio.

Table 4.1: Summary of the QFLS and lifetime on absorbers with [Cu]/[In] = 1.8

Sample	Growth temperature	QFLS	Lifetime
A	550 °C	806 meV	197 ± 35 ps
B	590 °C	839 meV	209 ± 32 ps
C	650 °C	875 meV	208 ± 33 ps

4.3.2 Quasi-Fermi level splitting and effective lifetime on Cu-rich $CuInS_2$ absorbers

For absorbers processed at 650 °C (black dots), there is a clear increase of more than 40 meV in QFLS with increasing Cu/In ratio, but the lifetime does not show a corresponding increase. In fact, the lifetime scatters around 200 ps. For the high Cu/In ratios, different growth temperatures are shown. Again, the QFLS increases with growth temperature, whereas the lifetimes scatter around 190 ps.

The origin of this indiscriminate distribution becomes obvious in Fig. 4.3b where the decay times τ_1, τ_2 and τ_3 are plotted with respect to the QFLS measured on the same sample. The times τ_1 and τ_2 are ~ 30 ps and ~ 200 ps respectively, and not correlated with QFLS. τ_1 and τ_2 are responsible for the main part of the observed decays. τ_3 arises from the decay tail where the influence of noise becomes much more important and thus τ_3 even more randomly distributed between 400 ps and 800 ps. Regardless of the growth temperature or Cu/In of the absorbers studied, the lifetime is always the same. This indicates that, the improved QFLS is not due to reduction in the rate of recombination. Thus, an increase in

doping with higher Cu/In ratios or higher growth temperatures must be the reason for the increase in QFLS.

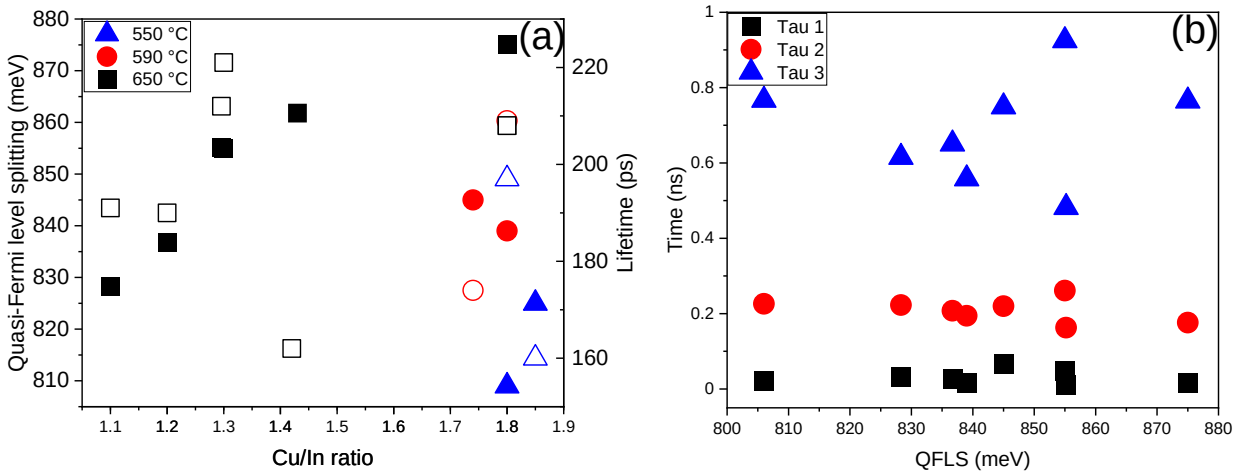

Figure 4.3: (a) QFLS (filled) and lifetime (open) plotted against Cu/In ratio for absorbers with different growth temperatures of 550° C (blue), 590 °C (red) and 650 °C (black). The quasi-Fermi level splitting data of growth temperature 650 °C has been shown previously by Lomuscio et al. [114]. (b) The distribution of the different decay times $\tau 1$, $\tau 2$ and $\tau 3$ are plotted against QFLS.

4.4 Doping level and quasi-Fermi level splitting on $CuInS_2$

Here, the effect of doping concentration on QFLS is studied. The estimation of doping concentration from the measurement of the QFLS and the lifetime is described. In a p-type absorber where the majority carrier are holes, the minority carrier can be generated by an external source, and it is possible to estimate the electron concentration from the photon flux (ϕ) on the absorber. Since the QFLS is measured under steady state excitation, the generation rate is considered for a steady state light source. For the excitation source, it is assumed that every photon is absorbed and generates an electron-hole pair. Then the excess

carrier concentration can be determined from the lifetime. Assuming that the diffusion length of the charge carrier is large enough to achieve a constant carrier concentration over the film thickness, the charge carriers diffuse throughout the thickness (d) of the absorber, then the excess carrier concentration is

$$\Delta n = \frac{\phi\tau}{d} \tag{4.2}$$

and the charge balance is $np = \frac{\phi\tau}{d} N_A$, with n, p and N_A being the electron concentration, hole concentration and doping concentration respectively. Then, the dependence of doping concentration on the quasi-Fermi level splitting is

$$\frac{\phi\tau}{d} N_A = n_i^2 \exp\left(\frac{\Delta E_F}{K_B T}\right) \tag{4.3}$$

where, n_i is the intrinsic carrier concentration, ΔE_F is the quasi-Fermi level splitting, K_B is the Boltzmann constant and T is the temperature in Kelvin. The electron and hole effective masses of $0.16m_0$ and $1.3m_0$ respectively, m_0 being the free electron mass, for $CuInS_2$ as given by Binsma et al [135]. to calculate the intrinsic carrier concentration are utilized. These constants, together with the measured opto-electronic quantities of effective lifetime and QFLS, allows the estimation of the doping concentration of the p-type absorbers.

The calculated doping concentration is plotted against the Cu/In ratio in Fig. 4.4. It can be observed that, the plot mirrors the Fig. 4.3a where QFLS is plotted against Cu/In ratio. We expect this correlation when the lifetime is constant, since then the QFLS is proportional to the logarithm of the doping concentration. For samples A, B and C with similar Cu/In ratio of 1.8, the doping concentration is seen to increase with the growth temperature. To support these series of calculations, doping concentration was also estimated from a CV measurement, performed on finished devices. Due to shunting, it was not possible to do a CV measurement on all the absorbers. However, it was found that; the absorbers processed at 650 °C, with Cu/In ratio higher than 1.4, have doping concentration in the order 10^{17} cm^{-3}, while those absorbers with Cu/In ratio ~ 1.3 or lower were in the order of 10^{16} cm^{-3}. These observations show that, the increase of QFLS with growth temperature or with Cu/In ratio results from higher doping concentration and not from a decrease in recombination rate.

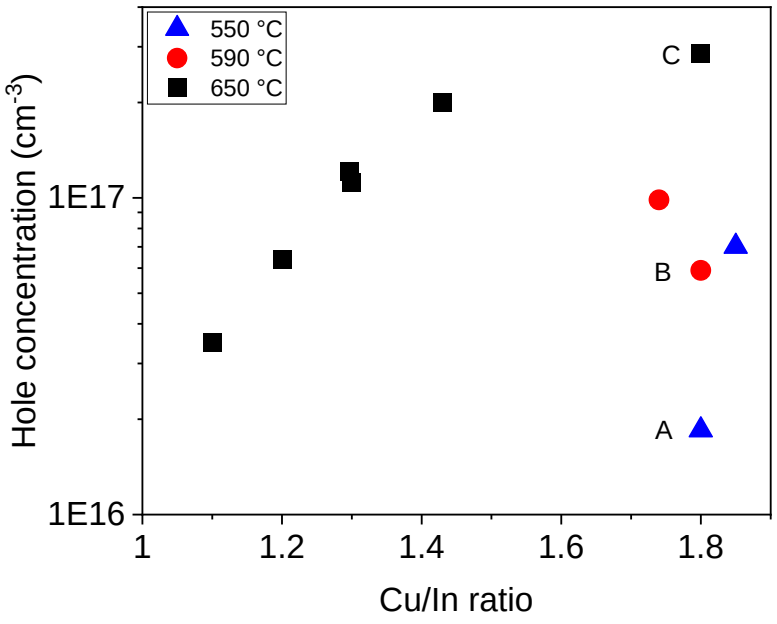

Figure 4.4: Estimated doping concentration on the different absorbers plotted against the Cu/In ratio. The absorbers labelled A, B and C with Cu/In ratio of 1.8 were processed at temperatures of 550°C, 590°C and 650°C respectively.

To summarise this chapter, the cause of improvement in QFLS with higher deposition temperature and higher Cu/In ratio in Cu-rich $CuInS_2$ absorbers has been studied. We showed that, although a higher absorber processing temperature and a higher Cu/In ratio in Cu-rich $CuInS_2$ absorbers lead to a significant improvement in the QFLS, these parameters do not influence the effective lifetime. Rather, the improvement in QFLS with growth temperature and Cu/In ratio, results from an increase in doping concentration, which expectedly shifts the position of the hole Fermi energy level lower and closer to the valence band. Although we previously saw a lower density of deep defects, the minority carrier lifetime is not affected by the changes in deposition temperatures and Cu/In ratio. As such, to optimize $CuInS_2$ solar cells for higher efficiency, it is still necessary to reduce the recombination channels that reduces the effective lifetime.

Chapter 5

Defects in wide-gap $CuGaS_2$

$Cu(In,Ga)S_2$ (CIGS) is not only a promising material for a single junction solar cell, but also a strong candidate as a top cell in tandem applications to absorb high-energy photons of the solar spectrum [15, 23]. Nevertheless, $Cu(In,Ga)S_2$ is still limited by a high deficit in Voc and lower photoconversion efficiency in comparison to its chalcopyrite equivalent $Cu(In,Ga)Se_2$ [24, 113, 136, 137]. The plethora of research works on $Cu(In,Ga)Se_2$ and its parent compounds, $CuInSe_2$ and $CuGaSe_2$, have – among many other findings – established an understanding of the electronic structure and of the impact of elemental substitution, and the Cu excess or deficiency in $Cu(In,Ga)Se_2$ [43, 138-142]. Accordingly, defects, donor and acceptor levels have been identified in both $CuInSe_2$ and $CuGaSe_2$. Particularly, for the wide bandgap $CuGaSe_2$, Spindler et al. have reported that defects levels shift mid-gap and defects that were otherwise shallow in $CuInSe_2$ become deeper in $CuGaSe_2$ [142]. Thus, as Ga is substituted for In, shallow defects become deeper and hence form deep levels which serve as channels for unwanted nonradiative recombination in $Cu(In,Ga)Se_2$ absorbers [138-143]. On the other hand, very few studies of defects in $Cu(In,Ga)S_2$ absorbers exist [120, 144]. However, recently there are new insights into the defect structures of the ternary $CuInS_2$ absorbers, where three shallow acceptors and two deep broad defect bands close to 0.8eV and 1.1 eV have been reported [27, 145]. Although several reports have revisited $CuGaS_2$ in more recent times [58, 61, 72, 146], the prevailing defect structure of $CuGaS_2$ ternary is still unclear. Previous reports (see Fig. 2.7) on $CuGaS_2$ have shown the occurrence of two donor-acceptor (DA) transitions around 2.39-2.41 eV, and these transitions were attributed to a common shallow donor around 20-25 meV [67, 146]. Earlier studies also reported a similar shallow donor energy level at 45-50 meV [58, 61]. In addition, there are reports of deep level transitions around 2.25 eV and 1.8 eV [60, 74]. The likely origin of the donor level has been accorded to a V_S or Ga_{Cu} and one of the acceptors to V_{Cu} [58, 60, 64, 147].

In this work, photoluminescence spectroscopy has been performed on $CuGaS_2$ absorber layers grown by physical vapour deposition to understand the electronic defect structure. This chapter will conclude by presenting a novel solar cell on Cu-rich $CuGaS_2$ absorber. Apart from this

contribution advancing the comprehension of defects structure in $CuGaS_2$, it is also believed that it will supplement the understanding of the role of Ga in $Cu(In,Ga)S_2$.

5.1 Deposition process for $CuGaS_2$ absorbers

The polycrystalline $CuGaS_2$ absorbers investigated in this work were deposited by one-stage co-evaporation of elemental copper and gallium with a source temperature of ~1250°C and ~1150°C, respectively, under a sulfur atmosphere. The one-stage deposition profile is illustrated in Fig. 3.7. The various compositions of the $CuGaS_2$ films were obtained by changing the temperatures of the elemental sources. The deposition was on a molybdenum coated HT-glass with better heat resistance than soda-lime glass [114] at actual substrate temperature of ~ 690°C. Such high substrate temperature is necessary to obtain a high-quality Ga-containing films particularly for pure $CuGaS_2$ [36, 148, 149]. This is partly due to: (i) the slow elemental migration and reaction velocity of Ga relative to In, and the relatively melting point of Ga-based samples than In-based samples [36, 40, 150], as seen in the Cu_2S-In_2S_3 and Cu_2S-Ga_2S_3 phase diagrams [36, 40]. (ii) The higher melting point of sulfides compared to selenides due to the difference in the mean atomic weight and lattice strain of S and Se [151-153]. Lower substrate temperatures resulted in poor quality absorbers showing unidentifiable crystallographic phases among those close to $CuGa_3S_5$ and $CuGa_5S_8$ [31, 37, 154]. This shares a similarity to $CuGaSe_2$ when deposited at low temperatures [155]. Conversely, at these high deposition temperatures, group VI elements such as sulfur and selenium, have low sticking coefficient and are extremely volatile, which increases the possibility and the rate of sulfur loss and re-evaporation [63, 73, 156, 157]. The growth properties of absorbers grown at various sulfur vapour pressures and substrate temperatures, labeled G1-G4, are presented in Table 5.1; the X-ray diffractogram on them are also shown in Fig. 5.1. Analysis of the chemical composition of the absorber G1, deposited with actual substrate temperature of 600° C and chamber pressure of $3.7 \cdot 10^{-5}$ mbar, showed that the [S]/([Cu]+Ga]) was 0.69. From the X-ray diffractogram in Fig. 5.1, the deficiency of sulfur in G1 promoted the growth of a γCu9Ga4 phases. An increase in the growth temperature to 620 °C in G2 minutely increased the S content to 0.71 and the slight decrease of the γCu9Ga4 phase. Ultimately, by simultaneously

increasing both the deposition temperature and chamber pressure to ~ 690°C and 5.9 · 10^{-5} mbar respectively, the S content increased to 1.0 and the unwanted γCu9Ga4 phases were suppressed.

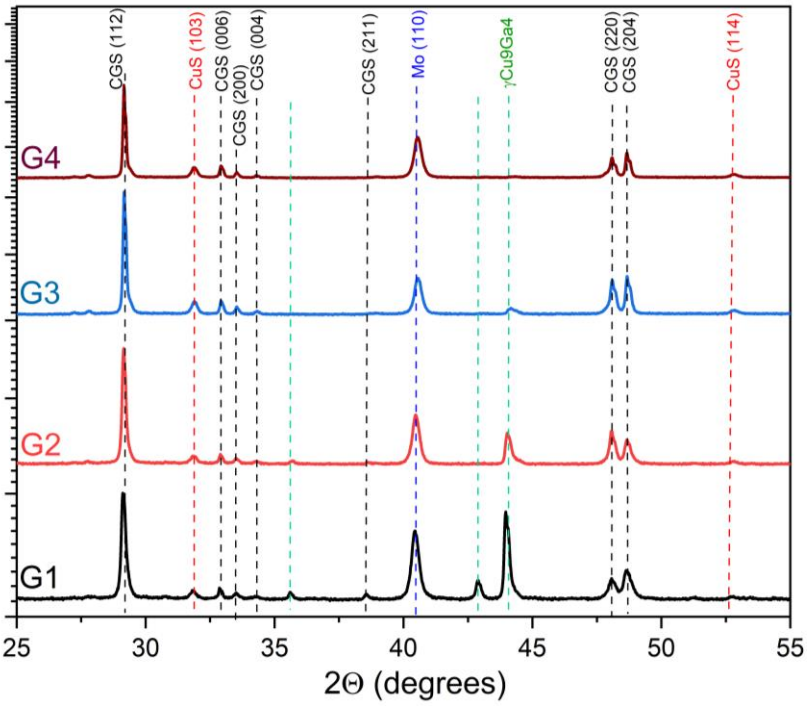

Figure 5.1: X-ray diffractogram of various absorbers showing the effect of increasing different growth temperatures and chamber pressures from G1-G4. The details are presented in Table 5.1.

Hence, the deposition of $CuGaS_2$ requires a large S overpressure [58], than would be needed for pure $CuInS_2$ or $Cu(In,Ga)S_2$ [148, 158], in order to mitigate sulfur loss. Consequently, during the $CuGaS_2$ deposition process, the chamber pressure is maintained in the range of 5.9-8.5 · 10^{-5} mbar. The deposition time of ~ 2 hours is used to achieve thicknesses of nearly 2μm. The characterization of the crystallinity, phases and vibrational properties of the absorbers was by X-ray diffraction (XRD) using the CuKα radiation, and Raman spectroscopy with an excitation wavelength of 532 nm. The surface morphology and cross-section micrographs were obtained by a scanning electron microscope (SEM), and the chemical composition was determined by energy dispersive X-ray spectroscopy (EDX) with beam energy of 20 kV on as-grown absorbers before etching. Therefore, the compositional ratio mentioned in this report is an integration of the ternary chalcopyrite phase and secondary copper sulfide (Cu_xS) phases. As such, Cu-poor absorbers refer to the ratio

[Cu]/[Ga] ≤ 1, while the Cu-rich refers to [Cu]/[Ga] ≥ 1. The Cu-excess phases were removed by etching in an aqueous solution of 10 % potassium cyanide (KCN) for 5 minutes [125], before the photoluminescence measurements.

Table 5.1: Influence of deposition properties on the sulfur-content in $CuGaS_2$ absorbers

Absorber label	Actual substrate temperature	Chamber pressure	[S]/([Cu]+[Ga])
G1	600 °C	$3.7 \cdot 10^{-5}$ mbar	0.69
G2	620 °C	$3.7 \cdot 10^{-5}$ mbar	0.71
G3	640 °C	$4.7 \cdot 10^{-5}$ mbar	0.81
G4	690° C	$5.9 \cdot 10^{-5}$ mbar	1.0

5.2 Effect of growth conditions on the structural properties of the absorber

Before presenting the results and discussing the optical characterization of different spectral regions on the absorbers, it is imperative to ascertain the quality of the absorbers under investigation. Hence, in the following section, the material characterization in terms of composition analyses, preferential chalcopyrite orientation, crystallinity and microstructural structural properties obtained from SEM-EDX, XRD and Raman analyses will be examined.

The chemical composition of the different films studied, as analyzed by EDX, is between 0.94 and 2.0 in [Cu]/[Ga] atomic ratio. Fig. 5.2 shows the SEM micrographs depicting the typical surface morphology and cross-sectional images of Cu-rich and Cu-poor absorbers. The specific composition of the absorbers shown are [Cu]/[Ga] = 1.3 for the Cu-rich absorber, and [Cu]/[Ga] = 0.94 for the Cu-poor absorber. The micrographs were obtained after the Cu_xS secondary phase was etched by 10 % KCN solution. The top-view, Fig. 5.2b, and the cross-sectional image, Fig. 5.2d of the Cu-poor absorber show rough granular surface with pyramidal grains which are compact and well-connected to the back on the Mo back-contact. On the other hand, both micrographs in Fig. 5.2a and Fig. 5.2c show that the Cu-rich films featured smoother surfaces with larger and

denser grains. This is in accordance with other chalcopyrite compounds, where it is well established that copper-excess promotes the formation of large grain sizes and improves crystallinity [27, 69, 103, 159, 160]. Additionally, the high deposition temperature and pressure could have contributed to the quality of both Cu-rich and Cu-poor absorbers, as these conditions foster effective nucleation and improve the quality of the grain growth [73, 114].

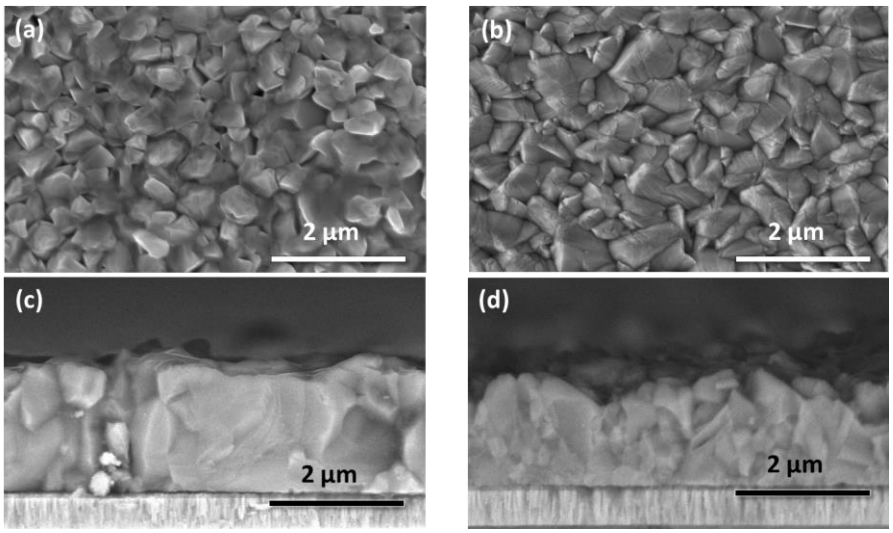

Figure 5.2: SEM micrograph showing the microstructure of $CuGaS_2$ absorbers. Top-view and topographical view of typical Cu-rich absorber ((a) and (c)), and Cu-poor absorber ((b) and (d)).

The characteristic crystallographic orientation of the prevalent phase in the layers obtained from XRD is depicted in the diffractogram in Fig. 5.3a. The ICDD database - ICDD PDF 00-025-0279 is used as a reference to index the peaks. The most prominent peak is the (112) plane of $CuGaS_2$. The (110) peak at 41° in Fig. 5.3a is due to Mo. A measure of the absorber crystal quality is manifested in the occurrence of the 220 and 204 planes, resulting from the tetragonal splitting occurring in the chalcopyrite unit cell. The crystal quality of the absorbers investigated is also corroborated by the absence of secondary phases in Fig. 5.3a. Fig. 5.3b shows the Raman spectrum on a $CuGaS_2$ absorber. The dominant line at 310 cm^{-1} is the A1 mode, known as the breathing mode, and it corresponds to the vibration of the sulfur (or group VI) atom [161, 162]. This mode is also the dominant mode for chalcopyrite compounds such as $CuInS_2$, $CuInSe_2$, $CuGaSe_2$, etc. [163, 164]. The other less intense but notable Raman-active modes appearing at 276 cm^{-1}, 364 cm^{-1} and 384 cm^{-1} correspond to the highest longitudinal optical phonon modes [161], while the peak

at 408 cm^{-1} has been attributed to MoS_2 [165]. The impact of the modes will be revisited in relation to the observed peaks in the PL spectrum discussed in the subsequent section below. To summarize, the results from the SEM-EDX, XRD and Raman analyses on the $CuGaS_2$ thin films investigated attest to the good quality of the absorbers.

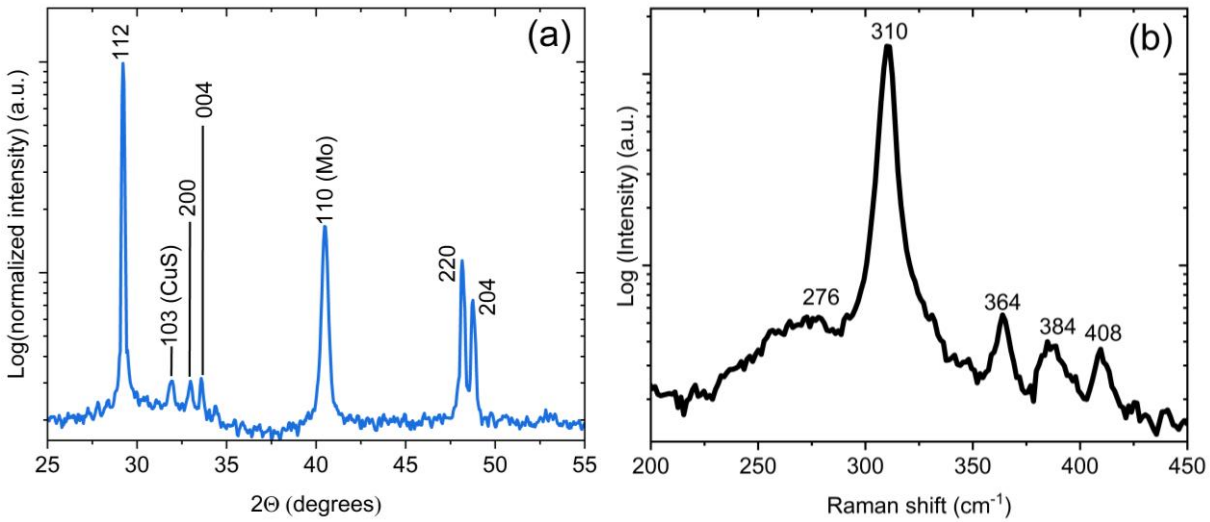

Figure 5.3: (a). X-ray diffractogram of a typical $CuGaS_2$ absorber showing the reflection planes. (b) Raman spectrum of a Cu-rich $CuGaS_2$ absorber with the Raman active modes.

5.3 Photoluminescence features of $CuGaS_2$ at low temperature

First, a summary of the spectral belonging to various $CuGaS_2$ absorbers with varying compositional ratios is presented. Afterwards, the methods used in analyzing and assigning the different peaks to a specific transition are discussed. Fig. 5.4 shows an overview of different $CuGaS_2$ PL spectra by composition at 10 K. The spectral features (i) band edge emissions with sharp intense excitonic (EXC) peaks around 2.48 eV, 2.49 eV and 2.502 eV; (ii) defect-related emissions between 2.3 eV and 2.45 eV: several free-to-bound (FB) and donor-acceptor transitions (DA) with their respective phonon replicas, and (iii) broad deep defect peak at ~ 2.15 eV. The influence of the [Cu]:[Ga] composition on some peaks can be observed in the 2.3 eV transition

(DA3), where the intensity of the peak increases with increasing Cu content, even dominating and screening other peaks in the spectrum for the absorber with [Cu]/[Ga] ratio = 2.

For slightly Cu-rich absorbers with [Cu]/[Ga] ratio of 1.3 for example, the relative intensity of the 2.3 eV transition to the other peaks reduces, and it is noticeable that the 2.3 eV transition overlaps with a broad peak around 2.15 eV. In contrast, the intensity of the broad peak at ~ 2.15 eV and another at 1.85 eV (not shown in Fig. 5.4) increases with lower Cu-content and it dominates the Cu-poor absorber alongside the excitonic transition at 2.48 eV and transitions around 2.40 eV.

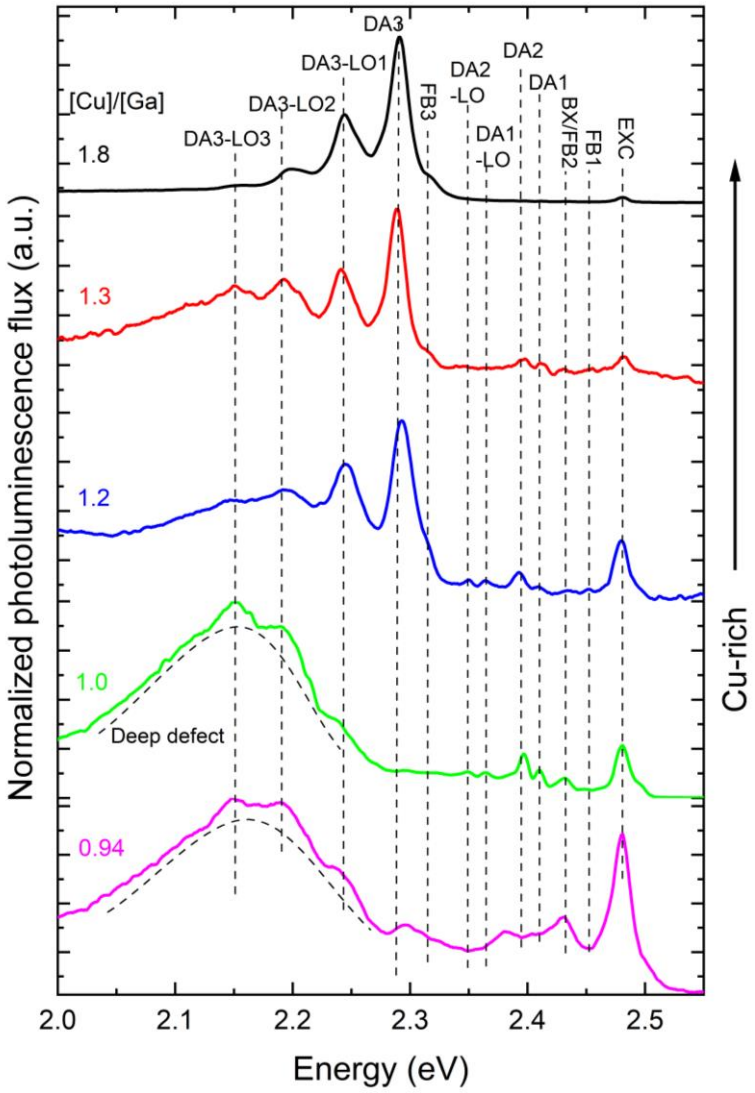

Figure 5.4: Photoluminescence spectra of shallow defects for $CuGaS_2$ absorbers of different chemical compositions at 10 K. The attribution of the peaks to the transitions in the figure will be derived in the following sections.

To investigate the different spectral regions, the intensity of the transitions described above is considered, as such, the band-edge emissions and shallow defects are investigated using the near stoichiometric and Cu-rich absorbers, while the deep defects are studied with Cu-poor and near-stoichiometric absorbers. The assignment of a peak to a specific transition follows the evaluation of PL flux and energy position in dependence of the excitation intensity in a double logarithmic scale and semi-logarithmic scale, respectively [49]. A simplified single exponential power law described by equation (5.1) is then used to analyze the dependence of the integrated PL flux on laser excitation intensity [49].

$$I_{PL} \propto \phi^{k} \tag{5.1}$$

I_{PL} is the laser excitation intensity, ϕ is the integrated PL flux and k is the power law exponent, taking values $k \leq 1$ for DA and FB, and $1 \leq k \leq 2$ for excitonic transitions [49, 166]. However, the high luminescence of some samples allowed for a wide range of excitation intensity, and the double-logarithmic plot of the excitation-dependent integrated PL flux of such samples result in a curvature which cannot be described by a single power law. The curvature is inherent and occurs when multiple defect levels participate in the recombination process [167]. Using rate equations and charge balance, exhaustive conditions beyond just the simple case, where a single power law can describe PL flux dependence on excitation intensity, has been reported in Ref [166-168]. A more comprehensive double-power law expression that better describes the curved shape

$$I_{PL} \propto \frac{\phi^{k_1+k_2}}{1+\left(\frac{\phi}{\phi_0}\right)^{k_1}} \tag{5.2}$$

where k_i, (i = 1, 2) take on multiples of $\frac{1}{2}$ and ϕ_0 is a turning point or crossover excitation at which a state involved in the recombination process becomes saturated [167]. Essentially, for a curved double-log plot, the k-values are such that for exciton-related transitions, $\frac{2}{2} \leq k \leq \frac{4}{2}$, whereas for defect-related transitions $\frac{1}{2} \leq k \leq \frac{3}{2}$ [167]. A simple summary of k-value for different transitions investigated in this work is presented in Table 5.2, however, more complex cases can be found in Ref. [166, 167].

Table 5.2: Summary of the behaviour of the power law exponent (k) and β-values in dependence of excitation intensity. The values of k take on multiples of $\frac{1}{2}$.

Transition	**Power law exponent (k)**		**Change of energy position (β-value)**
	Low (ϕ)	**High (ϕ)**	
Exciton	$\frac{4}{2}$	$\frac{2}{2}$	0
Donor-to-acceptor (DA)	$\frac{3}{2}$	$\frac{1}{2}$	1-5 meV/decade
Free-to-bound (FB)	$\frac{3}{2}$	$\frac{1}{2}$	0

Between the DA and FB transition, the DA transition is distinguished by a characteristic blue-shift of its transition energy position with increasing excitation intensity. This energy position is expressed by,

$$E_{DA} = E_G - (E_D + E_A) + \frac{q^2}{4\pi\varepsilon_0\varepsilon_r R_{DA}} \tag{5.3}$$

where E_{DA} is the DA peak energy position, E_G is the bandgap, E_D is the donor defect energy and E_A is the acceptor defect energy. The last term is the Coulomb energy, with q being the elementary charge, ε_0 is vacuum permittivity, ε_r is the relative permittivity and R_{DA} is the spatial distance between the donor and acceptor [49, 169]. As the excitation intensity increases, the density of neutralized donors and acceptors increases, and the spatial distance R_{DA} between the donor and acceptor atoms decreases, thereby increasing the influence of the Coulomb interaction. The relationship between the transition energy position in dependence of excitation is empirically described by

$$E_{DA}(\phi) \propto E_{DA}(\phi_0) + \beta \log\left(\frac{\phi}{\phi_0}\right) \tag{5.4}$$

where β typically takes values between 1-5 meV per decade of excitation intensity [170].

5.4 Near band-edge (2.46-2.53 eV) luminescence of $CuGaS_2$

The band-edge emissions are assessed using the absorber with the highest Cu-content of [Cu]/[Ga] ratio = 2.0, due to its high luminescence flux and well-resolved peaks. The luminescence strength of this absorber also supports the enhanced crystallinity when absorbers are processed under high Cu excess. A plot of the PL spectra in the band-edge region between 2.46 eV and 2.53 eV at different excitation intensities is illustrated in Fig. 5.5.

Of the five peaks delineated, the most intense peak is at ~ 2.481 eV (D), with transitions at 2.488 eV (C) and 2.496 eV (B) at lower intensities. On the high-energy end, the weak line at ~2.518 eV (A) is visible only at high excitation, and on the low-energy end, the intensity of a transition at ~2.474 eV (E) decreases while the 2.468 eV (F) peak is more resolvable at higher excitation intensities. In Fig. 5.5, the lines at A-D do not show a shift of energy positions with increasing excitation intensity, which preliminarily leaves them as either excitonic or free-to-bound transitions. To discriminate between the two possibilities, the photon flux in dependence of the excitation intensity for the different peaks is evaluated in the double-log plot shown in Fig. 5.6. A fit of the points by the equation (5.1) to determine the power law exponent (k) result in values between $1.2 < k < 1.3$ for all the transitions as presented in Fig. 5.6a. Such superlinear dependence of PL flux is characteristic of excitonic transitions [49], although it is evident that the double-log plots are curved and cannot be fittingly described by the single power law. The multiple-power law in equation (5.2) is rather used to fit the curves, and the fit of the emission line 2.496 eV (B) is presented in Fig. 5.6b.

The k-exponent results in $\sim\frac{3}{2}$ at low excitation intensity, and in $\sim\frac{2}{2}$ at high excitation intensity. As mentioned in the introduction to this section, the exponents take on multiples of $\frac{1}{2}$, and the change of exponent occurs when competing transitions or a defect involved in the transition saturates. The line B transition at 2.496 eV in Fig. 5.5 is attributed to the free exciton transition, since it occupies the highest energy position (apart from line A which is only detected at higher excitation intensity and will be discussed later). Bound excitons appear at lower energies due to larger binding energies of the exciton to defects [49, 61, 135]. Consideration of the 2.496 eV as a free exciton is further

substantiated by its subsequent use in deducing the free exciton binding energy (E_x) from the first excited state, as shown next.

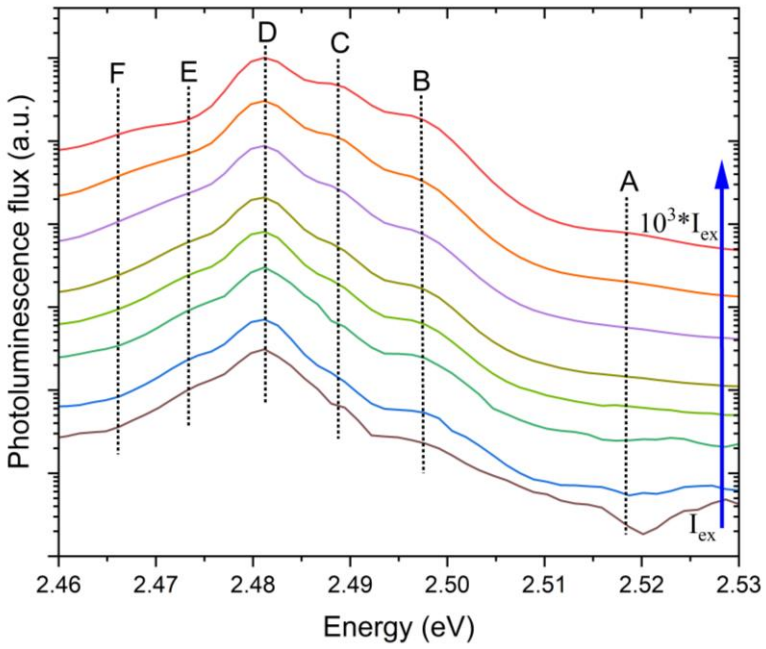

Figure 5.5: Excitonic spectra of Cu-rich $CuGaS_2$ measured at 10 K taken at several excitation intensities over three orders of magnitude. The transition peaks are at ~2.474 eV (E), 2.481 eV (D), 2.488 eV (C), 2.496 eV (B) and 2.518 eV (A). The dashed lines highlight the constant energy positions with increasing excitation intensity.

In previous reports, and in agreement with this report, free exciton has been observed between 2.489 eV and 2.504 eV from photoreflectance spectroscopy and PL analyses [57, 61, 64]. In the different reports, the disparity of the free exciton energy positions were linked to lattice strain during the deposition processes and the different analytical techniques [63]. The emission line A at 2.518 eV in Fig 5.5 matches the first excited state (n = 2) of the free exciton, and the free exciton binding energy can be determined from the energy difference between the ground state $E_{FX}(n=1)$ and the first excited state $E_{FX}(n=2)$ using $E_x = \frac{4}{3}(E_{FX}(n=2) - E_{FX}(n=1))$. The determined free exciton binding energy of 29 meV is in the range of reported free exciton binding energy for $CuGaS_2$ between 28-32 meV [21, 61, 74], which further justifies the designation of line

A as the first excited state of the free exciton. The knowledge of E_X makes it possible to deduce the bandgap value, which will be important in the determination of the defect level energies.

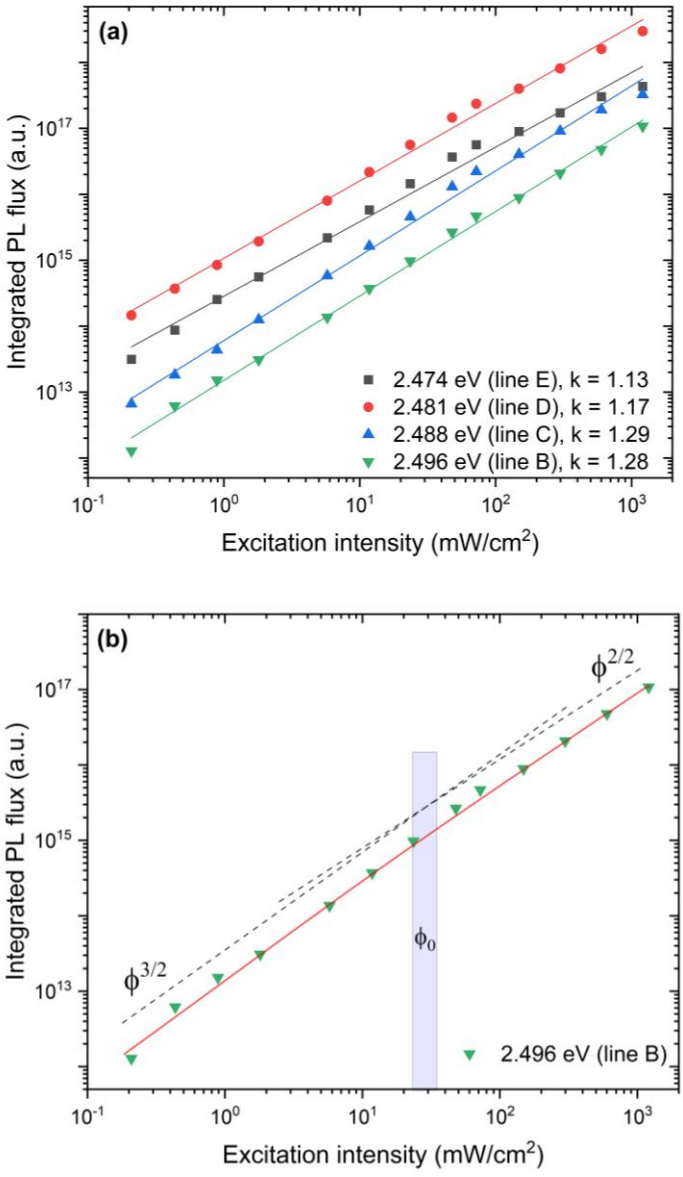

Figure 5.6: (a) Excitation intensity dependence of integrated PL flux for transitions lines 2.474 eV (E), 2.481 eV (D), 2.488eV (C) and 2.496 eV (B) fitted with a single power law. (b) A fit of the emission line 2.496 eV (B) with two power laws exponents $k = \frac{3}{2}$ and $k = \frac{3}{2}$ at high and low excitation, respectively. ϕ_0 denotes the turning point between the two excitation regimes, i.e., the flux where one of the defects is saturated.

Therefore, in this study, we report the corresponding bandgap, ($E_g = E_{FX} + E_X$), for $CuGaS_2$ as 2.525 eV at 10K. For $CuGaS_2$, the hole effective mass (m_h) deduced from Hall-effect analysis and by calculation is $m_h = 0.69\, m_o$ [171, 172], where m_o is the electron mass, and the dielectric constant obtained from optical-absorption analysis is ε_o= 8.5 [147]. Different values between 0.12-0.19m_o have been reported for the reduced mass of $CuGaS_2$ by different groups, consequently, the electron effective mass (m_e) deduced from the reduced mass is between 0.13-0.26 m_o [61, 153, 171-173]. Therefore, the mass ratio (m_e/m_h) for $CuGaS_2$ is between 0.19-0.38. Sharma et al. found that the limit of mass ratio for solving the Schrodinger equation for electron and hole around a charged donor and a charged acceptor is 0.20 and 0.29 respectively [174], as such, the mass ratio for $CuGaS_2$ suggests that the binding of excitons to both ionized donors and acceptors in $CuGaS_2$ would result in unstable ionized complexes [174].

However, binding energy for the neutral complex of both the donor (D^0, X) and the acceptor (A^0, X) can be found from the expressions

$$E_{(D^0,X)} = 0.12E_D + E_X \tag{5.5}$$

$$E_{(A^0,X)} = 0.07E_A + E_X \tag{5.6}$$

where, E_D and E_A are donor and acceptor energies respectively [61, 174, 175]. Similar to the deduction of the binding energy for free exciton, the difference between a bound exciton and the bandgap corresponds to the binding energy of the bound exciton [176, 177].

From the knowledge of the bandgap and exciton binding energy, the probable ionization energies of the donors or acceptor corresponding to an emission line can be calculated from equations. (5.5) and (5.6). The values are summarized in Table 5.3 for emission lines C to F. Previous reports have associated similar transition to the line C at 2.488 eV to a bound exciton recombination [69, 146], while some other reports have attributed a comparable emission to the 2.481 eV line (D) as a FB recombination involving a transition between a neutral donor and the valence band-edge [69, 178]. According to the estimation presented in Table 5.3, it seems that the 2.488 eV exciton (C) is bound to neutral acceptor at 67 meV or neutral donor at 114 meV, while the 2.481 eV emission (D), is bound exciton to a neutral donor at 125 meV or a neutral acceptor 214 meV. The existence of either of these levels and applicable level is presented in the succeeding sections.

Table 5.3: Estimated values of exciton binding energies, neutral donor and acceptor energy levels calculated using equations. (5.5) and (5.6) for the emission lines C-F.

Line	Emission (eV)	Binding energy (meV)	Neutral donor E_D (meV)	Neutral Acceptor E_A (meV)
C	2.488	37	67	114
D	2.481	44	125	214
E	2.474	51	183	314
F	2.468	57	233	400

Lastly, in previous reports, transitions identical to the line E have been assigned to a FB transition involving a shallow level [58, 61]. However, following the excitation-dependent analyses of the line E showing exciton-related behavior. The consideration of the transitions at 2.474 eV (line E) and 2.468 eV (line F) as exciton-related transitions would require that the exciton be bound to a much deeper defect level, as inferred from Table 5.3.

5.5 Shallow defects, donor-to-acceptor pair transitions and phonon coupling

Several sharp peaks dominate the typical PL spectrum of Cu-rich $CuGaS_2$ absorbers at 10 K, between the range of 2.42 eV and 2.10 eV, as seen in Fig. 5.7. Some of the peaks appear in groups at regular energy intervals, and as it will be shown in the following: these are phonon replicas associated with shallow donor-to-acceptor (DA) transitions. The series of sharp peak follows an intense line, known as the zero-phonon line (ZPL), which on its low energy end, several successive peaks of weakening intensities follow. These peaks are separated by the energy of the coupling LO-phonon. The excitation- and temperature-dependence behavior of the phonon-replicas is identical to the emission at the ZPL. As we show below, the spectral intensity dependence of such phonon-assisted transitions is well described by the Poisson distribution expressed by,

$$I_n \propto \exp(-S)\frac{S^n}{n!}, \tag{5.7}$$

where n is the number of phonons involved in the interaction, I_n is the intensity of the nth phonon replica and S, known as the Huang-Rhys factor, is the coupling strength of the electron-phonon interaction [179]. For shallow (non-localized) defects, the electron-phonon coupling is weak and $S < 1$, thus, the ZPL is the most intense peak and does not shift in peak energy. On the other hand, if $S = 1$, there is a change in the maximum intensity, as the first phonon replica is of the same intensity as the ZPL. Lastly, when $S > 1$ there is a strong electron-phonon coupling of localized defects, leading to a shift in the maximum intensity away from the ZPL to a lower energy, since the phonon replicas have higher intensities than the ZPL. It is worth mentioning that for broadened emission bands, phonon replicas do not manifest by the sharp peaks, rather by a broad asymmetric distribution [180-182].

In the next subsections, each of the donor-to-acceptor pair transitions (DA) peaks as shown in Fig. 5.7, that is, DA1, DA2 and DA3, along with their accompanying phonon replicas, will be discussed.

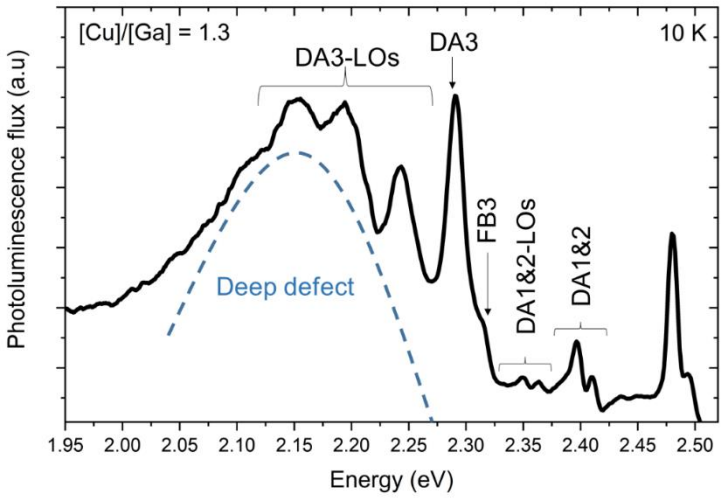

Figure 5.7: Low temperature (10 K) spectrum of Cu-rich $CuGaS_2$ absorber of [Cu]/[Ga] = 1.3 measured at 10 µW. Phonon replicas follow many DA transitions between 2.42 eV and 2.10 eV. This is the same absorber in Fig. 5.4 at a higher excitation intensity. The sample is chosen at this excitation power to highlight the appearance of several DA transitions and their replicas all together. The dashed line centered at approximately 2.15 eV delineates a broad transition around the said energy.

5.5.1 DA3 transition at ~ 2.29 eV

The low-temperature (10 K) PL spectrum showing the transition relating to 2.29 eV, measured at a low excitation intensity where the peaks are well resolved and without the strong influence of other defect peaks, is presented in Fig. 5.8. It is worth noting that the sample in Fig. 5.8 is the same as the sample in Fig. 5.4 with [Cu]/[Ga] = 1.8. However, while the spectrum presented in Fig. 5.8 is measured at 10 µW, the spectrum presented in Fig. 5.4 is at 100 µW. The spectrum (Fig. 5.8) features a series of peaks with the most intense line at ~ 2.29 eV followed by several successive lines of weakening intensities on the lower energy end. These weakening lines are energy-spaced by ~ 45±1 meV, corresponding to the highest optical phonon modes of 45.2 meV, 47.6 meV and 49 meV [161, 183], which are equivalent to the Raman modes observed at the frequencies of 364 cm^{-1}, 384 cm^{-1} and 408 cm^{-1} as seen in the Raman spectrum of $CuGaS_2$ presented in Fig. 5.2b.

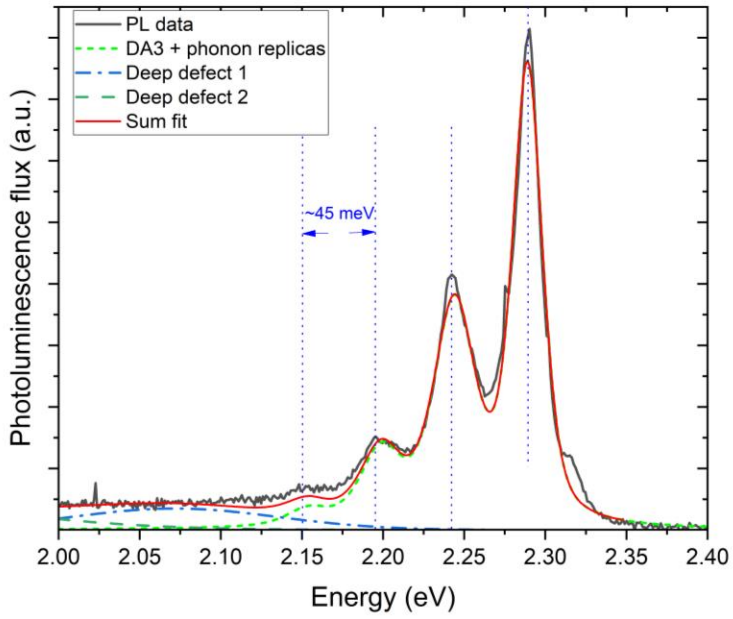

Figure 5.8: Low-temperature (10 K) PL spectrum of a $CuGaS_2$ absorber of [Cu]/[Ga] = 1.8 between 2.0-2.4 eV. The figure shows a fit of the phonon-assisted transition at ~ 2.29 eV (DA3) by Poisson function with consideration for deep defects. The low intense peak at ~ 2.32 eV is an associated FB transition related to DA3 which will be discussed afterwards.

A fit of the spectral and intensity pattern by the Poisson distribution in equation (5.7), while also considering deep defects, yielded a Huang-Rhys factor $S \approx 0.80 \pm 0.05$ and a ZPL at ~ 2.285 eV. This value of S indicates a strong and localized electron-phonon coupling, which suggests the involvement of a deep defect [49, 181].

To identify the exact nature of the transition, the PL spectra acquired at different excitation intensities for the energy between 2.10-2.35 eV are presented in Fig. 5.9a. It is visible that there is a blue-shift of peak positions for the ZPL and the phonon replicas as the excitation intensity is increased. Such a shift in energy position is due to the influence of Coulomb interaction and indicative of a DA transition as stated in Section 5.3 and expressed by the equation (5.4).

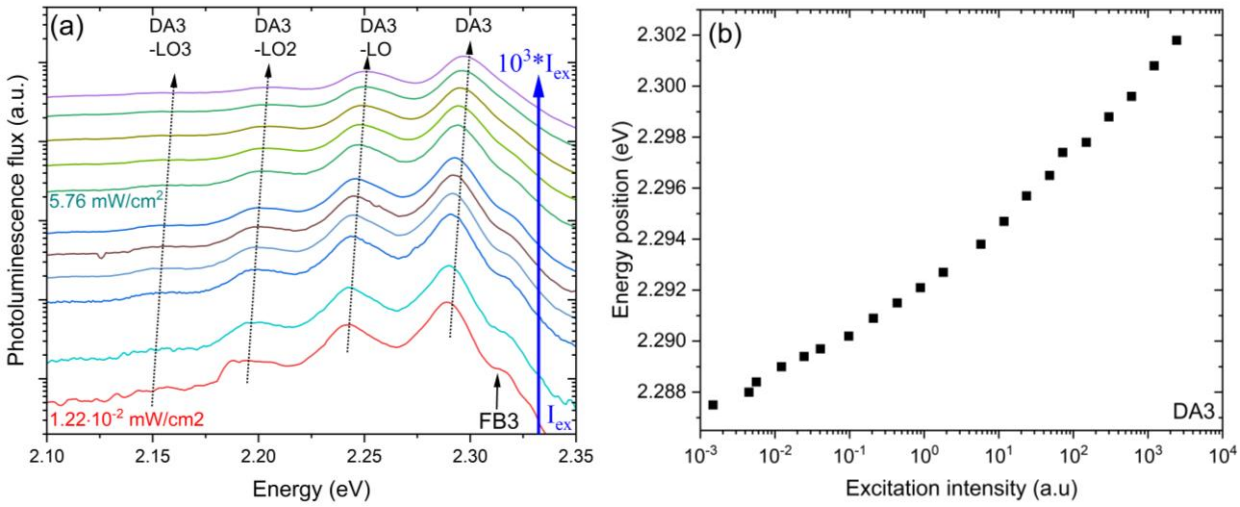

Figure 5.9: (a) The low-temperature (10 K) PL spectra of Cu-rich $CuGaS_2$ at different excitation intensity, demonstrating the shift of energy position of DA3 and its phonon replicas with the increase in excitation intensity. The dotted arrows are used to guide the eye for the shift in energy position. (b) Excitation intensity dependence of the energy position of DA3 transition in a semi-logarithm plot at 10 K.

The actual shift of energy position can be extracted from a plot of the energy positions against the excitation intensity. As shown in Fig. 5.9b, for the transition at ~ 2.29 eV, the plot of energy position

against excitation intensity shows a curvature. This is due to the fact that, for a sufficiently wide range of excitation intensity, the energy positions of DA transitions assume an S-shape behaviour [167, 184]. The peak position approaches the energy position for infinite donor-acceptor pair separation at the lowest excitation, while at the highest excitation; the peak position approaches the summation of infinite donor-acceptor pair separation and the Coulomb energy for minimum donor-acceptor pair separation [184]. Excitation dependence of the integrated PL flux for the DA3 transition is reported in a double-logarithm plot shown in Fig. 5.10. A preliminary fitting with a single power law in equation (5.1) results in an exponent k = 0.74, as would be expected for a DA transition. However, it can be seen, that the plot in Fig. 5.10 is a curvature which equation (5.1) is not a good fit, rather it is adequately evaluated by equation (5.2). The fitting by two power law exponents results in $k = \frac{2}{2}$ at low excitation intensity and $k = \frac{1}{2}$ at higher excitation intensity. The change of exponents, referred to as crossover, occurs at ~ 3-6 mW/cm^2 of excitation intensity. This crossover indicates that a defect level or a deeper mid-gap level interacting with the recombination process of DA3 transition saturates [167].

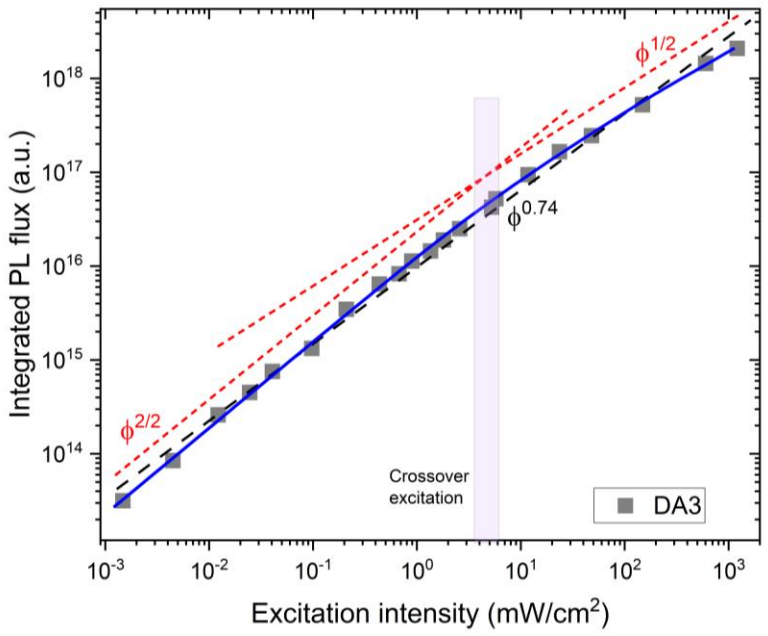

Figure 5.10: Double logarithmic plot of the DA3 transition with the integrated PL flux as a function of excitation intensity. The values are extracted from the integrated PL flux of the Cu-rich $CuGaS_2$ spectra in Fig. 5.9a.

On the high-energy end of DA3, is a low-intensity peak at ~ 2.32 eV as seen in Fig. 5.8 and Fig. 5.9a. The peak becomes more intense with increasing excitation intensity, as shown in Fig. 5.9a, until it is eventually obscured by the broadening DA3 transition. Nevertheless, it is still noticeable in Fig. 5.9a that the energy position barely changes with increasing excitation intensity. Given that the energy position of FB transition does not shift with energy position, and owing to its proximity to the DA3 transition, the weak peak at ~ 2.32 eV is assigned FB3. It is noteworthy that the FB3 transition might account for the curvature of the excitation dependence of PL flux for DA3 as illustrated in Fig. 5.10, since a shallow defect participating in the DA3 transition could saturate [167]. This is established by the value of the crossover excitation at ~ 3-6 mW/cm2 in Fig. 5.8 being close to the screening of FB3 in Fig. 5.9a, as seen above in the PL spectrum at 5.76 mW/cm^2 in Fig. 5.9a. Temperature-dependent analyses of the PL spectra shown in Appendix 7, further provide insight into the transitions DA3 and FB3. As the temperature increases, the intensity of DA3 decreases as the intensity of FB3 decreases before the thermal quenching of the transition.

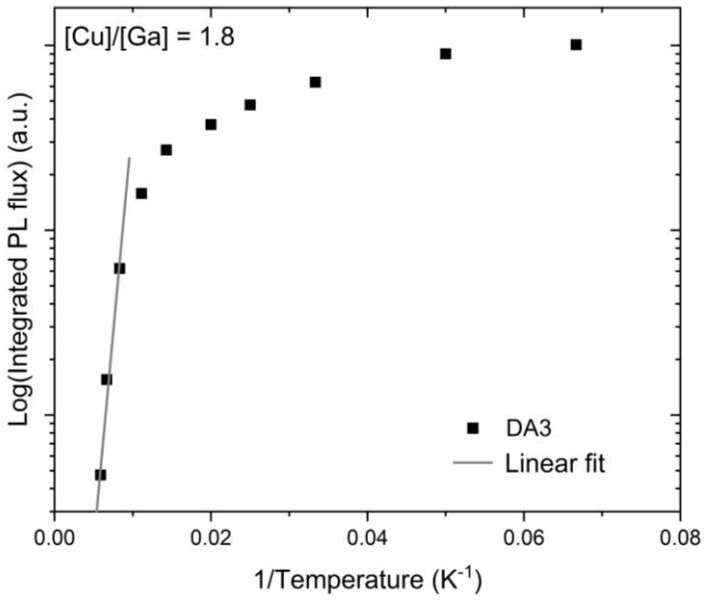

Figure 5.11: Arrhenius plot of the integrated PL flux with respect to temperature for the thermal quenching of the DA3 transition in a Cu-rich $CuGaS_2$ absorber.

This is another reason to associate FB3 with DA3 because, ideally, shallow defect involved in a DA transition is thermally emptied with increasing temperature, hence leaving FB transition. The

Arrhenius plot of the integrated PL flux against the inverse temperature for the thermal quenching of the DA3 transition is shown in Fig. 5.11. The thermal activation energy was obtained as ~ 35 meV. Using the bandgap of 2.525 eV calculated for $CuGaS_2$ at 10 K and energy differences of FB3 and DA3, DA3 is determined to involve an acceptor ~ 205 meV above the valence band and a shallow donor ~ 35 meV below the conduction band.

5.5.2 DA1 and DA2 transitions around 2.40 eV

As it will be shown in detail in the following, below the band-edge around 2.32-2.46 eV, two donor-to-acceptor transitions are identified at 2.410 eV and 2.398 eV, followed at ~ 46 meV by peaks at 2.35 eV and 2.363 eV respectively, as shown in Fig. 5.12a. Additionally, on the high energy wing, two free-to-bound transitions were detected at ~ 2.43 eV and 2.45 eV. Fitting the donor-to-acceptor lines with the Poisson distribution determined the zero phonon lines to be at 2.410 eV (DA1) and 2.398 eV (DA2). The Huang-Ryhs factors were $S_{DA2} = 0.50 \pm 0.10$ and $S_{DA1} = 0.55 \pm 0.10$ for DA1 and DA2, respectively. These values are smaller in comparison to the *S* factor for the DA3 as a result of the deeper defect level from which DA3 originates, since the deeper the defect level, the more localized and tightly bound the carriers are to the defects, hence an even stronger electron-phonon coupling [181].

Excitation intensity-dependent analyses of the energy positions for DA1 and DA2 presented in Fig. 5.12b show that, for both transitions, there is a blue-shift of energy positions with increasing excitation intensity, as is the case for DA transitions. The energy shift as a function of excitation intensity evaluated by equation (5.4) results in β-values of 2.2 meV/decade and 1.3 meV/decade for DA1 and DA2, respectively. These β-values are within the range for DA transitions [49]. The PL flux in dependence on excitation intensity show that both DA1 and DA2 can be fitted by a single power law yielding an exponent $k \approx \frac{2}{2}$. As mentioned in the preceeding Section 5.3, *k* takes on multiples of $\frac{1}{2}$, and for DA transitions in particular, *k* approaches $\frac{2}{2}$ at low excitation intensities [167]. Hence, it can be concluded that the study of DA1 and DA2 transition in this study is within the limiting region of low excitation.

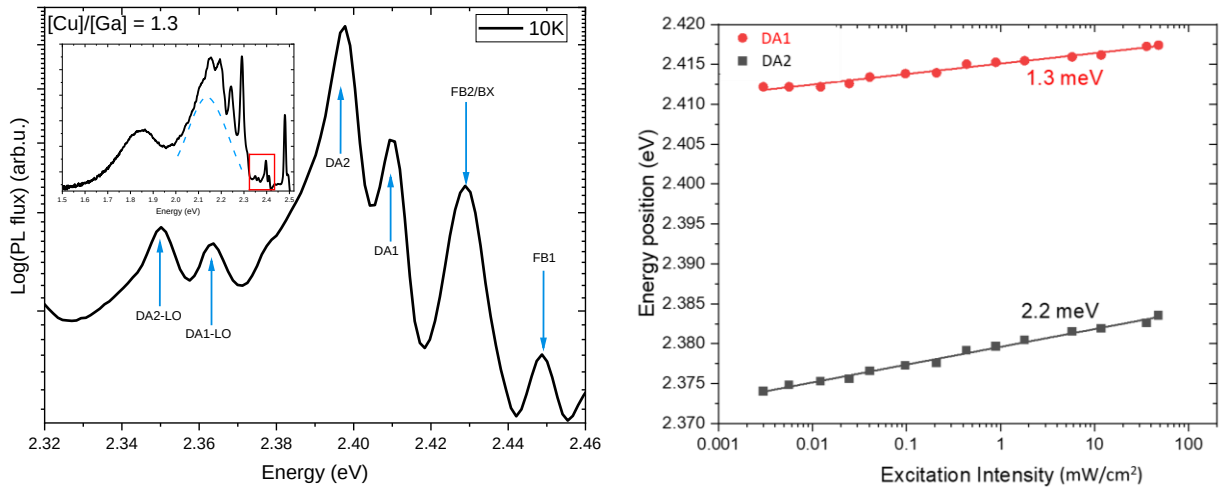

Figure 5.12: (a) Low temperature (10 K) PL spectrum of Cu-rich $CuGaS_2$ measured at 10 µW, showing phonon replicas accompanying the DA transitions at 2.42 eV and 2.10 eV. The sample used to analyze these transitions is the absorber with [Cu]/[Ga] = 1.3 in Fig. 5.4. In Inset is the full spectrum of the absorber. The dashed line centered at approximately 2.15 eV delineates a broad transition around said energy. The region in focus is indicated by the red box in the inset. (b) Energy position in dependence of excitation intensity for 2.410 eV (DA1) and 2.398 eV (DA2).

For the transitions at ~ 2.43 eV and 2.45 eV indicated as FB2/BX and FB1 respectively in Fig. 5.12a, the integrated PL flux for both peaks with respect to excitation intensity in a double-log scale is shown in Fig. 5.13a. The single power law fit of both transitions gives a power law exponent $k = \frac{2}{2}$ for both transitions. This linear dependence of the PL flux on excitation intensity can be interpreted as transitions originating from DA at low excitation, FB transitions or BX transition [49, 167], although both transitions at ~ 2.43 eV and 2.45 eV have been tentatively reported as FB transitions [64, 146]. The energy positions in dependence of excitation intensity which is presented in Fig 5.13b show no significant shift of energy position with increasing excitation intensity over three orders of magnitude for the 2.45 eV peak, making its consideration as an FB transition compelling.

The behaviour of the ~ 2.43 eV transition in Fig. 5.13b shows a shift of energy position, where the energy position is initially at ~ 2.433 eV later shifting to ~ 2.428 eV. While the behaviour of the 2.43 eV transition in Fig. 5.13b can be misconstrued for the S-shape in the excitation dependence

of a DA transition [184], it should be noted that such pattern appears with excitation over many orders of magnitude [167, 184], whereas the excitation in Fig. 5.13b is just over three orders of magnitude.

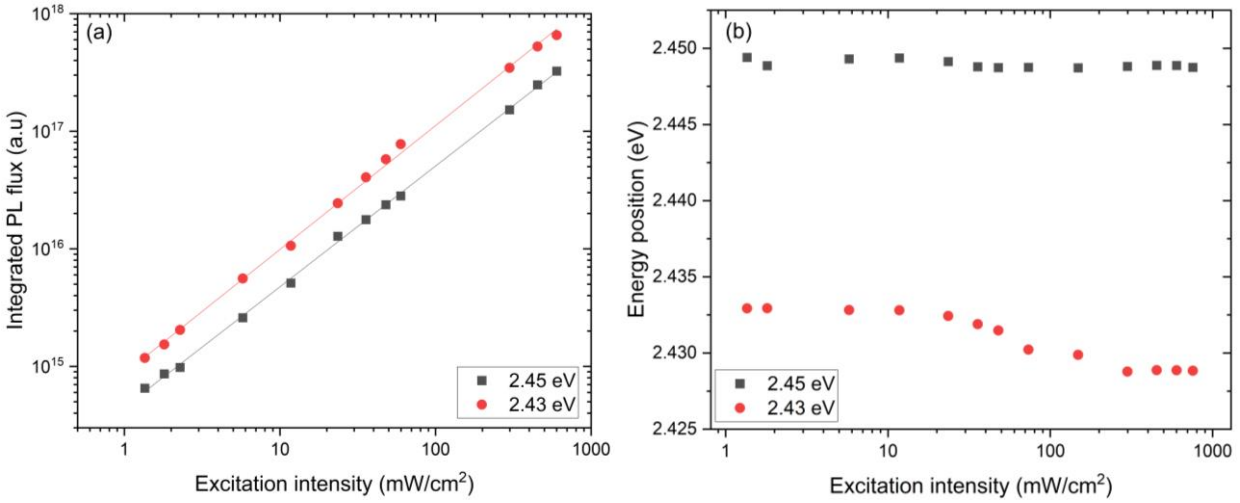

Figure 5.13: (a) PL flux in dependence of the excitation intensity for the transition peaks at 2.43 eV and 2.45 eV. (b) Energy position in dependence of peak energy position for transitions at 2.43 eV and 2.45 eV.

The explanation for the energy shift of 2.43 eV peak is by the existence of two transitions occurring around 2.35 eV, i.e., ~ 2.428 eV and 2.436 eV, which are better resolved by the temperature-dependent analysis. Nonetheless, it could be surmised that, below the excitation intensity of 10 mW/cm^2 in Fig. 5.13b, the 2.428 eV transition dominates, however, as the excitation intensity increases beyond 10 mW/cm^2, the intensity of the 2.436 eV transition increases and dominates, hence the shift of energy position observed in Fig. 5.13b.

Temperature-dependent measurements were performed to understand the behaviour of the DA1 and DA2 transitions, and to know the influence of temperature on the associated FB or excitonic transitions associated with DA1 and DA2. This is because shallow defects will be thermally emptied with increasing temperatures, and contribute to a FB transitions [49].

The temperature-dependent spectra presented in Fig 5.14, show that as the temperature increases, the intensity of the DA1 and DA2 peaks decrease since a shallow defect level involved in the

transitions are thermally emptied. It becomes obvious that the 2.43 eV line (labelled FB2/BX in Fig. 5.12a) consists of two peaks, one at 2.428 eV and another at 2.436 eV. It is observed that the relative intensity of the 2.428 eV line rapidly decreases and is quenched at approximately 50 K.

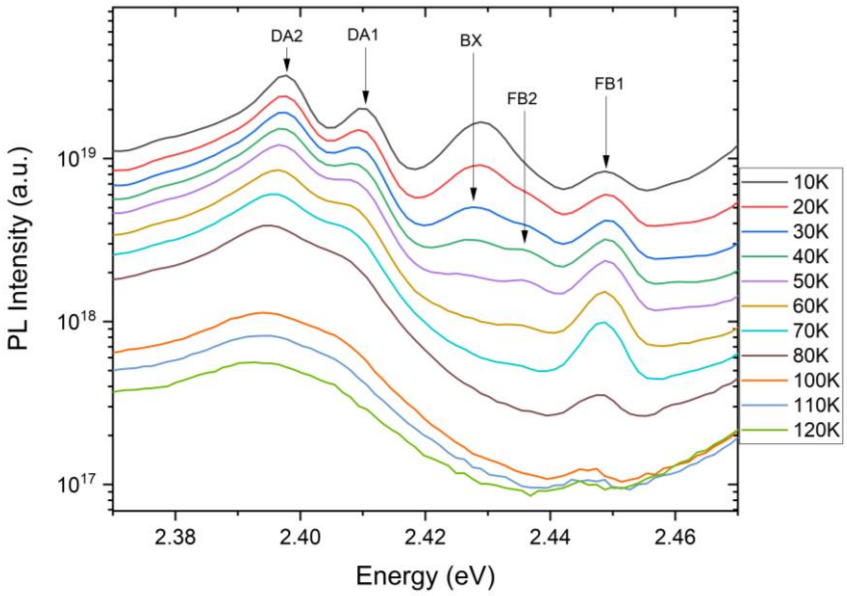

Figure 5.14: Temperature dependent PL spectra on Cu-rich absorber with [Cu]/[Ga] ratio of 1.3. The temperature-dependent measurement leads to the resolution of bound exciton transition at 2.428 eV and free-to-bound peaks at 2.436 eV and 2.449 eV.

The relative intensity of the 2.436 eV and 2.448 eV lines increases as temperature increases up to 70 K before decreasing and quenching at 120 K. The rapid quenching of the transition at 2.428 eV is characteristic of a bound exciton, and its energy position suggests that, it is bound to a much deeper defect. In contrast, the phenomenon of increasing intensity with increasing temperature can be attributed to FB transitions, and given the proximity to the energy positions of DA1 (2.410 eV) and DA2 (2.398 eV), the transitions at 2.449 eV and 2.436 eV can be sufficiently associated with the DA1 and DA2 transitions as the related FB transitions at, FB1 (2.449 eV) and FB2 (2.436 eV) respectively. By the energy difference between the DAs and FBs, FB1 and FB2 appear to involve a common shallow donor at 35 meV. In accordance with the attribution of FB1 and FB2, and the estimated $CuGaS_2$ bandgap of 2.525 eV at 10K, the 2.449 eV (FB1) and 2.436 eV (FB2) transitions are estimated to involve defect levels at ~ 75 meV and ~ 90 meV, respectively.

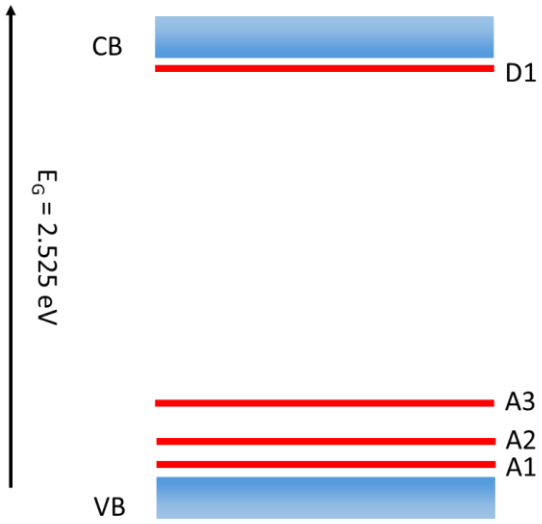

Figure 5.15: Tentative shallow defect levels in $CuGaS_2$ showing a donor level (D1) and three shallow acceptor levels (A1, A2 and A3).

At this point, in the analyses of the different transition peaks of $CuGaS_2$ studied in this report, a summary of the tentative shallow defects in $CuGaS_2$ can already be drawn. The transitions DA1, DA2 and DA3 are assigned donor-to-acceptor transitions due to the shift of their energy positions (β-value) in dependence to excitation intensity, and by the nature of their power law exponents (k). For DA3, the power law exponent changed from $k = \frac{2}{2}$ to $k = \frac{1}{2}$, while k is 1 for both DA1 and DA2. Summarily, there exist a common shallow donor (D1) level at ~ 35 meV and three shallow donor levels at 75 meV (A1), 90 meV (A2) and 210 meV (A3). The tentative shallow defect levels are illustrated in Fig. 5.15.

5.6 Deep defects at 2.15 eV and 1.85 eV

The PL spectra of all the absorbers (in Fig. 5.4) investigated show that, as the compositional ratio of [Cu]/[Ga] decreases, the spectrum is dominated by two broad transitions in the range between 1.6 eV and 2.3 eV. The two transitions centered at 2.15 eV and 1.85 eV are as shown in Fig. 5.16a.

The occurrence of the transition at 2.15 eV is strongly composition related, as shown by the reports of Botha et al. and Metzner et al. [65, 74]. Both groups report that in Ga-rich samples the transition shifts to ~ 2.0 eV, while in Cu-rich samples the transition shifts to higher energies around 2.12-2.18 eV. Hence it is possible that one or more defects are involved in the 2.15 eV, and this may account for the broadness of the peak. Given that a Cu-rich absorber is used to investigate this peak in this report, the transition is considered to be centered at 2.15 eV. Additionally, the phonon replicas on DA3 superpose on the 2.15 eV peak, thereby imposing constraints when fitting with an assumed Gaussian shape.

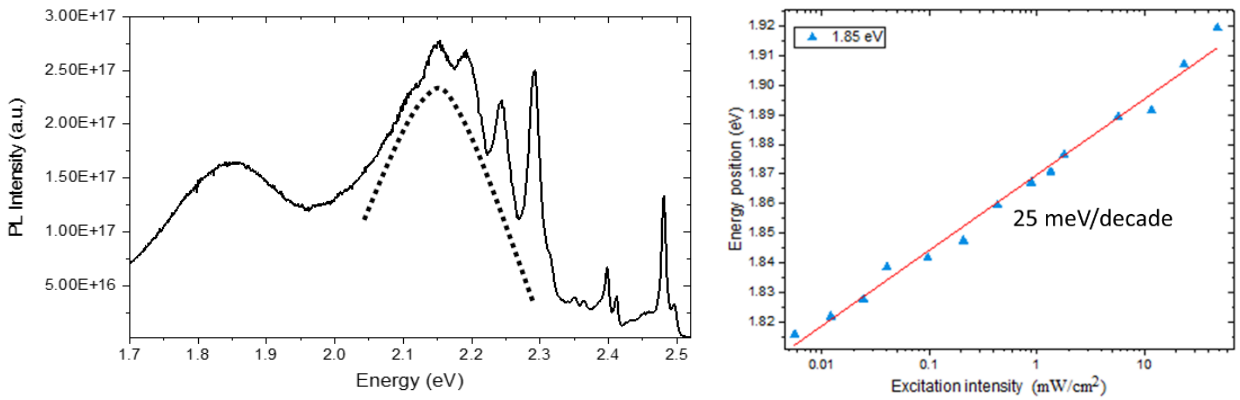

Figure 5.16: (a) Region of broadband deep defects featuring transitions centered at approximately 1.85 eV and 2.15 eV. (b) Energy position as a function of excitation intensity for the deep defect at ~ 1.85 eV.

Analyses of the power law dependence for both transitions yield exponents k ~ 1. The energy position with respect to excitation intensity over four orders of magnitude show a blue-shift of ~ 5 meV per decade for the 2.15 eV peak, while the 1.85 eV peak shows a larger blue-shift of ~ 25 meV per decade with respect to excitation intensity as presented in Fig 5.16b. While the 2.15 eV transition show features of a typical donor-acceptor transition, the blue-shift with 1.85 eV is much larger than expected for a typical DA transition. Various sources have reported this large blue-shift of the 1.85 eV transition, however, it has been attributed to potential fluctuations of the band-edges [74]. Although it is apparent that both transitions likely involve broad density of states, the large blue-shift of the 1.85 eV transition might also be due to stronger phonon coupling manifested with deep defects.

5.7 Summary and tentative shallow defect levels in $CuGaS_2$

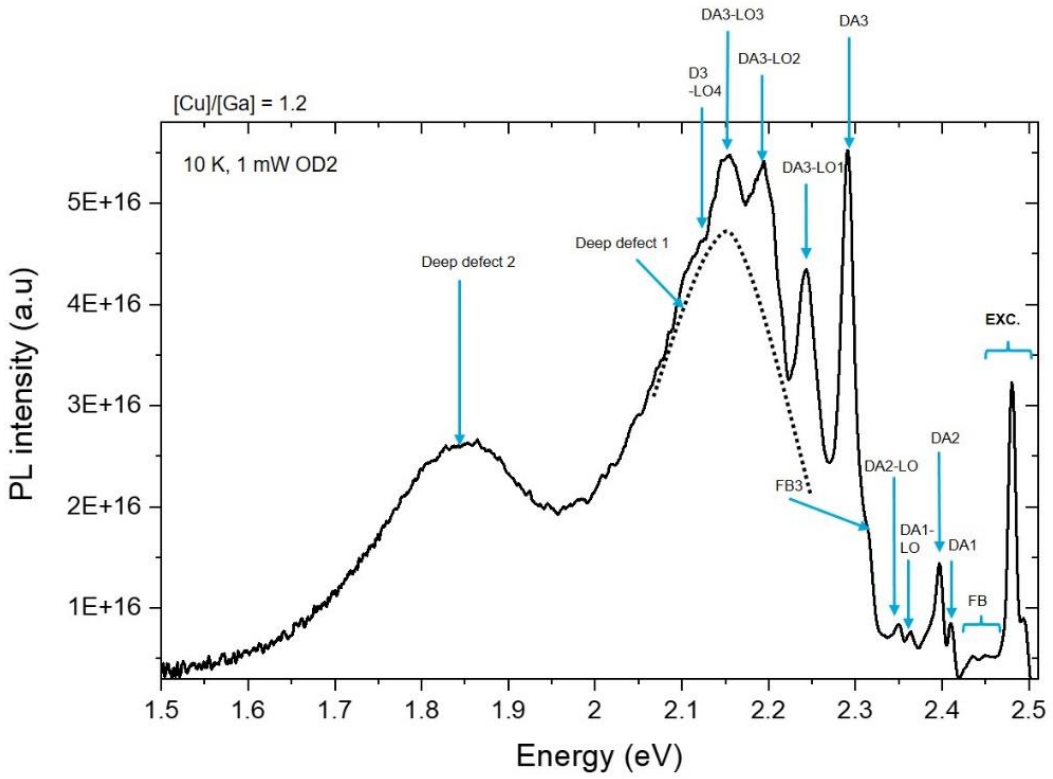

Figure 5.17: Summary of identified transitions for a Cu-rich $CuGaS_2$ absorber at 10 K

Fig. 5.17 summarizes the photoluminescence spectra of a slightly Cu-rich $CuGaS_2$ with all the peaks identified. In the course of investigating the $CuGaS_2$ absorbers in this present work, several well-resolved exciton-related transitions were detected. The bandgap at 10 K is determined as 2.525 eV from the free exciton and its first excited state at 2.496 eV and 2.518 eV, respectively.

In this report, several sub-band edge transitions, were identified as DA transtions interacting with a common shallow donor level at 38±2 meV and shallow acceptors 75 meV (DA1) and 90 meV (DA2). Metzner et al. have reported similar transitions and defect level, assigning a shallow donor 25 meV occuring due to S vacancy, and two shallow acceptors at 89 meV and 109 meV due to metal vacancies [146]. Also identified is a rather deeper acceptor level at 205 meV (DA3) which becomes intense with higher Cu-content involving. DA3 is also shown to involve a shallow level

at ~ 35 meV. Botha et al. also reported such defect for slightly Cu-rich $CuGaS_2$ for acceptor 210 meV above the valence band with donor likely at ~ 53 meV. It is evident that DA1, DA2 and DA3 interact with a common shallow donor ~ 38±3 meV, which is a level that has been deduced from hydrogenic approximation and values approximated from photoluminescence analyses [49]. Lastly, two broad transitions at 2.15 eV and 1.85 eV were present in all the absorbers. Although both transitions are DA-related, the exact defect levels involved could not be identified, however, both transitions presumably involve broad density of states. Transitions involving these defects particularly dominate the PL spectrum of $CuGaS_2$ at room temperature. It is worth mentioning that defect levels identified in this report shares similarity with shallow and deep defects identified in $CuGaSe_2$ [138-142] and even $CuInS_2$ [27, 145].

An overview of the transition energies identified from literature and those identified in this work is presented in Fig. 5.18. It can be observed that different transitions were identified independently by different groups. In this work, within the range of energies investigated, all the different transitions energies separately reported were identified.

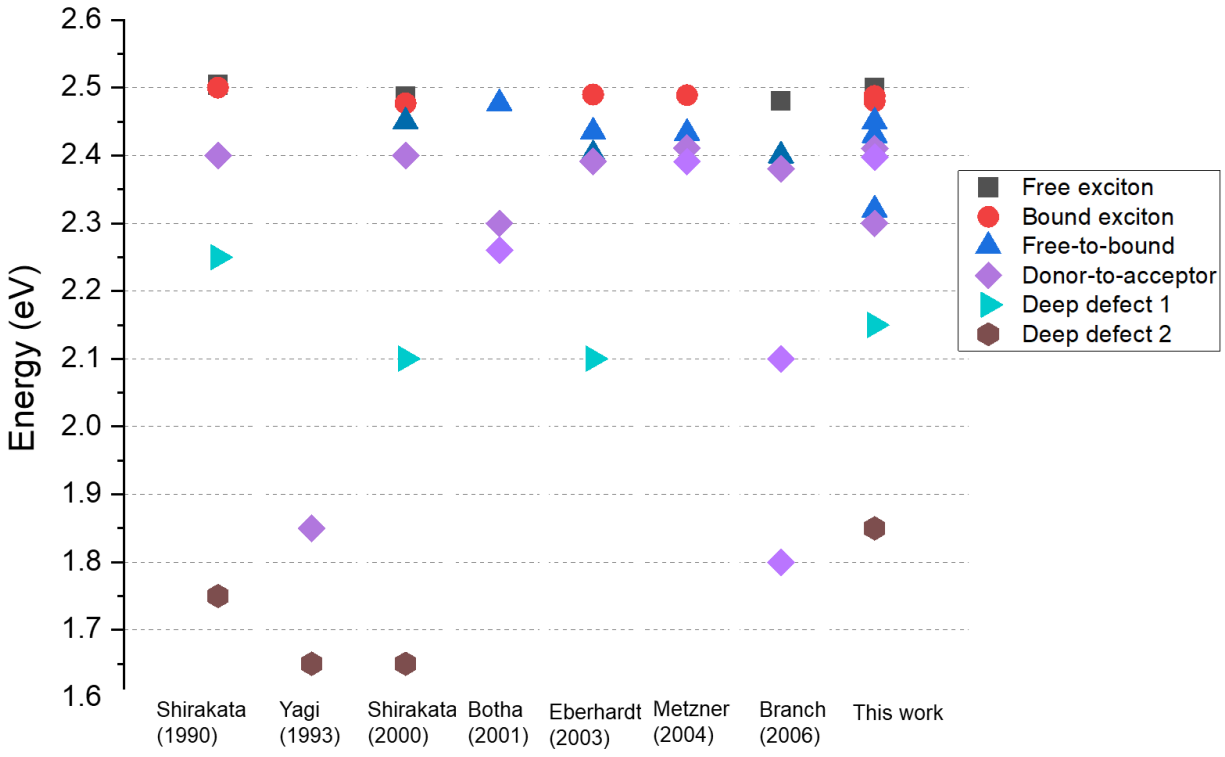

Figure 5.18: Overview of transition energies of $CuGaS_2$ from literature with transitions identified in this work.

The tentative defect levels on $CuGaS_2$ in Fig. 5.15 is update and summarized in Fig. 5.19. The existence of a shallow donor level ~ 35 meV (D1) and shallow acceptors 76 meV (A1), 90 meV (A2) with an additional acceptor deeper level at 210 meV (A3). Finally, two deep transitions level seem to originate from or involve two broad defect levels deep within the midgap.

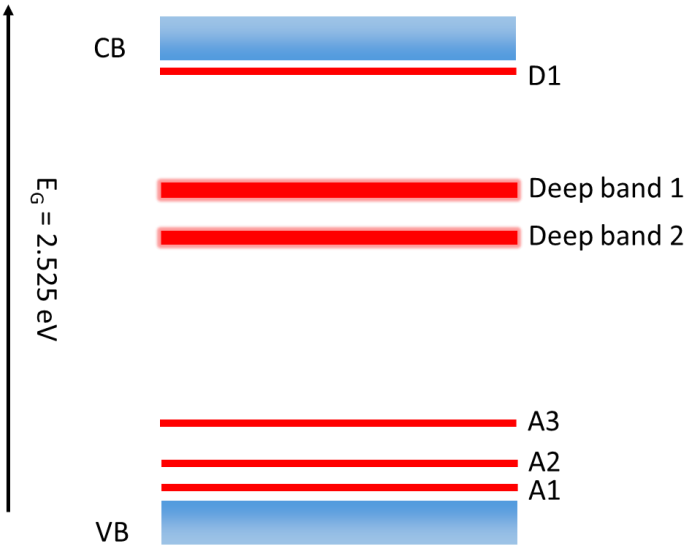

Figure 5.19: Tentative defect model for $CuGaS_2$ as reported in this work. A shallow donor level (D1) and three shallow acceptor levels (A1, A2 and A3) were identified. Two broad defect levels are also assumed to be involved in transitions in $CuGaS_2$

5.8 Novel solar cell on $CuGaS_2$

The room temperature bandgap of $CuGaS_2$ is around 2.45 eV. The wide bandgap makes it not interesting for use as a single junction solar cell. Nevertheless, it is also important to understand how the defects of $CuGaS_2$ might influence the electrical properties of a single junction solar cell. The absorber used is a Cu-rich absorber with the [Cu]/[Ga] ratio of ~1.3. The room temperature PL spectrum of the absorber is shown in Fig. 5.20. The room temperature spectrum is dominated by the broad transition centered around 1.5 eV as shown in Fig. 5.20. The device possesses a quasi-Fermi level splitting (QFLS) of 1.68 eV, and consequently a rather large deficit of 0.42 eV

compared to the Shockley-Queisser open-circuit voltage (V_{OC}^{SQ}) [13] owing to the defects in the material. The QFLS was determined by the ERE method described in Section 2.3.2.

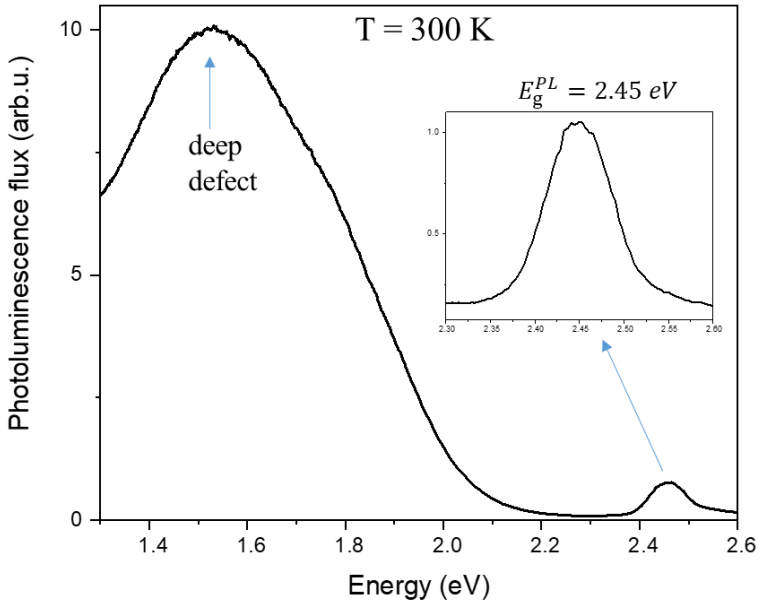

Figure 5.20: Room temperature photoluminescence spectrum of the $CuGaS_2$ absorber completed into solar cell. In inset is the magnification of the band-to-band transition.

Fig. 5.21 shows the current density-voltage curve of the $CuGaS_2$ device prepared with (Zn,Mg)O buffer layer. The device demonstrated a V_{OC} of 821 mV leading to a very high interface V_{OC} deficit [185] when compared to the quasi-Fermi level splitting. Thus, leading to a power conversion efficiency of mere 1.8%. We speculate that the high interface V_{OC} deficit originates from two factors: (i) from the near interface defects [185] as the device was prepared using the Cu-rich $CuGaS_2$ absorbers, (ii) a negative conduction band offset at the $CuGaS_2$/(Zn,Mg)O interface, due to high conduction band minimum of $CuGaS_2$ and relatively low conduction band minimum of (Zn,Mg)O. While the former limits the V_{OC} by reducing the QFLS near the interface and can be mitigated by doing a chalcogen treatment [186], the later limits the V_{OC} by reducing the QFLS, and requires a buffer that is better matched to the conduction band minimum of the $CuGaS_2$. Nonetheless, This work demonstrates that it is possible to make working solar cells with $CuGaS_2$

though significant efforts are required to achieve V_{OC} and power conversion efficiency close to Shockley-Queisser limit [13].

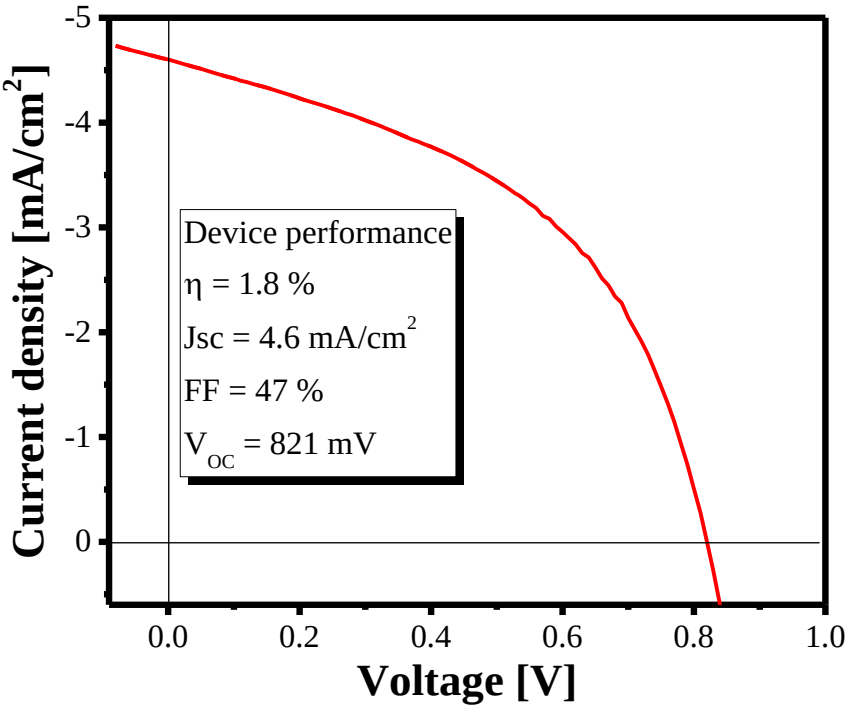

Figure 5.21: Current density-voltage curve of $CuGaS_2$ device prepared with (Zn,Mg)O buffer layer with Mg/(Mg+Zn) ~ 0.3 atomic percent.

Chapter 6

$Cu(In,Ga)S_2$ – based absorbers for single junction solar cells

This chapter encompasses a detailed description of studies performed on $Cu(In,Ga)S_2$ thin film. The details include the growth processes, results and findings from investigations performed on $Cu(In,Ga)S_2$ absorbers and the complementary solar cells thereof. In this context, the different characterization procedures performed on the bare absorbers and completed solar cells using different analytical techniques will be discussed. Consequently, the results from the experimental and optimization procedures will solve some challenges occurring in $Cu(In,Ga)S_2$ and also lead to the modification of the three-stage deposition process to achieve high quality $Cu(In,Ga)S_2$ absorbers.

The first Section 6.1 examines the influence of Cu-content on the properties and optoelectronic quality of $Cu(In,Ga)S_2$ absorbers, as well as the overall impact on the solar cells completed on such absorbers. This section will make clear why $Cu(In,Ga)S_2$ absorbers grown under Cu-deficient conditions are preferred, despite the excellent microstructural property of absorbers grown under Cu-excess conditions. Some results from Section 6.1 have already been published [110], and a comprehensive analysis of the electrical properties on the solar cells completed on some of the absorbers can be found in the doctoral dissertation of Mohit Sood [90].

As the three-stage deposition process is a breakthrough technique distinguished by the varying Ga content (Ga-grading) throughout the depth of the absorber [187], the front grading is crucial in absorption and photogenerated carrier extraction. During the growth process of $Cu(In,Ga)S_2$ absorbers, Ga is introduced during the first and third stages of deposition either to increase the bandgap or to achieve a front surface bandgap gradient. Section 6.2 demonstrate the impact of surface Ga on $Cu(In,Ga)S_2$ absorbers and solar cells. Then, the best surface Ga-content for high performing low-Ga content $Cu(In,Ga)S_2$ absorbers for good solar cells will be investigated. The knowledge derived from Section 6.2 will lead to the first modification of the three-stage deposition step used in processing $Cu(In,Ga)S_2$ absorbers; the modification will be described.

Next, in Section 6.3 the challenges encountered when increasing the Ga content in the absorber by the three-stage deposition process of Cu(In,Ga)S_2 absorbers will be shown. Through several analyses, the effect of phase segregation will be presented, and how the segregated phases hinder the optimum performance of solar cells will be shown.

Section 6.4 will show that it is possible to circumvent factors favoring segregated phases in high Ga-containing Cu(In,Ga)S_2 absorbers. The trade-off that needs to be considered and its mitigation will be presented. The Section 6.4 will also show the effect of several deposition parameters on the Cu(In,Ga)S_2 absorbers. These deposition parameters include the cracking of sulfur molecules, first-stage deposition temperature, Cu-excess deposition after stoichiometry and ramping of substrate temperatures.

6.1 Influence of copper-content on the quality of Cu(In,Ga)S_2 absorbers and devices

The trend of certified record efficiencies for Cu(In,Ga)S_2 solar cells is depicted in Fig. 6.1.

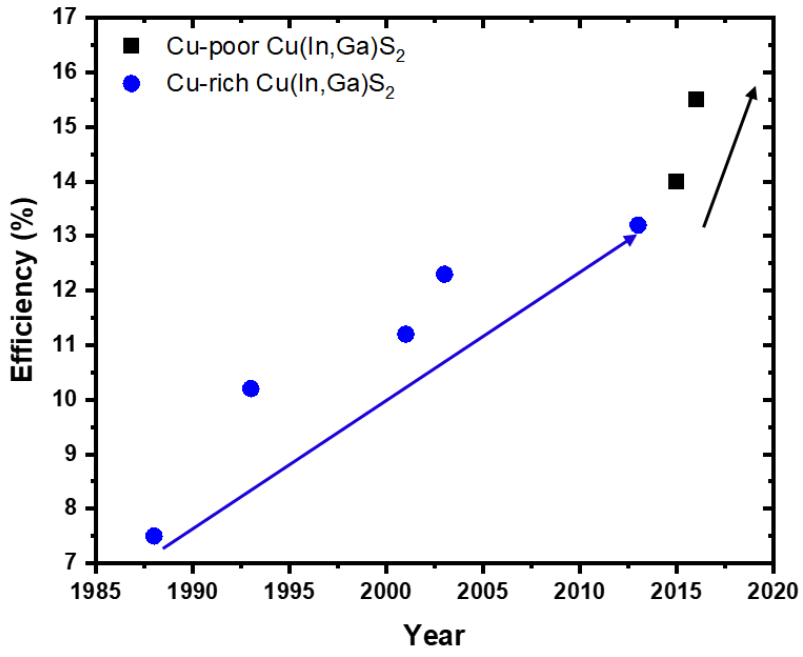

Figure 6.1: Certified record efficiency chart of Cu(In,Ga)S_2 solar cells between 1988 to 2016.

The efficiency trend can be divided into two parts; (i) a slow increase over a span of 25 years where the efficiency increases from 7.5 % to 13.2 % and (ii) a sharp increase in efficiency from the 13.2 % to 15.5% within 3 years. A distinguishing factor between these two regimes is the fact that the former consists of solar cells which were completed on Cu-rich absorbers, while in the latter, the solar cells were on Cu-poor absorbers. To understand why the Cu content in $Cu(In,Ga)S_2$ could induce such a trend as in Fig. 6.1, many $Cu(In,Ga)S_2$ absorbers with different Cu content have been studied. The need for a variation of Cu content in the $Cu(In,Ga)S_2$ absorbers in this study necessitated the utilization of multiple techniques to process the absorbers. Since the two-stage and three-stage processes could result in markedly different compositions, the Cu-rich absorbers were grown by the two-stage deposition method, while the Cu-poor absorbers were grown by the three-stage method. In both cases, the first stage substrate temperature was ~ 260 °C, while the second and third stage substrate temperature was at ~ 570 °C. The combination of all the $Cu(In,Ga)S_2$ absorbers were deposited with the control of sulfur flux either in the open- or closed-loop with the chamber pressure typically between 3×10^{-5} mbar to 7×10^{-5} mbar. Since the Cu-rich ([Cu]/([Ga]+[In]) > 1) absorbers are grown with additional secondary copper-sulfide (Cu_xS) phases, the Cu-rich absorbers were etched by 10 % solution of potassium cyanide (KCN) for 5 minutes to remove the Cu_xS phases before photoluminescence (PL) measurement are performed on them [125]. KCN etching was not required of the Cu-poor ([Cu]/([Ga]+[In]) < 1) absorbers before PL measurements, although they could be etched in 5 % solution of KCN for 30s to remove oxidized layers before they were processed into solar cells. $CuInSe_2$ and $Cu(In,Ga)Se_2$ bare absorbers have been shown to degrade upon exposure to air due to the oxidation of indium, hence, a thin layer of CdS acting as a passivation layer is often deposited on $CuInSe_2$ and $Cu(In,Ga)Se_2$ bare absorbers [126, 134]. $Cu(In,Ga)S_2$ absorbers required no such passivation layer as CdS because the surface remained stable over time [27].

After the growth of the $Cu(In,Ga)S_2$ absorber, a rudimentary evaluation could be performed to rapidly evaluate the luminescence characteristics of the absorber by observing the PL spectrum at room temperature. For an absorber processed under Cu-rich conditions, after the mandatory KCN etching of the secondary Cu_xS phases, its luminescence intensity is low and characterized by broad defect peak. Additionally, a non-luminescing absorber could be of substandard quality. However,

a luminescing absorber which does not require a KCN etching is possibly one which is Cu-poor. The luminescence spectrum of the Cu-poor absorber and the Cu-rich absorber possess different signatures depending on the relative Cu-content. For instance, a visual difference in the photoluminescence (PL) spectrum between a moderately Cu-rich absorber, [Cu]/([Ga]+[In]) (CGI) ratio = 1.29, and a Cu-poor absorber with CGI ratio = 0.93 with similar optical bandgaps is illustrated in Fig. 6.2a. The optical bandgap is taken as the maximum PL emission energy since this is expected to be the minimum energy in a Ga-graded absorber film. The PL spectrum of the Cu-rich absorber after etching typically features a broadband peak at the lower energy end of the band-edge emission, and several orders of magnitude more intense than the band-edge emission as shown in Fig. 6.2a. For the Cu-poor absorber, the spectrum is always dominated by an intense band-edge emission with a narrow bandwidth of ~ 10 meV at full width half maximum as in Fig. 6.2a. The fringes on the low energy end of the PL spectra in Fig. 6.2a are due to interference effect, particularly on absorbers with smooth and shiny surfaces. In general, depending on the Cu-content in absorber, the PL spectrum of a $Cu(In,Ga)S_2$ absorber features the signatures of both band-edge emission and broad defect emission peaks with varying intensities.

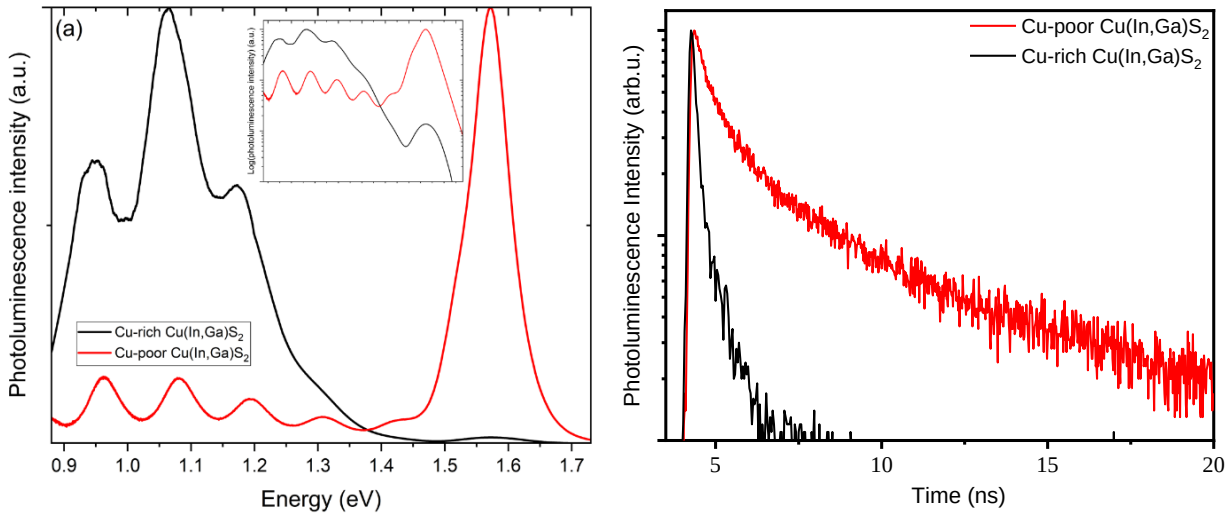

Figure 6.2: (a) The typical photoluminescence (PL) spectra of a bare Cu-rich and Cu-poor $Cu(In,Ga)S_2$ thin film. In the inset is the PL spectrum in logarithmic scale. The fringes on the low energy end of the spectra are due to interference effect. (b) Transient PL decay from a Cu-poor and Cu-rich absorber. All measurements were in ambient atmosphere.

The quasi-Fermi level splitting (QFLS), representing the upper-limit of open-circuit voltage achievable, is used as a figure of merit for the optoelectronic quality of the absorbers. QFLS was measured at the laser power corresponding to 1-sun illumination, then the quantity is evaluated by the Planck's generalized law or by evaluation of external radiative efficiency [13, 52, 56] as described in Section 2.3.2. In the case of low photoluminescence intensity as it will be the case in some Cu-rich absorbers, the absorbers were measured at higher laser powers corresponding to higher sun power, subsequently, the QFLS value is extracted at the higher sun power and extrapolated to 1-sun. For the model absorbers presented in Fig. 6.2, the QFLS is evaluated as 872 meV and 972 meV for the Cu-rich and Cu-poor absorbers, respectively. Example of the carrier lifetimes between a typical Cu-rich and Cu-poor acquired by time-correlated single photon counting (TCSPC) is presented in Fig. 6.2b. An assessment of the lifetime by a bi-exponential fit of the luminescence decay in Fig. 6.2b indicates that the Cu-rich absorber ($\tau_1 = 0.1\,ns, \tau_2 = 0.5\,ns$) exhibits a faster luminescence decay in comparison to the Cu-poor absorber ($\tau_1 = 0.56\,ns, \tau_2 = 3.2\,ns$).

The absorbers are completed into solar cell devices with cadmium sulfide (CdS) buffer layer and, intrinsic zinc oxide (i-ZnO) and aluminum doped zinc oxide (Al:ZnO) window layer. Although it has been shown that CdS is not appropriate for Cu(In,Ga)S_2 devices [90, 110], it is suitable for low-bandgap devices due to a lower conduction band offset at the absorber-buffer interface. In that regard, CdS buffer layer has produced highly efficient low-bandgap Cu(In,Ga)S_2 devices [28]. Additionally, CdS provides a quick means of completing the device to be assessed. The device characteristics measured on the solar cells are presented in Table 6.1, and the current-voltage (I-V) curves are shown in Fig. 6.3a. It can be seen that, the solar cell completed on the Cu-poor absorber, shows a higher open-circuit voltage (V_{OC}) of 734 mV, than the Cu-rich absorber with 607 mV. It is also obvious from the device parameters presented in Table 6.1 that the Cu-poor device outperforms the Cu-rich device. Comparing the QFLS with the V_{OC} in Fig. 6.3b for both devices, QFLS is not fully transformed into V_{OC}. Actually, there is a lower conversion of QFLS to V_{OC} for the Cu-rich device than for the Cu-poor device.

To address the origin of this discrepancy between the Cu-rich and the Cu-poor absorbers, the data set is expanded to consider more absorbers with more diverse CGI ratios and [Ga]/([Ga]+[In])

(GGI) ratios. The inclusion of absorbers having various GGI ratios account for absorbers with different optical bandgaps between 1.53-1.61 eV [188].

Table 6.1: Solar cell parameters for $Cu(In,Ga)S_2$ devices of different chemical composition.

Device	QFLS (meV)	V_{OC} (mV)	J_{SC} (mA/cm^2)	FF (%)	PCE (%)
Cu-poor $Cu(In,Ga)S_2$	972	734	19.1	60.7	8.6
Cu-rich $Cu(In,Ga)S_2$	872	607	18.5	59.7	6.7

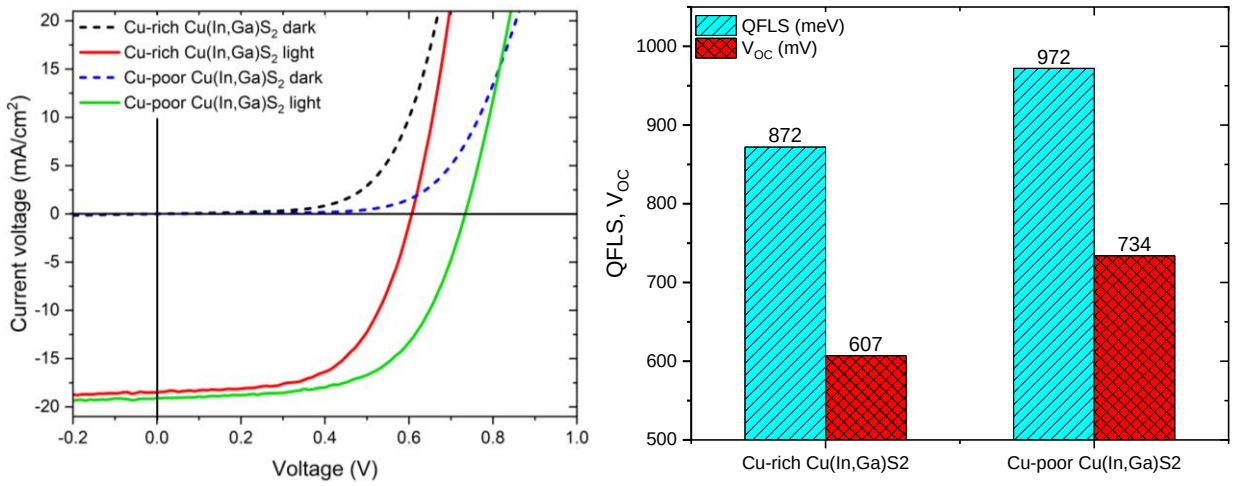

Figure 6.3: (a) Current-voltage (I-V) curves of a solar cell on a Cu-rich and Cu-poor absorber. (b) Comparison of the QFLS and V_{OC} of Cu-rich and Cu-poor $Cu(In,Ga)S_2$ absorbers and devices.

The overall GGI ratios of the different absorbers considered were between 0.12-0.20. The QFLS of the different absorbers, which are determined by either the Planck's generalized law or evaluation of the ERE, are presented against the corresponding optical bandgaps in Fig. 6.4. From Fig. 6.4, the distribution of the QFLS for the Cu-poor absorbers lies above the QFLS values measured on the Cu-rich absorbers. Ultimately, for two absorbers with similar bandgaps, the QFLS for the Cu-poor absorber will be higher than the QFLS for the Cu-rich absorber, rather the QFLS

values for higher bandgap Cu-rich absorbers compares with low bandgap Cu-poor absorbers. A linear fit of the QFLS distribution results in similar slopes for both sets of absorbers, with 0.95±0.19 and 0.97±0.23 for the Cu-poor and Cu-rich absorbers respectively. Although the slopes are less than 1 due to thermodynamic losses in photovoltaic devices [189], the similarity of the slopes for both Cu-poor and Cu-rich absorbers is an indication that, the change in QFLS with respect to bandgap is similar for both Cu-poor and Cu-rich Cu(In,Ga)S_2 absorbers. The large spread of the QFLS values around the slope can be explained by the fact that the exact CGI ratios are not considered, as it has been reported in Chapter 4 and references [27, 114] that, stoichiometry can influence the optoelectronic quality of an absorber. Nonetheless, it can be deduced from Fig. 6.4 that the average QFLS between two Cu(In,Ga)S_2 absorbers - one Cu-rich, the other Cu-poor - can differ by ~ 85±7 meV.

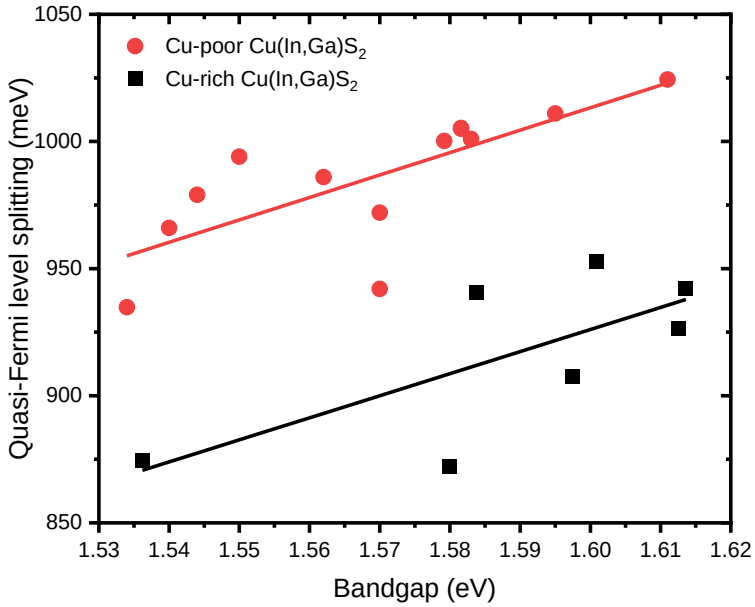

Figure 6.4: The distribution of QFLS values of different Cu-poor and Cu-rich Cu(In,Ga)S_2 absorbers in dependence of the optical bandgaps taken from the maximum of PL emission.

Another approach to consistently evaluate the non-radiative loss in an absorber is expressed by the difference between the theoretical V_{OC} $\left(V_{OC}^{SQ}\right)$ predicted by Shockley and Queisser [13] and the QFLS, i.e, $(qV_{OC}^{SQ} - QFLS)$, referred to as "V_{OC}^{SQ} deficit" in this work. As mentioned in Chapter 2, V_{OC}^{SQ} represents the open-circuit voltage in an ideal solar cell [13, 51]. Although the bandgap of an

absorber is needed to determine the V_{OC}^{SQ} value corresponding to an emission energy, the V_{OC}^{SQ} deficit is not directly contingent on variations of absorber bandgap, hence the nonradiative loss of different absorbers can be directly compared. From the definition of V_{OC}^{SQ} deficit above, it is apparent that the farther the QFLS is from the ideal V_{OC}^{SQ}, the higher the V_{OC}^{SQ} deficit will. Against this backdrop, the data points in Fig. 6.4 can be compared independent of the absorber bandgap and chemical composition as shown in Fig. 6.5, where the V_{OC}^{SQ} deficit of each absorber is plotted in dependence of the ERE. The relationship between the V_{OC}^{SQ} deficit and ERE follows a negative slope, showing that the higher nonradiative losses is, the higher V_{OC}^{SQ} deficit is.

The trend shows a slope of $-k_BT$ following the relationship $qV_{OC}^{SQ}\text{deficit} = -K_BT\,ln(ERE)$. From Fig. 6.5, the Cu-rich absorbers have lower radiative efficiencies, corresponding to higher V_{OC}^{SQ} deficit than the Cu-poor absorbers.

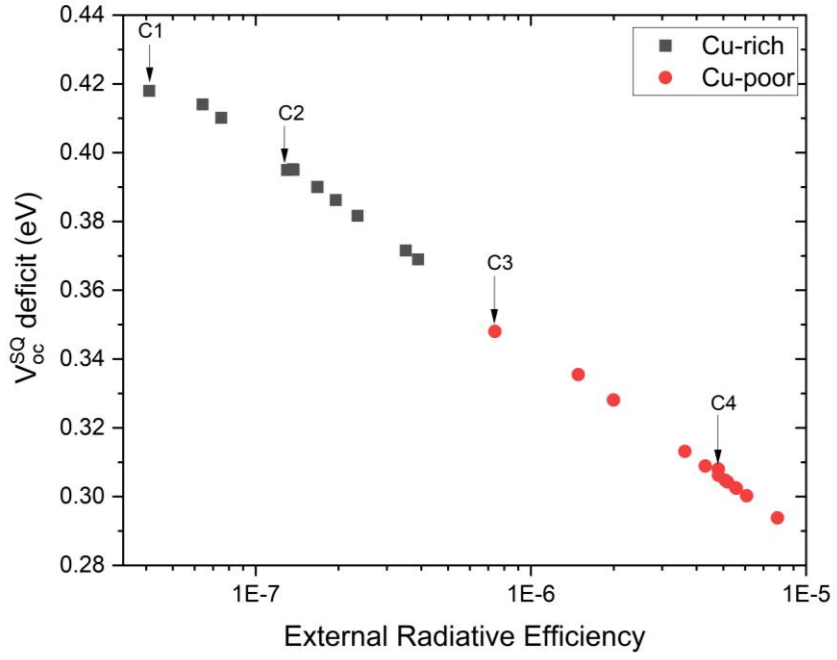

Figure 6.5: V_{OC}^{SQ} deficit in dependence of ERE external radiative efficiency (ERE) for the various absorbers Cu-rich and Cu-poor absorbers. The highlighted samples C1, C2, C3 and C4 are absorbers are [Cu]/([Ga]+[In]) (CGI) ratio 1.23, 1.02, 0.95 and 0.93 respectively.

To understand the origin of the different QFLS along the compositional divide, various absorbers with different QFLS and V_{OC}^{SQ} deficit from both the Cu-rich and Cu-poor absorbers were selected for further investigations at low temperatures analyses. The absorbers are labeled C1, C2, C3 and C4, with their properties presented in Table 6.2. The low temperature spectra of the absorbers C1-C4 are shown in Fig. 6.6. Starting with C1 with CGI ratio = 1.29, the band-edge luminescence is distinguished by two high energy peaks, rather than the singular band-edge emission in the absorbers C2, C3 and C4.

Table 6.2: Optoelectronic properties of different Cu(In,Ga)S_2 absorbers with various Cu-content.

Absorber label	**[Cu]/([Ga]+[In])**	E_g^{PL} **(eV)**	**QFLS (eV)**	V_{OC}^{SQ} **deficit (eV)**
C1	1.29	1.58	0.872	0.418
C2	1.02	1.62	0.944	0.395
C3	0.95	1.57	0.942	0.348
C4	0.93	1.57	0.972	0.308

The detection of the two peaks is likely due to the superior crystallinity of Cu-rich absorbers, as seen in both $CuInS_2$ [145, 190] and $CuGaS_2$ absorbers in Chapter 5. While the highest energy transition could be related to the band-edge emission, it is possible that the peak ~ 1.45 eV is related to donor-to-acceptor transition [144]. On the low energy end is a broadband deep defect, as also characteristic of Cu-rich absorbers at room temperature in Fig. 6.2a. The broad peaks could be resolved into two peaks by fitting with two Gaussian distributions centered at 1.3 eV and 1.1 eV. The two peaks referred to as D1 and D2 in Fig. 6.6 are considered to originate from mid-gap states. Going from sample C1, to C2 - of stoichiometric composition - and C3 with even lower Cu-content in Fig. 6.6, it is observed that the intensity of the bulk defect peaks D1 and D2 weakens as Cu-content decreases. Remarkably, D1 and D2 are effectively subdued in sample C4 with the lowest Cu-content. It should be noted that, although these absorbers are of different GGI ratio between 0.12-0.18, the low variation in Ga-content between the absorbers is sufficient to ascribe

the behavior of D1 and D2 in Fig. 6.6 to Cu-related defects, since Cu is the element strongly driving the compositional variation between the absorbers.

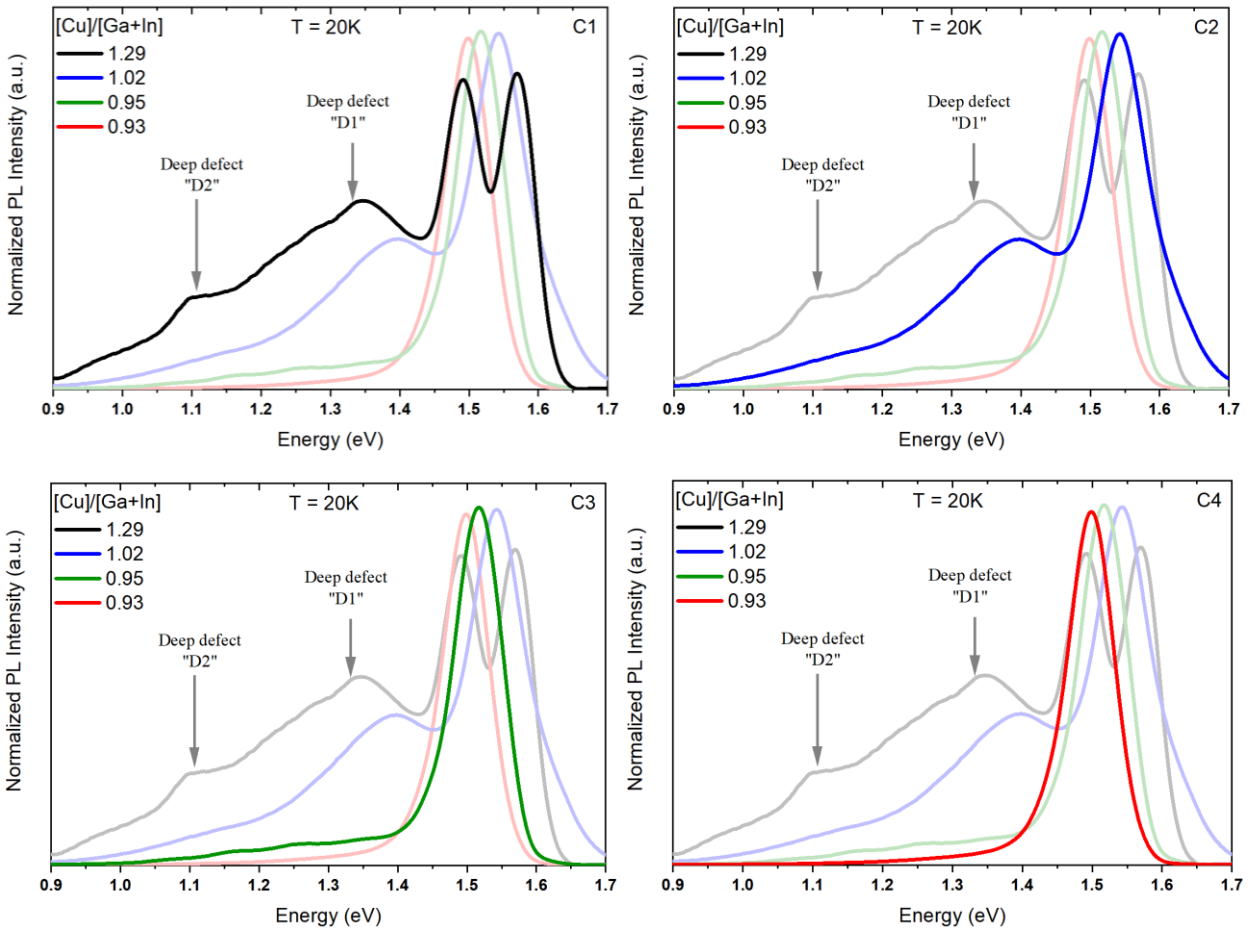

Figure 6.6: Low temperature PL spectra at 20 K for absorbers C1, C2, C3 and C4 with of CGI ratio 1.23, 1.02, 0.98 and 0.93 respectively, showing the evolution of the broadband deep defect with decreasing concentration of Cu in the absorbers.

The ERE and V_{OC}^{SQ} deficit are presented in dependence of CGI ratio for C1-C4 in Fig 6.7. The increase of ERE and complementary reduction of V_{OC}^{SQ} deficit in relation to decreasing Cu-content in Fig. 6.7, can be correlated with the suppression of deep defects D1 and D2 in Fig. 6.6. This implies that the suppression of Shockley-Read-Hall (SRH) recombination centers which appears to dominate Cu-rich absorbers, lead to an increase of (or higher) QFLS in Cu-poor absorbers as

seen in Fig. 6.4. This also explains the longer lifetime of Cu-poor absorbers than Cu-rich absorbers as seen in Fig. 6.2b.

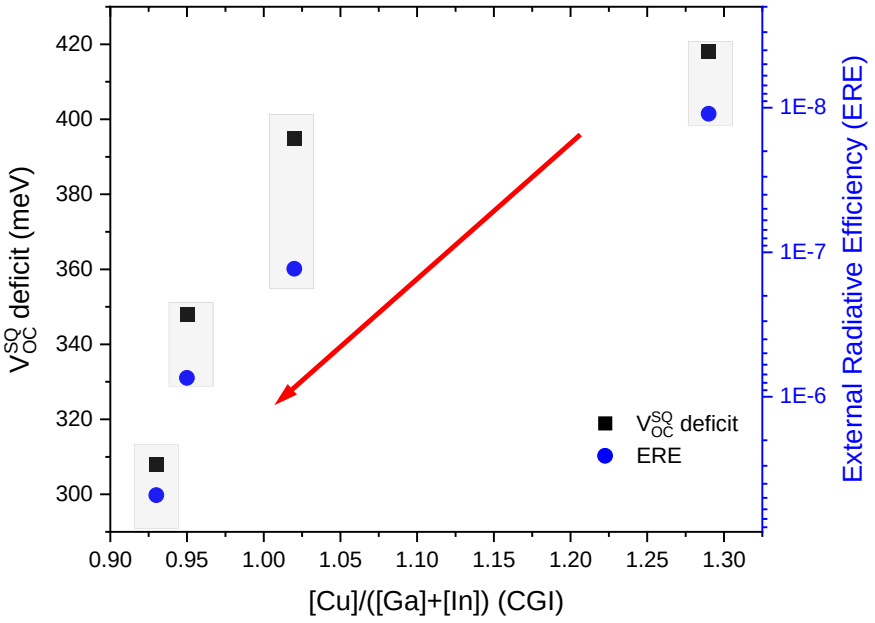

Figure 6.7: V_{OC}^{SQ} deficit and ERE in dependence of CGI ratio of samples C1, C2, C3 and C4.

For ease of quotation, the difference between QFLS and V_{OC} will be referred to as "V_{OC} loss". With the passivation of bulk defect realized in Cu(In,Ga)S_2 absorbers by going Cu-poor, there is still a disparity between QFLS and V_{OC} values as depicted in Fig. 6.3, since irrespective of the absorber composition, the QFLS is still not fully transformed into V_{OC} when solar cell devices are completed on the absorbers. The added layers to complete the device formation on the absorber suggest the origin of the deficit is interface-related, manifesting from the deposition of buffer layer. Research work on interface defects on Cu(In,Ga)S_2 have been done by Dr Mohit Sood, and readers are urged to refer to his Doctoral thesis for in-depth analyses [90] on the origin of V_{OC} loss in Cu-rich and Cu-poor absorbers. It was reported that, Cu-poor device with CdS buffer layer form a cliff-type offset or negative conduction band offset (CBO) at the absorber-buffer interface, which leads to interface recombination. The interface recombination can be passivated with Zn(O,S) buffer layer [90, 110, 191]. With this knowledge, CdS is not an ideal buffer layer for Cu(In,Ga)S_2 devices.

The solar cell device completed on the best Cu(In,Ga)S_2 absorber, C4, with Zn(O,S) buffer layer produced an efficiency of 15.2 % with V_{OC} of 902 mV [110]. A comparison of the efficiency with efficiencies of several $CuInS_2$ and Cu(In,Ga)S_2 solar cells is plotted against the respective bandgaps in Fig. 6.8. The bandgap of the solar cells are determined from the inflection point of their external quantum efficiency (EQE) curves. Although the device on C4 made the best high-bandgap solar cell at 1.60 eV, the device still suffers from a high loss between V_{OC}^{SQ} and device in comparison to the Cu(In,Ga)S_2 device holding the record-efficiency [24, 110].

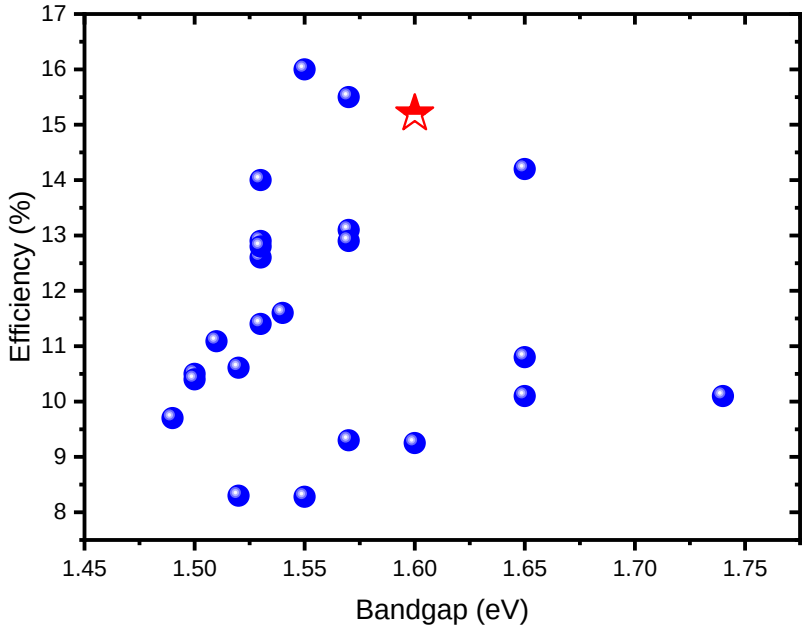

Figure 6.8: Efficiency of different $CuInS_2$ and Cu(In,Ga)S_2 solar cells plotted against the respective bandgap determined from external quantum efficiency (EQE) curves of the solar cells [24, 27, 28, 98, 110, 192-205]. The efficiency and performance of the solar cell on C4 (half-filled star) has been reported by Shukla and Sood et al. [110].

6.2 Surface gallium-grading in Cu(In,Ga)S_2 absorber

In the previous section, the influence of Cu-content on deep recombination centers/defects which limits the QFLS on Cu(In,Ga)S_2 absorbers have been discussed. As we have already seen that Cu-

poor absorbers have led to a change in the trend of certified record efficiencies of $Cu(In,Ga)S_2$ solar cells, see Fig. 6.1, the last section showed why Cu-poor absorbers would be the preferred choice for making high quality $Cu(In,Ga)S_2$ devices.

The initial objective of this section was to increase the Ga content in $Cu(In,Ga)S_2$ absorbers in order to obtain a higher bandgap, thus a higher QFLS. To grow the higher Ga-content absorbers, a procedure similar to that which was used to process the best absorber in Section 6.1 was used as a baseline. This Section 6.2 will show that the use of this baseline to process high Ga absorbers requires a modification. However, more importantly, this Section 6.2 will show the influence of surface Ga on $Cu(In,Ga)S_2$ absorbers and solar cells.

The idea and advantages of the double gallium or bandgap gradient derived from the three-stage deposition method was described in Section 3.6, where some of the advantages which make such bandgap profile or its adaptations the preferred standard was introduced. It has been shown in $Cu(In,Ga)Se_2$ absorbers that the height of the front surface Ga-gradient is crucial for the optimum performance of highly efficient devices [79, 206, 207]. However, if the front Ga-gradient is too high, the beneficial effect of the front gradient can be hindered by a barrier to photocurrent extraction and recombination at the absorber-buffer interface [79, 100]. With this background, this section examines the impact of front surface Ga-grading on the optoelectronic properties of $Cu(In,Ga)S_2$ absorbers and consequently the solar cells devised on the absorbers. The findings will serve as a precedent for a modification of the co-evaporation process in the succeeding sections within the context of gallium content in the third stage of a three-stage deposition.

6.2.1 $Cu(In,Ga)S_2$ absorbers and devices with high surface gallium

The three samples (H, M, and L) studied in this section were processed by the classical three-stage deposition method as described in Section 3.6, whereby the same In and Ga fluxes are evaporated in the first and third stage of deposition while Cu is deposited at the second stage [187]. Considering that the samples were deposited with the aim of increasing gallium content or the overall GGI ratio, the indium flux was kept constant during the first and third stages deposition for all the absorbers, and only the gallium flux was varied between the deposition of the absorbers.

The profile illustrating the deposition method is depicted in Fig. 6.9. The substrate temperature was heated at 265 °C during the first stage, and at 580 °C during the second and third stages. It should be mentioned that the temperatures mentioned are the estimated actual temperatures obtained from the substrate temperature calibration. The relationship between the set and real temperatures in presented in Appendix 2. The deposition process occurs under a sulfur atmosphere, as such, the sulfur flux was held constant by the closed loop method (see Section 3.6) to keep the evaporation chamber at approximately $(5.4 \pm 0.3) \times 10^{-5}$ mbar.

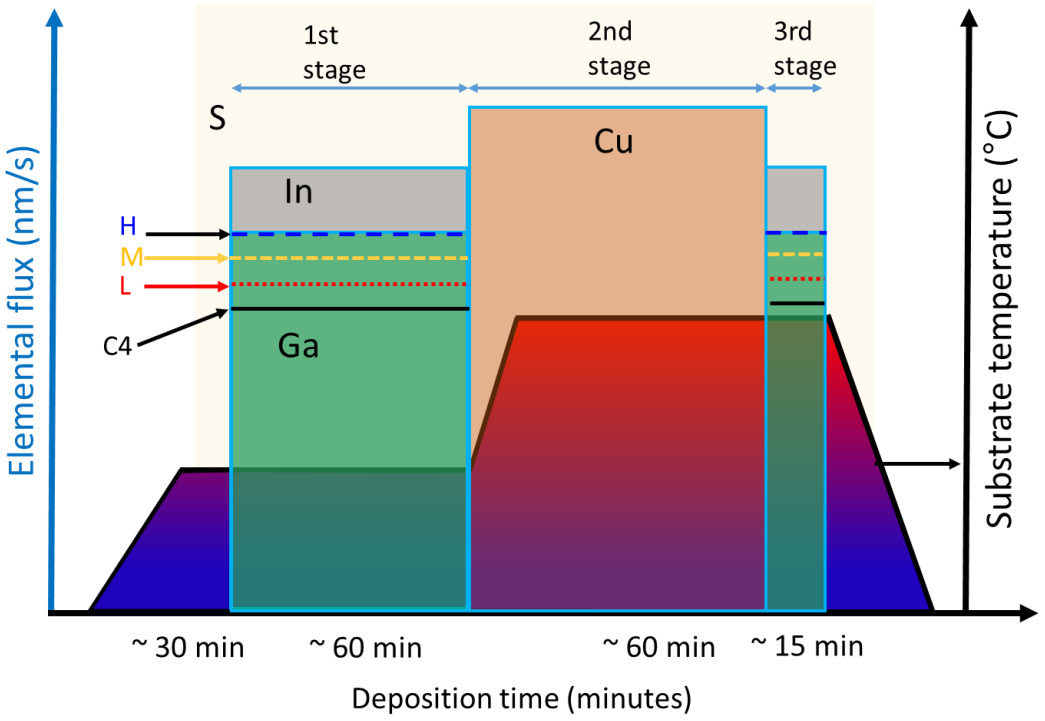

Figure 6.9: Schematic description of the three-stage deposition process used to vary Ga-content and surface GGI ratio of sample H, M and L. Here, the Ga fluxes remained the same in the first and the third stages of deposition. Samples H, M and L were deposited with similar In fluxes, but different Ga fluxes where H had the highest Ga flux and L had the lowest Ga flux. The Ga flux which corresponds to sample C4 in Section 6.1 has been indicated for comparison.

The average chemical compositions of the absorbers were analyzed by energy dispersive X-ray (EDX) spectroscopy at different acceleration voltages. In EDX, high-energy electrons impinge on a sample, with some incident electrons colliding with electrons orbiting the atoms in the sample.

The collision of the impinging electrons with the atom releases an electron in its lower energy level. An electron at a higher energy level in the atom then occupies the vacant low-energy level by releasing energy or X-ray characteristic to the atom. The penetration depth of the electrons impinging on the sample is dependent on the electron accelerating voltage, thereby allowing different depths of the absorber from the front surface layer to the back surface to be probed [208]. The penetration depth of electrons impinging on $Cu(In,Ga)S_2$ absorber in dependence of acceleration energy has been simulated using CASINO ("monte CArlo SImulation of electroN trajectory in sOlids") [209]. A schematic representation of the diffusion depth as a function of acceleration voltage at 5 keV, 10 keV and 20 keV is illustrated in Fig. 6.10. A more detailed view taken from CASINO of the different depth percentage for the different energies can be seen in Appendix 4. It was estimated that at acceleration energies of 5 keV and 20 keV, the maximum diffusion depth of the impinging electrons in $Cu(In,Ga)S_2$ are ~ 0.15 um and 1.5 um respectively. As such, the surface layer composition of the absorbers investigated is acquired at acceleration voltages of 7 keV, and the overall/average composition through the depth of the absorber is measured at 20 keV since the effective diffusion extends into the bulk of the absorber towards the back contact. Note that the acceleration energy of 5 eV was not used to acquire the near-surface composition since it is close to the characteristic X-ray emitted by indium.

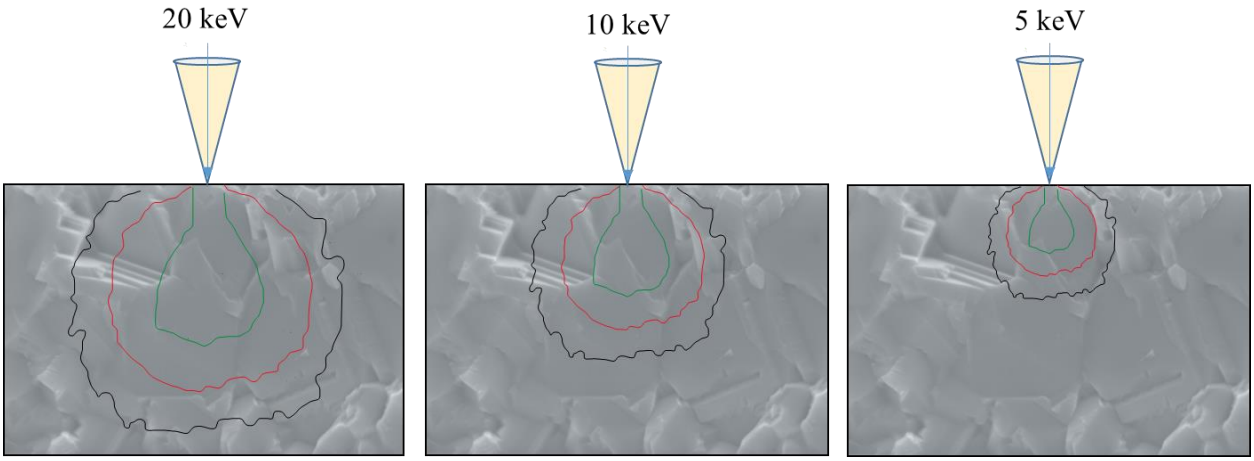

Figure 6.10: Simulation of penetration depth of energy dispersion X-ray at different acceleration voltages in a 3 um thick $Cu(In,Ga)S_2$ absorber. The outer black ring denotes the maximum diffusion region, while the innermost green ring represents the effective penetration depth. The illustration is adapted from Casino (monte CArlo SImulation of electroN trajectory in sOlids) [209].

The detailed chemical compositions as analyzed from EDX are presented in Table 6.3. For good comparison, all three absorbers were sufficiently Cu-poor with comparable [Cu]/([Ga]+[In]) (CGI) ratios between 0.91-0.94. Therefore, the influence of Cu-related recombination centers, which diminishes the optoelectronic quality between the absorbers, as shown in Section 6.1 and Ref. [110], are negligible. The front surface GGI ratios measured on the absorbers increased from (0.40) L to (0.62) H as the overall GGI ratio measured on the absorbers also increased from 0.19 (L) to 0.26 (H) as presented in Table 6.3. Hence, it can be concluded that the gallium content between the samples changes due to the higher Ga fluxes during deposition, with a stronger influence on the surface Ga.

Table 6.3: Chemical composition of absorbers processed with the same Ga fluxes at the first and third stages of deposition. Different Ga fluxes were used to process the various absorbers. The elemental composition was determined by EDX analyses. $\boldsymbol{E_g^{PL}}$ is the optical bandgap taken from the maximum of the PL peak.

Absorber	**Average GGI ratio**	**Surface GGI ratio**	**ΔGGI ratio**	**Average CGI ratio**	$\boldsymbol{E_g^{PL}}$ **(eV)**
Sample C4	0.13	0.17	0.03	0.93	1.57
Sample L	0.19	0.40	0.21	0.94	1.548
Sample M	0.22	0.47	0.25	0.91	1.558
Sample H	0.26	0.62	0.34	0.93	1.561

The gallium profile of the absorber measured by secondary ion-mass spectroscopy (SIMS) is available for only Sample H with the highest Ga content, and this is shown in Fig. 6.11a. Given the similar growth processes for the three samples H, M and L, the gallium profiles for samples L and M are assumed to be like sample H, with some differences in the notch height and the level/concentration of the surface gallium. For ease of comparing the gallium content measured on the absorbers without the SIMS gallium profiles for samples L and M, ΔGGI ratio is defined as

the difference between the overall and surface GGI ratios, and it is used for the relative comparison between the absorbers since they have different GGI ratios.

From optical measurement, the different surface GGI ratios had no strong influence on the shape of the emission spectra of the absorbers, as depicted by Fig 6.11b. From studies on Cu(In,Ga)Se_2, it has been reported that in a Ga-graded absorber, the PL emission energy is related to the bandgap minimum, since photogenerated carriers diffuse towards the position of minimum bandgap (notch) [103, 207, 210]. The PL emission energies presented in Table 6.3, show that there is no appreciable change in the emission energies between the samples compared to the GGI ratio as shown in Fig. 2.3. Rather, the optical bandgap extracted from the PL emission peak only increases from ~ 1.548 eV (L) to ~ 1.561 eV (H) despite the increase in the overall GGI ratio from 0.21 (L) to 0.34 (H) which would be expected to increase the bandgap [21, 35]. Even more remarkable is the fact that, although all three samples L, M and H possess higher GGI ratios than C4, they all have a lower optical bandgap in comparison.

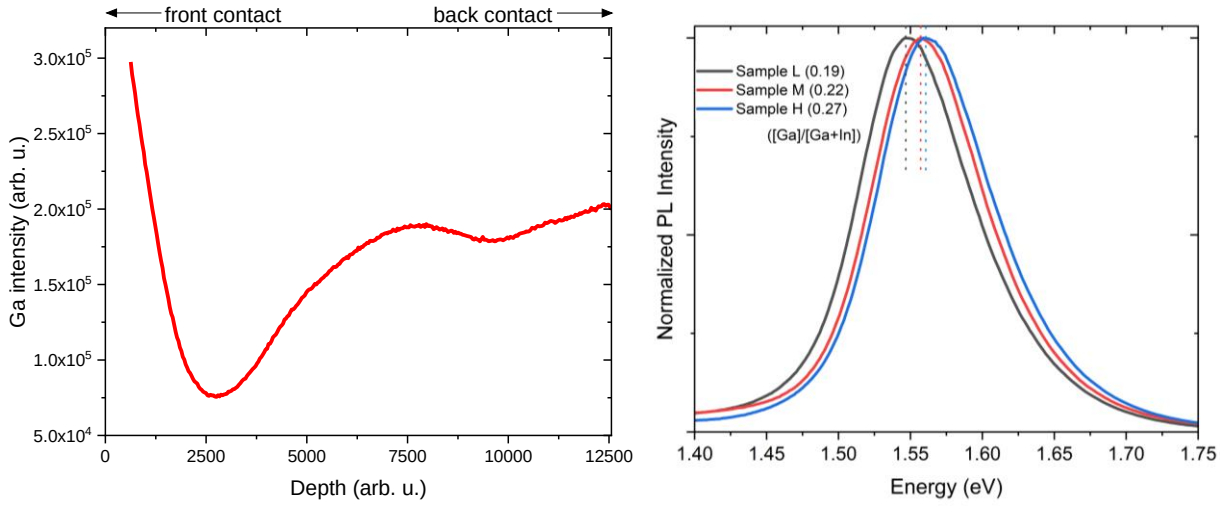

Figure 6.11: (a) Gallium profile of sample H (with high surface GGI ratio) measured by secondary ion-mass spectroscopy (SIMS). (b) Normalized PL spectra of the samples L, M and H.

The insignificant change in emission energy might be explained by the SIMS Ga profile of Sample H in Fig. 6.11a, where it can be observed that the intensity of the front surface Ga is approximately double the intensity of the back surface Ga, although the notch height is much lower. Owing to the high concentration of Ga on the front surface of the absorber, it could be assumed that the

additional Ga deposited during the third stage of growth process accumulates on the front of the absorber. Furthermore, the overall GGI ratio measured from EDX [211] is over-represented by the surface GGI ratio, which might lead to a discrepancy between the overall GGI ratio and optical emission energies as observed particularly in sample H.

The optoelectronic quality of the absorbers represented by the quasi-Fermi level splitting (QFLS) was evaluated using the external radiative efficiency (ERE) method, and for a good comparison, the values are again referenced against the highly efficient Cu-poor absorber (C4) with low surface and overall GGI ratio in section 6.1. The QFLS of each absorber evaluated at 1 sun illumination is presented in Table 6.4 and as a bar graph in Fig. 6.12. All three absorbers exhibited remarkable radiative efficiency resulting in QFLS greater than 1 eV, with improvement of +33 meV, +46 meV and +95 meV for Samples L, M and H respectively in comparison to the reference sample (C4). The gain in QFLS between L and H can be expected, since ideally, the theoretical V_{OC} as predicted by Shockley and Queisser increases with higher bandgap [13, 14], contrarily, C4 rather has a lower QFLS than L, M, and H although it has a higher bandgap than the three absorbers.

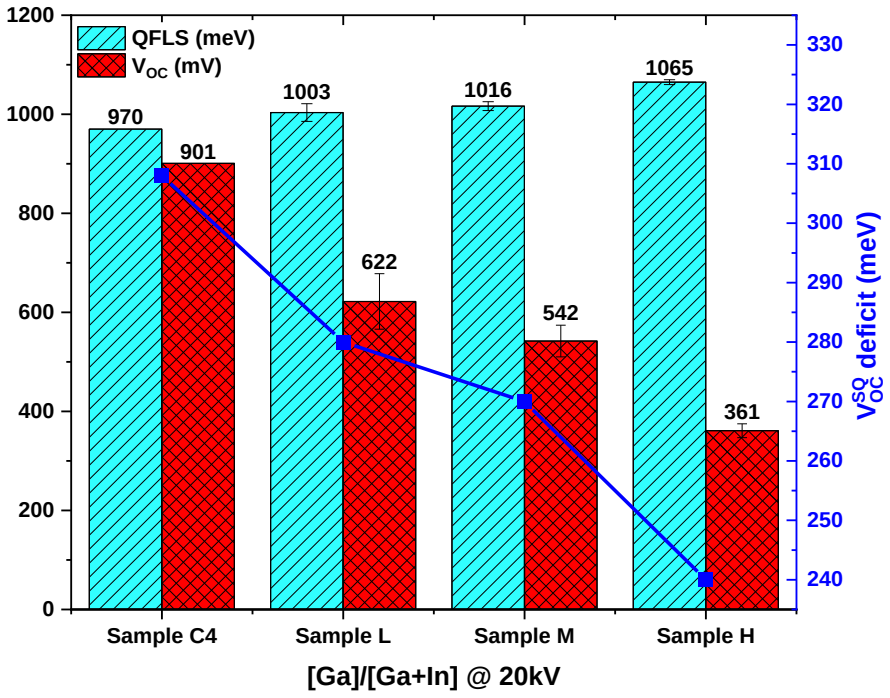

Figure 6.12: Graphical presentation of the QFLS and V_{OC} of Cu(In,Ga)S_2 absorbers with high surface GGI ratio. The line symbol shows the V_{OC}^{SQ} deficit. The solar cells were completed with Zn(O,S) buffer layer.

Due to the different bandgap among the absorbers, the V_{OC}^{SQ} deficit is used for a relative comparison of radiative losses among the samples independent of bandgap. From Table 6.4 and Fig. 6.12, it can be observed that V_{OC}^{SQ} deficit for the three samples significantly decreased in reference to C4 and it also decreased from sample L to H. The reduced V_{OC}^{SQ} deficit and the QFLS values indicate that the optoelectronic properties of the absorbers under study did improve with higher surface Ga. On one end, this could be because the high surface Ga/bandgap mitigates surface recombination [207], on the other hand, a higher front bandgap will be more transparent to longer wavelengths which can travel further into the absorber and generate charge carriers closer to the notch [100], and increase the carrier density and radiative efficiency of the absorbers.

Table 6.4: QFLS values and device parameters of the solar cell developed on the Cu(In,Ga)S_2 absorbers with high surface GGI ratio. The devices were made with Zn(O,S) buffer layer.

Sample	**QFLS (meV)**	**V_{OC}^{SQ} deficit (meV)**	**V_{OC} (mV)**	**V_{OC} loss (meV)**	**PCE (%)**	**FF (%)**	**J_{SC} (mA/cm^2)**
C4	970	308	901	69	14.3	71.6	21.8
L	1003	280	622	381	0.7	14.4	6.7
M	1016	270	542	474	0.1	18	1.0
H	1065	240	361	704	0.06	22	9.2

In the next step, solar cells are made on the absorbers, L, M and H with the stack of Zn(O,S), ZnO and Al:ZnO to inspect their electrical performance. The results of the optoelectrical and electrical performance are presented in Table 6.4 and Fig 6.12. The results show that V_{OC} strongly decreases from 622 mV in sample L to 361 mV in sample H. This contrasts with reports that Ga-grading in the space-charge region (SCR) significantly enhances V_{OC} [101, 212]. It is clear that the improved optoelectronic quality and high QFLS realized with high surface GGI ratio does not translate into high V_{OC}. The opposite is observed as seen in Fig. 6.13b, where the V_{OC} loss is correlated with the surface GGI ratio; it is seen that the higher the surface GGI ratio, the higher the V_{OC} loss. The

device parameters presented in Table 6.4 shows that the device performance registered on the solar cells made on the absorbers were equally bad.

The origin of the poor performance of the devices with high surface GGI ratio can be deduced from the I-V curves in Fig. 6.13a. It can be seen from Fig. 6.13a that the J_{SC} is less than J_{Ph}, which is an indication of a barrier for photogenerated carriers. This is corroborated by the S-shape and rollover effect seen in the I-V curves which becomes more pronounced with higher surface GGI ratio, particularly prominent in Sample H. It is also possible that with very high front surface Ga, the notch (or bandgap minimum) is shifted behind the SCR into the quasi-neutral region (QNR) [79]. This phenomenon, in addition to the low J_{SC} values (Table 6.4) adds to the suggestion that there is a barrier to photogenerated carriers, which is increases unwanted recombination thereby reducing V_{OC} and J_{SC} [93].

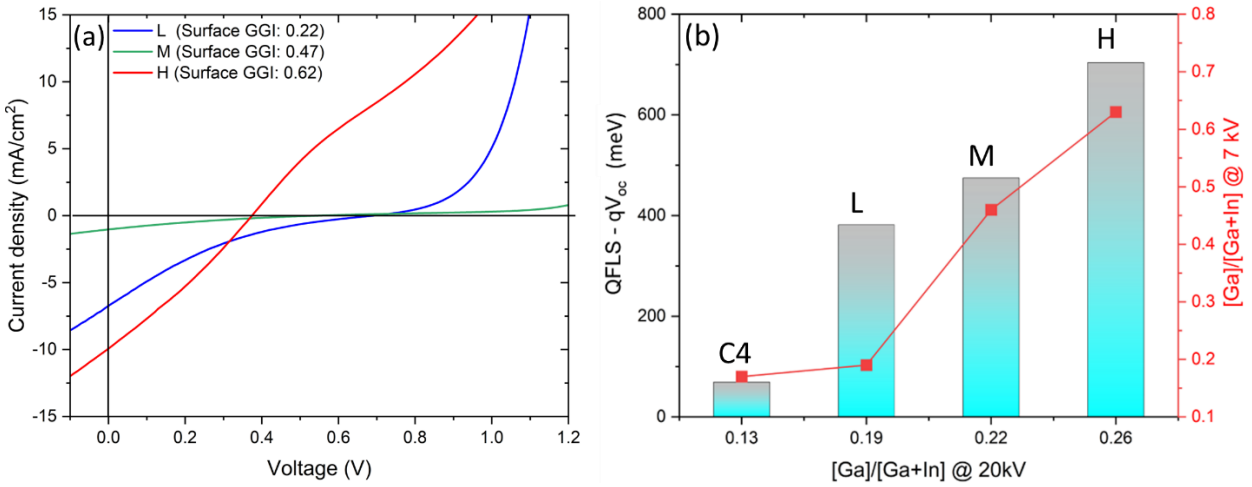

Figure 6.13: (a) Current-voltage (I-V) curves of the solar cells made on the absorbers with high surface GGI ratios . (b) Bar graph showing the correlation between V_{OC} loss (QFLS – qV_{OC}) and surface GGI ratio.

Chirila et al. reported on the influence of high surface GGI ratio on $Cu(In,Ga)Se_2$ [79], that with a high surface GGI ratio, there is a possibility that the notch formed at the conduction band is shifted behind the SCR into the QNR when forward biased. Owing to the high ΔGGI ratio, the high surface Ga acts as a barrier while the notch acts as confinement for the photogenerated electrons, which

easily recombines with holes in the valence band or mid-gap states [77, 79]. As the surface GGI ratio increases, the barrier effect is exacerbated leading to higher recombination. It is not understood if the same mechanism is occurring in the Cu(In,Ga)S_2 devices on absorbers L, M and H with high surface GGI ratio. A deeper understanding will require detailed device simulations and analyses which is not within the scope of this thesis. The interest in this thesis is limited to process optimization for the improvement of Cu(In,Ga)S_2 devices which continues in the next section.

6.2.2. Surface gallium for high performing Cu(In,Ga)S_2 devices

Findings from the preceding section have demonstrated that (i) the bandgap of Cu(In,Ga)S_2 is not significantly increased by the additional Ga deposited at the third stage of growth. (ii) Increased concentration of Ga on the front surface of Cu(In,Ga)S_2 absorbers is beneficial to the optoelectronic quality of the absorber, insofar as, QFLS increases and V_{OC}^{SQ} deficit is minimized due to a reduced surface recombination. Unfortunately, the high QFLS is not converted to a correspondingly high V_{OC}. Rather, the high concentration of front Ga leads to an undesirable barrier effect, which causes unwanted recombination and V_{OC} losses at the absorber-buffer interface. The results also suggest that, it is not adequate to have a high Ga flux or to maintain the same Ga flux in the first and third stage during the deposition of high Ga-content Cu(In,Ga)S_2 absorbers, although the same Ga flux ratio might be tolerable in low Ga-containing absorbers. Nevertheless, a higher-than-notch surface Ga or bandgap is still desired to garner the favorable outcomes and expectations of the Ga front gradient discussed in Section 3.6.

In a revision of the previous deposition profile depicted in Fig 6.10, an optimized profile where lower Ga flux at the third stage than in the first stage of evaporation is adopted. The elemental flux profile is exemplified in Fig. 6.14 with the Sample H in Section 6.2.1 used as a reference for comparison. The deposition conditions are such that the substrate temperatures at the first and second stages are 265 °C and 580 °C respectively with the chamber pressure ~ $(5.4 \pm 0.3) \times 10^{-5}$ mbar. In the revised deposition two samples labelled OL1 and OL2 were prepared. As illustrated in Fig 6.14, for both absorbers, the Ga fluxes at the third stage are lower than the Ga fluxes at the first stage. OL1 had a higher Ga flux than OL2 in the first stage while OL2 had a higher Ga flux

than OL1 in the third stage. The chemical composition showing the average CGI ratio, average and surface GGI ratios, from EDX analyses are presented in Table 6.5.

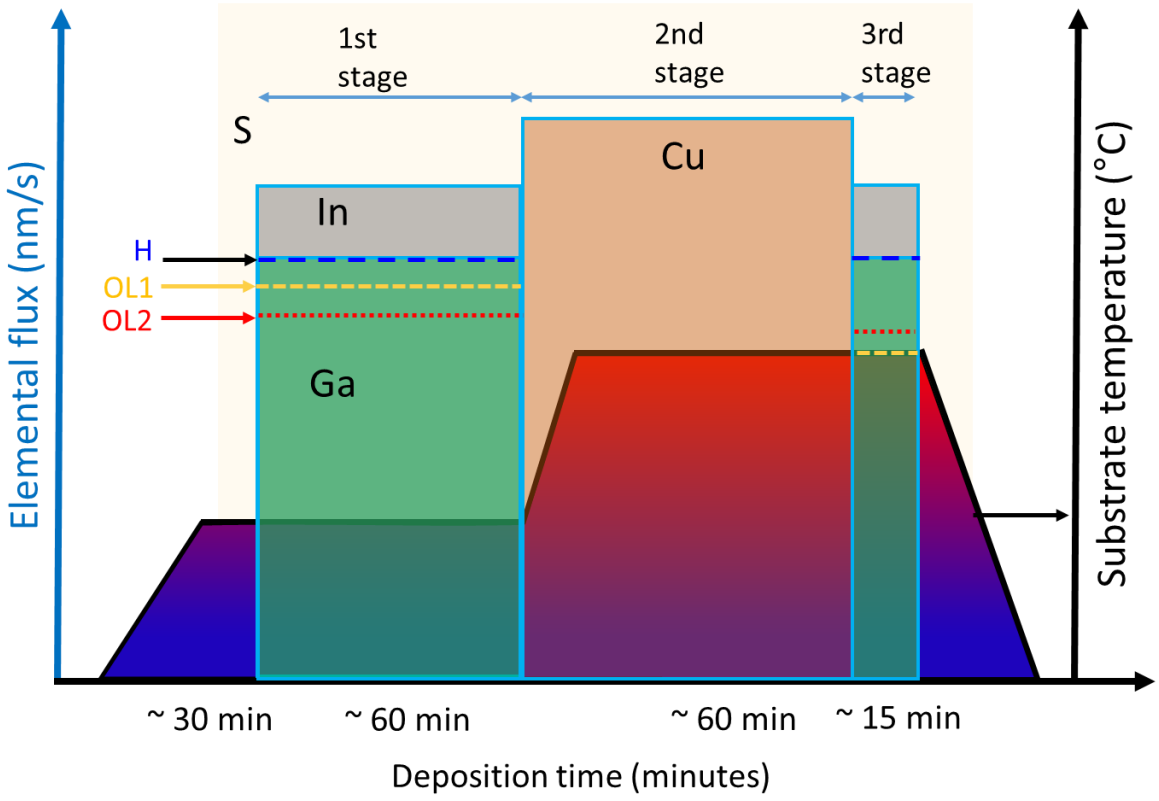

Figure 6.14: Revised three-stage deposition profiles for Cu(In,Ga)S_2 absorbers grown to have low surface GGI ratios.

Table 6.5. Chemical compositions extracted from EDX analyses for the Cu(In,Ga)S_2 absorbers grown with optimized deposition profile for lower Ga content.

Absorber	**Average GGI ratio**	**Surface GGI ratio**	**ΔGGI ratio**	**Average CGI ratio**	E_g^{PL} **(eV)**
Sample H	0.26	0.62	0.34	0.93	1.561
Sample OL1	0.13	0.33	0.20	0.90	1.545
Sample OL2	0.16	0.22	0.06	0.95	1.565

The front surface GGI ratio for OL1 at 0.33 is higher than that of OL2 at 0.22, while the average GGI ratio of 0.13 for OL1 is slightly lower than OL2 which is 0.16. From the bowing diagram showing of bandgap dependence on GGI ratio in Fig. 2.3 and comparing the average GGI ratio with the optical bandgaps in Table 6.5, it is noticeable that the bandgaps of OL1 and OL2 are better correlated with the average GGI ratio than in Sample H. Summarily, the surface-Ga optimized absorbers with lower GGI ratios are unlike Sample H where a much higher average GGI ratio rather showed a lower optical bandgap. Thus, the average GGI ratios of OL1 and OL2 are not heavily weighted by the front surface GGI ratio.

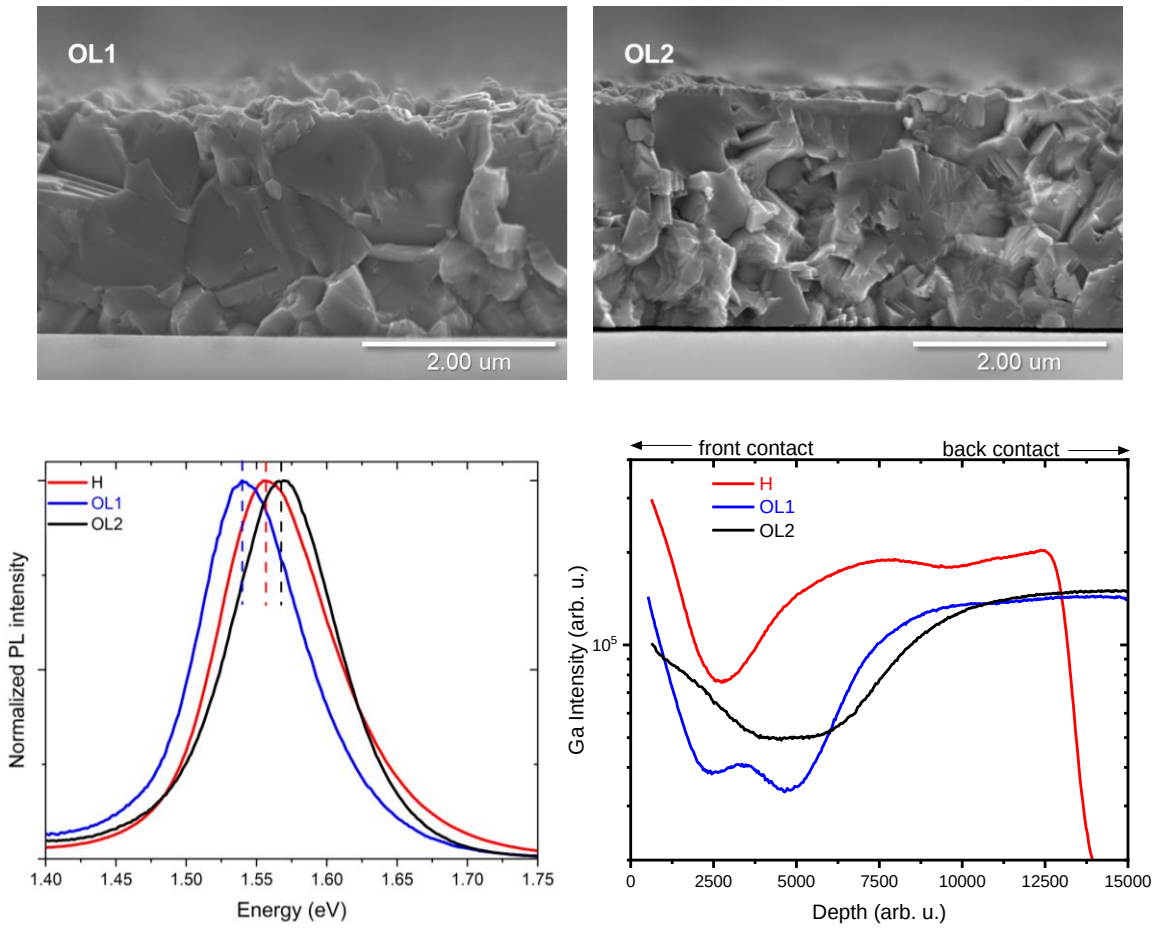

Figure 6.15: Cross-section SEM micrograph of (a)OL1 and (b) OL2. (c) Normalized PL spectra of the surface Ga-optimized absorbers, OL1 and OL2, along with H. (d) The uncalibrated Ga profile from SIMS of OL1, OL2 compared with H.

Fig. 6.15 shows the SEM cross-section of OL1 and OL2. The micrograph shows that OL2 has visibly smaller grain size in contrast to the larger grains of OL1. At this point, it is not clear if this is due to different Ga content in absorbers, although Ga is known to influence the grain size in absorbers [213-215].

The in-depth Ga profiles from SIMS analysis for OL1 and OL2 in comparison to Sample H are presented in Fig 6.15. From SIMS analysis of the Ga profile of OL1 and OL2, the notch height for OL2 is somewhat higher than OL1. The effect of the optimization on the front surface GGI ratio, highlighted by the difference between surface GGI ratio and the average GGI (ΔGGI) ratio, shows a reduction of the ΔGGI ratio from 0.34 in H to 0.20 and 0.06 in OL1 and OL2, respectively. The effect of reduced ΔGGI ratio is irrespective of the different Ga fluxes in the first stage of depositing the absorbers.

First, the influence of the reduced front GGI ratio on the optoelectronic quality is investigated on the bare absorbers by evaluating the QFLS which the details are presented in Table 6.6. The results presented in Fig. 6.16 are again compared with the reference absorbers, C4 in Section 6.1, and Sample H with high surface GGI ratio in Subsection 6.2.2. The average QFLS (and V_{OC}^{SQ} deficit) are evaluated as 962 meV (307 meV) and 979 meV (320 meV) for OLI and OL2, respectively. These values are comparable with C4 although QFLS is much lower than in Sample H. While the higher QFLS value of OL2 might be due to its higher bandgap than OL1 [14], its QFLS and V_{OC}^{SQ} deficit differs from Sample H with a similar bandgap by ~ 100 meV and 80 meV, respectively. This is due to the exceptionally high radiative efficiency of Sample H as reflected in Fig. 6.16. The exceptionally high surface GGI ratio (or high bandgap) for Sample H reduces surface recombination and this leads to improved photogenerated carrier collection. A consequence of such an assumption will be that the lower (front) bandgap of OL1 and OL2 increases surface recombination [207], which reduces photogenerated carriers at the notch and will reduce the radiative efficiency of absorbers with lower surface GGI ratio.

Ultimately, while a higher surface GGI ratio is beneficial to the radiative efficiency and QFLS of $Cu(In,Ga)S_2$ absorbers as seen in Fig. 6.16 and Fig. 6.12, contrarily, a higher surface GGI ratio does not strongly influence the bandgap of the absorber. This is as observed in Section 6.1.

In the next step to investigate the influence of the optimized surface GGI ratio in $Cu(In,Ga)S_2$, solar cell devices are completed on the absorbers with CdS buffer layers. Although Zn(O,S) buffer layer is more advantageous to $Cu(In,Ga)S_2$ devices due to a favorable conduction band alignment as mentioned in Section 6.1 and references [90, 110], CdS buffer is chosen in this step to circumvent the electron-barrier (appearing as rollover) which exists at the $Cu(In,Ga)S_2$/Zn(O,S) interface [90]. Additionally, CdS is used has it has been shown to impede the fill-factor loss with a non-optimal buffer even with a lower V_{OC}. Fig. 6.16a shows the I-V characteristics of Sample OL1 and OL2 along with the I-V characteristic of Sample H device completed with CdS buffer layer for good comparison, while the details of the device parameters are shown in Table 6.6. Note that in Section 6.1, the device parameters presented in Table 6.4 and Fig. 6.13 for Sample H are for device completed with Zn(O,S) buffer layer.

Table 6.6. QFLS and device parameters with CdS buffer layer on $Cu(In,Ga)S_2$ absorbers with optimized front GGI ratio.

Sample	**QFLS (meV)**	**V_{OC}^{SQ} deficit (meV)**	**V_{OC} (mV)**	**V_{OC} loss (meV)**	**PCE (%)**	**FF (%)**	**J_{SC} (mA/cm^2)**
C4	970	308	734	236	14.3	71.6	21.8
H	1065	240	655	410	0.07	22	0.5
OL1	961	307	773	188	6.4	46.1	17.8
OL2	962	320	830	132	10.4	52	21.3

The V_{OC} values are plotted with the QFLS for comparison and visualization of the losses incurred in Fig. 6.16c. The Sample OL1 exhibit FF, J_{SC} and PCE of 46.1 %, 17.8 mA/cm^2 and 6.4 % respectively. This is an improved performance in comparison with device performance of Sample H, detailed in Table 6.6. Although the V_{OC} of 773 mV and V_{OC} loss of 188 meV shows a better transformation of QFLS to V_{OC}, see Fig. 6.16 for comparison, other device parameters such as J_{SC}, FF and PCE are deficient. The origin of the deficiency might be understood from the I-V characteristics in Fig. 6.16a, as the attributes of barrier to photogenerated carriers can still be seen in the curve accredited to OL1. On the other hand, the device on OL2 absorber, sees the V_{OC}

increase to 830 mV, with V_{OC} loss of 132 meV, indicating a better QFLS-to-V_{OC} conversion than OL1 and the reference sample C4, Fig 6.16c.

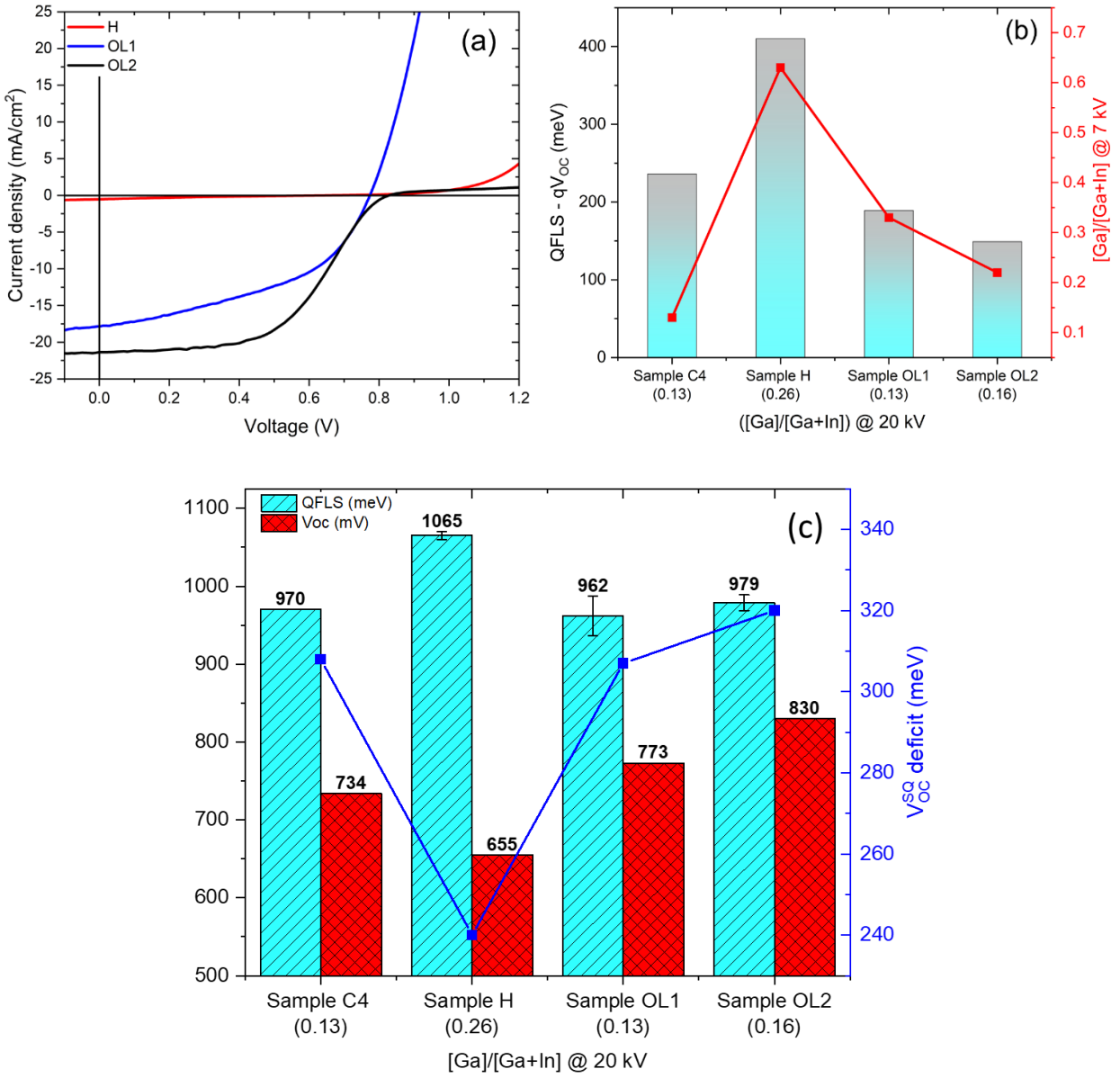

Figure 6.16: (a) I-V curve of Cu(In,Ga)S_2 device prepared on absorbers with moderate surface GGI ratio. (b) Loss between QFLS and V_{OC} (qV_{OC} deficit) in relation to surface GGI ratio. (c) Average quasi-Fermi level splitting (QFLS) on bare absorbers (turquoise bars) having lower surface GGI referenced with high surface GGI absorber. The V_{OC}^{SQ} deficit is represented by the line symbol (blue), and the open-circuit voltage (V_{OC}) measured on the CdS-buffered solar cells (red bars).

The FF, J_{SC} and PCE of 52 %, 21.3 mA/cm^2 and 10.4 % respectively for OL2 attest to the better performance of OL2 device as also shown by its I-V curve in Fig. 6.16a with less pronounced effect of photogenerated barrier. The correlation between the Voc loss and the front surface GGI ratio is presented against the average GGI ratio in Fig. 6.16b, where it can be observed that the lower the ΔGGI ratio, the lower the loss between QFLS and V_{OC}.

In summary, although a high surface bandgap does reduce recombination at the surface of Cu(In,Ga)S_2 absorbers, to benefit from front to surface Ga-grading in Cu(In,Ga)S_2 devices, the Ga profile needs to be moderated such that the surface Ga is not exceptionally high as to generate a barrier for photogenerated carriers. Furthermore, surface Ga did not substantially contribute to increasing the bandgap of the absorber. The high surface Ga poses a constraint on the third stage Ga flux during the three-stage deposition process when increasing the Ga content of the absorber. The Ga in the bulk can be increased without an exceptional increase at the surface by intentionally reducing the Ga flux at the third stage of deposition. There is a compromise in the lowering of the surface GGI ratio, in that, the recombination at the surface of the absorber increases, however, a barrier for photogenerated carriers is induced by a high surface GGI ratio.

6.3 Cu(In,Ga)S_2 back gallium-grading

An effect of incorporating Ga into $CuInS_2$ or increasing the Ga content in Cu(In,Ga)S_2 is to increase the bandgap, since there is an upward shift of the conduction band (CB) minima with Ga. Some knowledge of bandgap-grading from the counterpart and better-researched Cu(In,Ga)Se_2 were also discussed in Chapter 3 to better understand the outcome of the growth processes of Cu(In,Ga)S_2 absorbers.

In the need to overcome the theoretical working efficiency limitation in single junction solar cells, the concept of tandem application, where more than one solar cell is utilized has been presented in the introductory chapter. It was introduced that Cu(In,Ga)S_2 devices are viable as top cell due to the variability of its bandgap between 1.5 eV and 2.4 eV. For instance, if c-Si or Cu(In,Ga)Se2 is

used as the bottom cell, a solar cell with bandgap ~ 1.6-1.7 eV can be utilized as a top cell in tandem applications [17, 216]. Consequently, research on Cu(In,Ga)S_2 has found more interests recently [24, 28-31, 41, 113, 120, 193]. However, before the optimal use of Cu(In,Ga)S_2 in tandem applications, it is a prerequisite that the absorber possess a high QFLS and that high efficiency be achieved in Cu(In,Ga)S_2 single junction devices. Until now, in Section 6.1 and Section 6.2, the best high performing device demonstrated has an optical bandgap of ~ 1.57 eV or device bandgap of 1.6 eV, which is still lower than the desired bandgap between 1.6-1.7 eV. It should be mentioned that, it was recently shown that in a silicon-based bifacial tandem application, if Si is utilized as a bottom cell, a top cell of 1.5 eV bandgap is also suitable in a two-terminal tandem application [217], however for higher open-circuit voltage a higher bandgap than 1.5 eV is still necessary for the top cell in tandem applications.

In this current section, the aim is to increase the notch energy in Cu(In,Ga)S_2 absorbers to achieve optical bandgaps reaching up to 1.66 eV, in view of achieving a high performing solar cells. Section 6.2 has shown that when growing Cu(In,Ga)S_2 absorbers by the three-stage deposition process, a higher bandgap cannot be achieved by increasing Ga flux at the third stage of deposition, rather it is achieved with the increase of Ga flux at the first stage of deposition, since Ga evaporated at the first stage strongly influences the back Ga gradient.

This section will show the challenges encountered as the Ga in the first stage is increased to achieve a higher bandgap, that is, how the Ga content in the first stage of deposition influences the QFLS of the absorber and the impact on the device performance. Then, bulk analyses on the absorber will be used to investigate the crystalline phases, Ga depth profile, etc., will be performed to understand the origins of inhibitions to optimum performance. Again, the three-stage deposition technique will be utilized, in order to harness the qualities and benefits which has made bandgap-grading the standard technique in Cu(In,Ga)$(S,Se)_2$ absorbers. [218].

6.3.1 Challenges with high back-gallium Cu(In,Ga)S_2

The back Ga is varied or increased with the purpose of elevating the notch energy - point of the lowest Ga concentration - of the absorber to produce bandgaps between 1.6-1.7 eV. This bandgap

has been reported to correspond to overall GGI ratio of 0.3-0.35 [35]. As the primary focus in this section is the back Ga-grading in Cu(In,Ga)S_2 absorbers, the deposition will employ the baseline process in the previous Section 6.2, that is, the deposition of the absorbers will follow the three-stage co-evaporation sequence described in Section 3.6.3, but with a lower Ga flux at the third stage. To achieve a higher GGI ratio among the absorbers, only the gallium flux was adjusted in the first stage of deposition between all the absorbers, while the indium flux was kept constant to achieve the desired composition. Only Copper is deposited in the second stage. As a consequence of the knowledge obtained from the Section 6.2, at the third stage, the Ga flux is reduced to lower the surface GGI ratio, since Section 6.2 above showed that high surface GGI ratio has detrimental effect on Cu(In,Ga)S_2 devices. The deposition profiles depicting the Ga fluxes for the four Cu(In,Ga)S_2 samples, labeled BL1-BL4, are as illustrated in Fig. 6.17.

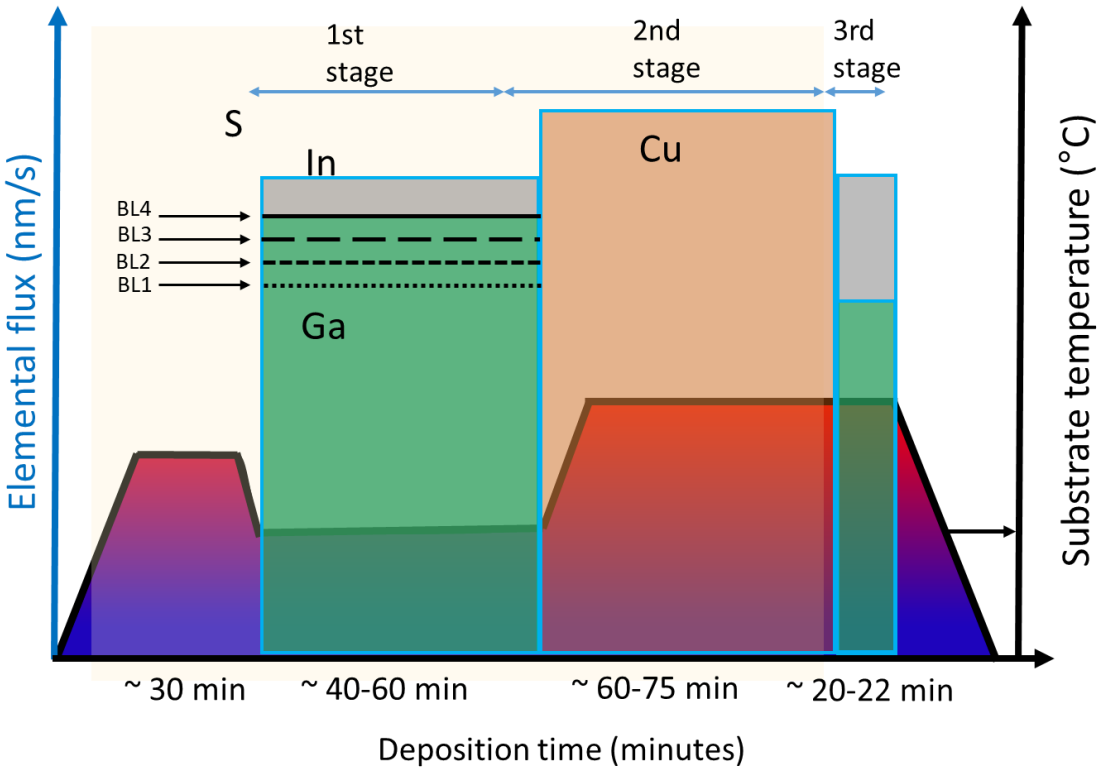

Figure 6.17: Illustration of the deposition profiles showing the increase of Ga fluxes at the first stage of deposition to achieve a higher notch energy in BL1-BL4. The same Ga flux was used at the third stage of deposition for all four samples.

All the absorbers were deposited on Mo-sputtered soda-lime glass (SLG) substrate. At the first stage, the substrate temperature was ~ 335 °C under a sulfur atmosphere with the chamber pressure of ~ $5.2 \cdot 10^{-5}$ mbar. At the second stage, the substrate temperature is increased to 595 °C at a heat ramp rate of 20 °C/minute, and the chamber pressure is increased ~ $6.0 \cdot 10^{-5}$ mbar by increasing the sulfur flux. Note that the temperatures are actual temperatures obtained from a calibration process, please find the corresponding set temperatures in the Appendix 2. As mentioned in Section 3.6, the heating of elements, opening and closing of shutters does influence the overall chamber pressure and the sulfur partial pressure is adjusted to account for the pressure changes, hence the increase in chamber pressure at the second stage. The deposition time at the first stage is between 45-60 minutes, approximately 60-75 minutes at the second stage and 20-22 minutes at the third stage. The different deposition times can be influenced by factors such as elemental fluxes, recrystallization of Cu-excess, and so on.

Table 6.7: The chemical composition extracted from EDX analyses and the optical bandgap $\left(E_g^{PL}\right)$ of the absorbers deposited with different first stage Ga flux to achieve higher bandgap.

Sample	**Overall GGI ratio @ 20 kV**	**Average CGI ratio @ 20 kV**	**Surface GGI ratio @ 7 kV**	$\boldsymbol{E_g^{PL}}$ **(eV)**
BL1	0.17	0.98	0.24	1.56
BL2	0.25	0.97	0.38	1.62
BL3	0.30	0.98	0.49	1.64
BL4	0.35	0.98	0.49	1.66

The specific chemical compositions of BL1-BL4 from EDX analyses, measured at 20 kV and 7 kV for overall and surface compositional ratios respectively, are presented in Table 6.7. All four samples have similar copper content with CGI ratio of 0.97-0.98. As intended, the overall GGI ratio steadily increased from 0.17 in BL1, the sample deposited with the lowest Ga flux, to 0.35 in BL4, the sample deposited with the highest Ga flux during the first stage. It is also observed from Table 6.7 that, there is an unintentional increase of the surface GGI ratio as the Ga fluxes in the

third stage increased. A likely explanation can be found in Section 6.2, where it is seen that much of the additional gallium at the third stage tends to agglomerate on the surface leading to a higher surface GGI ratio. Hence, for the samples BL1-BL4, as the back gallium was increased and the notch energy is elevated, the surface gallium and GGI ratio also increased even when gallium flux is reduced at the third stage.

The room temperature PL spectra of the absorbers BL1-BL4 showing the band-edge luminescence are presented in Fig. 6.18a. The effect of increasing the overall GGI ratio from 0.17 to 0.35, through the back gallium concentration, is seen by a shift in the band-edge emission by 0.1 eV, i.e., from 1.56 eV in BL1 to 1.66 eV in BL4, as seen in Fig 6.18a. The specific emission energies extracted from the PL peak are detailed in Table 6.7. For Cu(In,Ga)Se_2, the PL emission has been shown to originate from the notch [210], hence the shift of band-edge emission to higher energies indicates that the notch height is also influenced by the increasing back gallium (or first stage Ga flux) through a shift of the notch to a higher energies.

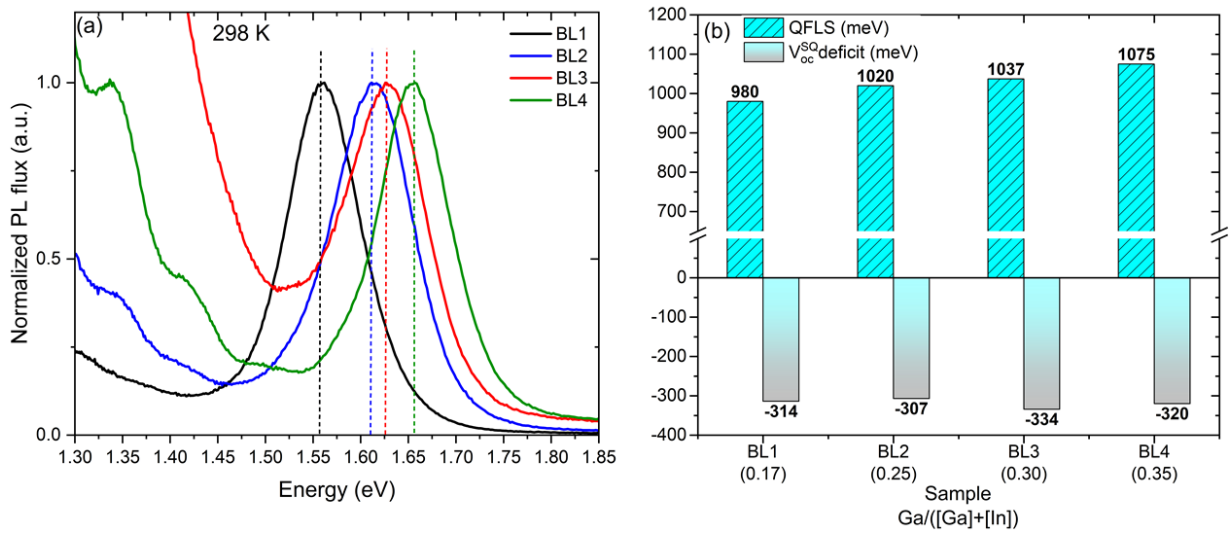

Figure 6.18: (a) Room temperature PL spectra of Cu(In,Ga)S_2 absorbers, BL1-BL4, deposited with varying first stage gallium flux. The PL spectra has been normalized to the band-edge emission peaks. A broad emission extending below 1.30 eV exists on the low-energy end. (b) A comparison of the QFLS and V_{OC}^{SQ} deficits of the same absorbers presented as a bar graph.

Also, in Fig. 6.18a is a characteristic broad band on the low energy end extending below 1.30 eV. In Section 6.1, a similarly positioned broad band was associated with copper related defect since the GGI ratio of those absorbers (C1-C4) are around 0.12-0.18 and Cu was rather largely varied. However, in this section, the CGI ratio of all the BL1-BL4 absorbers lie within 0.97-0.98 as detailed in Table 6.7, even though the most distinguishing factor is their gallium content, the attribution of the deep band to Ga is questionable and more investigations will be needed. Nevertheless, the results in Table 6.7 supports the fact that, apart from BL3, the intensity of the broad band increases as the gallium increases from BL1 to BL4. The band is most intense for BL3, despite being of lower average GGI ratio than BL4, although, of similar surface GGI ratio, which will make BL3 possess a higher ΔGGI ratio than BL4. Hence, for these gallium-varied absorbers BL1-BL4, the origin of the broad band beyond 1.3 eV is presumably gallium related. In Cu(In,Ga)Se2, such defect in high-gallium absorbers are attributed to Ga_{Cu} antisite, and as the energetic distance of the conduction band minima rises with increased gallium, these defects shift deeper into the mid-gap [168, 182].

The optoelectronic quality of the absorbers quantified by QFLS and V_{OC}^{SQ} deficit are reported in Fig. 6.18b and Table 6.8. The ERE method explained in Section 2.3.2 is used to evaluate the QFLS [52], and the bandgap is taken from the PL emission energy. Evidently, the effect of higher gallium content between the absorbers is also manifested by the increase in QFLS, as there is a gain of 95 meV in BL4 from 980 meV in BL1. For a change of 0.1 eV in band gap emission, the QFLS gain is consistent with the slope describing the change in QFLS in dependence of band gap in Fig. 6.4. Comparing the optoelectronic quality of the absorbers, it is important to mention that the higher QFLS achieved with increased Ga is not due to reduced nonradiative recombination loss, as the V_{OC}^{SQ} deficits in Fig. 6.18b and Table 6.8 show nearly identical values. Rather the higher QFLS is because of the higher band gap of the absorbers, since the energy difference between the electron Fermi level and hole Fermi level also increases with the higher CB minima [13, 14]. The V_{OC}^{SQ} deficits for the absorbers BL1, BL2 and BL4 are within 307-320 meV, indicating the similarity in optoelectronic quality. BL3 has a slightly higher V_{OC}^{SQ} deficit at 334 meV, which seems to be related to the particularly intense broad band on the low energy side of the band-edge emission, see Fig. 6.18a (this will be discussed after the device characteristics are presented below).

The absorbers are finalized into solar cell devices with CdS buffer layer and standard i-ZnO and Al:ZnO window layer. Although, we have already demonstrated that Zn(O,S) buffer layer is optimum for the overall performance of Cu(In,Ga)S_2 devices [90, 110], nevertheless, CdS buffer layer is used on these absorbers to investigate the performance of devices on BL1-BL4, since a better FF is reported of CdS-buffered device due to the absence of roll-over effect [90, 110].

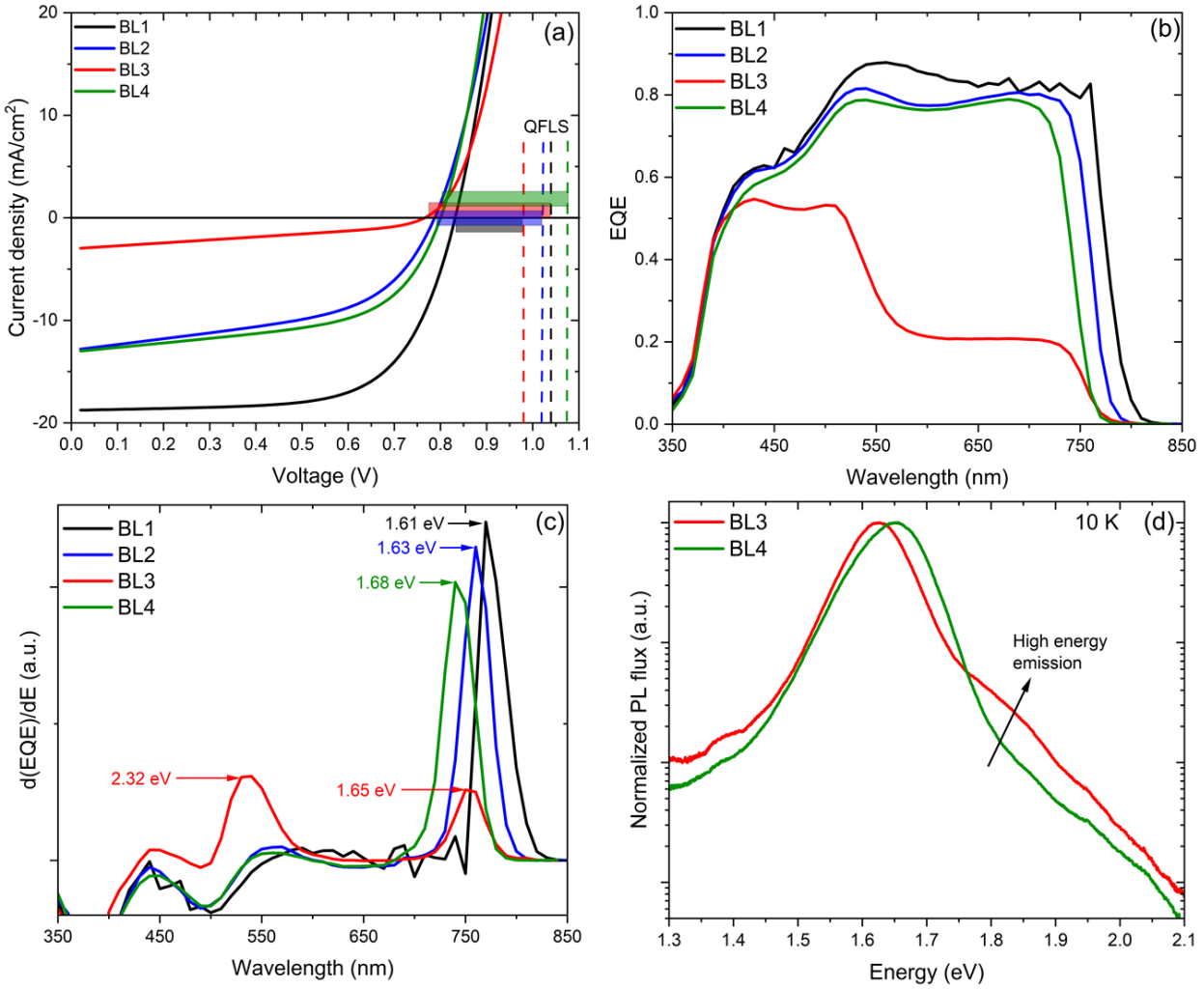

Figure 6.19: (a) I-V curve of the devices prepared on the high back Ga Cu(In,Ga)S_2 absorbers (BL1-BL4) with the dashed lines representing the QFLS values. (b) EQE corresponding to the devices. (c) First derivative of the EQE showing the inflection points $\left(E_g^{EQE}\right)$. (d) Low temperature (10 K) spectra of the near band-edge emission of the absorbers BL3 and BL4.

Additionally, in the LPV lab, the deposition of CdS buffer is a rather rapid process, thereby offering a quicker means of assessing the device performance. Fig. 6.19a and 6.19b respectively reports the I-V characteristics and external quantum efficiency (EQE) curves of the completed solar cell devices on BL1-BL4, with full detail of the parameters presented in Table 6.8. The EQE curves on all the devices in Fig 6.19b show a reduced blue response below 520 nm due to absorption by the CdS buffer layer. From Fig. 6.19a and Fig. 6.19b, the overall best performance, with the highest V_{OC}, J_{SC}, and FF (Table 6.8), is exhibited by the device on BL1, the absorber grown with the lowest gallium content. The V_{OC} loss of 149 mV indicates a better conversion of QFLS to V_{OC}, a conversion comparable to our best CdS-buffered device on Cu-poor absorber C4 in Section 6.1 and published results [110].

Table 6.8: Optoelectronic quality and I-V characteristics of the Cu(In,Ga)S_2 absorbers and devices deposited with higher back gallium. The devices were completed with CdS buffer layer.

Sample	**QFLS (meV)**	**V_{OC}^{SQ} deficits (meV)**	**V_{OC} (mV)**	**Voc loss (mV)**	**PCE (%)**	**FF (%)**	**J_{SC} (mA/cm^2)**
BL1	980	314	831	149	9.96	67.4	19.8
BL2	1020	307	796	224	5.27	51.8	14.3
BL3	1037	334	760	277	0.88	38	3.0
BL4	1075	320	801	274	5.87	56.7	12.9

The better V_{OC} and J_{SC} contributes to a PCE of 9.96 % on the BL1 device. The V_{OC} of devices on BL2 and BL4 are similar, although BL4 has a higher V_{OC} loss 274 mV compared to 224 mV in BL2, and BL4 has a higher FF and PCE likely due to the slightly higher maximum power output in Fig. 6.19a. Even though V_{OC} loss in BL3 is comparable to BL4, the device on BL3 show a rather poor performance with J_{SC} of 3 mA/cm^2 as shown in Fig. 6.19a. Theoretically, current density decreases towards high bandgap due to low electron-hole pair generation [13, 14], so the reduced J_{SC} from 19.8 mA/cm^2 (BL1) to 12.9 mA/cm^2 (BL4) is not surprising, however the particularly low J_{SC} in BL3 indicates a photocurrent loss from high recombination in the device [77]. The response of the EQE curve for BL3 in Fig. 6.19b, which drastically decreases after ~ 520 nm

towards the long wavelength, could better explain the origin of the poor J_{SC} and poor performance of the device. This region depicts a device with back surface recombination, low absorption of long wavelength or transport loss [219, 220], but also it portrays the response of a two-structure device with two bandgaps [213, 221]. This is affirmed by the inflection point of EQE curves, that is $\frac{\mathrm{d}(EQE)}{\mathrm{d}E}$, which is alternatively interpreted as the bandgap of a photovoltaic $\left(E_{\mathrm{g}}^{EQE}\right)$ device [222, 223], and has been used as such. The derivation of E_{g}^{EQE} for all the devices are shown in Fig. 6.19c. First to address the discrepancies between the bandgap emission from the PL (Table 6.8, Fig. 6.18a) and the EQE inflection points (E_{g}^{EQE}) in Fig. 6.19c; the difference in bandgap occurs as the PL is measured on the bare absorber, whereas the EQE is measured on the completed solar cell. Moreover, the PL emission originates from the notch [210], whereas the inflection point is taken from the absorption threshold [222-224]. Except for BL3, the devices show a single inflection point, and as realized in for the E_{g}^{PL}, the E_{g}^{EQE} of each device shifts to higher energy from 1.61 eV (BL1) to 1.68 eV (BL4) in correlation with the increased back gallium of the absorbers. BL3 rather has two inflection points, one at 1.65 eV and another at 2.32 eV, which confirms the presence of two bandgaps in the absorber. Lastly, the low temperature PL measured on BL3 and BL4 are displayed in Fig. 6.19d. Both absorbers are chosen due to the similarity of their surface GGI ratio, albeit with different overall GGI ratio. On the high energy end of the band-edge emissions (i.e., 1.60-1.65 eV), a low-intensity peak at ~ 1.8 eV which is discreet for BL4 is rather more intense in BL3. This peak is not likely to originate from the bulk or back of the absorber [210], rather from the surface of the absorber as confirmed by the high surface GGI ratio in BL3 (see Table 6.8).

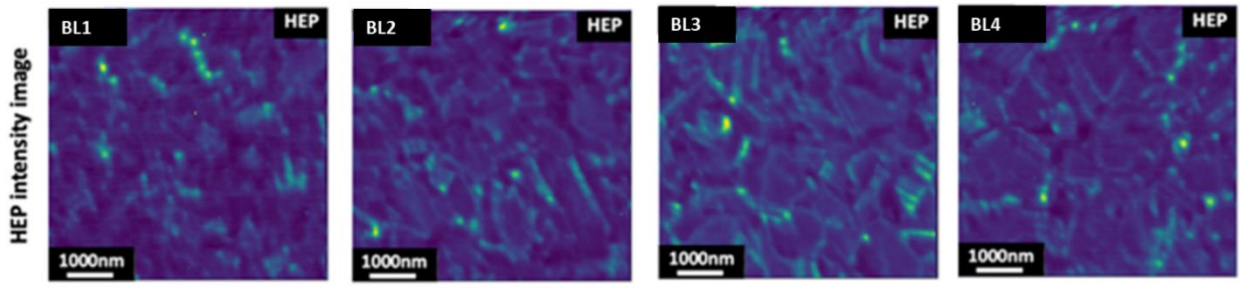

Figure 6.20: Cathodoluminescence hyperspectral imaging showing the intensity map of the front surface of BL1-BL4. The emission is centered at 2.2 eV with bandpass from 2.38 eV to 2.08 eV.

The high surface gallium is again confirmed by cathodoluminescence (CL) hyperspectral imaging performed on the samples in Fig. 6.20. In fact, three peaks are featured in the CL spectra; the main and most intense peak at the band-edge, a low energy defect peak at ~ 1.3 eV and a high energy peak localized around facets of some grains (~ 2.2 eV), which is presented in Fig. 6.20.

To summarise the observations so far, an increase of the GGI ratio in $Cu(In,Ga)S_2$ absorbers from 0.19 to 0.35 (BL1-BL4) obtained by increasing the first stage Ga flux (or back gallium), actively shifts the band-edge luminescence to high energies, with a corresponding increase in QFLS. However, the device performance deteriorates as the Ga content increases. An increase of surface gallium also leads to even poorer device performance.

To understand impediments that could be limiting the optimal performance of the devices vis-à-vis the absorbers (BL1-BL4), the microstructural and crystallographic properties of the absorbers are studied by SEM analysis, SIMS analysis, X-ray diffraction and cathodoluminescence imaging. The SEM cross-section images of the absorbers BL1-BL4 are shown in Fig. 6.21. The chemical compositions determined from EDX are already presented in Table 6.8 above. Since the absorbers are processed under Cu-deficient conditions, as also confirmed by the compositions, the SEM images are on the as-grown absorbers without the need for KCN etching. The images show that, a bi-layer in which rough smaller grains mark the lower layer extending to the Mo back-contact, while the upper layer exhibit smoother larger grains. BL1 and BL2 feature particularly larger sized grains with a thicker upper layer than the lower layer. As the back Ga increases in absorbers BL3 and BL4, the grains get smaller with the thickness of the upper layer reducing while the thickness of the back layer increases. The reason behind this phenomenon could be due to the higher Ga-content because, it was reported by Abou-Ras et al. that, in $Cu(In,Ga)Se_2$, the grain size increases with Ga content up to a GGI ratio of 0.23, above which the grain size decreases [34, 213]. This occurs due to lattice strain of the crystal structure induced by the smaller lattice parameters of gallium in comparison to indium [32, 225]. These cross-sectional images of BL1-BL4 in Fig. 6.21 are remarkably in contrast with those shown in Section 6.2 for OL1 and OL2, with similar growth technique albeit with lower Ga content, where a microstructure featuring large homogeneous grains are seen throughout the cross-section of the absorbers even in absorbers with overall GGI ratio up to 0.16.

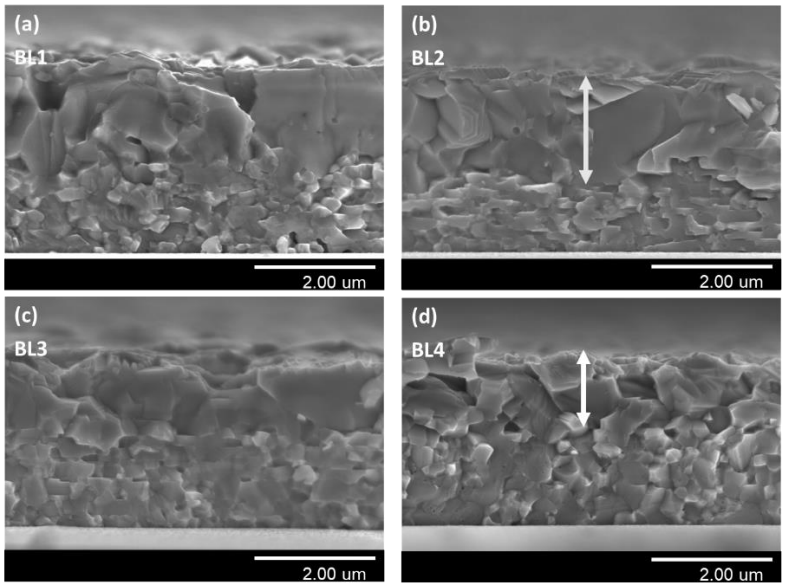

Figure 6.21: (a)-(d) Cross-sectional SEM micrograph showing the microstructure of Cu(In,Ga)S_2 absorber layers BL1-BL4 deposited on Mo-covered SLG. The absorbers were grown with various first stage Ga fluxes which increased from BL1 to BL4.

For the actual constitution of the bi-layer or segregated phases in BL1-BL4 absorbers, a qualitative EDX mapping is performed on the cross section of the absorbers, with BL1 and BL3, presented in Appendix 6. In both samples, the homogeneity of sulfur through the bulk of the absorber signals an even distribution of the chalcogen atom in the layers. In BL1, Cu appears better diffused across the absorber than in BL3, where it appears that there is a higher concentration of Cu at the back of the absorber. However, the major difference between both absorbers is the concentration of In and Ga. Already in BL1, the back layer has a higher Ga concentration than the top layer, while indium seems better diffused with a slight gradient from the top to the back of the absorber at the Mo back-contact. It should be stated that, due to the three-stage co-evaporation method, a higher concentration of Ga at the back of the absorber is typical. However, the abrupt contrast in the Ga concentration questions the extent of the Ga-gradient in the absorber. In comparison to BL1, the back Ga in BL3 is more intense, indicating a higher concentration of back Ga. Noticeably, there is also a substantial concentration of Ga at the top layer of BL3 in agreement with the high surface GGI ratio recorded for BL3 in Table 6.8. In-between these two Ga-rich areas is a Ga-deficient region which is rather indium-rich. Ultimately, the EDX mapping of BL1 and BL3, confirms that

the separated phases in all the absorbers consists of a strongly Ga-rich back layer, and in the case of the higher Ga samples, specifically BL3 and BL4, there is an additionally high concentration of Ga at the front surface. From three-stage-deposited $CuGaSe_2$ or high Ga containing $Cu(In,Ga)Se_2$, it is not unusual for the grain size to vary throughout the depth of an absorber or for the appearance of smaller grains at the back of an absorber, as this is associated with the inadequate migration or diffusion of Ga during the growth of the absorber [214, 226]. Nonetheless, similar phase separation/segregation phenomenon in chalcopyrite $Cu(In,Ga)S_2$ has been reported by Thomere et al. [29]. It was shown that during the growth of the absorbers by the three-stage deposition method, phase segregation already starts appearing as soon as Cu is evaporated at the second stage of deposition [29]. To discuss the tentative origin of the phase segregation, the crystallographic phase of the absorbers is first investigated. X-ray diffraction is performed on the samples to analyze the phase compositions and crystal structure of the absorbers.

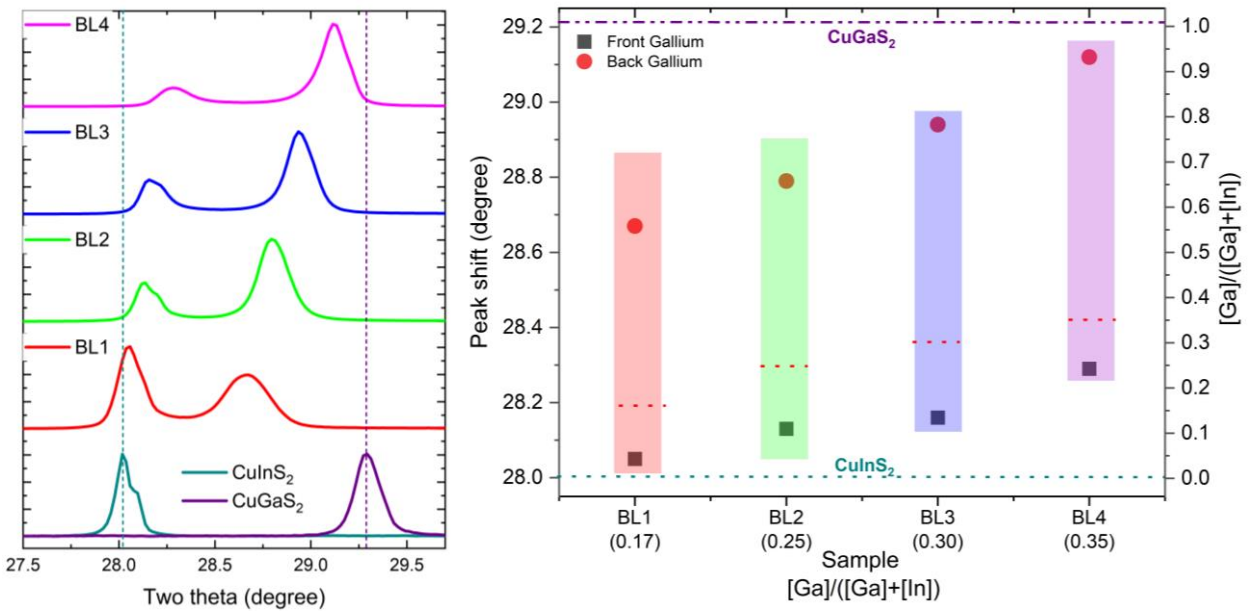

Figure 6.22: (left) XRD reflection pattern around the chalcopyrite (112) peaks between 27.5° and 29.7° of the absorbers BL1 to BL4 where the back gallium has been increased. For reference, the reflection on $CuInS_2$ and $CuGaS_2$ processed and measured in the same machines has been included. (right) The (112) peak positions presented along with the expected [Ga]/([Ga]+[In]) ratio in dependence of the overall GGI ratio evaluated on the absorbers.

The diffractogram of the absorbers showing the diffraction pattern between 27.5° and 29.7°, a range selected for emphasis on the behavior of the dominant (112) peak concerning the chalcopyrite structure, is illustrated in Fig. 6.22. In a single-stage deposited Cu(In,Ga)(S,Se_2) absorber where Ga is more uniformly distributed, since a single phase prevails, a single dominating peak is observed, and this peak shifts to higher angles as Ga is incorporated [144, 227]. For instance, in a pure $CuInS_2$ where the chalcopyrite peak is at ~ 28°, when Ga is substituted for In, the peak shifts towards 29.2 °, since the gallium atom is smaller than the indium atom, the lattice contracts [29, 32, 110, 225]. The shift of the dominant diffraction peak in dependence of Ga content follows a linear relationship described by Vegard's law [228]. The relationship goes from 0 in pure $CuInS_2$, to 1 in pure $CuGaS_2$ [228]. In Ga-graded absorbers, the likes of which is induced by the three-stage deposition method, the chalcopyrite peak could be broad, or more than one peak belonging to multiple chalcopyrite phases could appear due to the intermixing and diffusion of the elements [110, 227, 229].

In Fig. 6.22(left), the XRD reflection on the four absorbers BL1-BL4 show that the chalcopyrite phase is composed of two structures, one at a lower angle and the other at a higher angle. The peak shift for pure $CuInS_2$ and $CuGaS_2$ processed and measured by similar processes are also shown for references. Reports have shown that the lower angle corresponds to the front - low gallium part - of the absorber while the higher angle originates from the gallium rich back of the absorber [30, 227]. Fig. 6.22(left) also shows that the (112) peak positions change with Ga content, in that, as the Ga concentration increased, the peak positions shift to higher angles. The intensity of the low angle peak weakens with increasing Ga while the intensity of the high angle peak strengthens with the increased Ga content. Fig. 6.22(right) shows the extracted (112) peak positions compared with the expected [Ga]/([Ga]+[In]) from the Vegard law [228], in dependence of the overall GGI ratio. The low angle peak for BL1 occurs at ~ 28.05°, (i.e., GGI ratio = 0.05), close to the angle corresponding to pure $CuInS_2$, and the high angle peak is at ~28.65° (i.e., GGI ratio = 0.67), while for BL4 with the highest Ga content, the peaks are at ~ 28.29° (i.e., GGI ratio = 0.25) and ~29.12° (i.e., GGI ratio = 0.93) for the low and high angle peaks, respectively. The angle-spacing between both peaks increases from ~ 0.62° in BL1 to 0.88° in BL4, suggesting that as the back gallium is increased, there is a weak In-Ga intermixing between the front and the back compositions of the absorbers. Finally, the depth profile measured by SIMS analyses for BL4 is presented in Fig. 6.23.

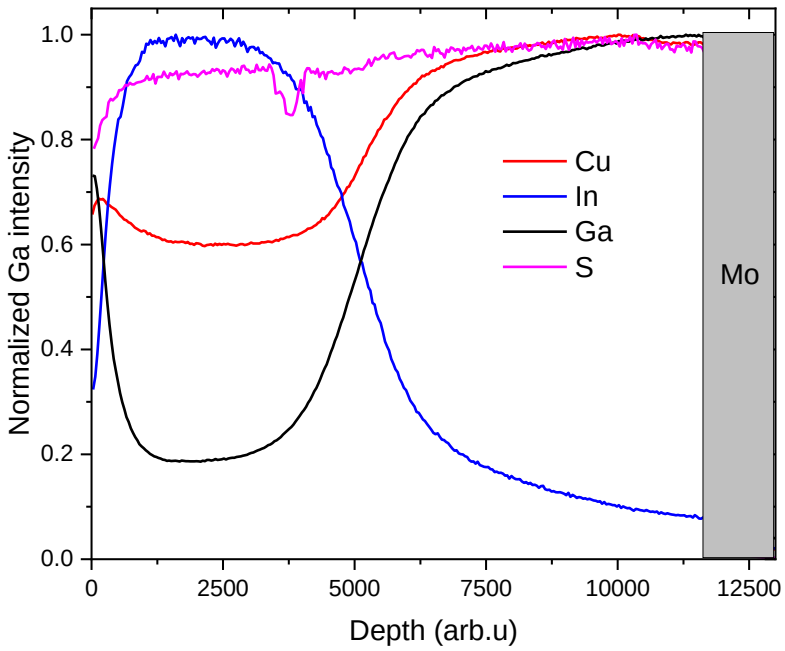

Figure 6.23 SIMS depth profile measurement showing the normalized intensities of the element through the depth of the absorber BL4.

The SIMS profile shows a flat Ga-rich back that is about 10 percent indium, while the front is In-rich with about 20 percent gallium, which is in agreement with the EDX mapping and XRD reflection patterns. There is a very steep Ga-gradient between the nearly flat Ga-rich back layer and the equally flat In-rich front layer, that is, the notch. The notch shape here is also far from the typical V-shaped seen in $Cu(In,Ga)Se_2$ [11, 230], however, such flat notch has been observed in $Cu(In,Ga)S_2$ absorbers [29, 30], and this has been attributed to different formation mechanism in the selenides than in the sulfides [29]. Thus far, the various analyses on the absorbers BL1-BL4, all with increasing back gallium content deposited to increase the optical bandgap, have highlighted the challenge of phase segregation when making $Cu(In,Ga)S_2$ absorbers with high Ga content. Referring to similar observations [28, 30], the origin of the phase segregation in $Cu(In,Ga)S_2$ is identified in the pseudo-ternary phase diagram of $Cu_2S–In_2S_3–Ga_2S_3$ which implicates a dual phased Cu-poor $Cu(In,Ga)S_2$ region [31]. It was shown that the Cu-poor region comprise a cubic and a trigonal phase that do not mix, forming a compositional plateau [29, 31].

6.4 Gallium profile optimization in Cu(In,Ga)S_2 absorbers

The results from the preceding section have shown that there are pitfalls when increasing the gallium content in Cu(In,Ga)S_2 absorbers, especially under Cu-deficient conditions. It is seen that as the GGI ratio is increased towards 0.30-0.35 to achieve bandgap of ~ 1.60-1.65 eV, the phases involved in the absorber growth along with the crystal and microstructural properties drastically change the absorbers. This influences the device performance on absorbers grown in such condition. Apart from the intrinsic origins of the phase separation effect explained above, the steep gallium gradient observed in all the absorbers also suggests a low intermixing of Ga and In [231, 232], particularly Ga, since it accounts for the bandgap variation in the bulk of the absorber. Several factors that can influence the Ga-gradient in the bulk of the absorber include sulfurization or annealing temperature, and substrate temperature since the intermixing and diffusion of the elements are temperature-dependent [98, 193, 232, 233].

In this section, in efforts to alleviate the challenges highlighted in Section 6.3, the impact of growing Cu(In,Ga)S_2 absorbers under different conditions such as, sulfur atmosphere, substrate temperature, different heat ramping rates and Cu-excess recrystallization, on the absorber attributes and device performance will be investigated. Table 6.9 lists the expected outcomes of the various deposition parameters. At the end of the Section 6.4 a similar table will be revisited to check if the outcomes are as expected.

Table 6.9: Expected outcome of tunning various deposition parameters during the deposition process of Cu(In,Ga)S_2 absorbers.

Deposition parameter	**Expected outcome**	**Relevant subchapter**
Sulfur cracker temperature	Better reaction of Ga and In with S	Section 6.4.1
First stage substrate temperature	Improve Ga diffusion and In-Ga intermixing	Section 6.4.2
Ramping of substrate heater temperature	Less steep Ga gradient and low surface Ga	Section 6.4.4
Cu excess recrystallization	Vary notch energy	Section 6.4.5

6.4.1 Influence of thermal cracking of sulfur on the Ga profile of $Cu(In,Ga)S_2$

The sulfur unit in the PVD system in which the $Cu(In,Ga)S_2$ absorbers are processed at LPV is designed such that the crucible can be heated at temperatures of 80-120°C. For detailed description of the system, please refer to Chapter 3. Upon evaporation from the crucible, the sulfur vapour travels through a valve tube which regulates the flow of sulfur and an injector or thermal cracker which both operate at the minimum temperatures of 250 °C, as described in Section 3.6.1. At these temperatures, the dominant sulfur phases are the larger and less chemically reactive S_8, S_7, S_6 and S_5 molecules with formation enthalpy of 24.32 $kcal_{th}$ mol^{-1}, 27.17 $kcal_{th}$ mol^{-1}, 24.36 $kcal_{th}$ mol^{-1} and 25.14 $kcal_{th}$ mol^{-1} respectively [234, 235]. When these species of sulfur pass through the thermal cracker at high enough temperatures, the S_8, S_7, S_6 and S_5 molecules are broken into the smaller and more reactive S_4, S_3 and S_2 molecules with formation enthalpy of 34.84 $kcal_{th}$ mol^{-1}, 33.81 $kcal_{th}$ mol^{-1} and 31.20 $kcal_{th}$ mol^{-1} respectively [234, 236]. With this knowledge, the influence of thermal cracking of sulfur in $Cu(In,Ga)S_2$ absorbers and devices will be investigated.

Four different $Cu(In,Ga)S_2$ absorbers named SC300, SC500, SC650 and SC800 were deposited under different sulfur atmosphere, where the sulfur cracker temperatures of 300 °C, 500°C, 650°C and 800°C were used to grow the respective absorbers. The growth of the absorbers was by the three-stage deposition method for a Cu-deficient composition, and under identical deposition steps to minimize drastic variations between the absorbers. The substrate temperature at the first stage was 335 °C while the substrate temperature at the second and third stages was 590 °C. The control of sulfur flux into the evaporation chamber was under a closed feedback loop to ensure a constant and stable sulfur flux throughout the deposition process. To prevent the complexity and possibility of a bi-layer structure, the evaporated Ga is reduced to a flux identical to those which resulted in GGI ratio ~ 0.13 in Section 6.1 to Section 6.2, since the microstructure of those absorbers showed minimal to no bilayer features. The SEM images showing the microstructure of the absorbers deposited under the different sulfur cracker temperatures are shown in Fig. 6.24. All the absorbers do not show a structure constituting a phase separation although SC800 shows voids and cavities near the Mo back-contact.

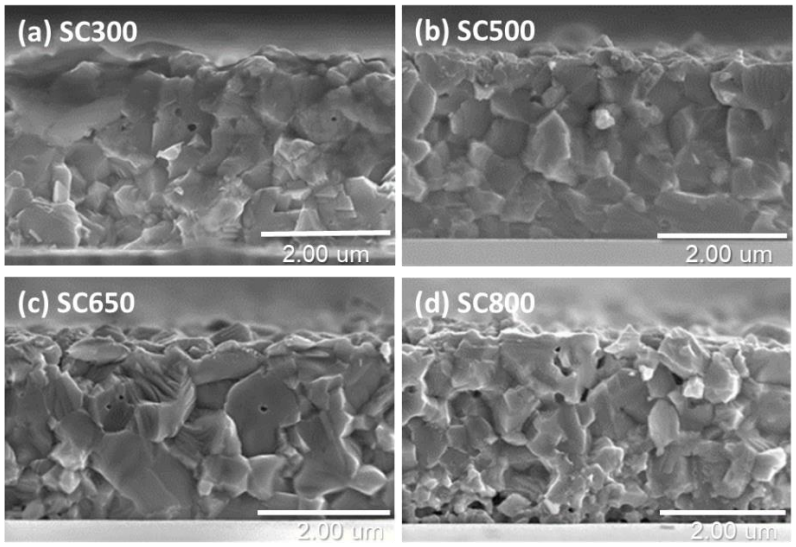

Figure 6.24: SEM micrographs showing the cross-sectional images of the Cu(In,Ga)S_2 absorbers deposited under different thermally cracked sulfur atmosphere of (a) 300 °C, (b) 500 °C, (c) 650 °C and (d) 800 °C named SC300 SC500 SC650 and SC800, respectively.

A comparison of SC300 and SC500 shows no clear difference in absorber morphology with sulfur cracker temperatures of 300 °C and 500°C. On the other hand, the morphology of SC650 show larger grain in comparison with all the other absorbers. The chemical compositions of the absorbers are detailed in Table 6.10. From the Table 6.10, EDX analyses show that there is no difference in the sulfur content of the absorbers, and the average CGI ratio of all the samples is identical within the values 0.94-0.95. However, the GGI ratio was not the same for all the absorbers, as the absorbers SC300 and SC500 have a similar GGI ratio of 0.13, while the GGI ratio slightly decreases to 0.12 and 0.11 in SC650 and SC800, respectively.

To explain these observations, Fig. 6.25a shows a diffractogram of the XRD analysis performed on SC500, SC650 and SC800, with a focus on only the vicinity of the (112) planes highlighting the dominant chalcopyrite phases occuring in the absorber. A (112)-plane is occurring at ~ 28° while the other is at ~ 28.3°. The higher angle corresponds to the region of maximum gallium content at the back of the absorber while the lower angle corresponds to region of minimum gallium at the front. The diffractogram has been normalized to the intensity of the low gallium peak at 28° to observe the behaviour of the high gallium peak. From the comparison of the intensity

of the peaks, it is immediately obvious that the peak at 28.3° drastically decreases from SC500 to SC800.

Table 6.10: The chemical compositions of the $Cu(In,Ga)S_2$ absorbers processed under different thermally cracked sulfur atmospheres.

Sample	Sulfur cracker temperature	Average CGI ratio @ 20 kV	Average GGI ratio @ 20 kV	S/([Cu]+[Ga]+[In]) @ 20 kV
SC300	300 °C	0.94	0.13	0.99
SC500	500 °C	0.95	0.13	1.00
SC650	650 °C	0.95	0.12	1.00
SC800	800 °C	0.94	0.11	0.99

The SIMS analysis of SC300 and SC650 showing the Ga profile is presented in Fig. 6.25b. It can be observed that, the intensity of the back-Ga in SC650 is strongly reduced in comparison to SC300 as the cracking temperature increases from 300 °C to 650 °C. The origin of this difference could be that the more reactive sulfur provided by the thermal cracker, increases the thermal motion of sulfur and as this molecule of sulfur is more reactive with indium, the formation of an indium-rich phase is favored. This might also explain the bigger grains observed in the SEM cross-section corresponding to SC650, since evidence from EDX and SIMS shows that this absorber has lower gallium content than SC300 and SC500. It has been shown in $Cu(In,Ga)(S,Se)_2$ that, the grains of absorber becomes smaller as Ga-content increases, particularly when the process is optimized for In-rich absorbers. The QFLS of the absorbers is evaluated by the ERE method. The optical bandgap is taken from the PL peak, and it is used to obtain the V_{OC}^{SQ}. The analyses show that, as the thermal cracker temperature is increased, the QFLS of the absorbers rapidly decreases. Taking the different bandgaps into account, evaluation of the V_{OC}^{SQ} deficit shows an increase of nonradiative loss from 306 meV to 390 meV as the cracker temperature increased from 300 °C to 800 °C. The cause of the increasing V_{OC}^{SQ} deficit cannot be attributed to poor crystal quality, but rather to the

lower back Ga-content in the absorber. The XRD diffractogram on the absorbers shown in Fig. 6.25a, can explain the origin of the increasing V_{OC}^{SQ} deficit with higher cracker temperature. The details of the optoelectronic properties and the device parameters are presented in Table 6.11 and Fig. 6.26. In Section 3.4, it has been explained that, among the advantages of the back gallium gradient is a reduced back surface recombination and additional driving force which reduces for photogenerated charge carriers towards the notch, leading to an increased photon flux [77]. The decreasing intensity of the high angle peak in Fig. 6.25a indicates a reduction in the back gallium, thus, there will be an increased back surface recombination and a lower number of electrons reaching the notch. Ultimately, this leads to QFLS loss as witnessed by the results in Table 6.11 and Fig. 6.26.

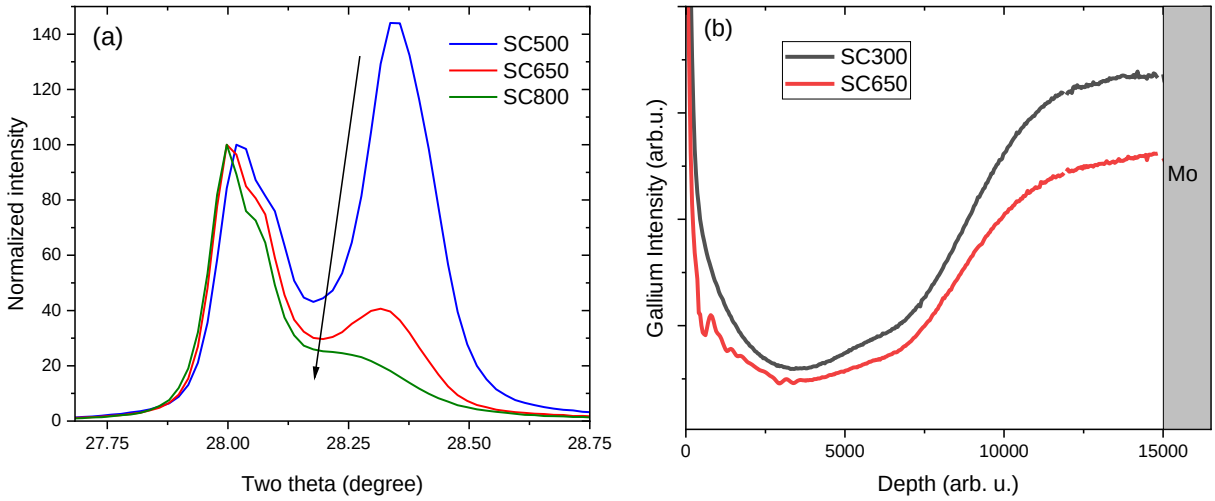

Figure 6.25: XRD diffractogram on absorbers deposited with sulfur thermal cracker of 500 °C, 650 °C and 800 °C (SC500, SC650 and SC800). (b) Ga profile for SC300 and SC650.

Devices were completed on the absorbers with CdS buffer layer, and the results are shown in Table 6.11 and Fig. 6.26. The device performance indicates an overall decrease in the J_{SC} and the V_{OC} as the temperature of the thermal cracker increases. Again, this is likely due an increasing recombination at the absorber-back contact interface as explained above. Although, the V_{OC} loss reduces as the thermal cracker temperature is increased, this is due to an already degrading QFLS rather than improved absorber or device. In general, the performance of the device worsens with higher thermal cracking temperature as shown by the FF and PCE in Table 6.11.

Table 6.11: QFLS values at 1 sun illumination on Cu(In,Ga)S_2 absorbers which have been processed with different sulfur thermal cracking temperatures. The device parameters on the corresponding solar cells completed with CdS buffer layer are also presented.

Sample	E_g^{PL} **(eV)**	**QFLS (meV)**	V_{OC}^{SQ} **deficit (meV)**	**V_{OC} (mV)**	**J_{SC} (mA/cm^2)**	**FF (%)**	**PCE (%)**
SC300	1.56	971	306	769	21.0	61	9.83
SC500	1.56	955	332	728	19.2	51	7.03
SC650	1.56	915	370	738	19.9	49	6.66
SC800	1.54	878	390	707	19.3	46	6.15

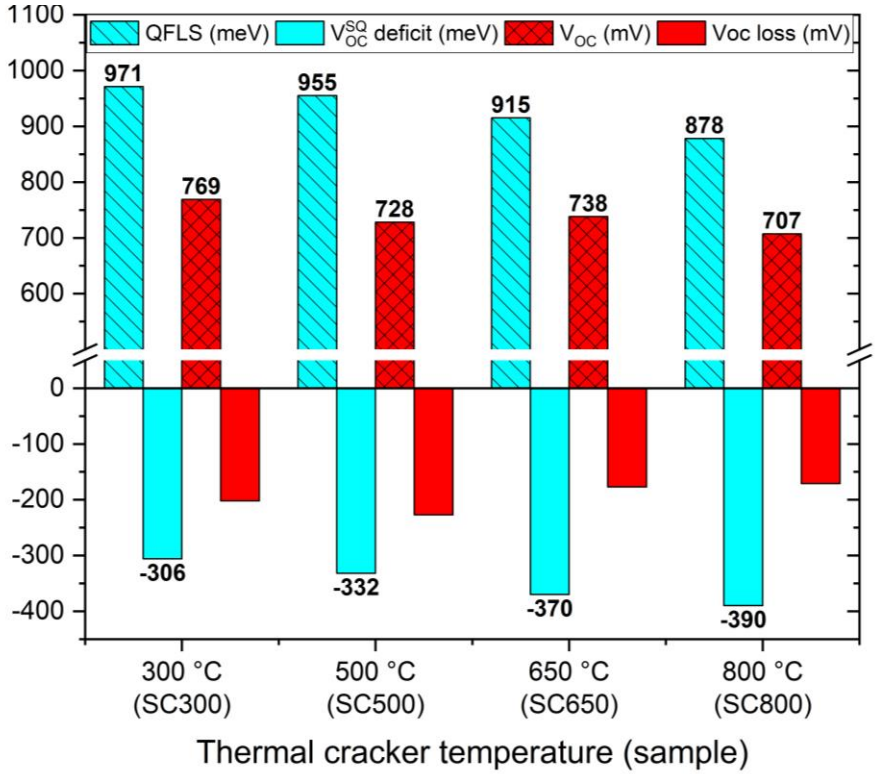

Figure 6.26: Bar charts showing the QFLS, V_{OC}^{SQ} deficit, V_{OC} and V_{OC} losses in the absorbers that have been processed with different sulfur thermal cracking temperatures.

In summary, this section has established that, the thermal cracking of sulfur is detrimental to the quality of Cu(In,Ga)S_2 absorbers and devices with the current deposition profile employed. The more reactive sulfur seems to favorably reacts with indium, and the loss of back-Ga is observed. A reduction of the back-Ga reduces the bandgap towards the absorber-Mo interface which will lead to higher back surface recombination. It is noteworthy that the thermal cracking of sulfur could actually be beneficial in reducing the too high back-Ga in Cu(In,Ga)S_2 absorbers, particularly in low temperature processes requiring low substrate temperature.

Since the best results were obtained when the thermal cracker is heated at 300 °C, it appears that the use of high thermal cracker temperature requires an optimized deposition process, which accommodates the thermodynamic changes and steps in such depositions. In this PVD, the lowest temperature at which the injector/thermal cracker and valve are designed to operate is 250 °C, this is to prevent condensation of sulfur in the quartz tube guiding the sulfur flow into the chamber. Because of these results from Section 6.4.1 which shows that high sulfur temperatures are unfavorable to the absorber quality, from here on, the sulfur thermal cracker is operated at a temperature of 250 °C.

6.4.2 Effect of first stage substrate temperature on Cu(In,Ga)S_2 absorbers and devices

The last section showed how the thermal cracking of the sulfur molecule can influence the gallium content in a Cu(In,Ga)S_2 absorber. This influence is seen by a reduction of Ga at the back of the absorber, however, the reduction of Ga increased back surface recombination. Still, temperature has been reported to enhance structural or optical properties of absorbers, be it one-stage deposition temperature or sulfurization temperature [232], and have been reported to influence the microstructural properties of absorbers and led to improved performance of Cu(In,Ga)Se_2 and Cu(In,Ga)S_2 devices [98, 114, 232, 233, 237, 238].

In this section, the influence of first stage substrate temperature during the growth of Cu (In,Ga)S_2 absorber layers will be investigated. Particularly, the influence of first stage substrate temperature

on the intermixing of In and Ga, Ga gradient profile, crystal structure and microstructure will first be examined. Subsequently, the optoelectronic attribute of the absorbers and device performance will be discussed.

The $Cu(In,Ga)S_2$ absorbers were processed under a Cu-deficient condition and with low Ga content with GGI ratio of 0.11-0.12 by the three-stage deposition method, all following identical steps to maintain similar composition and to reduce discrepancies caused by unintentionally induced variations. Three absorbers were investigated for the influence of the first stage substrate real temperature at 335 °C (SH1), 385 °C (SH2) and 435 °C (SH3); the corresponding set temperatures can be found in Appendix 2. Since only the influence of the first stage substrate temperature is of interest, the second and third stage temperatures were kept constant at actual substrate temperature of 590 °C. The sulfur-cracker temperature used was 250 °C and the chamber pressure maintained between $4.7\text{-}5.2\cdot10^{-5}$ mbar. As a reminder, at the third stage, Ga flux is particularly kept low to prevent the detrimental effect of high surface gallium (see Section 6.2). The cross-sectional SEM micrographs of the three absorbers, SH1, SH2 and SH3, deposited at the various first stage substrate temperatures are shown in Fig. 6.27. A primary assessment of the three images shows that the first stage substrate temperature has a visible influence on the microstructure of the absorbers especially when the temperature is varied over a hundred degrees. First to consider the cross-section of SH1 and SH2 in Fig. 6.27a and Fig. 6.27b respectively, there is no obvious phase segregation as observed for the absorbers BL1-BL4 in Fig. 6.21, rather the morphological structure of both absorbers features large and compact grains in micrometers range which extends from the top to the back contact of the absorbers. It is not necessary that the grain size is solely due to the growth temperature, since these are low gallium content with GGI ratio ~ 0.11-0.12, and as already seen in the preceding sections, it is not uncommon for low Ga $Cu(In,Ga)S_2$ absorbers to have larger grain size. Nevertheless, in Fig. 6.27c, SH3 which was grown at a higher first stage substrate temperature of 435 °C show a starkly different feature from SH1 and SH2. There are two distinct features; the top half is composed of large compact grains while the lower half extending to the Mo back contact is rather made up of smaller porous grains. Given that the sole discriminant of all three absorbers is the first stage substrate temperature, it is apparent that the distinct microstructure of SH3 is due to the deposition temperature.

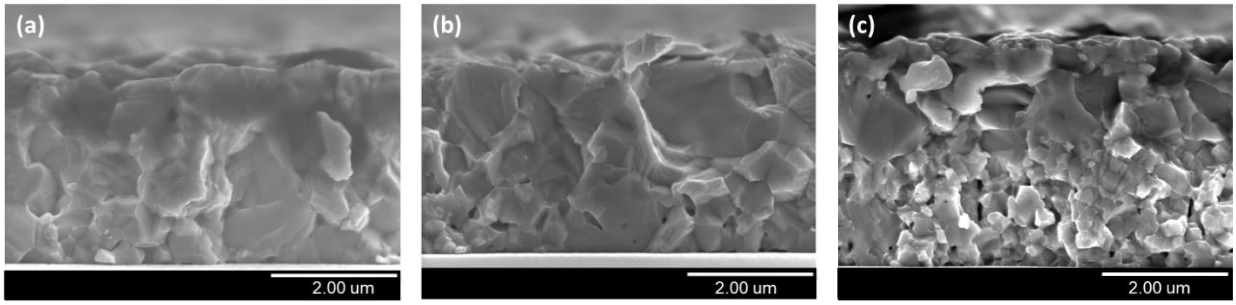

Figure 6.27: Cross-sectional SEM micrographs of $Cu(In,Ga)S_2$ absorber layers deposited by three-stage method at different first stage substrate temperature of (a) 335 °C (SH1), (b) 385 °C (SH2) and (c) 435 °C (SH3). The second and third stage substrate temperate was 590 °C.

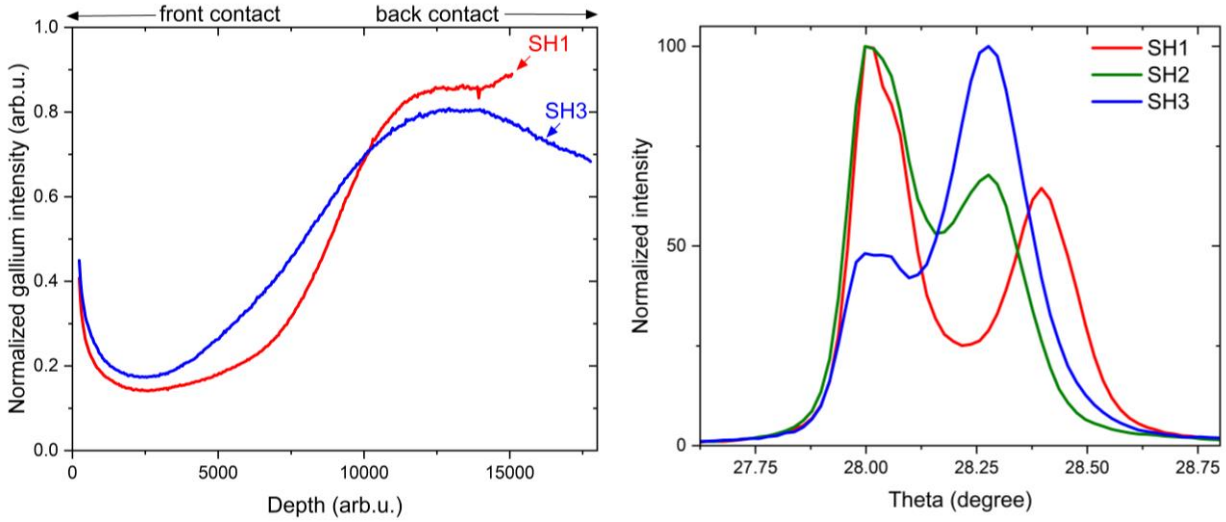

Figure 6.28: (a) Secondary ion mass spectrometry (SIMS) profile showing the normalized gallium profile of $Cu(In,Ga)S_2$ absorbers grown that first stage substrate temperature of 335 °C and 435 °C. (b) XRD diffraction angle around the main chalcopyrite peak for absorbers SH1-SH3 grown at various first stage deposition temperatures of 335 °C, 385 °C and 435 °C, respectively.

Insights into the different microstructure observed in the SEM cross-sections in Fig. 6.27, is gained by a crystallographic examination of the absorbers by XRD and Ga profile through SIMS depth analysis. The depth profile showing the Ga profile for SH1 and SH3 are presented in Fig. 6.28a, and the XRD diffractogram of the three absorbers showing the dominating phases occurring in the

absorbers are shown in Fig. 6.28b. The SIMS profile shows a steep gallium gradient between the front and the back of the absorber SH1 which was processed at the lowest first stage substrate temperature. It can also be observed that the Ga concentration remains flat at the back towards the Mo back-contact, while a wide notch is seen towards the front of the absorber. From the XRD analysis on SH1, the two participating peaks which are separated by ~ 0.4° indicates the prevalence of two different sub-layers with different Ga phases. The peak at the lower angle correspond to the phase with the minimum Ga concentration while that at the higher angle corresponds to the phase with the maximum Ga concentration [29, 227]. Although inhomogeneous, the proximity of the two peaks suggests that the two phases are more similar than in BL1-BL4. This is likely so since the absorbers were processed with low Ga content.

With the first stage substrate temperature at ~ 100 °C higher in SH3, the SIMS profile shows a less steep gallium gradient in comparison to SH1. The Ga profile in Fig. 6.28a indicates a gradually decreasing gallium concentration from the back into the bulk of the absorber. However, at the rear of the absorber towards the Mo back-contact, in Fig. 6.28a, there is a negative gradient of Ga towards the Mo back-contact indicating a decreased Ga concentration. This indicates the depletion of gallium towards to the back-contact. The influence and mitigation of such depletion will be discussed in the next section.

Although the SIMS Ga profile of SH2 is not available, the XRD diffractogram of SH2 in Fig. 6.28b might give an insight into the intermediate step occurring between SH1 and SH3. In Fig. 6.28b, the high angle peak shifts to a lower angle from SH1 to SH2, that is, when the first stage substrate temperature is increased from 335 °C to 385 °C. It could be assumed that the first stage substrate temperature of 385 °C enhanced the intermixing of gallium and indium, and back-Ga diffused from the back-contact further into the absorber bulk, therefore reducing the abruptness of the Ga gradient. As this intermixing and gallium diffusion occurs, so does the bandgap evenly reduce from the back towards the notch. Extending this phenomenon to SH3, it can be concluded that, increasing the first stage substrate temperature up to 435 °C improves the intermixing of Ga and In, which reduces the indium concentration at the front and drives more gallium into the bulk of the absorber. This is supported by the reduced intensity of the low angle peak and the increased intensity of the high angle peak of SH3 in Fig. 6.28b. The origin of the depleted Ga towards the

Mo back-contact in SH3 was not investigated, however, it can be considered that, the increased diffusion of gallium into the absorber-bulk with higher first stage substrate temperature seems to exhaust the absorber-back of gallium as observed in the SIMS Ga profile shown in Fig. 6.28a. Therefore, the reduction or loss of Ga towards the Mo back-contact at 435 °C has the effect of creating crevices and voids or pinholes at the back of the absorber SH3 as seen in Fig. 6.27c. We also consider that the first stage substrate temperature of 435 °C is high enough to cause a high diffusion of Na from the SLG substrate into the bulk of the absorber [82, 83]. As such, it could be that the high Na has an influence on Ga diffusion, and this could be a reason for the negative back-Ga gradient towards the Mo back-contact. The chemical compositions of SH1-SH3 extracted from EDX analysis and optical properties from photoluminescence measurements on the absorbers are presented in Table 6.12.

Table 6.12: The chemical compositions evaluated from EDX analyses, and the optical properties of the Cu(In,Ga)S_2 absorbers deposited at different first stage substrate temperatures.

Sample name	**First stage substrate temperature**	**Average CGI ratio**	**Average GGI ratio**	**Surface GGI ratio**	E_g^{PL} **(eV)**	**QFLS (meV)**	V_{OC}^{SQ} **deficit (meV)**
SH1	335 °C	0.95	0.11	0.19	1.55	963	318
SH2	385 °C	0.97	0.12	0.19	1.55	980	296
SH3	435 °C	0.95	0.11	0.20	1.53	920	345

From Table 6.12, the three absorbers are Cu-poor with average CGI ratios within 0.95-0.97, and with surface GGI ratios lying within 0.19-0.20. These are indications that the different first stage substrate temperatures have no drastic effect on the overall Cu-content and surface Ga. The average GGI ratio and the bandgap presented in Table 6.12, taken from the maximum of the PL peak, show a shift of the average PL maximum from 1.55 eV in SH1 and SH2 to ~ 1.53 eV in SH3. Fig. 6.29 which shows the band-edge energy map from CL emissions also supports the shift of PL emission to lower energy from SH1 to SH3. It should be noted that, due to the characteristic inhomogeneity present in the absorbers during growth as described in Appendix 3, it cannot be

categorically concluded that the change in bandgap is directly influenced by the first stage substrate temperature. This is because, although the SIMS Ga profile in Fig. 6.28a shows a redistribution of the gallium with the different first stage substrate temperatures, it is uncalibrated and the exact notch energy cannot be deduced from the SIMS measurement.

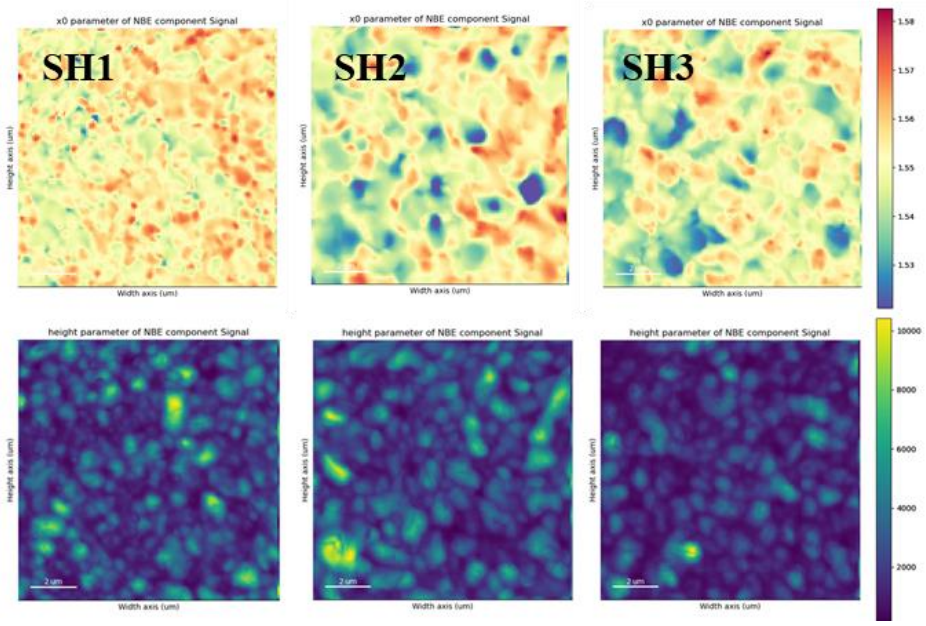

Figure 6.29: CL intensity map of the band-edge emissions of the first stage substrate temperature dependent absorbers SH1 (335 °C), SH2 (385 °C) and SH3 (485 °C).

The optoelectronic quality of the absorbers are summarized in Table 6.12, and the QFLS and the V_{OC}^{SQ} deficit are plotted in Fig. 6.30a. The results show that there is an improvement of QFLS by 34 meV as the first stage substrate temperature is increased from 335 °C (SH1) to 385 °C (SH2). However, ~ 40 meV is lost when the first stage substrate temperature is further increased to 435 °C (SH3). This is supported by comparing the nonradiative losses in the absorbers in Fig. 6.30a, which shows that SH2 had the least V_{OC}^{SQ} deficit among the three absorbers. It can be concluded from these values that, although the QFLS is improved by increasing the first stage substrate temperature from 335 °C to 385 °C, the QFLS gained at 385 °C is lost at 485 °C. The influence of the first stage substrate temperature on the optoelectronic quality of the absorber is substantiated by the transient PL measurement shown in Fig. 6.30b. The decay curve of SH2 has a slightly longer decay time than SH1, whereas the decay time of SH3 significantly reduces in comparison to SH1

and SH2. The faster decay time in SH3 indicates a higher non-radiative recombination in comparison to SH1 and SH2.

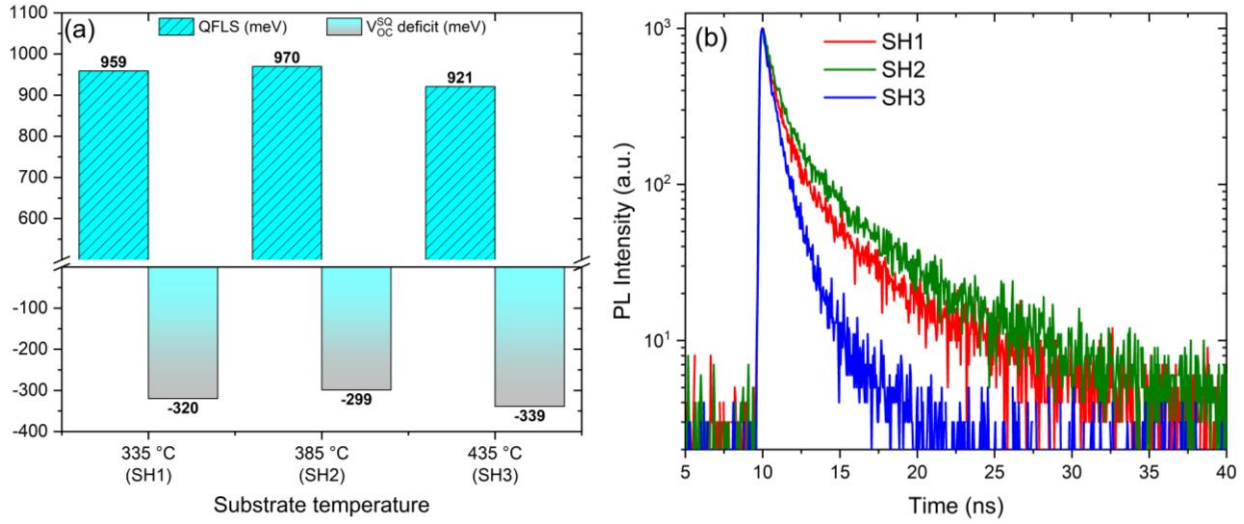

Figure 6.30: (a) QFLS and V_{OC}^{SQ} deficit of the Cu(In,Ga)S_2 absorbers deposited at different substrate temperatures at the first stage (SH1-SH3). (b) Photoluminescence decay of the absorbers SH1-SH3.

The low temperature PL spectra of the absorbers SH1-SH3 at 10 K are shown in Fig. 6.31. The spectrum is dominated by a near-band edge transition at approximately 1.48 eV [144], while a deeper broadband transition exists on the low energy end between 1.1-1.3 eV. The spectrum belonging to SH3 is slightly shifted to a lower energy in reference to both SH1 and SH2, since it has a lower bandgap in comparison to both absorbers, see Table 6.12 for details. In Fig. 6.31b are the PL spectra on the logarithmic scale, it is noticeable that the broad defect is more intense in SH3. For all the absorbers, the shape of the spectra are identical to the low temperature PL spectra of the Cu-poor Cu(In,Ga)S_2 absorbers C3 and C4 with CGI ratio of 0.95 and 0.93 respectively, in Fig. 6.6. This is in fact due to the Cu deficiency of the three absorbers, as already discussed in Section 6.1 and Ref [110]. It was shown that deep Cu-related defects at 1.3 eV and 1.1 eV are effectively suppressed with low Cu content (Fig. 6.6). Hence, since the chemical composition of the absorbers SH1-SH3 are identical, the broad defects cannot be attributed to the compositions of the absorbers, but tentatively to the effect of the deposition temperature.

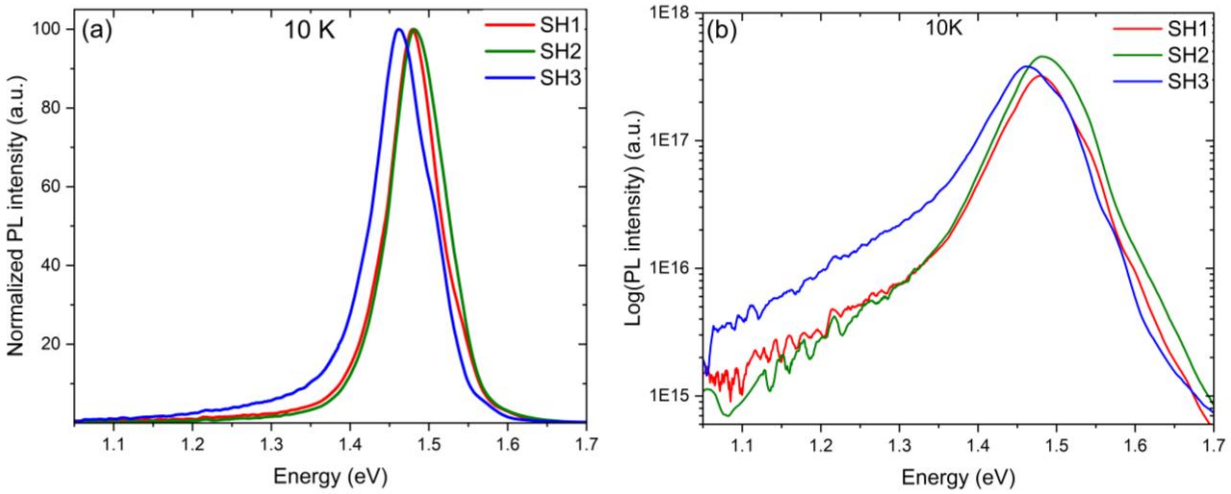

Figure 6.31: (a) Normalized PL spectra at low temperature (10 K) (b) and in logarithmic scale of the Cu(In,Ga)S_2 absorbers grown on different first stage substrate temperatures (SH1-SH3).

A clearer picture correlating the low temperature PL spectra and the optoelectronic quality of these Cu(In,Ga)S_2 absorbers, SH1-SH3, is seen in the PL spectra at 100 K, presented in Fig. 6.32a-c. Before discussing the likely influence of the deposition temperature on the spectra, the peaks in view are described. The four notable peaks have been highlighted as follows; the highest energy peak Q0, at 1.55 eV for SH1 and SH2 and 1.54 eV for SH3, is related to the band-band luminescence in consideration of the optical bandgaps reported in Table 6.12. Q0 is the most intense in SH2 and is of lower intensity in SH1 and SH3, as seen in Fig. 6.32b. The peak Q1 which dominates the spectrum of SH1 and relatively less intense in SH2 and SH3 (Fig. 6.32a) at ~ 1.48 eV is likely a near-band edge transition as reported in defect analyses of $CuIn_{1-x},Ga_xS_2$ [65, 74, 144, 145, 190]. The deep band on the low energy end of the spectra can be ascribed to two deep transitions, Q2 at ~ 1.3 eV and Q3 ~ 1.1 eV, due to its broadness and energy position. The defect band Q2 is the most intense for SH3, see Fig. 6.32c. The cathodoluminescence (CL) hyperspectral mapping of defect-related emission in SH1-SH3 are also presented in Fig. 6.32d-f.

The two main transitions in the CL spectra are near-band-related emission (NBE) at 1.54-1.56 eV and defect-related emission (DDE) at 1.3 eV, thus, the CL hyperspectral maps presented in Fig. 6.32d-f is the ratio of the normalized intensity of NBE to the normalized intensity of DDE.

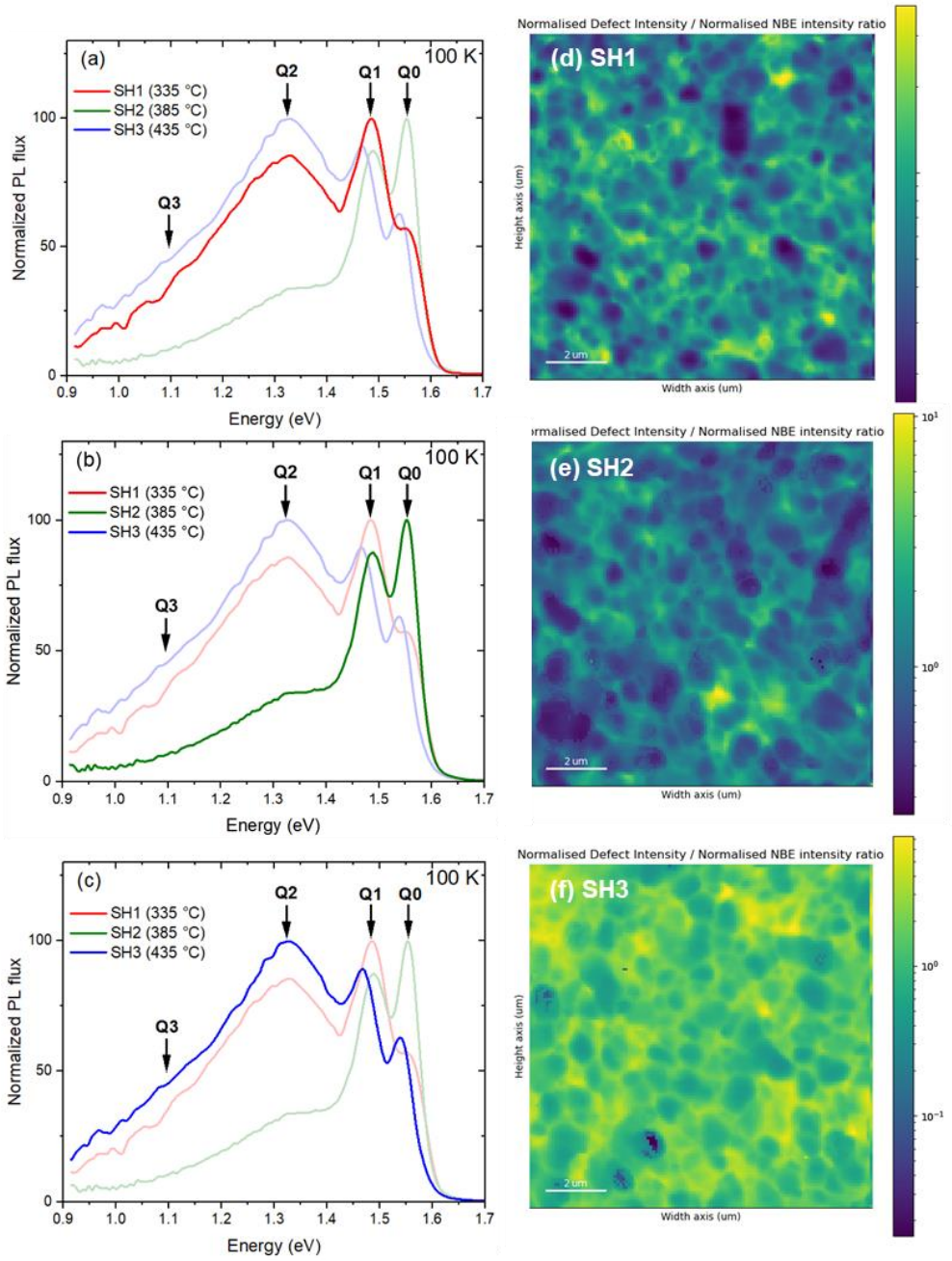

Figure 6.32: Low temperature photoluminescence spectra at 100K of Cu(In,Ga)S_2 absorbers processed at different first stage substrate temperatures of (a) 335 °C, SH1 (b) 385 °C, SH2 and (c) 435 °C, SH3. (d)-(f) Cathodoluminescence (CL) mapping of defect emission at 1.3 eV on the Cu(In,Ga)S_2 absorbers (SH1-SH3) deposited at different first stage substrate temperatures. The CL hyperspectral image shown is the ratio of normalized defect density against normalized near-band edge emission.

Correlating the first stage substrate temperature with PL spectra of SH1-SH3 at 100K, the increment of the temperature from 335 °C in SH1 to 385 °C in SH2, lowers the intensity of the broad deep band Q2, Fig. 6.32b. This is indicative of a reduced concentration of deep defects contributing to unwanted recombination paths in the absorber. The CL hyperspectral map also supports the observed phenomenon as seen in the comparison of the luminescence features of the microstructures in Fig. 6.32d and 6.32e. It is noticed that the spots of DDE are present in both SH1 and SH2, Fig. 6.32d and 6.32e, as also seen in the PL spectrum of both absorbers, however, in Fig. 6.32b for SH2 where the first stage substrate temperature is higher, the intensity of DDE reduces with the weakening intensity of Q2 in Fig. 6.32b. The low intensity of DDE corresponds with the reduced nonradiative loss, in other words, the reduction of V_{OC}^{SQ} deficit in SH2 to 299 meV, as presented in Table 6.12 and Fig. 6.32. Remarkably, the trends reverse in SH3 where the first stage substrate temperature is further increased to 435 °C as the broad band Q2 becomes the most intense peak in Fig. 6.32c and in the corresponding CL map showing the intensity of the DDE in Fig. 6.32f. There is a simultaneous loss of QFLS as the V_{OC}^{SQ} deficit in SH3 increases to 339 meV. With these observations, since Q0 and Q1 are emissions related to the band-edges, it is clear that the broad band emission at Q2 influences the optoelectronic quality of the absorber. Although the likely origin of these defect peaks and how they influence the quality of the absorbers requires more studies, Q3 does not seem to be strongly affected by the first stage substrate temperature, since the spectra in Fig. 6.32 shows that the dominant defect impacting nonradiative loss is Q2. Additionally, the defect Q3 is likely related to the defect D1 in Section 6.1 and Ref [110], which is shown to be related to the Cu content in Cu(In,Ga)S_2 absorber, and given the identical composition of SH1-SH3, it is assumed Q3 is not strongly influenced by the first stage substrate temperature.

To examine if QFLS is translated to V_{OC}, and to inspect how first stage substrate temperature affects the performance of the solar cell devices on the absorbers SH1-SH3, the devices are completed with CdS buffer layer deposited by chemical bath deposition and sputtered with i-ZnO and Al:ZnO window layer, then completed with Ni/Al contact grids. The I-V characteristics at AM 1.5 illumination and EQE curves of the devices are reported in Fig. 6.33a and 6.33b respectively, and the overall performance of the absorbers and devices is graphically summarized in Fig. 6.34.

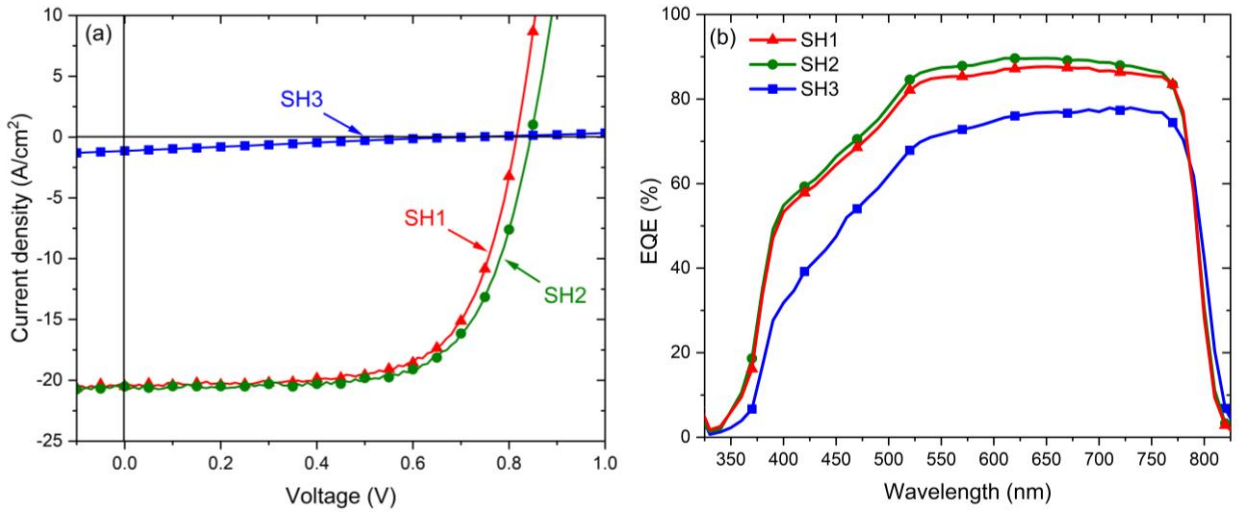

Figure. 6.33 (a) I-V curves of devices prepared on Cu(In,Ga)S_2 absorbers SH1-SH3 at different first stage substrate temperatures (b) The corresponding EQE curves of the same devices.

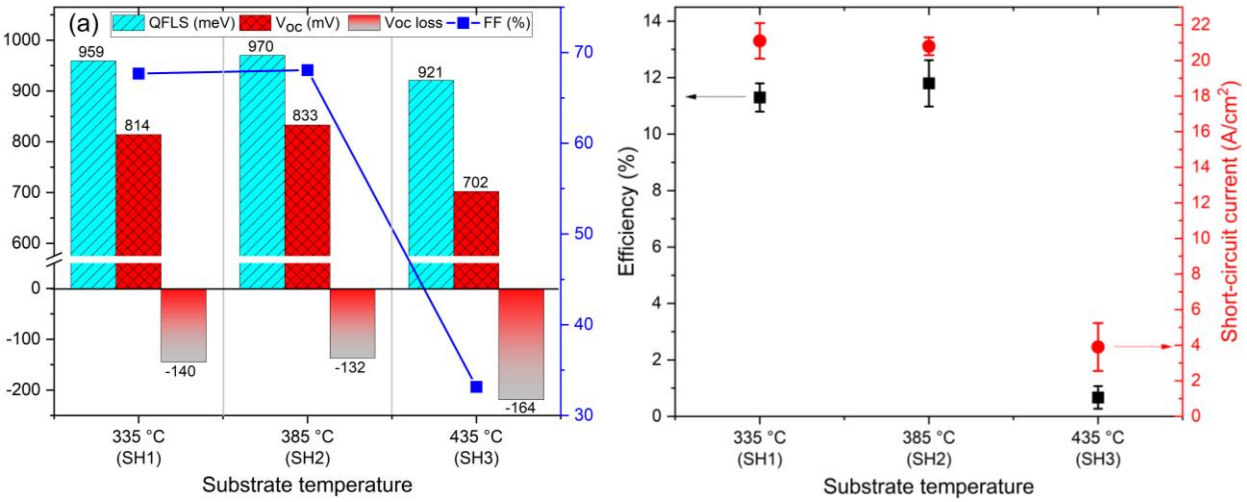

Figure 6.34: Graphical summary of the optoelectronic quality and device performance in dependence of first stage substrate temperature showing (a) the QFLS, open-circuit voltage and fill factor, (b) efficiency and short-circuit current of the devices completed on the absorbers.

The V_{OC} of 814 mV and 833 mV were recorded for devices on SH1 and SH2, respectively. Fig. 6.34a shows that there is a good translation of QFLS to V_{OC}, and the device performance is

comparable to the performance the lab's previous champion $Cu(In,Ga)S_2$ solar cell with CdS buffer layer [110]. Although both devices possess similar J_{SC}, SH2 exhibits a higher overall performance with a PCE of 11.8 % compared to 11.3 % for SH1, due to a better V_{OC} and FF as seen in Fig. 6.34a and Fig. 6.34b respectively. This indicates that the enhanced crystallinity and better gradient achieved with a first stage substrate temperature of 385 °C, also contributes to an improved performance of the device. In contrast to SH1 and SH2, a relatively lower QFLS is translated to V_{OC} for SH3 (Fig. 6.34a), the device performance is rather dissatisfactory with exhibition of strong shunting features shown in the I-V curve in Fig. 6.33a. It is obvious from the SEM cross-section micrograph of SH3 in Fig. 6.27c, that the cause of the shunting behaviour involves the microstructure of the absorber, where the lower layer at the Mo back contact is full of voids and pinholes creating shunting paths in the device processed on the absorber deposited at 435 °C (SH3).

To recapitulate the results and observations of this section, it is obvious that the first stage substrate temperature plays a substantial role in the quality of $Cu(In,Ga)S_2$ absorbers. To discuss SH1 and SH2 first, the fact that the absorber deposited at 335 °C (SH1) had good optoelectronic qualities which resulted in device performance comparable to the lab's previous champion solar cells deposited at 260 °C [90, 110], indicates that higher first stage substrate temperature is favourable for $Cu(In,Ga)S_2$. However, even with low Ga content at 335 °C, phase segregation was still present in SH1 (Fig. 6.28). The first stage substrate temperature of 385 °C is clearly more advantageous in reducing the phase segregation than 335 °C, which improves the quality of the absorber and device. A reason for the improvements at higher temperatures requires revisiting the likely origin of the phase segregation from the Cu_2S-In_2S_3-Ga_2S_3 pseudo-ternary phase diagram reported by Thomere et al. [31]. It was shown that there exist two immiscible Cu-deficient phases, namely trigonal and cubic phases. When growing $Cu(In,Ga)S_2$ absorbers by the three-stage deposition method, during the second stage of deposition when Cu is introduced to the $(In,Ga)_2S_3$ precursor for the formation of the chalcopyrite phase, the growing absorber has to go through the immiscible Cu-poor phases. It is necessary to state that the aforementioned pseudo-ternary phase diagram was studied at room temperature, and the temperature dependence of the phases are not clear. It is likely that at higher temperature the trigonal and cubic phases do not form, or that high temperature is not favorable for the phases and their immiscibility at room temperature is not critical at high

temperature. As such, with higher first stage substrate temperature, as demonstrated by the results above, there is less phase segregation in Cu(In,Ga)S_2.

However, a lingering question is; why is the absorber deposited at 435 °C bad, although phase segregation was diminished and a good Ga-gradient was achieved in this absorber? An inkling of the problem can be found by revisiting the SIMS Ga profile of SH3, shown again in Fig. 6.35. The Ga-profile of SH3 shows that there is a trade-off between an improved Ga-gradient and the depletion of back-Ga, demonstrated by the negative Ga gradient towards the Mo back-contact. The Ga-depletion resulted in increased back recombination and poor performance of the absorber.

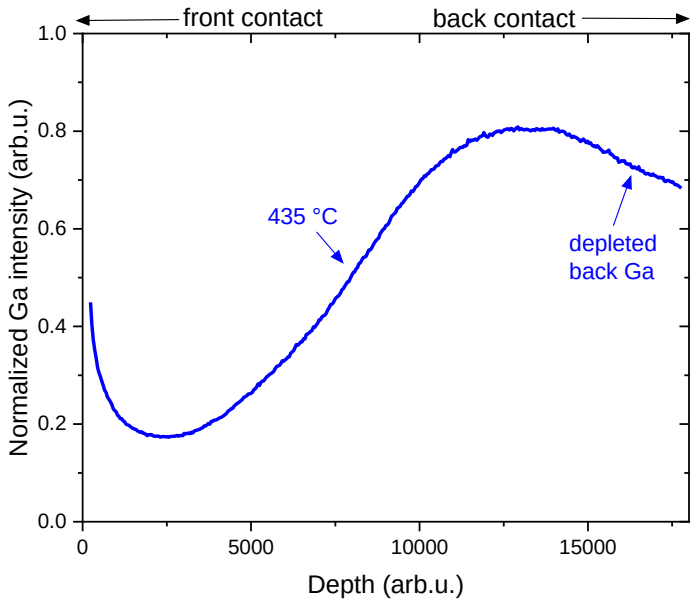

Figure 6.35: SIMS profile showing the Ga profile in Cu(In,Ga)S_2 absorbers (SH3) grown at first stage substrate temperature of 435 °C.

The cause of the back-Ga depletion in SH3 was not investigated in this thesis; however, we speculate on the influence of Na diffusion from the SLG. Although the influence of Na is also not within the scope of this thesis, nevertheless, preliminary studies (in unpublished data) of in-situ sodium treatment on Cu(In,Ga)S_2 absorbers deposited on SLG showed that, the deposition of NaF at high temperatures has a detrimental effect on the optoelectronic quality of the absorber. Hence, it is necessary to consider that, maybe the first stage substrate temperature of 435 °C is high enough to introduce too much Na into the absorber during growth, which depletes the back Ga. Also, there

is a possibility that, as more Ga moves into the bulk of the absorber with higher substrate temperature, the back-Ga, if low, is readily depleted. Nonetheless, the depleted back-Ga results in poor optoelectronic quality. Further analyses would be needed to understand the exact cause of the back-Ga depletion.

To take advantage of the reduced phase segregation and improved Ga gradient in the absorber deposited at the first stage substrate temperature of 435 °C, the next section will try to counter the back Ga depletion by controlling Ga flux during the first stage deposition. This is encouraged by the fact that although the Ga distribution in an absorber cannot be perfectly controlled, however it is possible to manipulate Ga flux during deposition. In the next section, Ga flux will be manipulated to replenish Ga loss at the back of the absorber.

6.4.3 Mitigation of the negative Ga-gradient (back-Ga depletion) in $Cu(In,Ga)S_2$ absorbers

Two $Cu(In,Ga)S_2$ absorbers, GSH2 and GSH3, were processed using the same deposition steps for SH2 and SH3 respectively, specifically using the same first stage substrate temperature of 385 °C and 435 °C. However, during the first stage deposition, the Ga flux was increased in comparison to the first stage Ga flux for SH2 and SH3. This higher Ga flux is to supply enough Ga to replenish the depleted back Ga layer during the gallium migration into the bulk of the absorber. Essentially, the higher Ga flux during the first stage of deposition is to compensate for the negative Ga-gradient or Ga depletion observed in the SIMS Ga profile of SH3 in Fig. 6.35.

Analyses of the chemical composition on the absorbers show that, due to the increased Ga flux at the first stage, the average GGI ratio increases from 0.11 (SH2) to 0.13 for GSH2, and increases from 0.12 (SH3) to 0.14 for GSH3, while the average CGI ratio remains 0.96 for both absorbers. Next, the microstructure of GSH2 and GSH3 are presented in Fig. 6.36 to inspect the effect of the higher Ga flux at the first stage of absorber growth. For a good comparison, the SEM cross-sectional view of GSH2 and GSH3 are presented alongside SH2 and SH3. Starting with the

absorbers grown that 435 °C, GSH3 and SH3 in Fig. 6.36a, where the effect of back-Ga depletion is already seen for SH3. Note that SH3 has already been discussed in the previous section.

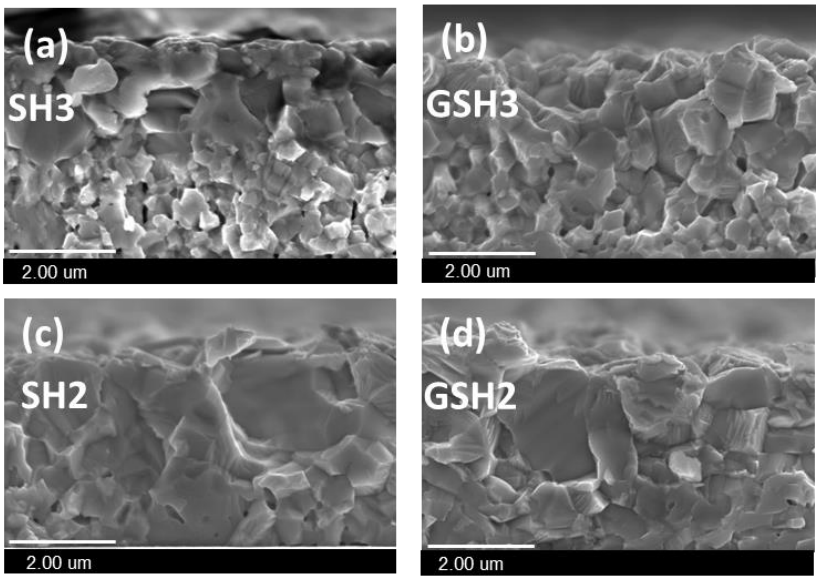

Figure 6.36: (a)-(d) SEM cross-sectional images of Cu(In,Ga)S_2 absorbers deposited at first stage substrate temperatures of 435 °C (SH3, GSH3) and 385 °C (SH2, GSH2). GSH2 and GSH3 have the same deposition steps as SH2 and SH3 respectively, however, GSH2 and GSH3 were deposited with higher Ga flux during the first stage of deposition.

In Fig. 6.36b showing the microstructure of GSH3, it is noticeable that the concentration of voids and pinholes at the bottom half of the absorber has been significantly reduced in comparison with SH3 in Fig. 6.36a. It should be mentioned that the smaller grain size close to the Mo back-contact in GSH3 is not due to phase segregation, but because of the higher back gallium than in the front of the absorber. For the Cu(In,Ga)S2 absorber deposited at 385 °C, the slight increase of Ga flux in GSH2 (Fig. 6.36d) did not seem to change its microstructure substantially in comparison to SH2 (Fig. 6.36c).

The influence of the higher Ga flux in GSH2 and GSH3 on defect emission is also investigated by low-temperature photoluminescence measurement and cathodoluminescence imaging. The PL spectra of GSH3 and GSH2 at 100 K are presented in Fig. 6.37a and 6.37b respectively with SH3 and SH2 for comparison.

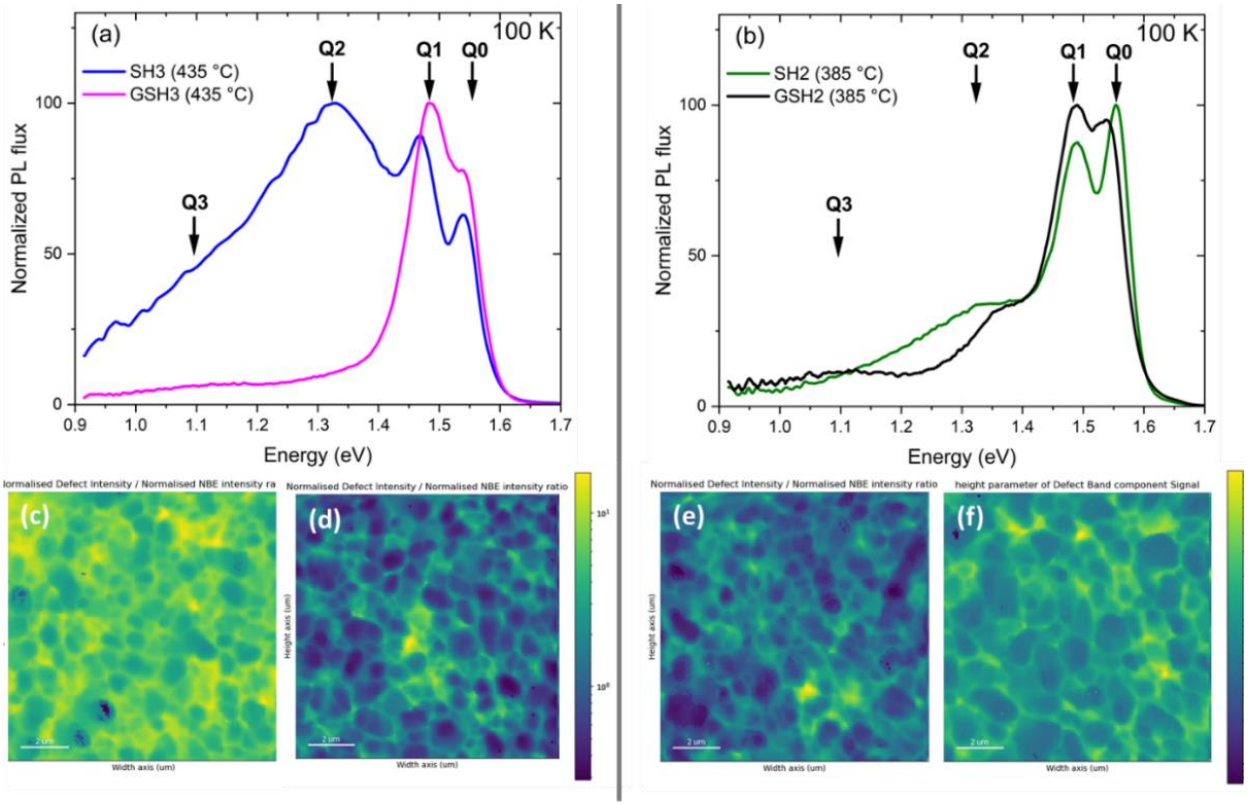

Figure 6.37: Low temperature photoluminescence spectra at 100 K of Cu(In,Ga)S_2 absorbers processed at first stage substrate temperatures of (a) 435 °C (SH3 and GSH3) and (b) 385 °C (SH2 and GSH2). Cathodoluminescence hyperspectral map of defect emission at 1.3 eV for (c) SH3, (d) GSH3, (e) SH2 and (f) GSH2. GSH2 and GSH3 were deposited with higher Ga flux at the first stage of deposition.

Remarkably, there is a significant influence of higher first stage gallium flux on the PL spectra of GSH3. In Fig. 6.37a showing the spectrum of GSH3 with the spectrum of SH3 for comparison, the intensity of the broad band peak labeled Q2 is considerably reduced for GSH3, to the extent that the main transitions dominating the spectra are the near-band-edge transitions Q0 and Q1. This indicates the suppression of the defect emission Q2 which dominates the PL spectrum of SH3. On the other hand, for GSH2 in Fig. 6.37b, there was no drastic change other than the Q2 peak which slightly changes with the energy position shifting from 1.3 eV to 1.35 eV. The transition at Q1 now marginally dominates the spectrum of GSH2 instead of Q0 which dominated the spectrum of SH2. The observation in the low temperature PL spectrum of GSH3 is well correlated with its CL hyperspectral map in Fig. 6.37d. In contrast to the CL defect map of SH3 in Fig. 6.37c, it is

evident that in GSH3, the intensity of the defect emission (DDE) has been suppressed and contained to fewer spots. The reduced intensity of DDE emission seems related to the suppression of the Q2 band in the 100 K PL spectrum of GSH3 in Fig. 6.37a. From the PL spectrum of GSH2 in 6.37f, the defect emission seems more intense across the absorber than in SH2 as seen in Fig. 6.37e, although this cannot be linked to only the suppression of the Q2 peak.

Table 6.13: QFLS of the absorbers SH2, SH3, GSH2 and GSH3, and the device parameters of the corresponding solar cells completed the absorbers with CdS buffer layer.

Sample	**QFLS (meV)**	**V_{OC}^{SQ} deficit (meV)**	**V_{OC} (mV)**	**Voc loss (mV)**	**FF (%)**	**PCE (%)**	**J_{SC} (mA/cm^2)**
435 °C (SH3)	921	339	730	191	33.15	0.7	3.9
435 °C + Ga (GSH3)	984	288	837	147	50	8.7	19.7
385 °C (SH2)	970	299	833	137	68.07	11.8	20.8
385 °C + Ga (GSH2)	960	303	836	124	67.48	10.8	20.3

Results of the analyses of the optoelectronic quality and device performance on the absorbers SH2, SH3, GSH2 and GSH3 are presented in Table 6.13. The QFLS and V_{OC} of GSH3 have also been plotted with SH1, SH2 and SH3 in Fig. 6.38 for comparison. Relative to SH2, the QFLS of GSH2 slightly reduces by 10 meV, whereas there was a significant gain of 60 meV for GSH3 from SH3. Since the absorbers have different bandgaps which can influence QFLS, the V_{OC}^{SQ} deficit is used as a figure of merit to ensure that the improved QFLS in GSH3 is not just due to the higher Ga content. From Table 6.13, the V_{OC}^{SQ} deficit between GSH2 and SH2 remains the same, indicating that there is no change in non-radiative loss with higher Ga flux for the absorber deposited at 385 °C. Alternatively, from Table 6.13 and Fig. 6.38, it can be observed that, there is a reduced non-

radiative loss by ~ 50 meV for GSH3, since the V_{OC}^{SQ} deficit reduced from 339 meV in SH3 to 288 meV in GSH3.

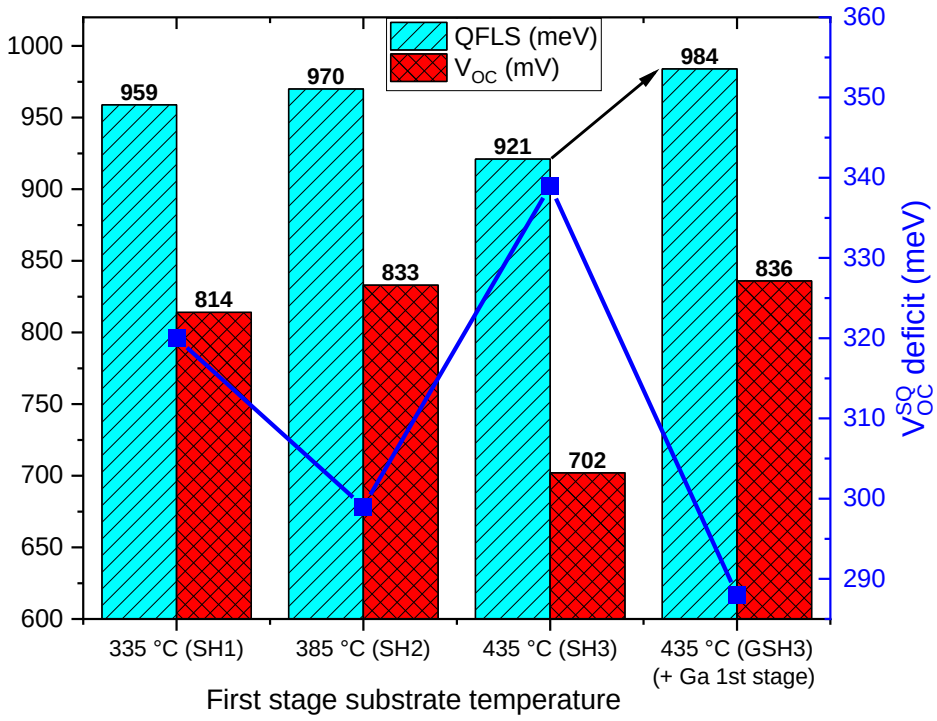

Figure 6.38: Comparison of QFLS, V_{OC} and V_{OC}^{SQ} deficit of SH1, SH2, SH3 and GSH3. Cu(In,Ga)S_2 absorbers prepared at different first stage substrate temperatures of 335 °C, 385 °C and 435 °C. GSH3 was processed with higher Ga flux at the first stage of deposition.

The improved QFLS and lower V_{OC}^{SQ} deficit in GSH3 can be associated with the subdued Q2 defect in its low temperature PL spectrum as seen in Fig. 6.37a, similar to the suppressed DDE in the CL emission shown in 6.37d. This is because such bulk defect acts as unwanted recombination channel which captures photogenerated carriers, thereby reducing the QFLS. The photoluminescence decay measured on SH2, SH3, GSH2 and GSH3 are presented in Fig. 6.39. Evidently from Fig. 6.39a, GSH3 has a longer decay time in comparison with SH3, demonstrating a longer minority carrier lifetime for GSH3. This can be attributed to a reduced non-radiative recombination by the suppression of the bulk defect (Q2) in parallel with the higher QFLS. Overall, the V_{OC}^{SQ} deficit and

PL decay are indications of improved quality of absorber the GSH3. On the other hand, an evaluation of the transient PL measured on GSH2 and SH2 show that both absorbers possess similar PL decay times. This means that the increased first stage Ga flux for GSH2 did not improve the quality of the absorber.

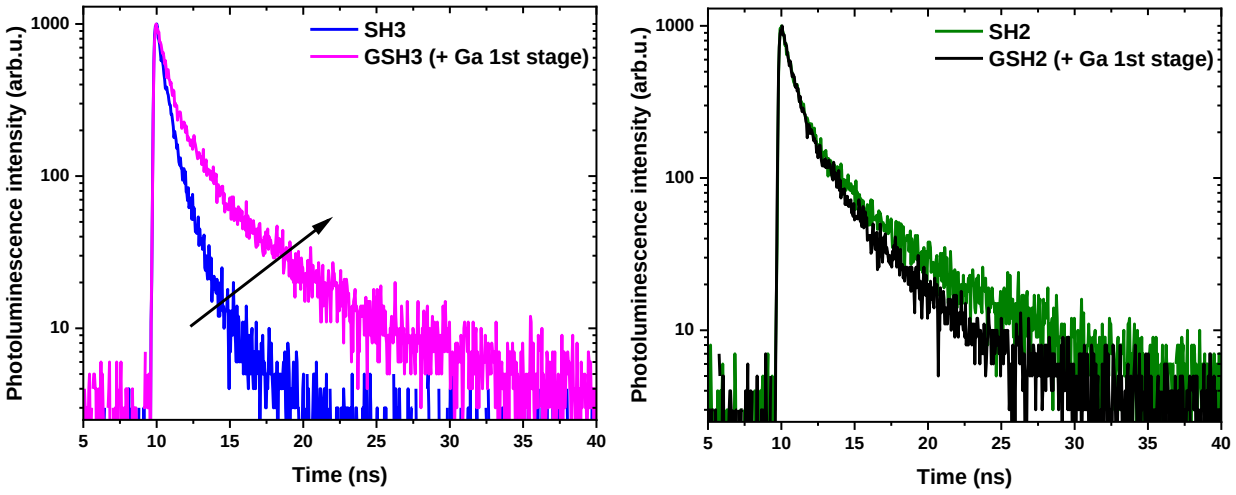

Figure 6.39: Photoluminescence decay curves of the Cu(In,Ga)S_2 absorbers grown at (a) 435 °C and (b) 385 °C in the first stage of deposition. GSH3 and GSH2 are distinguished by a slightly higher gallium content than SH3 and SH2.

Finally, the I-V characteristics and EQE curves showing the performance of the devices on SH2, SH3, GSH2 and GSH3 are presented in Fig. 6.40, and the details of device output performance are summarized in Table 6.13. An overall enhanced performance is recorded for GSH3 in comparison to SH3, in consistency with the better quality of the absorber as attested by the QFLS value. The device on GSH3 produces a higher V_{OC} with a better translation of QFLS to V_{OC} as indicated by the reduced V_{OC} loss from 191 mV in SH3 to 147 mV in GSH3. A better J_{SC} of 19.7 mA/cm^2 is also recorded for GSH2 as opposed to 3.9 mA/cm^2 in SH3, see Fig 6.40a. This superior device performance of GSH3 in comparison to SH3 is also corroborated by the EQE curve which demonstrates an increased and uniform response as shown in Fig. 6.40c. Although, the I-V curve of GSH3 still has some signature of series resistance which leads to a FF of 50 %, the higher J_{SC} and V_{OC} of GSH3 contribute to a PCE of 8.7 %, which is a substantial increase from 0.7 % in SH3.

The device performance for GSH2 in comparison with SH2 is quite similar as the devices possess the same V_{OC} and similar EQE response as seen in Fig. 6.40b and Fig. 6.40d respectively.

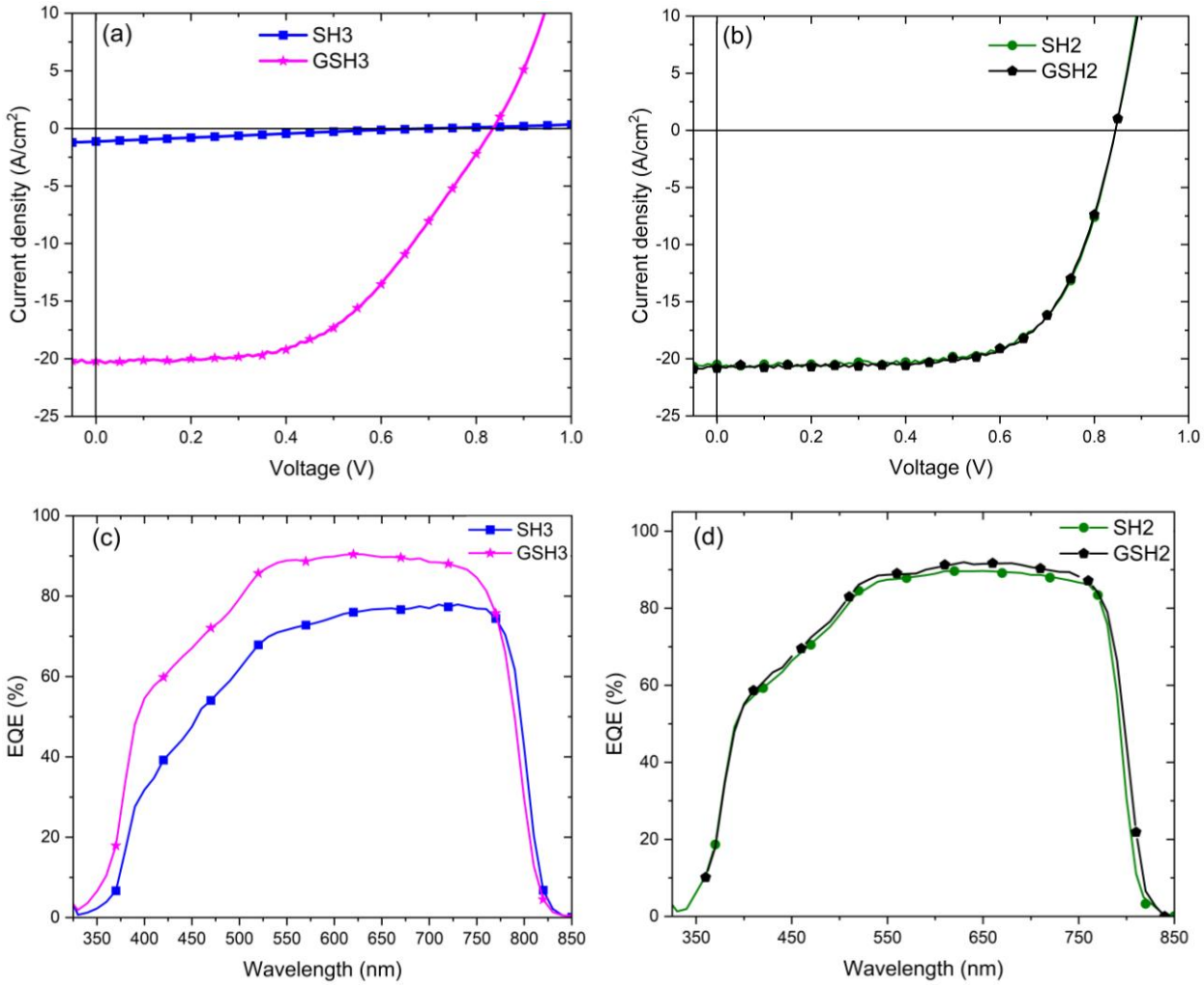

Figure 6.40: (a)-(b) EQE curves and (c)-(d) I-V curves of solar cell devices fabricated on Cu(In,Ga)S_2 absorbers process at first stage substrate temperatures of 385 °C (SH2, GSH2) and 435 °C (SH3, GSH3). GSH2 and GSH3 were processed with higher first stage Ga flux.

The previous Section 6.4.2 and this Section 6.4.3 have established how the first stage substrate temperature influences phase segregation and gallium gradient in Cu(In,Ga)S_2 absorbers. In Section 6.4.2, it was seen that phase segregation is mitigated by utilizing higher first stage substrate temperatures. For the three different temperatures that were investigated, the absorber grown at

the first stage substrate temperature of 385 °C had the best performance. Also, the suppression of a defect peak was observed at this temperature, which seems to have contributed to the improved QFLS. At 435 °C, it was evident from XRD that a more homogenous phase is achieved in the absorber, and SIMS analysis showed that a better gallium gradient is achieved. However, there was a trade-off between an improved Ga gradient and a depleted back-Ga which increases back recombination in the absorber. Eventually, the absorber and device have poor performance. This Section 6.4.3 showed that, it is possible to replenish depleted back-Ga in the absorber grown at the first stage substrate temperature of 435 °C, which recovers and even enhances the optoelectronic quality of the absorber and V_{OC} of the device. SIMS profile in Section 6.3.5 will show that increasing the Ga flux when absorbers are deposited at first stage substrate temperatures of 435 °C passivates the depletion of back gallium layer. Still, the device on absorber grown at the first stage substrate temperature of 435 °C and higher Ga flux has a low FF in comparison to those grown at 385 °C; this is likely due to high series resistance. For the absorber deposited at the first stage temperature of 385 °C, increasing the Ga flux at the first stage did not improve the quality of the absorber. So, while higher first stage substrate temperature mitigates phase segregation and improves Ga gradient, a higher Ga flux is equally necessary when the first stage substrate temperature is very high to mitigate back-Ga depletion.

6.4.4 Effect of heat ramping of the substrate temperature on Cu(In,Ga)S_2 thin films

Considering the trade-off between back-Ga depletion and improved Ga-gradient in absorbers deposited at first stage temperature of 435 °C, this section will explore the possibility of improving the gallium gradient of the Cu(In,Ga)S_2 absorbers at the first stage substrate temperature of 385 °C, by varying the heat ramping rate of the substrate heater. This is to avert the back-Ga depletion at 435 °C and to take advantage of the uniform homogeneity of the absorbers even with higher gallium content (see Fig. 6.36b). Essentially, the influence of heating ramp rate of the substrate heater from the first to the second stage deposition temperature on Cu(In,Ga)S_2 absorbers will be investigated in this section.

The deposition of the Cu-poor Cu(In,Ga)S_2 absorbers studied in this section follows the familiar three-stage deposition process used in the previous sections. The first stage substrate temperature was 385 °C while the second and third stage substrate temperature was 595 °C. For all the absorbers, the first stage Ga flux has been increased to achieve a GGI ratio higher than 0.2. Nevertheless, the main discriminator in preparing these absorbers is the heat ramping rate of the substrate heater from the first stage to the second stage of deposition, that is, a variation of the time taken to increase the substrate temperature from 385 °C to 595 °C. This is illustrated in Fig. 6.41. The ramping rates of 20 °C/minute, 30 °C/minute and 40 °C/minute were considered, changing the duration between the first stage and second stage substrate temperatures from ~ 7 minutes (at 20 °C/minute) to ~ 4 minutes (at 40 °C/minute). It should be added that, the evaporation of copper at the second stage of deposition was from the outset of the ramping phase, i.e., copper was simultaneously evaporated during the ramping phase.

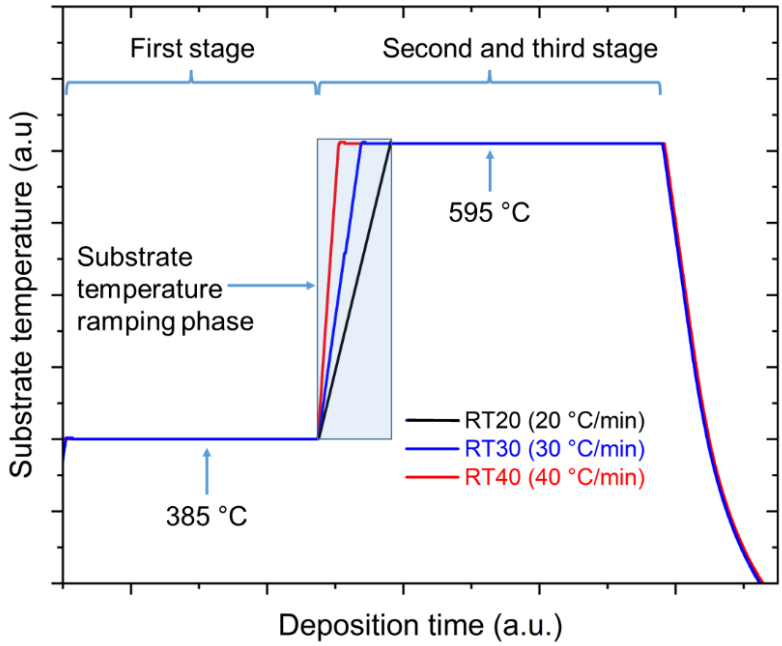

Figure 6.41: The substrate temperature profile for the Cu(In,Ga)S_2 absorbers deposited with different heat ramping rates of 20-40 °C/minute. The blue box highlights the period of the heat ramping, and its influence on the duration between the first stage and the second stage substrate temperatures.

Three different absorbers, RT20, RT30 and RT40 were processed at the heat ramping rates of 20 °C/minute, 30 °C/minute and 40 °C/minute, respectively. The chemical composition of average CGI ratio and GGI ratio of the absorbers is between 0.96-0.97 and 0.25-0.29 respectively, and the front surface gallium corresponded to GGI ratio ~ 0.26 for all the absorbers. The SEM cross-section of the absorbers RT20 and RT40 are presented in Fig. 6.42. The thickness of RT40 decreased by ~ 0.5 um in comparison to RT20, and the different heat ramping rate had no substantial different on the microstructure of the absorbers, as seen in Fig. 6.42.

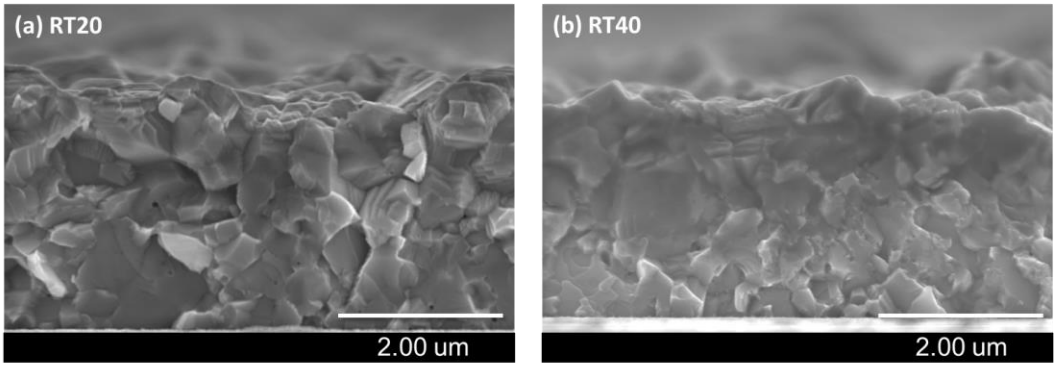

Figure 6.42: SEM cross-section of $Cu(In,Ga)S_2$ absorbers processed at heat ramping rate of (a) 20 °C/mins (RT20) and (b) 40 °C/mins (RT40). Heat ramping of the substrate heater leads to a reduced thickness of the absorber RT40 by ~ 0.5 um in comparison to RT20.

Fig. 6.43a shows the SIMS depth profile for Ga distribution in RT20 and RT40. The Ga profile of both absorbers show quite identical gradients, indicating that the ramp rate has a negligible influence on the diffusion of the back gallium into the bulk of the absorber. However, the heat ramping rate has three main influences on the gallium profile of the absorbers. First, the influence of the different ramping rates is observed in the depth of the absorbers, as the thickness of RT40 is lesser than that of RT20. This difference is corroborated by the thickness of the absorbers as seen in the cross-section images of the absorbers shown in Fig. 6.42, where RT20 is 0.5 µm thicker than RT40. From the SIMS analysis, the second distinct influence of the ramping rate is the notch width of the absorbers. The notch of both absorbers is narrower than the wide and flat shape seen previously in the phase segregated absorbers, as seen in Fig. 6.23 for example. Nevertheless, RT40 has a narrower notch width than RT20. The third observation is in comparing the notch energy between RT20 and RT40 in Fig. 6.43a, the notch is shifted to a higher energy by increasing the heat ramping rate. Since the notch in RT40 is narrower and higher than in RT20, it can be implied

that, as the ramping rate is increased and the substrate heater reaches a higher temperature quicker, this shortens the deposition process. By reaching a high substrate temperature faster, the diffusion of Cu is enhanced and the duration for the crystallization of the Cu_xS phases is shortened, hence leading to a thinner absorber, as observed for RT40. Fig. 6.43b shows the XRD diffractogram (between 2.75° and 29.4°) from which the influence of the different ramping rate on the contributing phases in the absorbers are examined. The absorbers crystalize into a chalcopyrite structure as indicated by the (112) peaks. The intensity of the peaks has been normalized to the (112) peak at a higher angle. The proximity of the (112) peaks suggests that there is a more homogenous composition in the absorbers and that the different Ga sub-layers are similar. This agrees with the less steep Ga gradient in Fig. 6.43a. The broadness of the high angle peak is due to the thickness of the back Ga layer in both absorbers, as readily verified by the SIMS profile. Ultimately, as the heat ramping rate is increased from 20 °C/minute to 40 °C/minute, it is observed that the intensity of the low angle peak weakens and this can be interpreted as the reduction of the front low-gallium specie which aligns with the narrowing of the notch as observed in the SIMS profile of RT40. Interestingly, the optical bandgap of the absorbers did not reflect the difference in notch energies of the absorbers; RT20 and RT40 had bandgap of 1.58 eV while RT30 had a bandgap of 1.57 eV.

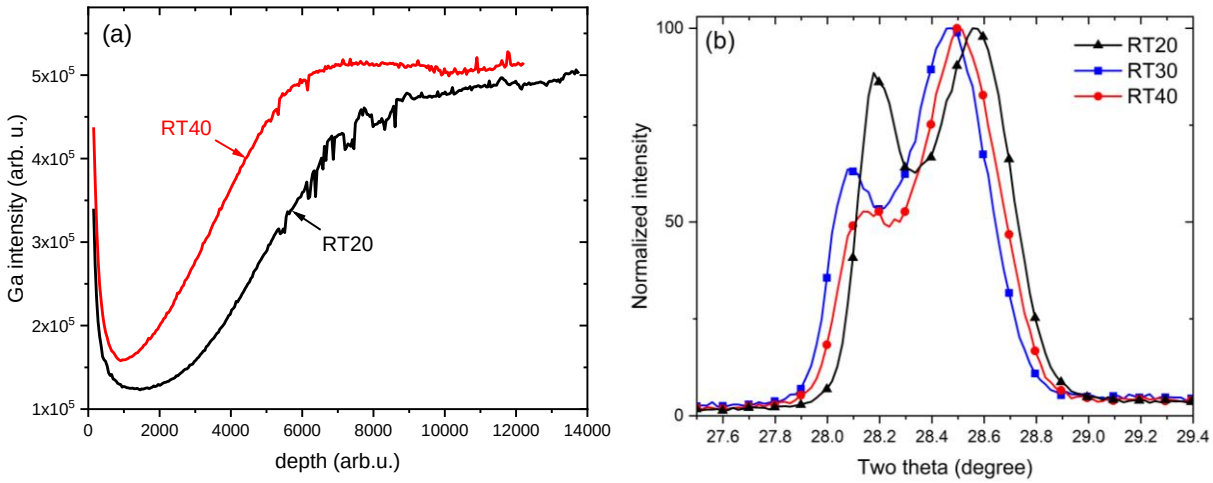

Figure 6. 43: (a) The gallium profile from SIMS analysis on the $Cu(In,Ga)S_2$ absorbers grown with different heat ramping rates between the first and second stage substrate temperature. (b) Normalized intensity of the XRD diffractogram around the (112) main chalcopyrite peaks of the absorbers processed by the different heat ramping rates.

Table 6.14: Optoelectronic quality of the Cu(In,Ga)S_2 absorbers RT20, RT30 and RT40 and the device parameters of the corresponding solar cells completed with CdS buffer layer.

Sample	**QFLS (meV)**	**V_{OC}^{SQ} deficit (meV)**	**Voc (mV)**	**Voc loss (mV)**	**FF (%)**	**PCE (%)**	**Jsc (mA/cm^2)**
20 °C/min (RT20)	1009	296	778	231	62.7	8.6	18
30 °C/min (RT30)	1042	256	803	239	56.4	7.7	17
40 °C/min (RT40)	1042	262	791	251	51.5	6.5	16

The details of the optoelectronic quality evaluated at 1 sun equivalent illumination and the device parameters on RT20, RT30 and RT40 are presented in Table 6.14, and summarized in Fig 6.44. The QFLS analysis on the absorbers show a gain of 33 meV for both RT30 and RT40 in comparison to RT20, which corresponds to a reduced V_{OC}^{SQ} deficit of ~ 40 meV. The better quality of the absorber RT30 and RT40 over RT20 is also reflected in the PL decay measurements on the absorbers presented in Fig. 6.44b. Although there is no drastic improvement in the minority lifetime, the PL decay tail of RT30 and RT40 is slightly improved relative to RT20.

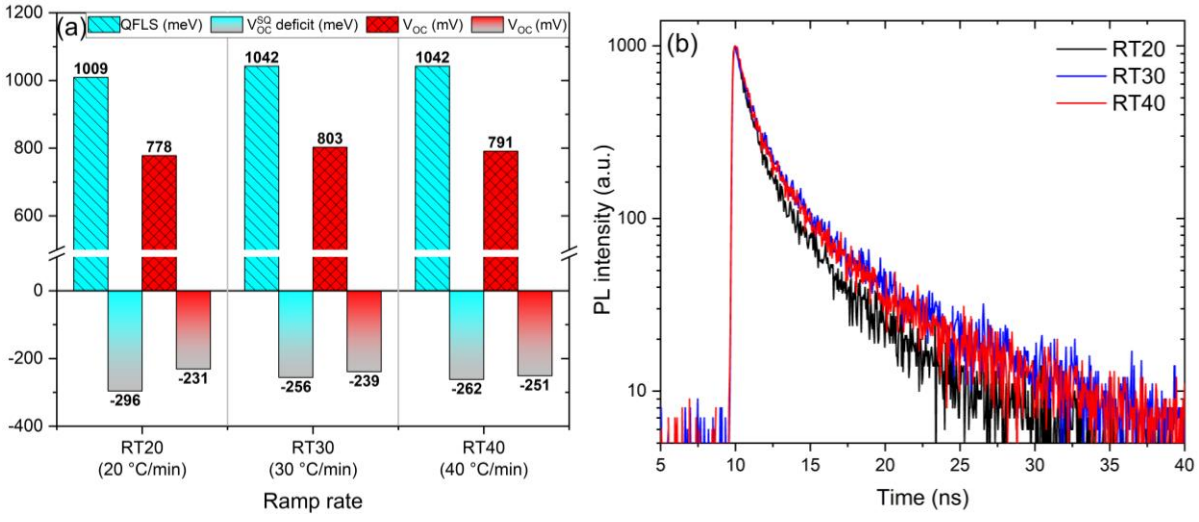

Figure 6.44: (a) A bar chart representation of the optoelectronic property of the absorbers and device performances on RT20, RT30 and RT40. (b) PL decay curves measured on the absorbers.

The cause of the improvement in QFLS cannot be completely explained by the CL mapping of the defect emission on the absorbers RT20, RT30 and RT40 shown in Fig. 6.45. First, to discuss the overall observation, the spots of defect luminescence in RT30 (Fig. 6.45a) is more intense than RT20 and RT40. Although this could suggest a higher defect concentration in RT40, however, this absorber has higher band-edge emission in CL and PL in comparison with RT20 and RT30, as such, a conclusion on the defect emission cannot be drawn. To compare the defect mapping of RT20 and RT40 in Fig. 6.45a and Fig. 6.45c respectively, the intensity of the defect luminescence in RT40 is reduced compared with RT20, which might be the origin of the improved QFLS in RT40.

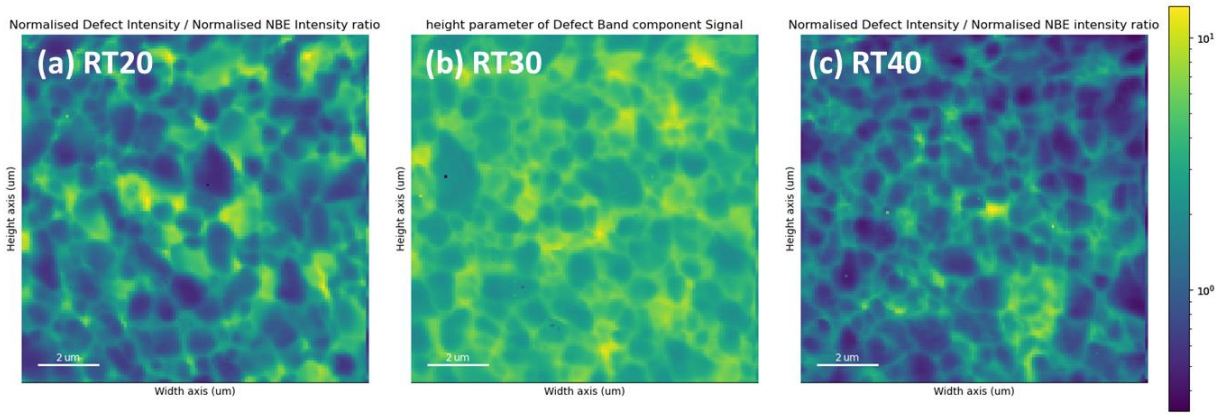

Figure 6.45: CL hyperspectral mapping of defect emission at 1.3 eV of the Cu(In,Ga)S_2 absorbers (RT20, RT30 and RT40) processed at different heat ramp rates of 20 °C/minute, 30 °C/minute and 40 °C/minute between the first and second stages of deposition. The signal is the ratio of normalized defect density against normalized near-band edge emission.

For the device performance on the RT20, RT30 and RT40 absorbers, they have been completed with CdS buffer layers. The V_{OC} on the devices has been plotted along with the QFLS to in Fig. 6.44a, and the detail of the device parameters is presented in Table 6.14. Although it might seem that a higher V_{OC} is achieved on the devices on the RT30, and that there a better translation of QFLS to V_{OC} in the RT20 device, as seen in Fig. 6.44a, actually, the V_{OC} is limited by the CdS buffer layer. The limitation is evidenced by the similarity in V_{OC}. This is a result of the poor

conduction band alignment at the absorber-buffer interface [191]. The higher V_{OC} in RT30 and RT40 is possibly due to their corresponding higher QFLS.

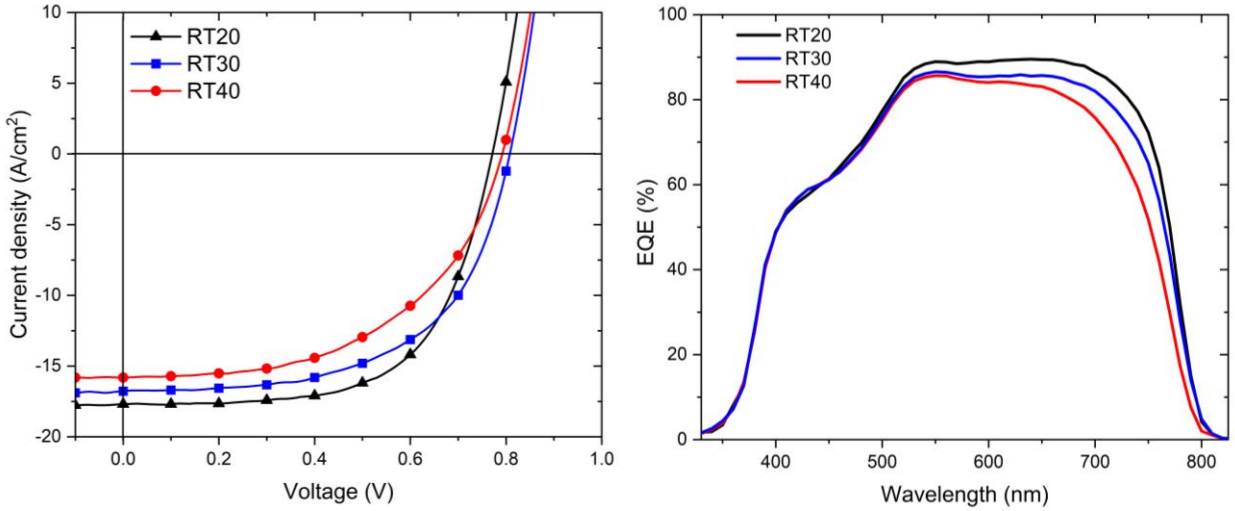

Figure 6.46: (a) I-V curves of the Cu(In,Ga)S_2 devices fabricated on absorbers processed at various substrate heat ramping rates (RT20, RT30 and RT40). (b) The corresponding EQE curves of the devices on RT20, RT30 and RT40.

For the other device parameters, as the heat ramping rate increases from RT20 to RT40, J_{SC} and FF reduces as seen in Fig. 6.46a and Table 6.14. The lower J_{SC} and FF contribute to a reduction of overall device performance as the PCE reduces from 8.6 % to 6.5 % as the ramp rate is increased from 20 °C/minute to 40 °C/minute. This lower J_{SC} and FF can be explained by the EQE curve presented in Fig. 6.46b. The results show that, as the heat ramping rate is increased from 20 °C/minute to 40 °C/minute, that is, from RT20 to RT40, there is a poor response to a long wavelength. As a phenomenon is likely to occur due to low absorption of longer wavelengths or higher back surface recombination. However, given that the SIMS analysis of RT20 and RT40 shown in Fig.6.43a indicate, increasing the substrate heater ramp rate narrows the notch width, and a narrower notch width will reduce the absorption rate of the device [103, 229].

To summarize the outcome of this section, the effect of manipulating the heat ramp rate of the substrate heater between the first and the second stage of deposition, is a strong influence on the notch width. It was observed that the higher the ramp rate, the narrower the notch width gets. Also, at a higher ramp rate of 30 °C/minute and 40 °C/minute, improved QFLS was realized on the

absorbers. However, the narrowing of the notch width reduced photon absorption rate in the absorbers, which results in overall poor device performance.

6.4.5 Effect of Cu-excess deposition after the first stoichiometric point

In Section 6.4.2 and 6.4.3, it was demonstrated that increasing the first stage substrate temperature is optimum for improving Ga-gradient. At a first stage substrate temperature of 435 °C, a better Ga-gradient was achieved, although it was necessary to compensate for a depleted back-Ga layer which deteriorates the quality of the absorber. Even with such back-Ga compensation, the fill-factor and overall device performance is still limited. In this section, the influence of Cu_xS recrystallization time after the first stoichiometric point on $Cu(In,Ga)S_2$ absorbers and devices will be investigated. To take advantage of a better gallium gradient, the deposition at the first stage will be at a substrate temperature of 435 °C, and the back-Ga will be increased not only to mitigate back-Ga depletion, but also to increase the overall GGI ratio to ~ 0.20.

To reiterate, the subject of investigation in this section is the influence of excess copper after the first stoichiometric point, during the second stage of $Cu(In,Ga)S_2$ absorber deposition. As explained in Section 3.6, the stoichiometric point is dictated by assessing the pyrometer readout and the output power of the substrate heater. This is because both parameters are dependent on the emissivity of the absorber, and with higher emissivity of the absorber caused by the formation of additional Cu_xS phases after stoichiometry, the temperature readout of the pyrometer will increase, while the output power of the substrate heater also increases to maintain a constant substrate temperature. In this report, the excess Cu is categorized by the time Cu is deposited after the first stoichiometric point (T_{as}), to the total time that Cu is deposited during the second stage before the first stoichiometric point (T_{bs}). In Fig. 6.47, the points, and the durations which the different times are referencing are indicated in the deposition profile illustrating the progress of substrate temperature, pyrometer readout and output power of the substrate heater during absorber deposition. The third stage deposition times between the absorbers are different since the excess Cu influences the recrystallization time. For instance, the more Cu excess there is, the longer the recrystallization time required. As such, to have a consistent CGI ratio on the final absorber composition, it is ensured that regardless of the T_{as}, a constant time is maintained for the final

deposition of In and Ga after the second stoichiometric point. As a reminder, the second stoichiometric point occurs after the recrystallization of Cu during the third stage of deposition. The T_{as} for excess Cu was varied between 4-13 minutes corresponding to a $\left(\frac{T_{as}}{T_{bs}}\right)$ percentage between 6 % and 20 % in five absorbers, CR1-CR5.

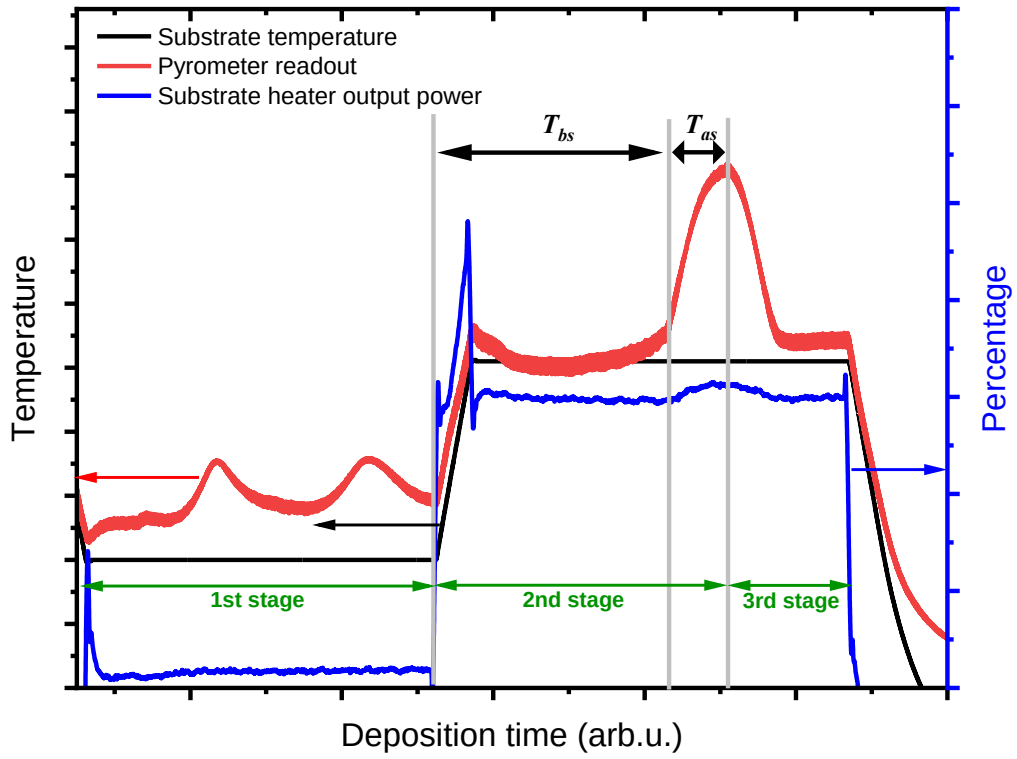

Figure 6.47: The typical three-stage deposition profile of a Cu(In,Ga)S_2 absorber showing the evolution of the substrate temperature, pyrometer readout and output power of the substrate heater at different steps during absorber growth.

The full detail of the Cu excess for each Cu(In,Ga)S_2 absorber, the average composition acquired by EDX, and the bandgap extracted from PL maximum are presented in Table 6.15. Generally, the average CGI ratio for all the absorber layers is between 0.96-0.97, which is consistent with the deposition time of In and Ga after the second stoichiometric point at the third stage. The most remarkable change is in the average GGI ratio between the absorbers, where there is an unintended increase in average GGI ratio from 0.20 in CR1, to 0.28 in CR5. The bandgap also increases from 1.58 eV (CR1) to 1.60 eV (CR5) in correlation with the increase in the average GGI ratio. To

deliberate the grounds for the changes in GGI ratio and optical bandgap, we look at the gallium distribution within the absorber from the SIMS depth profile, particularly considering CR1 and CR4 presented in Fig. 6.48a. Note that the SIMS measurements are uncalibrated and the exact GGI ratio and the bandgap from the gallium profile cannot be estimated from Fig. 6.48a.

Table 6.15: Cu-excess deposition time and chemical composition extracted from EDX analysis for the Cu(In,Ga)S_2 absorbers deposited with varied Cu-excess

Sample	T_{as} **(minute)**	$\left(\frac{T_{as}}{T_{bs}}\right)$ **(%)**	**Average CGI ratio**	**Average GGI ratio**	E_g^{PL} **(eV)**
CR1	13:00	20%	0.97	0.20	1.57
CR2	09:30	15 %	0.96	0.23	1.58
CR3	06:00	11 %	0.96	0.24	1.59
CR4	04:30	7 %	0.96	0.25	1.59
CR5	04:00	6 %	0.97	0.28	1.60

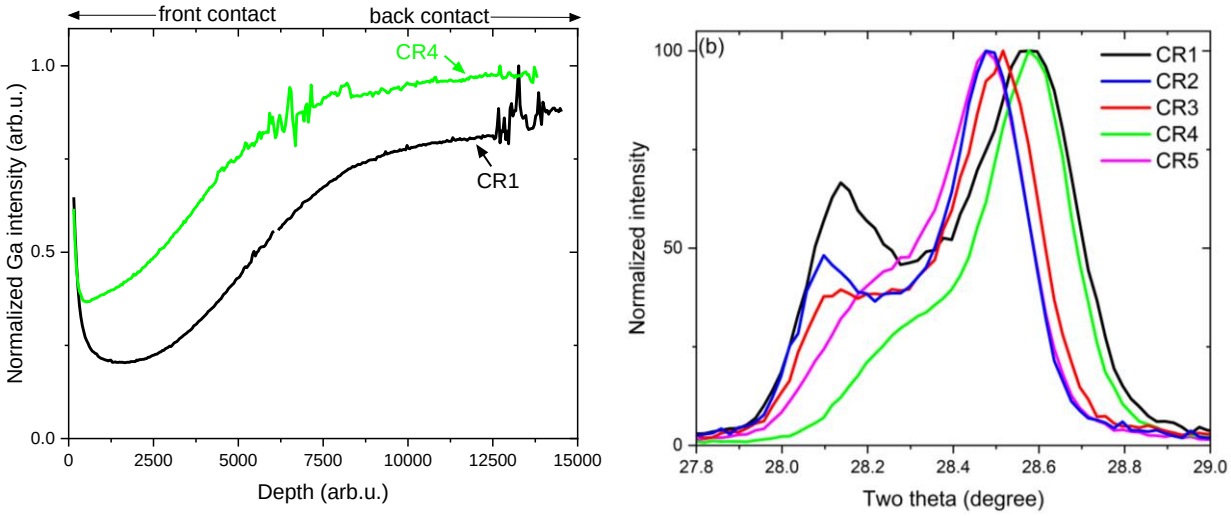

Figure 6.48: (a) Gallium depth profile acquired from SIMS measurement for CR1 and CR4. (b) Normalized X-ray diffraction pattern around the (112) chalcopyrite peak for the Cu(In,Ga)S_2 absorbers CR1-CR5, grown with different Cu-excess deposition times after the first stoichiometric point.

However, it is still possible to compare the shape of the gallium profile across the depth of the absorbers. The consequence of the different T_{as} is more apparent in the gallium minimum. CR1 features a broad and flat notch which is positioned at a depth which is approximately 10 % into the total depth of the absorber from the surface. Conversely, for CR4, the shape of the notch is narrower and steeper, and the notch is rather close to the surface of the absorber layer lying approximately within 4% of the total length of the absorber. The alteration to the width of the notch is attributed to the different times at which Cu-excess was deposited [239], while the difference in the notch position is ascribed to the length of the In and Ga deposition in the third stage. The influence of T_{as} on the optical bandgap of the absorbers can also be explained by the notch position, since the optical bandgap originates from the notch [210]. The notch occurs at a higher position as the duration of the Cu-excess phase is shortened, since the gallium gradient is also terminated at a higher position, if the Cu-excess is lower at the end of the second stage. X-ray diffraction is used to investigate the influence of the Cu excess on the crystal phase formed after the absorber growth, this is presented in Fig. 6.48b, with the range of interest around the (112) phases. For all the absorbers, it can still be seen that there are two closely separated peaks corresponding to high and low gallium regions at higher and lower angles, respectively. The high gallium peak is the most intense for all the absorbers and the two phases are more separated in CR1. From CR1 to CR3, it is observed that, the shorter the time excess Cu is deposited, the lower the intensity of the low gallium peak. In particular, for CR4 and CR5, the two peaks are rather overlapping suggesting a better intermixing and homogenization of the two phases.

The aftermath of the different T_{as} can also be seen in the SEM micrograph of the absorbers in Fig. 6.49a and 6.49b, where the cross-sectional view of both CR1 and CR4 are presented. The thickness of the absorbers differs by approximately 0.2 µm, with CR1 being ~ 3.2 µm and CR4 ~ 3 µm. This seems due to the longer duration of Cu deposition or overall longer deposition time in CR1 compared with CR4. Some differences can also be seen in the microstructure of the absorbers, notably by a dense upper layer with larger well-connected grains which is ~ 1.6 µm in CR1 and ~ 1.3 µm in CR4. The lower layer, which extends to the Mo-back, composed of much smaller grains rather features more in CR4 (Fig. 6.49b) than in CR1 (Fig. 6.49a). This is explained by the Cu_xS secondary phases formed on the surface of absorbers after stoichiometry, which has been shown to enhance the growth of large grains in $Cu(In,Ga)(S,Se)_2$ absorbers [27, 98], with the formation

of larger grains showing smoother microstructure. As such, for absorbers with prolonged deposition of Cu after the first stoichiometry, the thicker the layer of Cu_xS secondary phases formed on the surface of such absorbers, the larger the grains formed during Cu recrystallization in the third stage. The smaller grains at the lower half of the absorbers is due to the gallium rich back layer.

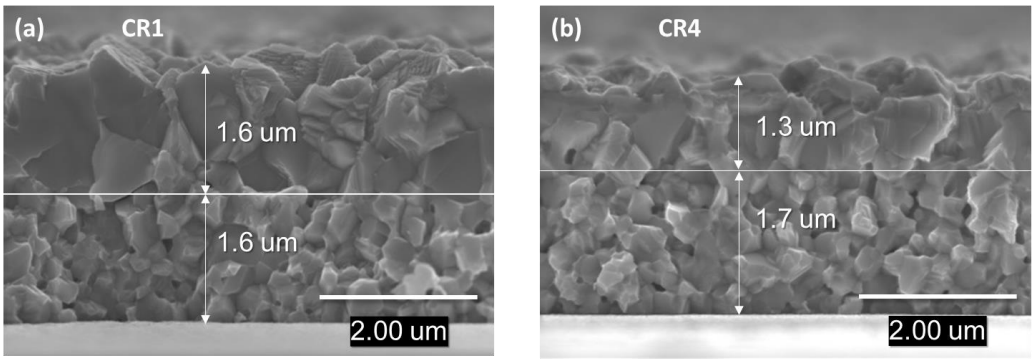

Figure 6.49: SEM micrograph showing the cross-sectional image of absorbers deposited with different Cu-excess at (a) 13:00 minutes (20 %) and (b) 04:30 minutes (6 %) after the first stoichiometric point.

The QFLS evaluated on the absorbers by the ERE method is shown in Fig. 6.50a and presented in Table 6.16. The strongest improvement is the gain of 113 meV, corresponding to the reduction of V_{OC}^{SQ} deficit by 104 meV, when the Cu-excess is reduced from 20 % (CR1) to 15 % (CR2). From CR2 to CR4, there is only a gain of 23 meV (or reduced V_{OC}^{SQ} deficit by 11 meV) as the Cu-excess reduces from 15 % to 7 % (Fig. 6.50a and Table 6.16). However, with a lower Cu-excess of 6 % (CR5), the QFLS is slightly reduced again. These QFLS values suggest that long Cu excess, especially over 15 %, is detrimental to the optoelectronic quality of the absorber. A reason could be the formation of the dense Cu-rich layer during the recrystallization phase which becomes even more prominent as the Cu excess increases with longer $T_{as.}$ Still the loss of QFLS in CR5 as the Cu excess is reduced suggests that there is an optimum level for the Cu excess after which the QFLS diminishes again. PL decay is measured on CR1 (with 20 % Cu-excess) and CR4 (with 7 % Cu-excess), shown in Fig. 6.50, both are chosen since they respectively possess the worst and best optoelectronic quality among these series. The PL decay curve for CR1 features a fast single exponential decay, while the decay curve for CR4 features a significantly longer and bi-

exponential. The shorter decay time in CR1 is an indication of a fast recombination occurring in the absorber, which supports the high V_{OC}^{SQ} deficit in CR1. The origin of this fast recombination is passivated in CR4, resulting in a longer decay time and improved QFLS.

To analyze the influence of the Cu excess on device performance, all the absorbers are processed into solar cells with CdS as the buffer layer. The device parameters are presented in Table 6.16, and the I-V characteristics and EQE curves on the devices are presented in Fig. 6.51a and 6.51b respectively. From the I-V characteristics and Table 6.16, except for CR1, the results show that, J_{SC} decreases as the Cu-excess decreases from 15 % (CR2) to 6 % (CR5). This is due to the narrowing of the notch which reduces the absorption length, and the elevation of the notch energy as seen in the SIMS analysis in Fig. 6.48a and the E_g^{PL} (Table 6.15), which shifts the absorption edge to higher wavelength as seen in the EQE curve (Fig. 6.51b). However, as detailed in Table 6.16, a remarkable effect of reducing the Cu-exccess on the devices, is an increased FF as the Cu-excess is decreased from 15 % (CR2) to 6 % (CR5). These two factors will decrease the cumulative photon flux and absorption edge of the absorbers [13, 14]. Although, these reasons do not justify the lower JSC in CR1. An explanation for the poor J_{SC} in CR1 can be found in the EQE curve in Fig. 6.51b, demonstrating signs of front surface recombination, which agrees with the optical analyses on the absorbers.

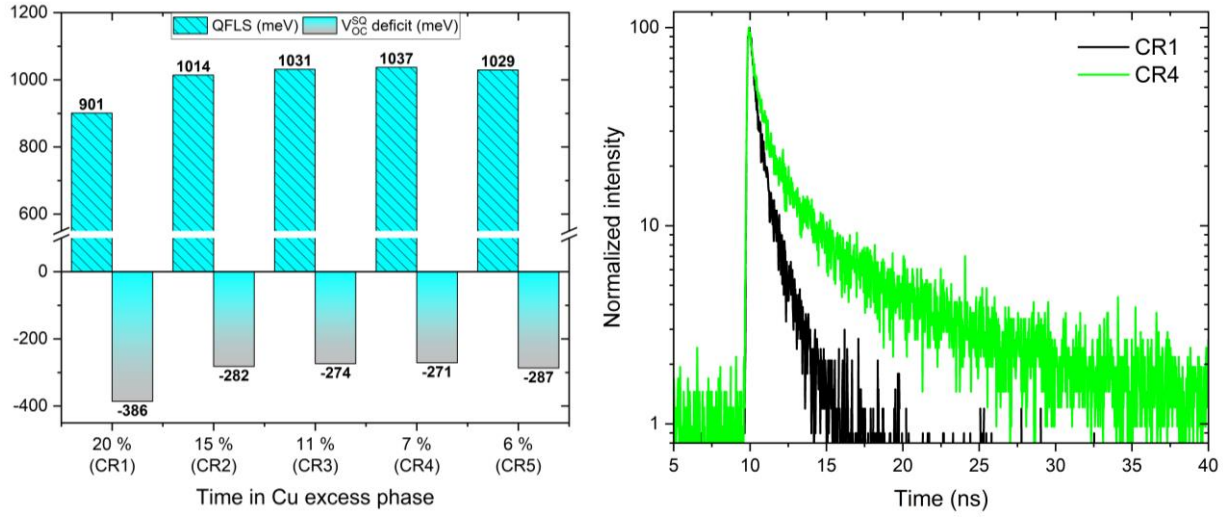

Figure 6.50 (a): QFLS and V_{OC}^{SQ} deficit evaluated on absorber grown with different Cu-excess. (b) PL decay curves on the absorber grown with 20 % (CR1) and 7 % Cu-excess (CR4).

Table 6.16: Optoelectronic quality and device parameters for Cu(In,Ga)S_2 absorbers (CR1-CR5) prepared with different Cu-excesses. The devices were completed with CdS buffer layer.

Sample	**QFLS (meV)**	**V_{OC}^{SQ} deficit (meV)**	**V_{OC} (mV)**	**FF (%)**	**PCE (%)**	**J_{SC} (mA/cm^2)**
CR1	897	386	803	55	7.1	16.5
CR2	1014	282	837	64	9.8	19.0
CR3	1031	274	825	65	9.3	17.6
CR4	1037	271	827	70	9.2	17.0
CR5	1029	287	816	66	8.9	16.9

A comparison of the V_{OC} on the devices presented in Table 6.16 and Fig. 6.51c, shows a lower V_{OC} for CR1 than CR2 to CR5. Actually, the V_{OC} on the devices on CR2 - CR5 are limited by the CdS buffer layer used in completing the devices [191], due to conduction band misalignment at the absorber-buffer interface. As such, the exact influence of the Cu-excess on the V_{OC} of the devices on CR1-CR5 cannot be stated.

The different analyses on the samples in this section has shown the many effects of varying the Cu-excess during the growth of Cu(In,Ga)S_2 absorbers. It was observed that decreasing the Cu-excess increased the notch energy and the optical bandgap of the absorbers. This is interesting because, it shows that it is possible to increase the bandgap of the absorbers without incorporating excess Ga during the deposition of the absorbers. The overall quality of the absorber also improved, as not only did the QFLS increase with high bandgap but also there was a lower V_{OC}^{SQ} deficit or non-radiative loss as the Cu-excess decreased. For the device performance, the remarkable effect of the reduced Cu-excess is an improvement in FF. Although the maximum achievable V_{OC} was not realized due to the CdS buffer layer used, in the next section, it will be shown that when a buffer which has a better conduction band alignment with Cu(In,Ga)S_2 absorber is used, a high V_{OC} is achievable.

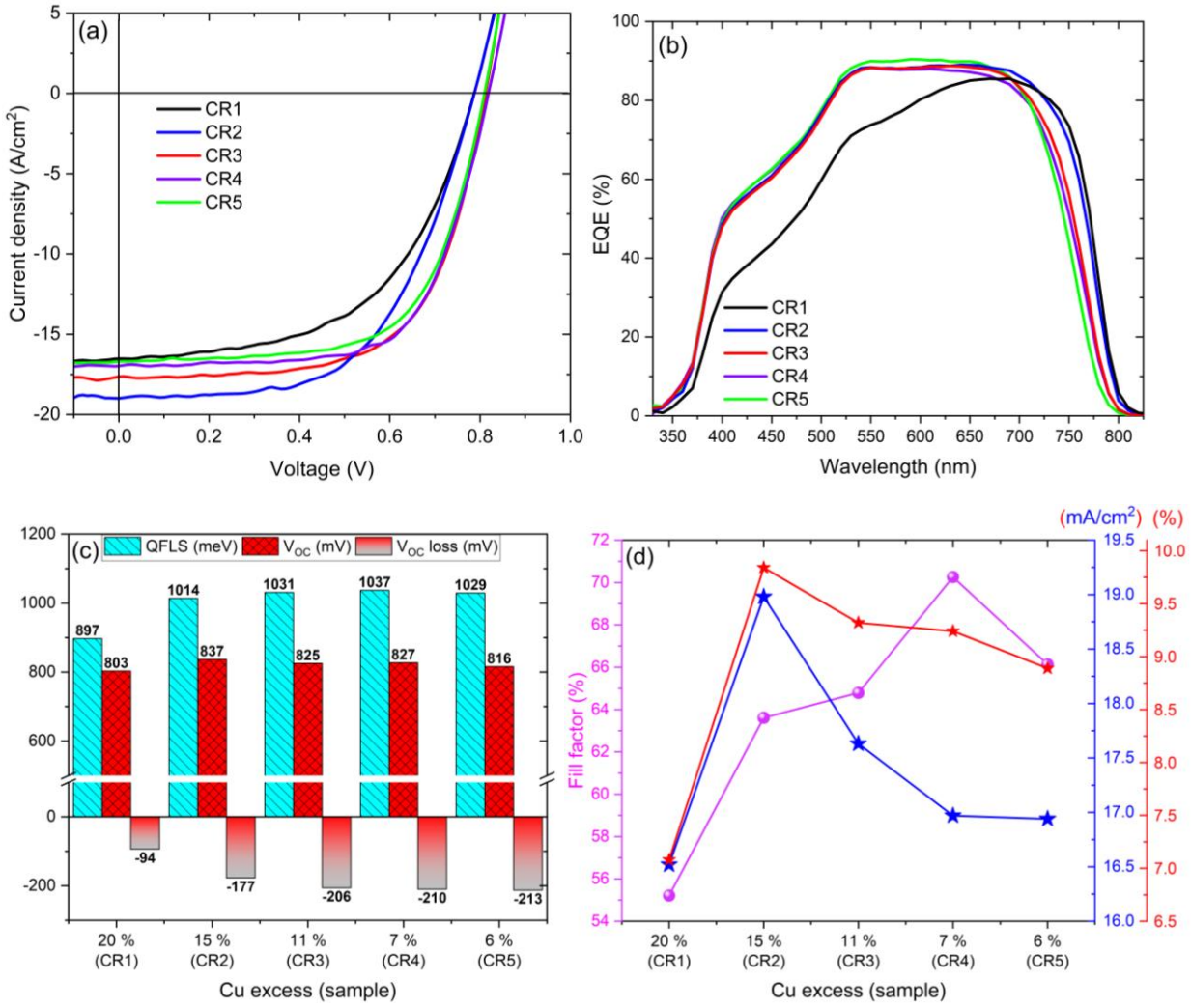

Figure 6.51: (a) I-V curves of the devices with different Cu-excess CR1-CR5, (b) the equivalent EQE curves on the devices, (c) the bar chart comparing the QFLS to V_{OC} translation on the devices and (d) a plot of the device parameters, i.e., FF, J_{SC} and efficiency of the devices.

At the beginning of Section 6.4, before investigating the influence of the different growth parameters on Cu(In,Ga)S_2, the expected outcomes of the various procedures were presented in Table 6.9. After these studies, there is a greater understanding of how to control different profiles of the Cu(In,Ga)S_2 absorber and how to mitigate prevailing challenges when preparing the absorber. To conclude this section, Table 6.9 is revisited to review the expected outcomes, and importantly to highlight and summarize the observations of all the different growth parameters investigated during the deposition of Cu(In,Ga)S_2 absorbers.

Table 6.17: Outcome of investigations on various deposition parameters during the growth of $Cu(In,Ga)S_2$ absorbers.

Deposition parameter	**Observed outcome**	**Relevant chapter**	**Samples**
Thermally cracking Sulfur	Higher cracker temperature → lower back-Ga	Section 6.4.1	SC300, SC500, SC650, SC800
1st stage substrate temperature	- Higher substrate temperature → Reduced phase segregation → Improved Ga gradient - Depleted back Ga mitigated by higher first stage Ga flux	Section 6.4.2	SH1, SH2, SH3 GSH3, GSH2
Ramping of substrate heater	Higher ramp rate → narrower notch	Section 6.4.4	RT20, RT30, RT40
Cu excess recrystallization	Lower Cu-excess → higher notch energy, higher optical bandgap	Section 6.4.5	CR1, CR2, CR3, CR4, CR5

6.5 What are the effects of all the optimization procedures with (ZnSn)O buffer layer?

A part of the objectives of these investigations is to improve the optoelectronic quality of high-bandgap $Cu(In,Ga)S_2$ absorbers, which is then translated to excellent device performance. This is particularly important for the use of $Cu(In,Ga,)S_2$ devices for a top cell in tandem applications. The high-bandgap has been achieved by increasing the Ga-content in $Cu(In,Ga)S_2$ absorbers. However, Section 6.3 highlighted the challenges of phase segregation which becomes more exacerbated with higher Ga-content. The challenge motivated the different investigations in Section 6.4. Even when phase segregation was mitigated, a high device performance was limited by CdS buffer layer which has been shown to be inappropriate for $Cu(In,Ga)S_2$ devices [90, 110]. Therefore, this last section will summarize and justify the optimization steps, and by completing a

device with a more appropriate (Zn,Sn)O buffer layer [240], it will be shown that a highly efficient high-bandgap Cu(In,Ga)S_2 device is achievable.

6.5.1 Comparison of absorbers before and after optimization

First, the influence of the growth parameters on the dominant crystallographic phases in the absorbers before and after the optimization processes are compared. For this, the absorber CR4 in Subsection 6.4.5 is compared with a phase-segregated absorber BL3 in Section 6.3. The different growth parameters for both absorbers are presented in Table 6.18, and the properties of the absorbers presented in Table 6.19.

Table 6.18: Growth parameters used in processing Cu(In,Ga)S_2 before and after optimization.

Parameter	**Before optimization (BL3)**	**After optimization (CR4)**	**After optimization (ST)**
Cracker temperature	300	250	250 °C
First stage substrate temperature (actual)	335 °C	435 °C	385 °C
Substrate temperature ramp rate	20 °C/minutes	20 °C/minutes	40 °C/minutes
Cu excess	25 %	7 %	7 %

To highlight the mitigated phase segregation, the XRD diffractograms showing the contributing phases existing in the absorbers BL3 and CR4 are presented in Fig. 6.52. For BL3 with GGI ratio of 0.30 and BL1 with lower GGI ratio, the phase segregation is indicated by the two separate chalcopyrite (112) peaks around 28 ° and 29 ° for BL3. On the other hand, CR4 shows a more homogenous phase centered around 28.5 °.

To compare the optoelectronic performance of the absorbers before and after optimization, BL3 will be compared with a different absorber (ST) that was prepared on account of the different optimization steps as presented in Table 6.18. Readers should note that the significance of ST is

that, at the end of the optimization procedures, this absorber had the best optoelectronic quality. CR4 will be reverted to in the next section when the device is completed with (Zn,Sn)O.

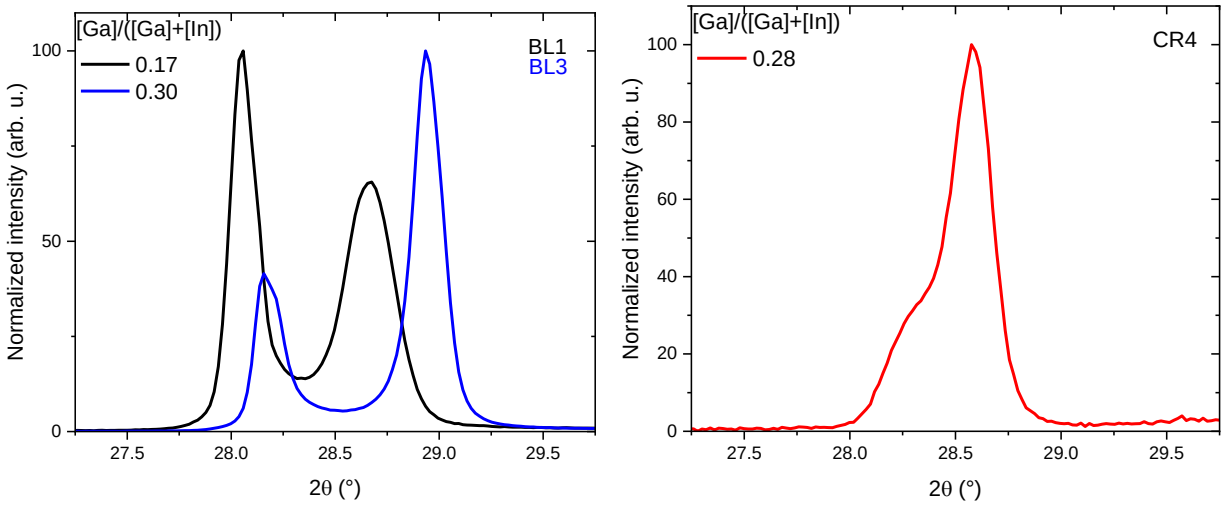

Figure 6.52: XRD diffractogram around the main chalcopyrite phase of Cu(In,Ga)S_2 absorbers with phase segregation before optimization and a more homogenous absorber after optimization.

The absorber properties of both BL3 and ST are detailed in Table 6.19. While the average GGI ratio and CGI ratio of both absorbers are identical, the surface GGI ratio is very different, with BL3 having a much higher value of 0.49 and ST a value of 0.24. As Section 6.2 and Section 6.3 shows, such a high surface GGI ratio in BL3 is not desired. As detailed in Table 6.17, there is also a large discrepancy between the bandgaps extracted from PL maximum (E_g) and the inflection points from EQE (E_g^{EQE}). Overall, BL3 has higher bandgaps, with E_g^{PL} higher by 0.06 eV, and with two inflection points because of the segregated phases, while ST has a single broad E_g^{EQE} at 1.61 eV. The improved quality of the absorbers is summed up in the reduction of V_{OC}^{SQ} deficit to 242 meV (ST) from 334 meV (BL3). The V_{OC}^{SQ} deficit of 242 meV is much closer to the average V_{OC}^{SQ} deficit of ~ 200 meV recorded on Cu(In,Ga)Se_2 absorbers made at LPV. This is a promising development since an improved optoelectronic quality of the absorber is a big step towards achieving excellent performance and high efficiency on Cu(In,Ga)S_2 devices.

Table 6.19: Optoelectronic quality of Cu(In,Ga)S_2 absorbers before and after optimization

	Before optimization (BL3)	**After optimization (CR4)**	**After optimization (ST)**
Average GGI ratio	0.30	0.25	0.31
Surface GGI ratio	0.49	0.26	0.24
Average CGI ratio	0.98	0.96	0.98
E_g^{PL} (E_g^{EQE})	1.64 eV (1.65 eV & 2.32 eV)	1.59 eV (1.63 eV)	1.58 eV (1.61 eV)
QFLS (eV)	1.037 eV	1.037 eV	1.056 eV
V_{OC}^{SQ} deficit	334 meV	271 meV	242 meV

Lastly, SEM-CL imaging of the in situ bandgap profile for ST is presented in Fig. 6.53. The image shows a bandgap-gradient from ~ 2.45 eV at the back to around 1.7 eV at the front.

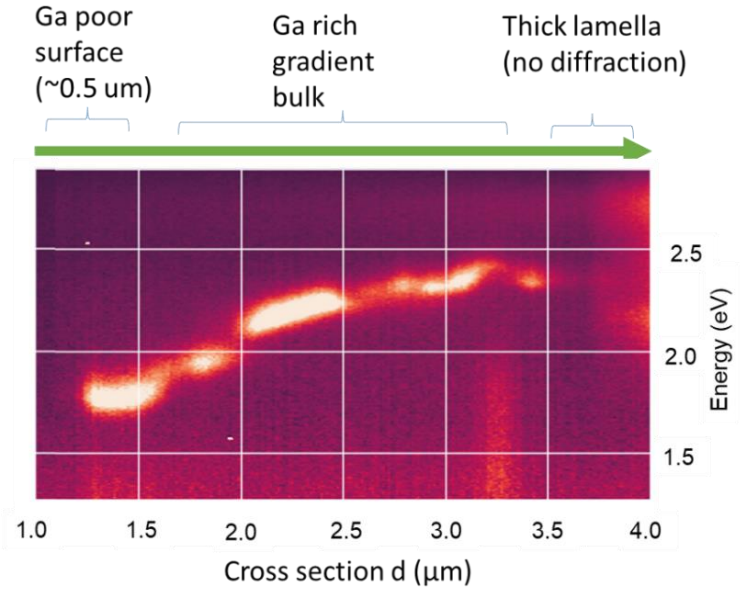

Figure 6.53: In situ imaging of the bandgap gradient by SEM-CL on a lamella of ST.

While Fig. 6.53 shows that it is possible to achieve a Ga or bandgap gradient in Cu(In,Ga)S_2 absorbers deposited by the three-stage process, it also raises a question on why there is a discrepancy on the optical bandgap between the bandgap minimum as seen in the imaging. From the in situ image, the minimum bandgap is ~ 1.7 eV while the optical bandgap (E_g^{PL}) taken from PL peak maximum is 1.58 eV. This makes for interesting investigation in future works.

6.5.2 Towards 16 % efficiency in high bandgap Cu(In,Ga)S_2 devices with (Zn,Sn)O buffer layer

So far in this thesis, and particularly in Chapter 6 where Cu(In,Ga)S_2 absorbers have been investigated, CdS buffer layer has been used to complete the solar cells. The highest efficiency achieved on these optimized absorbers is still below 12 %. The use of CdS buffer layer contradicts an earlier statement and our previous report that CdS is not the most optimum buffer layer for Cu(In,Ga)S_2 solar cells, rather Zn(O,S) buffer layer is more optimal [90, 110]. We have used CdS because it is a fast approach for completing solar cells, which also expedites the evaluation of the electrical performance of devices completed on the absorbers. We are now considering, and in fact have already shown that, ALD (Zn,Sn)O is an alternate buffer which promises even better device performance than Zn(O,S). This is because the high temperature annealing step in Zn(O,S) which is detrimental to the Cu(In,Ga)S_2 device is not needed with (Zn,Sn)O [240]. Hence, we examine the performance capability of the optimized Cu(In,Ga)S_2 absorber with atomic layer deposited (ALD) (Zn,Sn)O buffer layer and an anti-reflection coating. Note that these are preliminary results and the research on ALD (Zn,Sn)O buffer is not within the scope of this work.

A solar cell device is completed on the absorber CR4 discussed in the previous Section 6.5.1 and Section 6.4.5. The I-V characteristics of the solar cell device is shown in Fig. 6.54a. As a reminder the optical bandgap (E_g^{PL}) from PL maximum and solar cell bandgap $\left(E_g^{EQE}\right)$ taken from EQE inflection point are 1.59 eV and 1.63 eV respectively. A PCE of 15.6 % is achieved on the device on CR4 with (Zn,Sn)O buffer layer. This is a higher efficiency than our previous lab record on Cu(In,Ga)S_2 devices with a lower bandgap. Fig. 6.54b shows the efficiency of various $CuInS_2$ and

$Cu(In,Ga)S_2$ solar cells from literature plotted against their respective bandgaps determined from EQE. In comparison, this device also becomes the highest efficiency recorded on a high bandgap of 1.63 eV for a $Cu(In,Ga)S_2$ device. This result is particularly significant because it demonstrates that high efficiency can be obtained on high bandgap single-junction $Cu(In,Ga)S_2$ devices and this brings us closer to potentially using this device for a top cell in tandem applications.

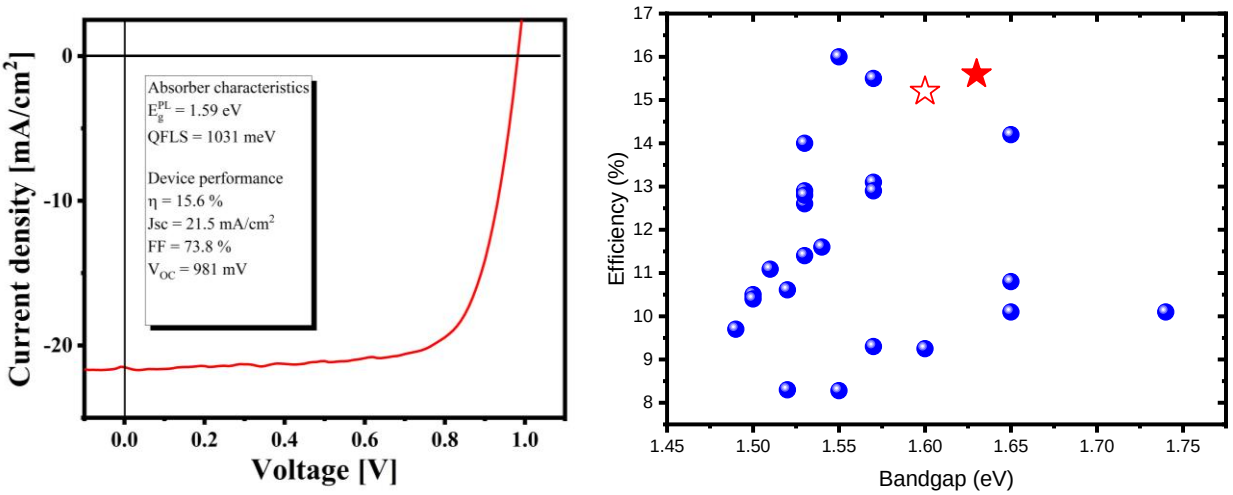

Figure 6.54: (a) I-V characteristics of an optimized $Cu(In,Ga)S_2$ absorber completed with ALD (Zn,Sn)O. (b) Efficiency of $CuInS_2$ and $Cu(In,Ga)S_2$ solar cells plotted against the respective bandgaps determined from external quantum efficiency (EQE) curves of the solar cells [24, 27, 28, 98, 110, 192-205]. The previous best lab efficiency by Shukla and Sood et al. [110] is indicated by the unfilled star. The efficiency of CR4 is indicated by the filled star.

Chapter 7

Summary

In this thesis, various investigations were performed on three different compounds; the ternary compounds of $CuInS_2$ and $CuGaS_2$, and later their quaternary $Cu(In,Ga)S_2$ alloy. The research was in threefold: (i) Time-resolved measurements were performed on $CuInS_2$ to understand the origin of improvements earlier reported. (ii) Defect spectroscopy by photoluminescence analyses were carried out on $CuGaS_2$, further contributing more information on the electronic structure of I-III-VI chalcopyrite family. (iii) Significant measures were taken to solve problems limiting the achievement of high efficiency in high bandgap $Cu(In,Ga)S_2$ absorbers.

Foremost, lifetime measurements were performed on Cu-rich $CuInS_2$ absorbers, and we have used the understanding of the relationship between lifetime and the quasi-equilibrium state to understand the improved optoelectronic quality which accompany (a) higher deposition temperature and (b) higher [Cu]/[In] ratio. We show that the improved QFLS under these deposition conditions is not due to the mitigation of non-radiative recombination from a reduced density of deep defects, rather the improvement is due to an increased doping level.

Clear insights were provided on the electronic structure of $CuGaS_2$. It was observed that the main transition dominating Cu-rich $CuGaS_2$ samples is DA3 occurring at ~ 2.29 eV. Its origin was shown to involve a somewhat deep acceptor level at 205 meV above the valence band and a shallow donor level at ~ 35 meV from the conduction band. As Cu-content reduces, DA1 and DA2 with peaks around 2.4 eV become more intense, however, the peak occuring at 2.4 eV is rather broad in Cu-poor absorbers. Both transitions were shown to involve a common donor at 35 meV and two shallow acceptors at 75 meV (DA1) and 90 meV (DA2). Two broad defect peaks at 2.15 eV and 1.85 eV are seen on all the absorbers. However, for Cu-poor absorbers, the peak at ~ 2.15 eV and an exciton-related transition at 2.48 eV dominated. These peaks are assumed to involve a deep defect with broad density of state. Ultimately, the two broad peaks at 2.15 eV and 1.85 eV dominate the PL spectrum of $CuGaS_2$ at room temperature.

To understand the broad defects in $CuGaS_2$ which might influence the electrical properties of a single junction solar cell, a novel solar cell device was completed on a high-quality Cu-rich $CuGaS_2$ absorber with QFLS of 1.68 eV. The device achieved a V_{OC} of 821 mV with a power conversion efficiency of 1.8%. Factors limiting the performance of such high-bandgap device include defects in the absorber which serve as unwanted recombination channels, near-interface defects and negative conduction band offset.

The last part of this thesis is dedicated to several investigations on $Cu(In,Ga)S_2$. We addressed: (1) Origin of bulk recombination in $Cu(In,Ga)S_2$. (2) Front surface Ga-grading of $Cu(In,Ga)S_2$. (3) Back surface gradient and mitigation of phase segregation in high Ga $Cu(In,Ga)S_2$.

(1) It was observed that, although absorbers processed under high Cu-excess conditions possess high crystal quality, they generally exhibited low QFLS, lifetime and radiative efficiency in comparison to Cu-deficient absorbers. By low-temperature photoluminescence measurements on a series of $Cu(In,Ga)S_2$ absorbers spanning different CGI ratios, we observed that Cu-related defects are responsible for bulk recombination path in the Cu-excess absorbers. By using Cu-deficient absorbers, the non-radiative recombination channels are suppressed resulting in an increased QFLS and high V_{OC} on the device.

(2) Next, the influence of front surface Ga on the optoelectronic quality of $Cu(In,Ga)S_2$ absorbers and devices was investigated. We showed that, while a high surface Ga leads to improved radiative efficiency and QFLS in $Cu(In,Ga)S_2$, it is detrimental to device performance since this creates a barrier at the absorber-buffer interface which hinders photogenerated carriers. We also observed that Ga deposited at the third stage does not strongly influence the notch energy or optical bandgap, rather, it merely aggregates on the surface of the absorber and contributes to an exceptionally high surface GGI ratio. It is necessary to reduce Ga flux at the third stage of a three-stage deposition of $Cu(In,Ga)S_2$ absorber.

(3) Different growth parameters have been used to solve the problem of phase segregation in $Cu(In,Ga)S_2$ absorbers. The problem becomes particularly prominent when increasing the bandgap through increased Ga content by the three-stage deposition method. (i) The thermal cracking of S_8 molecule into smaller more reactive species was rather detrimental to the QFLS of the absorber and the device performance. This is likely due to the preference of the smaller species to react with indium rather than gallium, which is not beneficial for the bandgap gradient. In this work,

ultimately, the preferred cracker temperature is 250 °C. (ii) The first stage substrate temperature was used to manipulate the bandgap-gradient profile of $Cu(In,Ga)S_2$ absorbers. The results demonstrate that higher first stage substrate temperature mitigates phase segregation leading to enhanced Ga-gradient, since there is an improved intermixing of indium and gallium. However, the quality of the absorber deteriorates when the first stage substrate temperature is too high because of back-Ga depletion. The back-Ga depletion can be compensated with a higher first stage Ga-flux. (iii) The influence of ramping the temperature of the substrate heater was also investigated, and it was observed that, the shorter the ramping time, the narrower the width of the notch becomes. (iv) Finally, the effect of different Cu excesses on $Cu(In,Ga)S_2$ absorbers were investigated. The outcome demonstrates that high Cu excess up to 20 % is detrimental to the optoelectronic quality of the absorber, and a Cu-excess of 7 % was optimum. Additionally, it was observed that Cu-excess could be used to vary the notch position and the bandgap of the absorber, as decreasing Cu-excess increased the bandgap of the absorber.

In the last part, It was shown that through the manipulation of different growth parameters; it is possible to grow high bandgap $Cu(In,Ga)S_2$ absorbers without phase segregation. More so, the device completed on the absorbers with (Zn,Sn)O buffer layer produced solar cells with high performance. Nevertheless, with the challenge of phase segregation mitigated, the plateauing of the bandgap, where the optical bandgap does not increase even as the Ga content is increased was observed.

Outlook

As the outcomes of the different works presented in this thesis improved our knowledge of the compounds studied and solved major challenges limiting the quality of the absorbers, the results raised many more questions and future works which need to be addressed.

The influence of increased surface Ga in improving the quasi-Fermi level splitting of $Cu(In,Ga)S_2$ absorbers was seen in this thesis. This was attributed to a reduction in front surface recombination. Ideally, the increase of surface Ga should also increase the open-circuit voltage achievable on the completed device. However, the contrary was observed as open-circuit voltage decreased and there was an indication of a barrier blocking photogenerated carriers. Investigations on buffer layers were concurrent with the research on $Cu(In,Ga)S_2$ absorbers in this thesis, and good buffer layers forming better conduction band alignment at the absorber-buffer interface for $Cu(In,Ga)S_2$ devices, have demonstrated improved performance. To get higher open-circuit voltage, it is worth exploring – through simulations and further investigations – how to harness the possibility of high voltage with surface Ga.

The role of substrate temperature in achieving high optoelectronic quality in all the compounds studied cannot be understated. In fact, the $Cu(In,Ga)S_2$ absorbers were grown close to the softening temperature of the soda-lime glass substrate. This temperature-dependence would be a challenge for when growing absorbers on substrates that cannot tolerate high temperatures such as ITOs. Nowadays in chalcopyrite photovoltaics research, silver has become the metaphorical "silver bullet" in for improving the quality of $Cu(In,Ga)Se_2$ [241, 242], it has been shown to reduce the melting temperature of $Cu(In,Ga)Se_2$ during growth which circumvents the need for very high deposition temperatures [243], improve elemental interdiffusion [244], and enhance formation of larger grains [245]. Silver has also been shown to improve carrier transport in $Cu(In,Ga)Se_2$ solar cells [246]. Therefore, the incorporation of silver in $Cu(In,Ga)S_2$ makes for a compelling study.

The thermal cracking of sulfur did not really improve Ga-gradient or the phase segregation, however, it was shown to reduce Ga content at the back of the absorber. In low-temperature deposition processes, where Ga is likely to agglomerate at the back of the absorber, an alternative means of reducing the back-Ga could be by the thermal cracking of sulfur.

$Cu(In,Ga)Se_2$ solar cells have achieved remarkable milestones with alkali-treatment. In $Cu(In,Ga)Se_2$, alkali treatments have been suggested to improve the quality of p-n junctions by widening the surface bandgap of the absorber, improve hole concentration and increase minority carrier lifetime [25, 247]. Although the role of alkali-treatment was not investigated in this work, preliminary findings on $Cu(In,Ga)S_2$ at LPV have already shown that in-situ alkali treatment result in high quasi-Fermi level splitting. As such, similar impressive records achieved in $Cu(In,Ga)Se_2$ solar cells could be possible in $Cu(In,Ga)S_2$ solar cells with alkali-treatment.

In exploring ways to overcome the phase segregation and plateauing bandgap limiting the quality of $Cu(In,Ga)S_2$ absorbers, an alternative deposition method which overlapped the first and the second stages of deposition was used to process the absorbers. This method was to exploit the chalcopyrite phase near stoichiometric compositions as seen in the $Cu(In,Ga)S_2$ phase diagram by Thomere et al [31]. This deposition method is similar to the CuPRO method which has been utilized in $Cu(In,Ga)Se_2$ [248], and has been employed in $Cu(In,Ga)S_2$ to achieve high efficiency [28]. A short description of the deposition process and the properties of the absorbers can be found below in Appendix 1. The absorbers had good optoelectronic quality, however, the deposition approach did not solve the underlying challenges. Nevertheless, the devices completed on the absorbers with (Zn,Sn)O buffer layers produced high open-circuit voltage above 1 V, but the other device parameters were poor. Having found means of mitigating phase segregation in $Cu(In,Ga)S_2$ absorbers, this deposition method should be revisited, understood and explored for its potential to produce high-quality absorbers and devices.

Many of the high-quality $Cu(In,Ga)S_2$ absorbers presented in these studies have bandgaps below 1.7 eV. The other main challenge that persists in $Cu(In,Ga)S_2$, is the plateauing of bandgap, that is, the bandgap does not increase beyond ~1.67 eV even when overall GGI ratio is increased. This is obviously a major obstacle that needs to be solved to achieve target bandgap of 1.6-1.7 eV for the top cell in tandem application.

Appendix

Appendix 1: Overlapping the first stage and second stage of deposition

To overcome the phase segregation which occurs in high back Ga Cu(In,Ga)S_2, an alternate deposition process similar to the CuPRO technique introduced by Kessler et al. was explored [248]. This is motivated by an attempt to circumvent the two immiscible trigonal and cubic Cu-poor phases present in Cu(In,Ga)S_2 as shown in the phase diagram studied by Thomere et al. [31]. This method also aims to explore the narrow chalcopyrite phase close to stoichiometric or Cu-rich composition without first going directly through the trigonal and cubic phases.

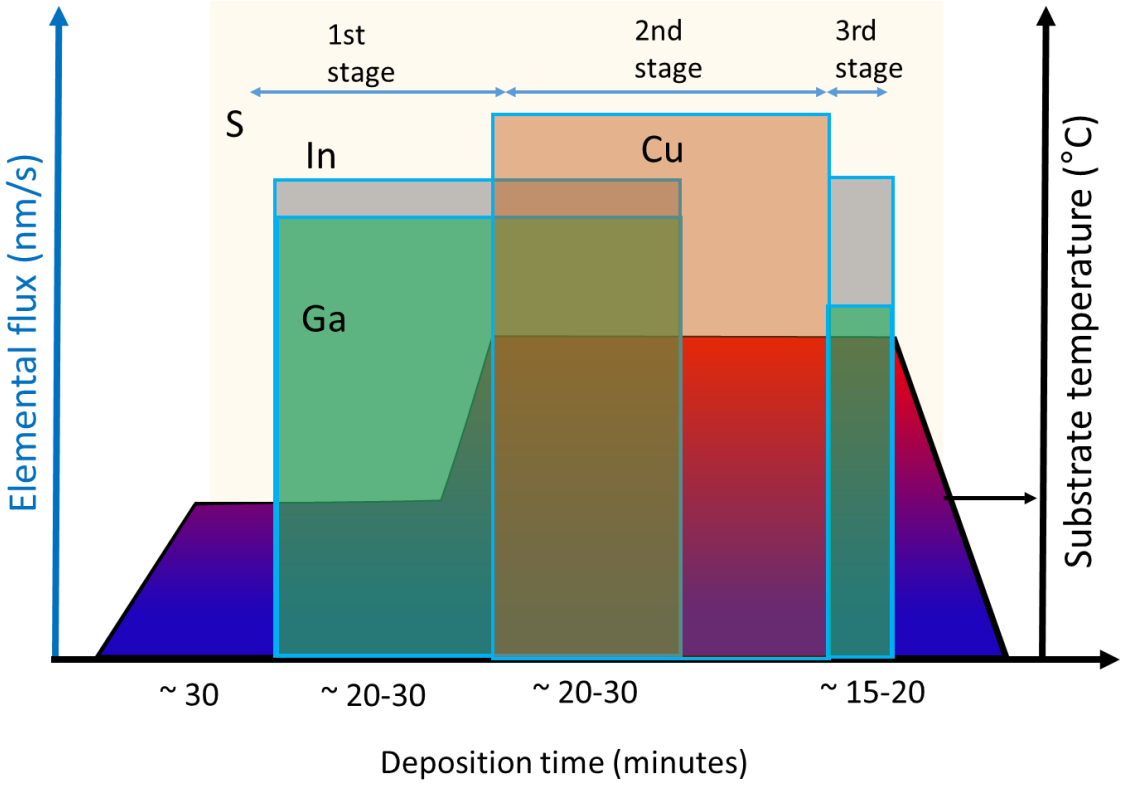

Figure A1: Schematic of the deposition profile of the overlapped first and second stage process.

The deposition process overlaps the first and the second stages of deposition, as illustrated in Fig. A1. In the depiction, midway through the deposition of Ga and In (first-half) at a temperature of 300 °C in the first stage, the evaporation of Cu begins as the substrate temperature is increased to 500 °C. The evaporation of Ga and In are halted after the second-half deposition and the evaporation of Cu continues until the stoichiometric point is reached. As shown in Fig. A1, the evaporation of Cu continues to achieve a Cu-rich phase, while Ga and In are evaporated again in the third stage to a achieve the final Cu-poor composition.

The SEM cross-sectional micrograph of the best absorber is shown in Fig. A2. By visual inspection, the appears more homogenous than the phase-segregated absorbers in Fig. 6.21 from Section 6.3. However, the following analyses and results suggest otherwise.

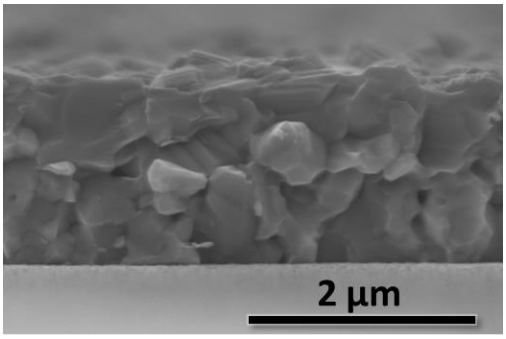

Figure A2: SEM cross-sectional images of a sample deposited by overlapping the first stage and second stage deposition steps.

The properties of two of the absorbers that were completed into solar cells are presented below. The chemical composition of the two absorbers LS1 and LS2 are presented in Table A1 along with their optical bandgaps. It is obvious from the average GGI ratios of both absorbers that they contain a high amount of Ga. This seems to be because of the Ga fluxes used during the deposition process. Nevertheless, the optical bandgaps (1.57 eV and 1.66 eV) measured on both absorbers are much lower in comparison to the predicted bandgap corresponding to such GGI ratio (0.53 and 0.69) from the bowing diagram in Fig. 2.3. The PL spectrum of LS2 is shown in Fig. A3.

From the chemical composition in Table A1, it is obvious that both absorbers have surprisingly lower front surface GGI ratio of 0.44 in comparison to the average GGI ratio. The origin of this

phenomenon is likely compositional plateauing, from the similar front surface GGI ratio of both absorbers stagnated at 0.44, and the bandgap plateau demonstrated by the mismatch of average GGI ratio with the optical bandgap. The compositional plateau occurring with phase segregation has been discussed in Section 6.3 and described in the works of Barreau et al. [29, 30].

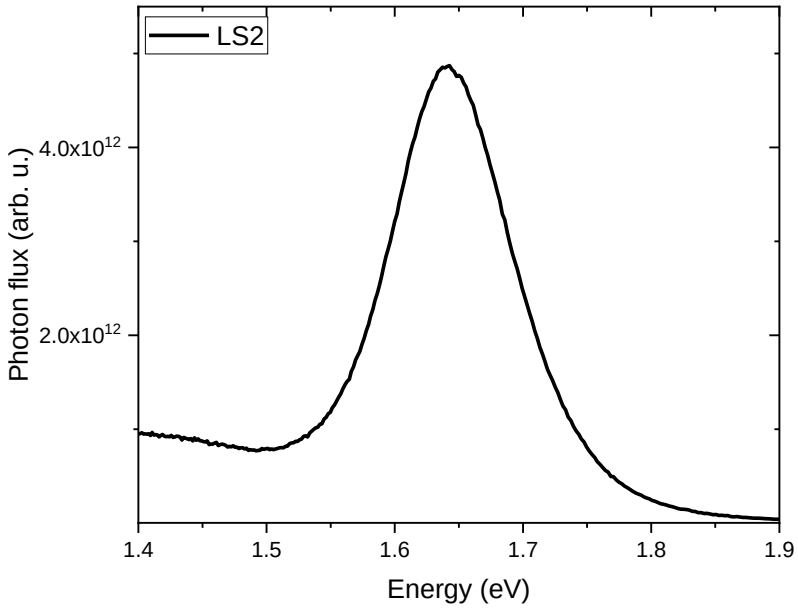

Figure A3: Photoluminescence spectrum of LS2, a sample deposited by the overlapping of the first and second stage of the deposition process.

Table A1: Chemical composition from EDX of Cu(In,Ga)S_2 absorbers processed by overlapping the first stage and second stage of deposition. The optical bandgap $\boldsymbol{E_g^{PL}}$ is taken from the maximum of the PL peak.

Absorber	**Average GGI ratio**	**Surface GGI ratio**	**Average CGI ratio**	$\boldsymbol{E_g^{PL}}$ **(eV)**
Sample LS1	0.53	0.44	0.97	1.57
Sample LS2	0.69	0.44	0.98	1.66

High QFLS above 1 eV were evaluated on both absorbers with the average of 1.018 eV and 1.056 eV for LS1 and LS2, respectively. The similarity of the V_{OC}^{SQ} deficit of both absorbers presented in Fig. A4, indicates that both absorbers possess similar optoelectronic quality.

The absorbers were completed into devices with (Zn,Sn)O buffer layer. The reason for the choice of (Zn,Sn)O buffer layer have been stated in Fig. 6.5.2, and the results of the device performance on these solar cells have been presented and published in Faraday discussions [240]. V_{OC} above 1 V was achieved on the solar cells completed on the absorbers, although other device parameters presented in Table A2 were poor. The I-V characteristics of the devices and their actual values have been plotted in Fig. A4 and Fig. A5. There was an excellent translation of QFLS to V_{OC} due to good absorber-buffer band alignment.

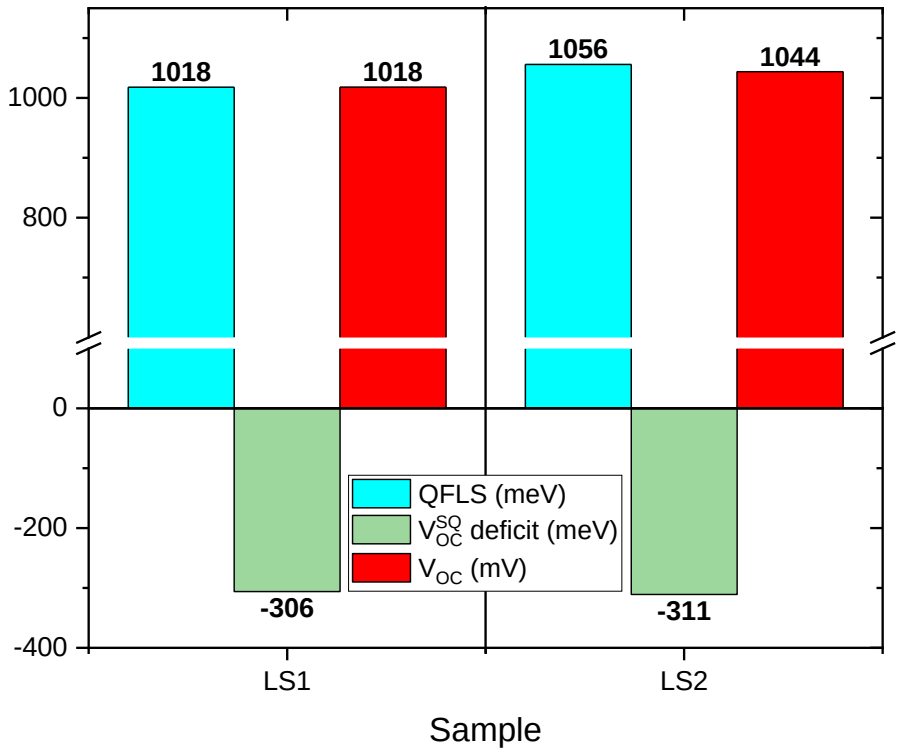

Figure A4: QFLS, V_{OC}^{SQ} deficit and V_{OC} of $Cu(In,Ga)S_2$ devices on absorbers processed by the overlapping the first and second stages of deposition. The devices were completed with (Zn,Sn)O buffer layer.

The origin of the poor device performance can be explained by the I-V characteristics and the inflection point from EQE curve on the devices. Firstly, from the I-V curves, it can be deduced that there is a barrier blocking the extraction of photogenerated carriers. Secondly, there are two inflection points in the derivative of the EQE curve, which is an indication of two bandgaps/phases occurring in the absorber.

Table A2: Device parameters of $Cu(In,Ga)S_2$ devices processed by the overlapping method. (Zn,Sn)O buffer was used to complete the devices.

Sample	PCE **(%)**	**Voc (mV)**	**Jsc (mA/cm^2)**	**FF (%)**
LS1	5.2	1000	14.3	36
LS2	4.7	1037	12.5	36

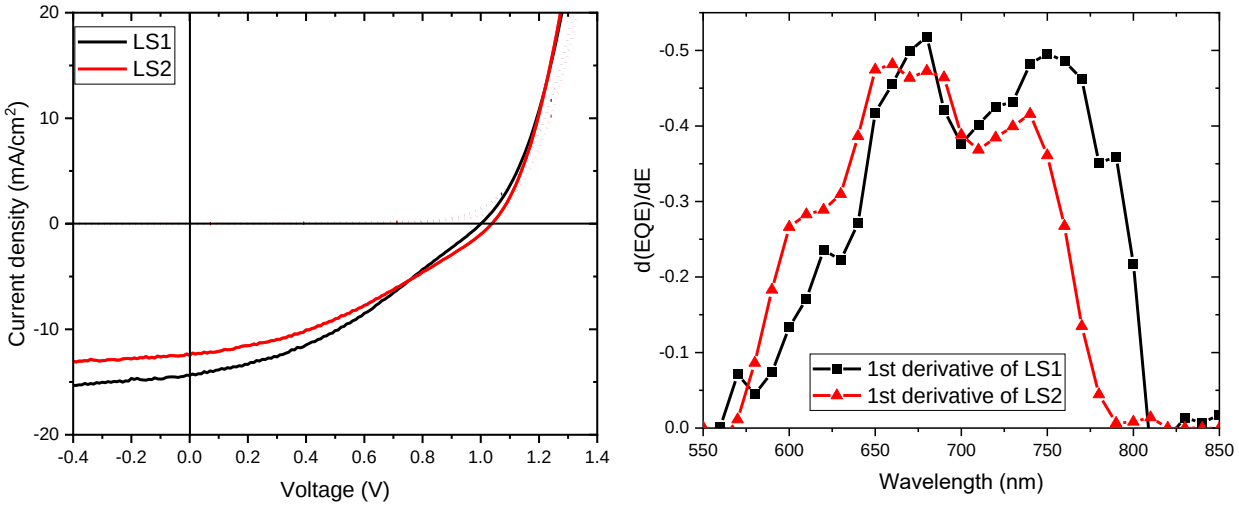

Figure A5: Current-voltage characteristics and the derivation of the EQE curve of devices made from the overlapping method. The buffer layer is (Zn,Sn)O.

These results show that the overlapping procedure is capable of producing a high quality $Cu(In,Ga)S_2$ absorber and devices. However, the phase segregation occurring in $Cu(In,Ga)S_2$ still

poses a challenge. As the works in this thesis has shown, it is possible to circumvent the origin of the phase segregation, it would be necessary to adapt/optimize this overlapping growth method to meet the full potential of producing high-quality absorbers.

Appendix 2: Substrate heater temperature calibration

There is a discrepancy between the set temperature of the substrate heater and the actual temperature measured on the substrate. The temperature measured on the substrate was calibrated with the knowledge of the softening temperature of the soda-lime glass (SLG) substrate used in this work, and the set temperature of the substrate heater at which the softening occurs. The temperature of the substrate was measured by a pyrometer.

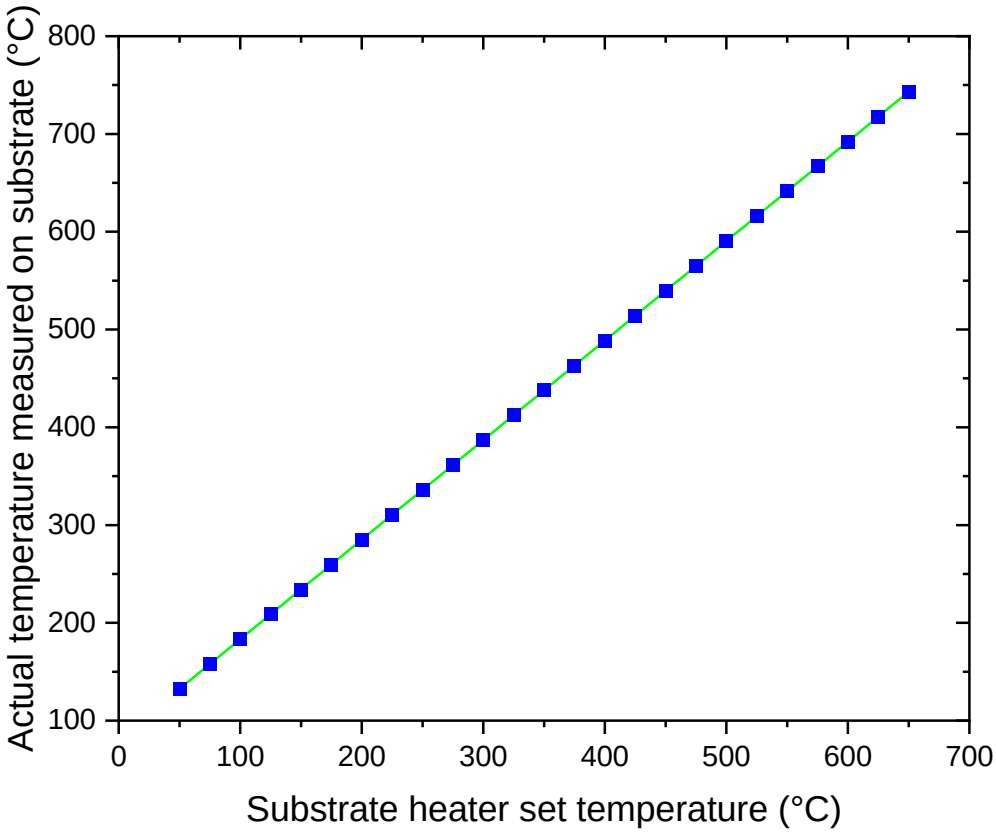

Figure A6: The actual temperature measured on the SLG substrate in dependence of the substrate heater set temperature.

Appendix 3: Lateral inhomogeneity of absorbers.

There is a lateral inhomogeneity in the composition of the absorber after deposition. In extreme cases there could be visible inhomogeneity too. This could be due to nonuniform heating of the substrates by the heater – and this is worsened when the surface of the heater is dirty – or misalignment of elemental sources. Another source of the inhomogeneity is the Mo-substrate holder which dissipates heat in homogeneously. A substrate holder made of pyrolytic graphite is used to mitigate the effect of the inhomogeneous heat dissipation. An example of the varying composition from EDX and SEM micrograph showing the top view at different spots on an absorber is illustrated in Fig. A7. Fig. A8, A9 and A10 shows the difference in PL flux, bandgap from PL maximum and QFLS, and V_{OC} that is measured from such an absorber.

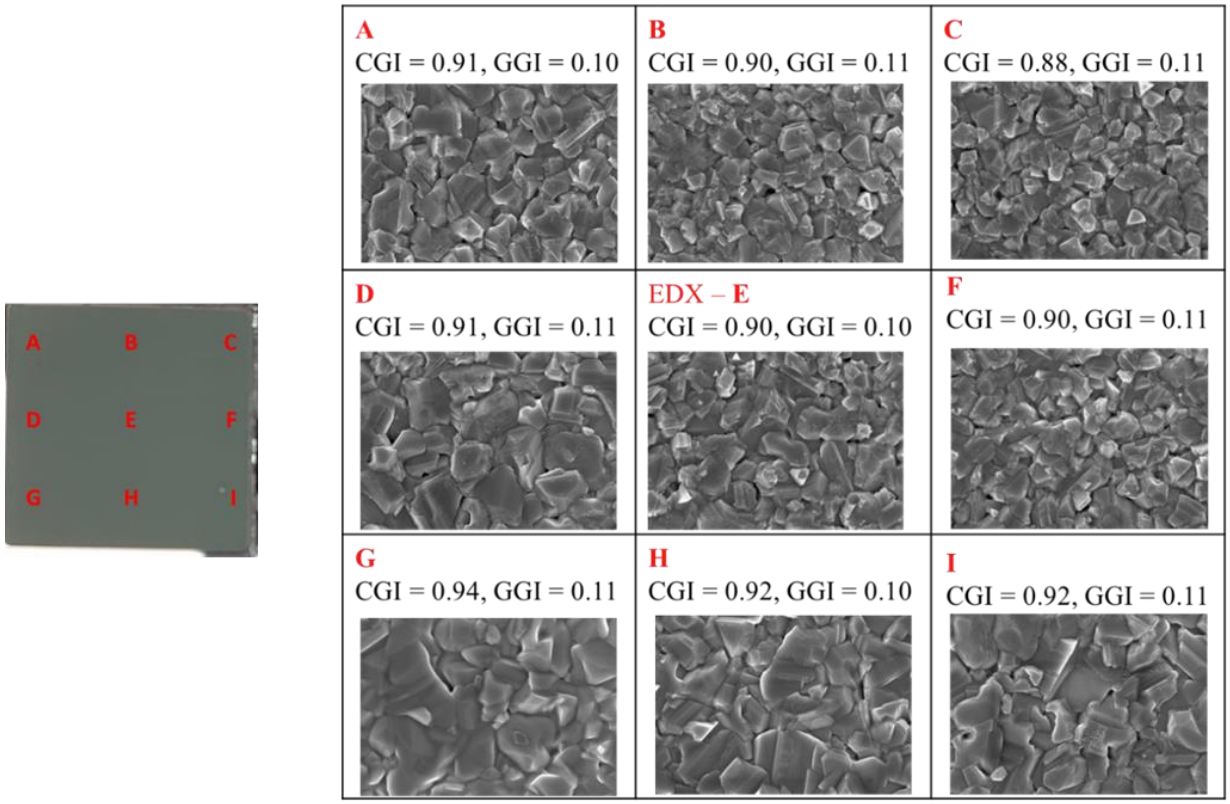

Figure A7: The different chemical compositions and SEM top view of an inhomogenous absorber which is shown on the left.

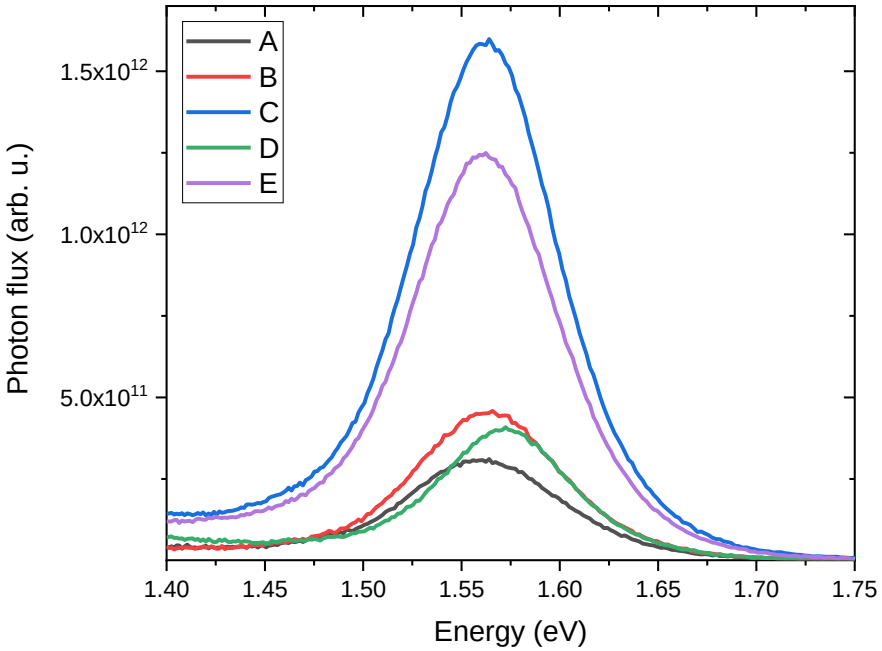

Figure A8: PL fluxes measured at different spots on an inhomogeneous absorber at different spots.

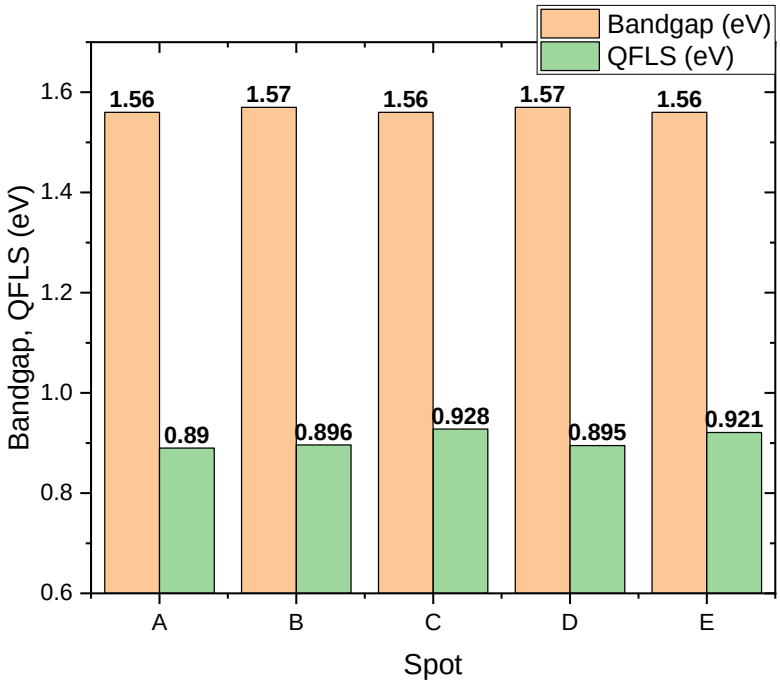

Figure A9: Bandgaps obtained from PL maximum and QFLS values (evaluated by Planck's generalized law) on an inhomogeneous absorber at different spots.

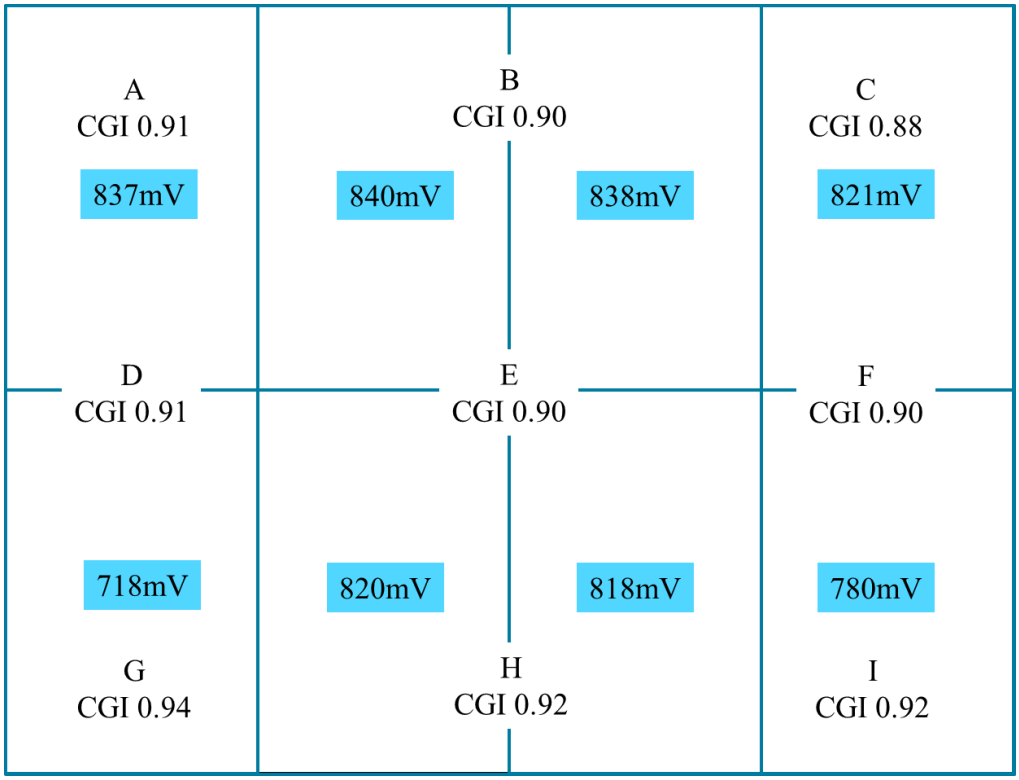

Figure A10: V_{OC} measured on the devices completed on the inhomogeneous absorber in Fig. A7 at different spots.

Appendix 4: Simulation of electron beam interaction with $Cu(In,Ga)S_2$ absorber

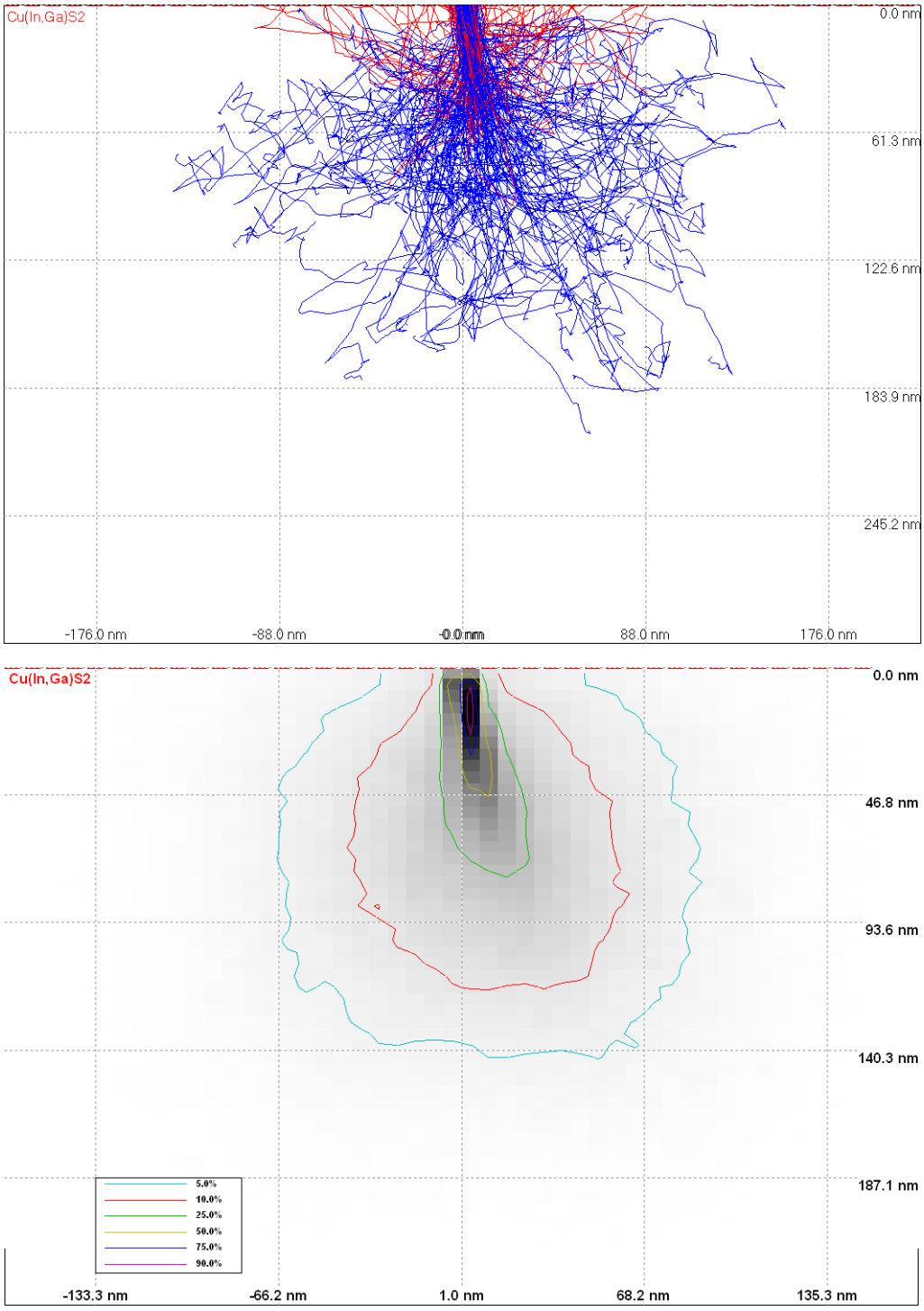

Figure A11: CASINO ("monte CArlo SImulation of electroN trajectory in sOlids") simulation of secondary and backscattered electron beam in a $Cu(In,Ga)S_2$ absorber at 5kV [209].

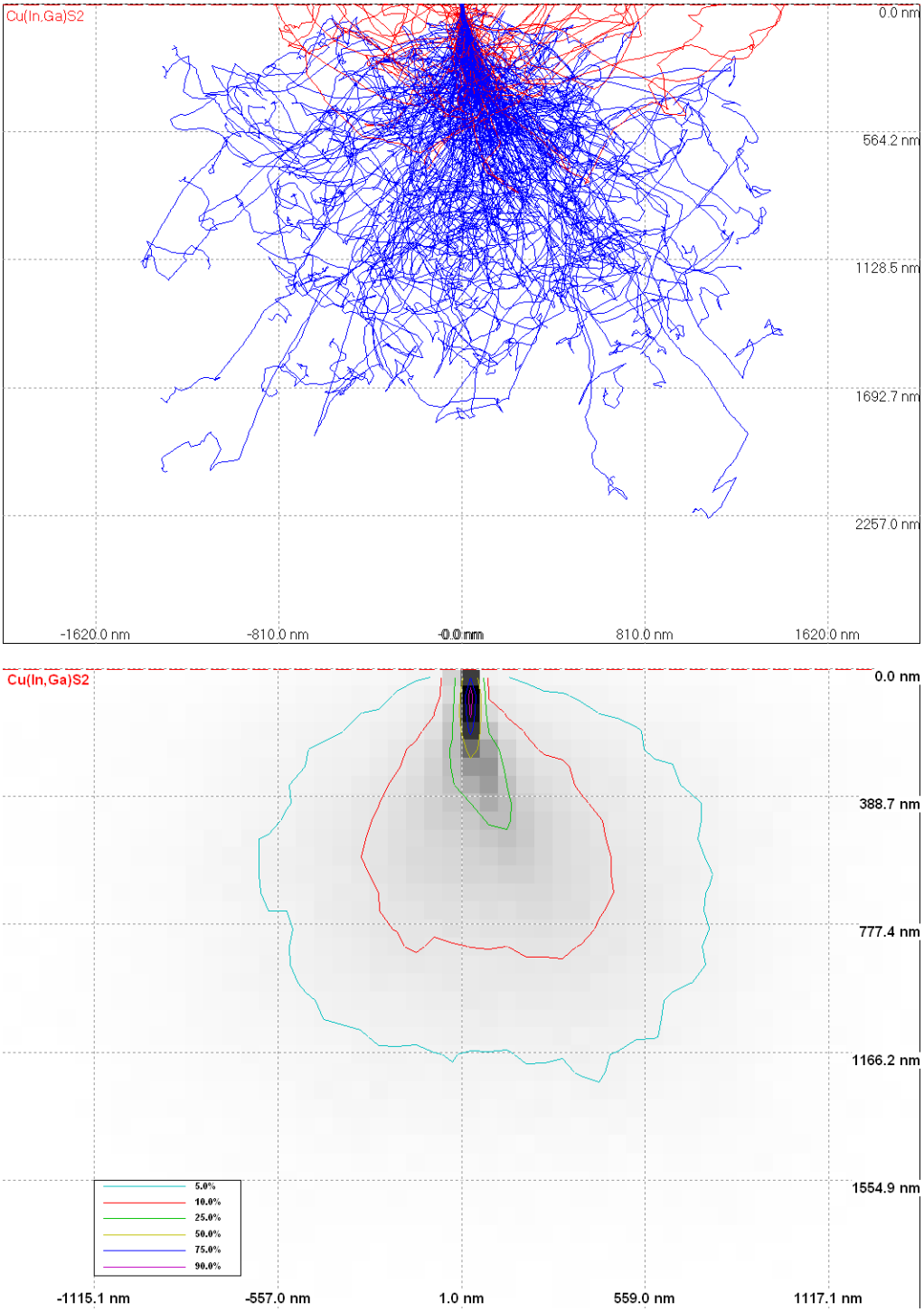

Figure A12: CASINO ("monte CArlo SImulation of electroN trajectory in sOlids") simulation of secondary and backscattered electron beam in a Cu(In,Ga)S_2 absorber at 20kV [209].

Appendix 5: SIMS measurement on phase-segregated Cu(In,Ga)S2 absorbers

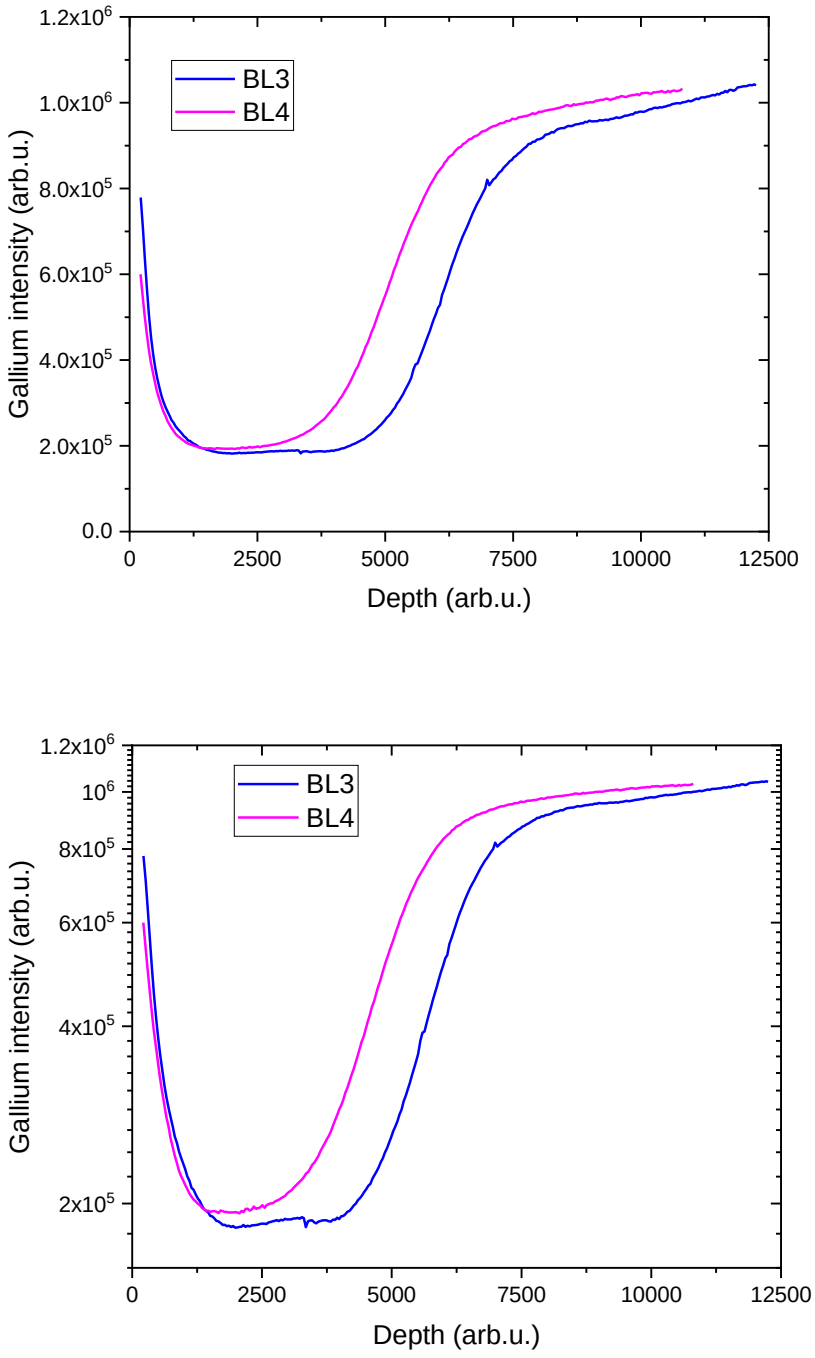

Figure A13: Ga profile from SIMS depth analysis in linear (top) and logarithm (bottom) scale of Cu(In,Ga)S_2 absorbers with phase segregation.

Appendix 6: Quantitative EDX mappings of the cross sections of BL1 and BL3

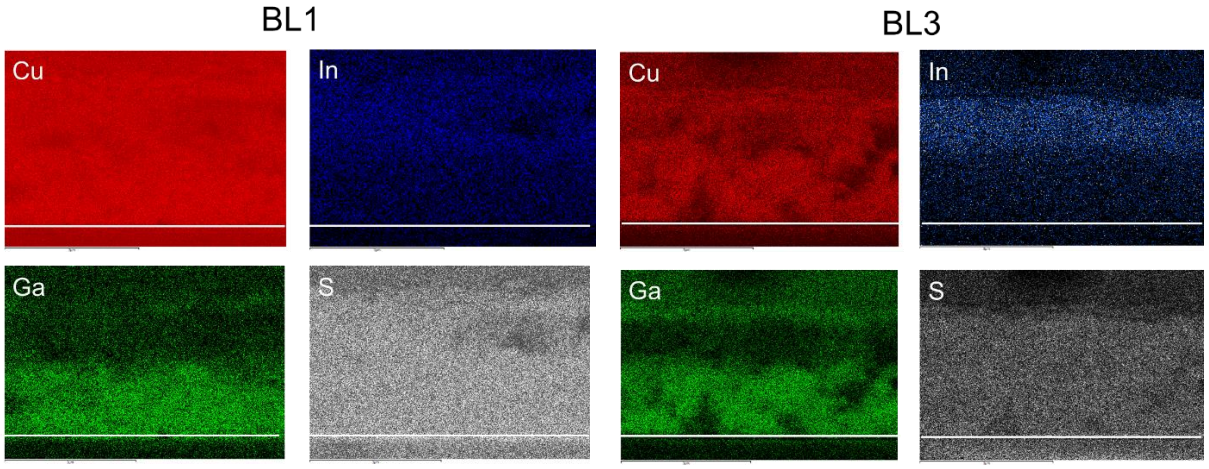

Figure A14: Quantitative EDX mapping of the cross-section of absorbers with phase segregation.

Appendix 7: Temperature dependence of Cu-rich CuGaS2 spectra

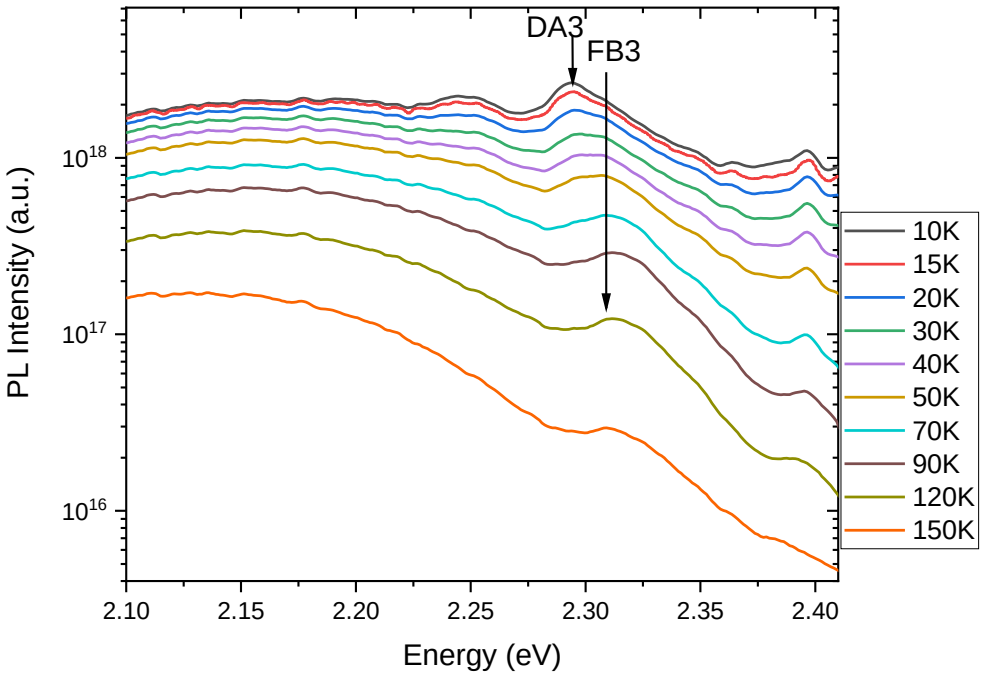

Figure A15: Temperature dependent PL spectra of $CuGaS_2$ between 2.10-2.40 eV showing the temperature-dependent evolution of DA3 and FB3

Appendix 8: SAMPLE LIST

BL1	CIGS312
BL2	CIGS313
BL3	CIGS316
BL4	CIGS317
SC300	CIGS414
SC500	CIGS415
SC650	CIGS417
SC800	CIGS418
SH1	CIGS421
SH2	CIGS422
SH3	CIGS423
GSH2	CIGS424
GSH3	CIGS426
CR1	CIGS432
CR2	CIGS435
CR3	CIGS433,
CR4	CIGS437
CR5	CIGS436
ST	CIGS443
LS1	CIGS370
LS2	CIGS365

List of Publications and Conferences

Publications

First author

1. **Adeleye, D**., Lomuscio, A., Sood, M., & Siebentritt, S. (2021). "Lifetime, quasi-Fermi level splitting and doping concentration of Cu-rich $CuInS_2$ absorbers". Materials Research Express, 8(2), 025905.

2. **Adeleye, D**., Sood, M., Melchiorre, M., & Siebentritt, S. "Compositional dependence of electronic defects in $CuGaS_2$". To be submitted 2023.

3. **Adeleye, D***., Sood, M*., Vanderhaegen, A., Melchiorre, M., Lanzoni, E. M., Torndahl, T., Hultqvist, A. Kusch, K., Oliver, R., & Siebentritt, S. "Mitigation of phase segregation in $Cu(In,Ga)S_2$ for highly efficient high bandgap devices". Under preparation 2023.
   *Equal contibution

Co-author

4. Sood, M., Elanzeery, H., **Adeleye, D**., Lomuscio, A., Werner, F., Ehre, F., ... & Siebentritt, S. (2020). "Absorber composition: A critical parameter for the effectiveness of heat treatments in chalcopyrite solar cells". Progress in Photovoltaics: Research and Applications, 28(10), 1063-1076.

5. Chu, V. B., Siopa, D., Debot, A., **Adeleye, D.**, Sood, M., Lomuscio, A., ... & Dale, P. J. (2021). "Waste-and Cd-free inkjet-printed Zn (O, S) buffer for Cu (In, Ga)(S, Se) 2 thin-film solar cells". ACS Applied Materials & Interfaces, 13(11), 13009-13021.

6. Shukla, S., **Adeleye, D**., Sood, M., Ehre, F., Lomuscio, A., Weiss, T. P., ... & Siebentritt, S. (2021). "Carrier recombination mechanism and photovoltage deficit in 1.7-eV band gap near-stoichiometric Cu (In, Ga) S 2". Physical Review Materials, 5(5), 055403.

7. Shukla, S., Sood, M., **Adeleye, D.**, Peedle, S., Kusch, G., Dahliah, D., ... & Siebentritt, S. (2021). "Over 15% efficient wide-band-gap Cu (In, Ga) S2 solar cell: Suppressing bulk and interface recombination through composition engineering". Joule, 5(7), 1816-1831.

8. Debot, A., Chu, V. B., **Adeleye, D**., Guillot, J., Arl, D., Melchiorre, M., & Dale, P. J. (2022). "Inkjet-printed indium sulfide buffer layer for Cu (In, Ga)(S, Se) 2 thin film solar cells". Thin Solid Films, 745, 139096.

9. Siebentritt, S., Lomuscio, A., **Adeleye, D**., Sood, M., & Dwivedi, A. (2022). "Sulfide Chalcopyrite Solar Cells—Are They the Same as Selenides with a Wider Bandgap?". physica status solidi (RRL)–Rapid Research Letters, 16(8), 2200126.

10. Prabhakar, R. R., Moehl, T., Friedrich, D., Kunst, M., Shukla, S., **Adeleye, D**., ... & Tilley, S. D. (2022). "Sulfur-Treatment Passivates Bulk Defects in Sb2Se3 Photocathodes for Water Splitting". Advanced Functional Materials, 2112184.

11. Sood, M., **Adeleye, D.**, Shukla, S., Törndahl, T., Hultqvist, A., & Siebentritt, S. (2022). "Low temperature (Zn, Sn) O deposition for reducing interface open-circuit voltage deficit to achieve highly efficient Se-free Cu (In, Ga) S 2 solar cells". Faraday Discussions.

12. Siebentritt, S., Rau, U., Gharabeiki, S., Weiss, T. P., Prot, A., Wang, T., **Adeleye, D.**, Drahem, M., & Singh, A. (2022). "Photoluminescence assessment of materials for solar cell absorbers". Faraday Discussions.

13. Sood, M., Gnanasambandan, P., **Adeleye, D.**, Shukla, S., Adjeroud, N., Leturcq, R., & Siebentritt, S. (2022). "Electrical barriers and their elimination by tuning (Zn, Mg) O buffer composition in Cu (In, Ga) S2 solar cells: systematic approach to achieve over 14% power conversion efficiency". Journal of Physics: Energy, 4(4), 045005.

14. Peedle, S., **Adeleye, D.**, Shukla, S., Siebentritt, S., Oliver, R., & Kusch, G. "Role of Nanoscale Compositional Inhomogeneities in Limiting The Open-circuit Voltage in $Cu(In,Ga)S_2$ Solar Cells". Under review 2022

Conferences

Oral presentation

1. **Adeleye, D.,** Sood, M., Shukla, S., Melchiorre, M., & Siebentritt, S. 1 eV quasi-Fermi level splitting in pure-sulfide $Cu(In,Ga)S_2$ absorber. EMRS Spring Meeting 2021, Virtual conference.

2. **Adeleye, D.,** Sood, M., Shukla, S., Melchiorre, M., & Siebentritt, S. Adding Ga is important to get good sulfide chalcopyrite solar cells. EU-PVSEC 2021, Virtual conference.

Poster presentation

3. Adeleye, D., Sood, M., Melchiorre, M., Siebentritt, S. "Optical characterization of defects in CuGaS2 absorber grown by physical vapour deposition." MASSENAYSC2021, Luxembourg, 2021.

Acknowledgements

In many ways, a lot of people contributed to the making of this thesis, directly and/or indirectly, and I appreciate the efforts and the impacts of everyone.

I would like to express my gratitude to Susanne Siebentritt who guided me through this research. Thank you for giving me the opportunity to work on this interesting project. I could always count on her knowledge and guidance from the outset; her keen insights helped sort ideas when lost in details. Notwithstanding her full calendar and busy schedule, she always made time for discussions and seeing to the progress of the project, besides that, her doors were always open for impromptu discussions. She also showed concern for one's personal growth and development.

I am thankful to Emmanuel Defay and Levent Gütay, the other members of my thesis supervision committee, who always had interesting suggestions during the CET meetings. I thank Nicolas Barreau and Alex Redinger for accepting to be part of my dissertation defence committee.

Truly, this was a laborious albeit gratifying project which could not have been rewarding without the teams I worked with. Many thanks to the (past) members of the Sulfides team (Mohit, Sudhanshu, Alberto, Michele, and Aradhana) who I have had the pleasure of working with, with some sense of camaraderie. Thank you to Mohit Sood for the discussions on device characteristics, and for performing electrical characterizations and buffer optimization on the solar cells; looking over the monitors was all the announcement of an incoming conversation. Thank you to Sudhanshu Shukla who was the literal "company in misery" at the beginning when faced with several challenges with the new PVD system. Through the bittersweet moments, we could talk about wide-ranging topics, exchange knowledge and had (fun) work-trips with Thomas; some catchphrases still survived. Many thanks to Alberto Lomuscio whose knowledge of PVD was helpful in inaugurating the PVD system and who introduced me to the co-evaporation technique. Alberto also introduced me to the photoluminescence measurements and analyses. I thank Michele Melchiorre who is always reliable for all the Mo depositions, etching procedures, SEM and EDX analyses, device completions and who was the go-to person for chemical procedures. Also, thank you to Aline Vanderhaegen who performed the lifetime measurements on the absorbers presented in Section 6.4, and thanks for the introduction to squash.

To the present and past colleagues from the LPV, LEM and SPM teams, thank you for the discussions, suggestions and the cordial atmosphere: Sevan, Valentina (who I took a few trips with), Taowen, Aubin, Omar, Alice, Hasan, Ricardo, Joana, Jonathan, Himanshu, Evandro, Uzair, Ajay, Robert, Shilpi (who proofread my thesis), Thomas Paul (who made us a "white elephant"), Conrad (who introduced me to the TRPL set-up), Daniel (who helped with EDX), Thibaut, Ben, Florian, Max, Christian. Also, thank you to colleagues from LIST whom I either worked with or enjoyed conversations with; Emmanuella, Christina, Youri, Nikhah, Robert, Rutuja, Vishnu, etc.

Thank you to Patricia Ramoa for taking care of the administrative work and entertaining some "minutes of disturbance". I thank Thomas Schuler who I could readily consult for advice on technical issues on the PVD; his genius somehow and sometimes perform magic.

Also, I thank Ulrich Siegel, Olga Astasheva and Robert Himelrick who always offered technical support at Campus Limpertsberg.

I would like to thank collaborators from the GaN laboratory of Cambridge university for all the cathodoluminescence experiments and discussions on this analytical technique: Dr. Gunnar Kusch, Benson Chun Pang Law and Prof. Rachel Oliver. I also thank Dr. Tobias Törndahl and Dr. Adam Hultqvist from the Angstrom lab of Uppsala University who performed (Zn,Sn)O depositions on our absorber layers. Thank you to Dr. Mael Guennou for Raman spectroscopy on $CuGaS_2$.

A special thank you to Mr. Matthew, Ms. Joyce, Tobi, Moses, Aisha Bola, Azmah, Tosin, Adewumi, Martinson, Michael, and Justice for the interest in my project and its development. To friends, thank you for making my stay in Luxembourg fun and memorable through various well-planned or spontaneous activities, get-togethers, travels, sports, cultural exchanges, conversations, and a lot more.

A big thank you to my family. Thank you for always taking care of me, particularly during difficult moments, and helping me get back up after setbacks. Your unconditional love means so much to me. To my parents, who inspired me and encouraged me to pursue my dreams, your unwavering support always gives me the motivation and strength to face challenges. To my dependable sister, who always has time to give some wise counsel and give me different perspectives.

Lastly, there are many more people that I have not mentioned here; I thank you very much for your contributions, act of kindness, generosity, and considerations.

Bibliography

[1] H. Ritchie, M. Roser, Natural disasters, Online Resource, DOI https://ourworldindata.org/natural-disasters(2014).

[2] UN, Climate Change Around The World: A View From The UN Regional Commissions, XLIV, No. 2 (2007).

[3] M. Becker, M. Sauga, "The Coming Winter Could Be One of the Worst in History", Web Page, DOI https://www.spiegel.de/international/business/european-commissioner-gentiloni-the-coming-winter-could-be-one-of-the-worst-in-history-a-547f9ef7-9796-4d28-985f-c8b4cc3a26c4(2022).

[4] J. Yeung, A. Renton, R. Picheta, E. Upright, A. Sangal, A. Vogt, M. Macaya, M. Chowdhury, CNN, Russia attacks Ukraine, Web Page, DOI https://edition.cnn.com/europe/live-news/ukraine-russia-news-02-23-22/h_82bf44af2f01ad57f81c0760c6cb697c(2022).

[5] P. Wintor, 'We were all wrong': how Germany got hooked on Russian energy, Web Page, DOI https://www.theguardian.com/world/2022/jun/02/germany-dependence-russian-energy-gas-oil-nord-stream(2022).

[6] L. Alderman, P. Cohen, Europe braces for a winter without Russian gas, Web Page, DOI https://www.nytimes.com/2022/11/01/business/europe-energy-crisis.html(2022).

[7] T.T.E. Parliament, Inflation in the wake of coronavirus and war [What Think Tanks are thinking], Web Page, DOI https://www.europarl.europa.eu/thinktank/en/document/EPRS_BRI(2022)729336.

[8] U. nations, Paris Agreement, Web Page, DOI https://unfccc.int/sites/default/files/english_paris_agreement.pdf(2015).

[9] OurWorldinData, Installed solar energy capacity, Web Page, DOI https://ourworldindata.org/grapher/installed-solar-pv-capacity.

[10] O.W.i. Data, Solar PV module prices, DOI https://ourworldindata.org/grapher/solar-pv-prices.

[11] M. Nakamura, K. Yamaguchi, Y. Kimoto, Y. Yasaki, T. Kato, H. Sugimoto, Cd-Free Cu(In,Ga)(Se,S)2 Thin-Film Solar Cell With Record Efficiency of 23.35%, IEEE Journal of Photovoltaics, 9 (2019) 1863-1867.

[12] F. ISE, PHOTOVOLTAICS REPORT, DOI https://www.ise.fraunhofer.de/content/dam/ise/de/documents/publications/studies/Photovoltaics-Report.pdf(2022).
[13] W. Shockley, H.J. Queisser, Detailed balance limit of efficiency of p-n junction solar cells, J. Appl. Phys., 32 (1961) 510-519.
[14] S. Rühle, Tabulated values of the Shockley–Queisser limit for single junction solar cells, Solar energy, 130 (2016) 139-147.
[15] A. Al-Ashouri, E. Köhnen, B. Li, A. Magomedov, H. Hempel, P. Caprioglio, J.A. Márquez, A.B. Morales Vilches, E. Kasparavicius, J.A. Smith, Monolithic perovskite/silicon tandem solar cell with> 29% efficiency by enhanced hole extraction, Science, 370 (2020) 1300-1309.
[16] R.K. Kothandaraman, Y. Jiang, T. Feurer, A.N. Tiwari, F. Fu, Near-infrared-transparent perovskite solar cells and perovskite-based tandem photovoltaics, Small Methods, 4 (2020) 2000395.
[17] G.E. Eperon, M.T. Hörantner, H.J. Snaith, Metal halide perovskite tandem and multiple-junction photovoltaics, Nature Reviews Chemistry, 1 (2017) 1-18.
[18] M. Jošt, E. Köhnen, A. Al-Ashouri, T. Bertram, S.p. Tomšič, A. Magomedov, E. Kasparavicius, T. Kodalle, B. Lipovšek, V. Getautis, Perovskite/CIGS Tandem Solar Cells: From Certified 24.2% toward 30% and Beyond, ACS Energy Letters, 7 (2022) 1298-1307.
[19] J. Liu, M. De Bastiani, E. Aydin, G.T. Harrison, Y. Gao, R.R. Pradhan, M.K. Eswaran, M. Mandal, W. Yan, A. Seitkhan, Efficient and stable perovskite-silicon tandem solar cells through contact displacement by MgF x, Science, 377 (2022) 302-306.
[20] G. Nagabhushana, R. Shivaramaiah, A. Navrotsky, Direct calorimetric verification of thermodynamic instability of lead halide hybrid perovskites, Proceedings of the National Academy of Sciences, 113 (2016) 7717-7721.
[21] B. Tell, J.L. Shay, H.M. Kasper, Electrical Properties, Optical Properties, and Band Structure of CuGaS2and CuInS2, Physical Review B, 4 (1971) 2463-2471.
[22] S. Siebentritt, High voltage, please!, Nature Energy, 2 (2017) 840-841.
[23] S. Albrecht, B. Rech, Perovskite solar cells: On top of commercial photovoltaics, Nature Energy, 2 (2017) 1-2.

[24] H. Hiroi, Y. Iwata, S. Adachi, H. Sugimoto, A. Yamada, New World-Record Efficiency for Pure-Sulfide Cu(In,Ga)S2 Thin-Film Solar Cell with Cd-Free Buffer Layer via KCN-Free Process, IEEE Journal of Photovoltaics, 6 (2016) 760-763.
[25] P. Jackson, R. Wuerz, D. Hariskos, E. Lotter, W. Witte, M. Powalla, Effects of heavy alkali elements in Cu (In, Ga) Se2 solar cells with efficiencies up to 22.6%, physica status solidi (RRL)–Rapid Research Letters, 10 (2016) 583-586.
[26] A. Lomuscio, Optical Defect Spectroscopy in CuInS2 Thin Films and Solar Cells, University of Luxembourg, Esch-sur-Alzette, Luxembourg, 2020.
[27] A. Lomuscio, T. Rödel, T. Schwarz, B. Gault, M. Melchiorre, D. Raabe, S. Siebentritt, Quasi-Fermi-Level Splitting of Cu-Poor and Cu-Rich Cu In S 2 Absorber Layers, Physical Review Applied, 11 (2019) 054052.
[28] N. Barreau, E. Bertin, A. Crossay, O. Durand, L. Arzel, S. Harel, T. Lepetit, L. Assmann, E. Gautron, D. Lincot, Investigation of co-evaporated polycrystalline Cu (In, Ga) S2 thin film yielding 16.0% efficiency solar cell, EPJ Photovoltaics, 13 (2022) 17.
[29] A. Thomere, N. Barreau, N. Stephant, C. Guillot-Deudon, E. Gautron, M. Caldes, A. Lafond, Formation of Cu (In, Ga) S2 chalcopyrite thin films following a 3-stage co-evaporation process, Solar Energy Materials and Solar Cells, 237 (2022) 111563.
[30] N. Barreau, A. Thomere, D. Cammilleri, A. Crossay, C. Guillot-Deudon, A. Lafond, N. Stéphant, D. Lincot, M.T. Caldes, R. Bodeux, B. Bérenguier, High efficiency solar cell based on Cu(In,Ga)S2 thin film grown by 3-stage process, 2020 47th IEEE Photovoltaic Specialists Conference (PVSC), 2020, pp. 1715-1718.
[31] A. Thomere, C. Guillot-Deudon, M. Caldes, R. Bodeux, N. Barreau, S. Jobic, A. Lafond, Chemical crystallographic investigation on Cu2S-In2S3-Ga2S3 ternary system, Thin Solid Films, 665 (2018) 46-50.
[32] J.L. Shay, J.H. Wernick, Ternary chalcopyrite semiconductors: growth, electronic properties, and applications: international series of monographs in the science of the solid state, Elsevier2017.
[33] J.E. Jaffe, A. Zunger, Electronic structure of the ternary chalcopyrite semiconductors CuAlS2, CuGaS2, CuInS2, CuAlSe2, CuGaSe2, and CuInSe2, Physical Review B, 28 (1983) 5822-5847.

[34] D. Abou-Ras, R. Caballero, C. Kaufmann, M. Nichterwitz, K. Sakurai, S. Schorr, T. Unold, H. Schock, Impact of the Ga concentration on the microstructure of CuIn1–x Gax Se2, physica status solidi (RRL)–Rapid Research Letters, 2 (2008) 135-137.
[35] I. Bodnar, A. Lukomskii, The Concentration Dependence of the Band Gap for CuGaxIn1-xS2 and AgGaxIn1-xS2 Solid Solutions, physica status solidi (a), 98 (1986) K165-K169.
[36] M. Kokta, J. Carruthers, M. Grasso, H. Kasper, B. Tell, Ternary phase relations in the vicinity of chalcopyrite copper gallium sulfide, Journal of Electronic Materials, 5 (1976) 69-89.
[37] T. Maeda, Y. Yu, Q. Chen, K. Ueda, T. Wada, Crystallographic and optical properties and band diagrams of CuGaS2and CuGa5S8phases in Cu-poor Cu2S–Ga2S3pseudo-binary system, Japanese Journal of Applied Physics, 56 (2017).
[38] K. Ueda, T. Maeda, T. Wada, Crystallographic and optical properties of CuGa3S5, CuGa3Se5 and CuIn3(S,Se)5 and CuGa3(S,Se)5 systems, Thin Solid Films, 633 (2017) 23-30.
[39] H. Miyake, K. Sugiyama, Phase diagram of the CuGaS2-In pseudobinary system, Japanese journal of applied physics, 29 (1990) L998.
[40] J. Binsma, L. Giling, J. Bloem, Phase relations in the system Cu2S-In2S3, Journal of Crystal Growth, 50 (1980) 429-436.
[41] M.T. Caldes, C. Guillot-Deudon, A. Thomere, M. Penicaud, E. Gautron, P. Boullay, M. Bujoli-Doeuff, N. Barreau, S. Jobic, A. Lafond, Layered Quaternary Compounds in the Cu2S–In2S3–Ga2S3 system, Inorganic Chemistry, 59 (2020) 4546-4553.
[42] M. Cardona, Y.Y. Peter, Fundamentals of semiconductors, Springer2005.
[43] S. Siebentritt, M. Igalson, C. Persson, S. Lany, The electronic structure of chalcopyrites—bands, point defects and grain boundaries, Progress in Photovoltaics: Research and Applications, 18 (2010) 390-410.
[44] C.L. Bailey, L. Liborio, G. Mallia, S. Tomić, N.M. Harrison, Defect physics ofCuGaS2, Physical Review B, 81 (2010).
[45] D.A. Neamen, Semiconductor physics and devices: basic principles, New York, NY: McGraw-Hill2012.
[46] R.K. Ahrenkiel, Minority-Carrier Lifetime in III–V, Semiconductors and semimetals, DOI (1993) 39.
[47] S.M. Sze, K.K. Ng, Physics of semiconductor devices, John wiley & sons2006.
[48] J.A. Nelson, The physics of solar cells, World Scientific Publishing Company2003.

[49] J.I. Pankove, Optical processes in semiconductors, Dover Publications (1975).
[50] I. Pelant, J. Valenta, Luminescence spectroscopy of semiconductors, Oxford University Press2012.
[51] P. Würfel, U. Würfel, Physics of solar cells: from basic principles to advanced concepts, John Wiley & Sons2016.
[52] S. Siebentritt, U. Rau, S. Gharabeiki, T.P. Weiss, A. Prot, T. Wang, D. Adeleye, M. Drahem, A. Singh, Photoluminescence assessment of materials for solar cell absorbers, Faraday Discussions, DOI (2022).
[53] P. Wurfel, The chemical potential of radiation, Journal of Physics C: Solid State Physics, 15 (1982) 3967.
[54] R. Carron, E. Avancini, T. Feurer, B. Bissig, P.A. Losio, R. Figi, C. Schreiner, M. Bürki, E. Bourgeois, Z. Remes, Refractive indices of layers and optical simulations of Cu (In, Ga) Se2 solar cells, Science and Technology of advanced MaTerialS, 19 (2018) 396-410.
[55] R.T. Ross, Some thermodynamics of photochemical systems, The Journal of Chemical Physics, 46 (1967) 4590-4593.
[56] U. Rau, Reciprocity relation between photovoltaic quantum efficiency and electroluminescent emission of solar cells, Physical Review B, 76 (2007) 085303.
[57] J.L. Shay, B. Tell, H.M. Kasper, Visible Stimulated Emission in Ternary Chalcopyrite Sulfides and Selenides, Applied Physics Letters, 19 (1971) 366-368.
[58] G. Massé, Luminescence of CuGaS2, Journal of Applied Physics, 58 (1985) 930-935.
[59] G. Massé, Time resolved spectra in CuGaS2, physica status solidi (a), 87 (1985) K171-K173.
[60] M. Yagi, T. Terasako, N. Tsuboi, S. Iida, Deep Region Emissions of CuGaS2Crystals, Japanese Journal of Applied Physics, 32 (1993) 618.
[61] S. Shirakata, K. Saiki, S. Isomura, Excitonic photoluminescence in CuGaS2crystals, Journal of Applied Physics, 68 (1990) 291-297.
[62] S. Shirakata, S. Isomura, Photoluminescence Line at 2.29 eV in CuGaS2 Crystal, Japanese journal of applied physics, 30 (1991) 1666.
[63] S. Chichibu, S. Shirakata, M. Uchida, Y. Harada, T. Wakiyama, S. Matsumoto, H. Higuchi, S. Isomura, Heteroepitaxial growth of CuGaS 2 layers by low-pressure metalorganic chemical vapor deposition, Japanese journal of applied physics, 34 (1995) 3991.

[64] S. Shirakata, S. Chichibu, Photoluminescence of CuGaS2 epitaxial layers grown by metalorganic vapor phase epitaxy, Journal of Applied Physics, 87 (2000) 3793-3799.
[65] J. Eberhardt, H. Metzner, T. Hahn, U. Reislöhner, J. Cieslak, U. Grossner, R. Goldhahn, F. Hudert, G. Gobsch, W. Witthuhn, Optical properties of epitaxial CuGaS2 layers on Si(111), Journal of Physics and Chemistry of Solids, 64 (2003) 1781-1785.
[66] H. Metzner, J. Cieslak, U. Grossner, T. Hahn, U. Kaiser, J. Kräußlich, U. Reislöhner, W. Witthuhn, R. Goldhahn, J. Eberhardt, Structural and optical properties of epitaxial CuGaS2 films on Si substrates, Thin Solid Films, 431-432 (2003) 219-222.
[67] H. Metzner, T. Hahn, J. Cieslak, U. Grossner, U. Reislöhner, W. Witthuhn, R. Goldhahn, J. Eberhardt, G. Gobsch, J. Kräußlich, Epitaxial growth of CuGaS2 on Si(111), Applied Physics Letters, 81 (2002) 156-158.
[68] M.S. Branch, P.R. Berndt, J.R. Botha, A.W.R. Leitch, J. Weber, Structure and morphology of CuGaS2 thin films, Thin Solid Films, 431-432 (2003) 94-98.
[69] J.R. Botha, M.S. Branch, A.W.R. Leitch, J. Weber, Radiative defects in CuGaS2 thin films, Physica B: Condensed Matter, 340-342 (2003) 923-927.
[70] J.R. Botha, M.S. Branch, J. Weber, Steady state and time-resolved photoluminescence characterisation of copper gallium disulphide, Thin Solid Films, 431-432 (2003) 210-213.
[71] M.S. Branch, P.R. Berndt, A.W.L. Leitch, J. Weber, J.R. Botha, An investigation into the ordering of metal atoms in CuGaS2 grown by MOVPE, physica status solidi (a), 201 (2004) 2239-2244.
[72] M.S. Branch, P.R. Berndt, A.W.R. Leitch, J.R. Botha, J. Weber, Structural and optical characterisation of CuGaS2 thin films grown by MOVPE, Thin Solid Films, 480-481 (2005) 188-194.
[73] M.S. Branch, P.R. Berndt, A.W.R. Leitch, J.R. Botha, J. Weber, The influence of growth parameters on the structure and composition of CuGaS2 epilayers grown by MOVPE, Physica B: Condensed Matter, 376-377 (2006) 803-807.
[74] J.R. Botha, M.S. Branch, P.R. Berndt, A.W.R. Leitch, J. Weber, Defect chemistry in CuGaS2 thin films: A photoluminescence study, Thin Solid Films, 515 (2007) 6246-6251.
[75] M.S. Branch, Epitaxial growth and characterisation of CuGaS2, DOI (2006).

[76] J. Mooney, P. Kambhampati, Get the basics right: Jacobian conversion of wavelength and energy scales for quantitative analysis of emission spectra, ACS Publications, 2013, pp. 3316-3318.
[77] R. Scheer, H.-W. Schock, Chalcogenide photovoltaics: physics, technologies, and thin film devices, John Wiley & Sons2011.
[78] F. Kessler, D. Rudmann, Technological aspects of flexible CIGS solar cells and modules, Solar energy, 77 (2004) 685-695.
[79] A. Chirilă, S. Buecheler, F. Pianezzi, P. Bloesch, C. Gretener, A.R. Uhl, C. Fella, L. Kranz, J. Perrenoud, S. Seyrling, Highly efficient Cu (In, Ga) Se 2 solar cells grown on flexible polymer films, Nature materials, 10 (2011) 857-861.
[80] Y. Zhang, S. Lin, Z. Hu, S. Cheng, Z. He, Z. Zhou, S. Sun, W. Liu, Y. Sun, Towards an optimized gallium gradient for Cu (In, Ga) Se2 thin film via an improved constant low-temperature deposition process, Solar Energy Materials and Solar Cells, 209 (2020) 110425.
[81] A. Luque, S. Hegedus, Handbook of photovoltaic science and engineering, John Wiley & Sons2011.
[82] J. Hedstrom, H. Ohlsen, M. Bodegard, A. Kylner, L. Stolt, D. Hariskos, M. Ruckh, H.-W. Schock, ZnO/CdS/Cu (In, Ga) Se/sub 2/thin film solar cells with improved performance, Conference Record of the Twenty Third IEEE Photovoltaic Specialists Conference-1993 (Cat. No. 93CH3283-9), IEEE, 1993, pp. 364-371.
[83] L. Stolt, J. Hedström, J. Kessler, M. Ruckh, K.O. Velthaus, H.W. Schock, ZnO/CdS/CuInSe2 thin-film solar cells with improved performance, Applied Physics Letters, 62 (1993) 597-599.
[84] A. Hultqvist, P.M. Salomé, V. Fjällström, M. Edoff, B. Aitken, K. Zhang, Y. Shi, K. Fuller, C.K. Williams, Performance of Cu (In, Ga) Se2 solar cells using nominally alkali free glass substrates with varying coefficient of thermal expansion, Journal of Applied Physics, 114 (2013) 094501.
[85] D. Abou-Ras, G. Kostorz, D. Bremaud, M. Kälin, F. Kurdesau, A. Tiwari, M. Döbeli, Formation and characterisation of MoSe2 for Cu (In, Ga) Se2 based solar cells, Thin Solid Films, 480 (2005) 433-438.
[86] N. Kohara, S. Nishiwaki, Y. Hashimoto, T. Negami, T. Wada, Electrical properties of the cu (in, ga) se2/MoSe2/mo structure, Solar Energy Materials and Solar Cells, 67 (2001) 209-215.

[87] V. Brus, I. Orletsky, M. Ilashchuk, P. Maryanchuk, Electrical properties of thin-film semiconductor heterojunctions n-TiO2/p-CuInS2, Semiconductors, 48 (2014) 1046-1050.
[88] K.L. Chopra, P.D. Paulson, V. Dutta, Thin-film solar cells: an overview, Progress in Photovoltaics: Research and Applications, 12 (2004) 69-92.
[89] L. Weinhardt, O. Fuchs, D. Groß, G. Storch, E. Umbach, N. Dhere, A. Kadam, S. Kulkarni, C. Heske, Band alignment at the CdS⁄Cu (In, Ga) S 2 interface in thin-film solar cells, Applied Physics Letters, 86 (2005) 062109.
[90] M. Sood, Interface Open-Circuit Voltage Deficit In Cu (In, Ga) S2 Solar Cell: Characterization, Simulation and Mitigation, Doctoral dissertation. University of Luxembourg, Esch-sur-Alzette, Luxembourg, 2021.
[91] B. Misic, B. Pieters, J. Theisen, A. Gerber, U. Rau, Shunt mitigation in ZnO: Al/i-ZnO/CdS/Cu (In, Ga) Se2 solar modules by the i-ZnO/CdS buffer combination, physica status solidi (a), 212 (2015) 541-546.
[92] T. Feurer, P. Reinhard, E. Avancini, B. Bissig, J. Löckinger, P. Fuchs, R. Carron, T.P. Weiss, J. Perrenoud, S. Stutterheim, Progress in thin film CIGS photovoltaics–Research and development, manufacturing, and applications, Progress in Photovoltaics: Research and Applications, 25 (2017) 645-667.
[93] U. Rau, H.-W. Schock, Electronic properties of Cu (In, Ga) Se2 heterojunction solar cells–recent achievements, current understanding, and future challenges, Applied Physics A, 69 (1999) 131-147.
[94] D. König, K. Casalenuovo, Y. Takeda, G. Conibeer, J.F. Guillemoles, R. Patterson, L.M. Huang, M.A. Green, Hot carrier solar cells: Principles, materials and design, Physica E: Low-dimensional Systems and Nanostructures, 42 (2010) 2862-2866.
[95] F. Babbe, Optical Analysis of Efficiency Limitations of Cu (In, Ga) Se2 grown under Copper Excess, University of Luxembourg, Esch-sur-Alzette, Luxembourg, 2019.
[96] A. Klein, Energy band alignment in chalcogenide thin film solar cells from photoelectron spectroscopy, Journal of physics: Condensed matter, 27 (2015) 134201.
[97] R. Kaigawa, A. Ohyama, T. Wada, R. Klenk, Electrical properties of homogeneous Cu (In, Ga) S2 films with varied gallium content, Thin Solid Films, 515 (2007) 6260-6264.
[98] R. Kaigawa, A. Neisser, R. Klenk, M.-C. Lux-Steiner, Improved performance of thin film solar cells based on Cu (In, Ga) S2, Thin Solid Films, 415 (2002) 266-271.

[99] K.F. Tai, R. Kamada, T. Yagioka, T. Kato, H. Sugimoto, From 20.9 to 22.3% Cu (In, Ga)(S, Se) 2 solar cell: Reduced recombination rate at the heterojunction and the depletion region due to K-treatment, Japanese Journal of Applied Physics, 56 (2017) 08MC03.
[100] O. Lundberg, Band gap profiling and high speed deposition of Cu (In, Ga) Se2 for thin film solar cells, Acta Universitatis Upsaliensis, 2003.
[101] O. Lundberg, M. Edoff, L. Stolt, The effect of Ga-grading in CIGS thin film solar cells, Thin Solid Films, 480 (2005) 520-525.
[102] T. Dullweber, O. Lundberg, J. Malmström, M. Bodegård, L. Stolt, U. Rau, H.-W. Schock, J.H. Werner, Back surface band gap gradings in Cu (In, Ga) Se2 solar cells, Thin Solid Films, 387 (2001) 11-13.
[103] W. Witte, D. Abou-Ras, K. Albe, G.H. Bauer, F. Bertram, C. Boit, R. Brüggemann, J. Christen, J. Dietrich, A. Eicke, D. Hariskos, M. Maiberg, R. Mainz, M. Meessen, M. Müller, O. Neumann, T. Orgis, S. Paetel, J. Pohl, H. Rodriguez-Alvarez, R. Scheer, H.-W. Schock, T. Unold, A. Weber, M. Powalla, Gallium gradients in Cu(In,Ga)Se2 thin-film solar cells, Progress in Photovoltaics: Research and Applications, 23 (2015) 717-733.
[104] T.M. Friedlmeier, P. Jackson, A. Bauer, D. Hariskos, O. Kiowski, R. Menner, R. Wuerz, M. Powalla, High-efficiency Cu (In, Ga) Se2 solar cells, Thin Solid Films, 633 (2017) 13-17.
[105] D.M. Mattox, Handbook of physical vapor deposition (PVD) processing, William Andrew2010.
[106] K.S. Harsha, Principles of vapor deposition of thin films, Elsevier2005.
[107] N. Koteeswara Reddy, K. Ramesh, R. Ganesan, K. Ramakrishna Reddy, K. Gunasekhar, E. Gopal, Synthesis and characterisation of co-evaporated tin sulphide thin films, Applied Physics A, 83 (2006) 133-138.
[108] S. Hegde, P. Murahari, B.J. Fernandes, R. Venkatesh, K. Ramesh, Synthesis, thermal stability and structural transition of cubic SnS nanoparticles, Journal of Alloys and Compounds, 820 (2020) 153116.
[109] R. Scheer, T. Walter, H. Schock, M. Fearheiley, H. Lewerenz, CuInS2 based thin film solar cell with 10.2% efficiency, Applied Physics Letters, 63 (1993) 3294-3296.
[110] S. Shukla, M. Sood, D. Adeleye, S. Peedle, G. Kusch, D. Dahliah, M. Melchiorre, G.-M. Rignanese, G. Hautier, R. Oliver, S. Siebentritt, Over 15% efficient wide-band-gap Cu(In,Ga)S2

solar cell: Suppressing bulk and interface recombination through composition engineering, Joule, DOI https://doi.org/10.1016/j.joule.2021.05.004(2021).
[111] R. Hunger, K. Sakurai, A. Yamada, P. Fons, K. Iwata, K. Matsubara, S. Niki, In situ deposition rate monitoring during the three-stage-growth process of Cu(In,Ga)Se2 absorber films, Thin Solid Films, 431-432 (2003) 16-21.
[112] D. Adeleye, A. Lomuscio, M. Sood, S. Siebentritt, Lifetime, quasi-Fermi level splitting and doping concentration of Cu-rich CuInS2 absorbers, Materials Research Express, 8 (2021) 025905.
[113] H. Hiroi, Y. Iwata, K. Horiguchi, H. Sugimoto, 960-mV open-circuit voltage chalcopyrite solar cell, IEEE Journal of Photovoltaics, 6 (2015) 309-312.
[114] A. Lomuscio, M. Melchiorre, S. Siebentritt, Influence of stoichiometry and temperature on quasi Fermi level splitting of sulfide CIS absorber layers, 2018 IEEE 7th World Conference on Photovoltaic Energy Conversion (WCPEC) (A Joint Conference of 45th IEEE PVSC, 2, DOI 10.1109/PVSC.2018.8548252(2018).
[115] T. Unold, L. Gütay, Photoluminescence analysis of thin-film solar cells. Advanced Characterization Techniques for Thin Film Solar Cells, 1 (2016) 275-297.
[116] R.K. Ahrenkiel, Chapter 2 Minority-Carrier Lifetime in III–V Semiconductors, in: R.K. Ahrenkiel, M.S. Lundstrom (Eds.) Minority Carriers In III-V Semiconductors: Physics and Applications, Elsevier1993, pp. 39-150.
[117] B. Ohnesorge, R. Weigand, G. Bacher, A. Forchel, W. Riedl, F.H. Karg, Minority-carrier lifetime and efficiency of Cu(In,Ga)Se2 solar cells, Applied Physics Letters, 73 (1998) 1224-1226.
[118] M. Maiberg, T. Hölscher, S. Zahedi-Azad, W. Fränzel, R. Scheer, Investigation of long lifetimes in Cu(In,Ga)Se2 by time-resolved photoluminescence, Applied Physics Letters, 107 (2015) 122104.
[119] W.K. Metzger, I.L. Repins, M.A. Contreras, Long lifetimes in high-efficiency Cu(In,Ga)Se2 solar cells, Applied Physics Letters, 93 (2008).
[120] S. Kim, T. Nagai, H. Tampo, S. Ishizuka, H. Shibata, Large open-circuit voltage boosting of pure sulfide chalcopyrite Cu(In,Ga)S2 prepared using Cu-deficient metal precursors, Progress in Photovoltaics: Research and Applications, 28 (2020) 816-822.

[121] S. Mora, N. Romeo, L. Tarricone, Minority carriers lifetime measurements in CuInS2 by photoelectromagnetic effect, Solid State Communications, 29 (1979) 155-157.
[122] D.K. Schroder, Semiconductor material and device characterization, John Wiley & Sons2015.
[123] F. Werner, Hall measurements on low-mobility thin films, Journal of Applied Physics, 122 (2017) 135306.
[124] D. Abou-Ras, T. Kirchartz, U. Rau, Advanced characterization techniques for thin film solar cells, John Wiley & Sons2016.
[125] M. Weber, R. Scheer, H. Lewerenz, H. Jungblut, U. Störkel, Microroughness and composition of cyanide-treated CuInS2, Journal of The Electrochemical Society, 149 (2001) G77.
[126] D. Regesch, L. Gütay, J.K. Larsen, V. Deprédurand, D. Tanaka, Y. Aida, S. Siebentritt, Degradation and passivation of CuInSe 2, Applied Physics Letters, 101 (2012) 112108.
[127] D.V. O'Connor, D. Phillips, Time-correlated single photon counting, Academic Press, London; Orlando, 1984.
[128] M. Maiberg, R. Scheer, Theoretical study of time-resolved luminescence in semiconductors. II. Pulsed excitation, Journal of Applied Physics, 116 (2014).
[129] R.K. Ahrenkiel, Chapter 2 Minority-Carrier Lifetime in III–V Semiconductors, in: R.K. Ahrenkiel, M.S. Lundstrom (Eds.) Semiconductors and Semimetals, Elsevier1993, pp. 39-150.
[130] D. O'Connor, W. Ware, J. Andre, Deconvolution of fluorescence decay curves. A critical comparison of techniques, Journal of Physical Chemistry, 83 (1979) 1333-1343.
[131] M. Sood, H. Elanzeery, D. Adeleye, A. Lomuscio, F. Werner, F. Ehre, M. Melchiorre, S. Siebentritt, Absorber composition: A critical parameter for the effectiveness of heat treatments in chalcopyrite solar cells, Progress in Photovoltaics: Research and Applications, 28 (2020) 1063-1076.
[132] A. Redinger, S. Levcenko, C.J. Hages, D. Greiner, C.A. Kaufmann, T. Unold, Time resolved photoluminescence on Cu(In, Ga)Se2 absorbers: Distinguishing degradation and trap states, Applied Physics Letters, 110 (2017).
[133] T. Unold, L. Gütay, Photoluminescence analysis of thin-film solar cells. Advanced Characterization Techniques for Thin Film Solar Cells 1, 1 (2016) 275-297.

[134] F. Babbe, L. Choubrac, S. Siebentritt, Quasi Fermi level splitting of Cu-rich and Cu-poor Cu (In, Ga) Se2 absorber layers, Applied Physics Letters, 109 (2016) 082105.
[135] J. Binsma, L. Giling, J. Bloem, Luminescence of CuInS2: II. Exciton and near edge emission, Journal of Luminescence, 27 (1982) 55-72.
[136] M. Nakamura, K. Yamaguchi, Y. Kimoto, Y. Yasaki, T. Kato, H. Sugimoto, Cd-free Cu (In, Ga)(Se, S) 2 thin-film solar cell with record efficiency of 23.35%, IEEE Journal of Photovoltaics, 9 (2019) 1863-1867.
[137] S. Siebentritt, A. Lomuscio, D. Adeleye, M. Sood, A. Dwivedi, Sulfide Chalcopyrite Solar Cells—Are They the Same as Selenides with a Wider Bandgap?, physica status solidi (RRL) – Rapid Research Letters, 16 (2022) 2200126.
[138] S. Zott, K. Leo, M. Ruckh, H.W. Schock, Photoluminescence of polycrystalline CuInSe2 thin films, Applied physics letters, 68 (1996) 1144-1146.
[139] A. Bauknecht, S. Siebentritt, J. Albert, M.C. Lux-Steiner, Radiative recombination via intrinsic defects in Cu x Ga y Se 2, Journal of Applied Physics, 89 (2001) 4391-4400.
[140] N. Rega, S. Siebentritt, J. Albert, S. Nishiwaki, A. Zajogin, M.C. Lux-Steiner, R. Kniese, M. Romero, Excitonic luminescence of Cu (In, Ga) Se2, Thin Solid Films, 480 (2005) 286-290.
[141] S. Siebentritt, Shallow defects in the wide gap chalcopyrite CuGaSe2, Wide-gap chalcopyrites, DOI (2006) 113-156.
[142] C. Spindler, F. Babbe, M.H. Wolter, F. Ehré, K. Santhosh, P. Hilgert, F. Werner, S. Siebentritt, Electronic defects in Cu(In,Ga)Se2: Towards a comprehensive model, Physical Review Materials, 3 (2019) 090302.
[143] J. Pohl, K. Albe, Intrinsic point defects in CuInSe 2 and CuGaSe 2 as seen via screened-exchange hybrid density functional theory, Physical Review B, 87 (2013) 245203.
[144] S. Shukla, D. Adeleye, M. Sood, F. Ehre, A. Lomuscio, T.P. Weiss, D. Siopa, M. Melchiorre, S. Siebentritt, Carrier recombination mechanism and photovoltage deficit in 1.7-eV band gap near-stoichiometric Cu(In,Ga)S2, Physical Review Materials, 5 (2021) 055403.
[145] A. Lomuscio, M. Sood, M. Melchiorre, S. Siebentritt, Phonon coupling and shallow defects in CuIn S 2, Physical Review B, 101 (2020) 085119.
[146] H. Metzner, J. Eberhardt, J. Cieslak, T. Hahn, R. Goldhahn, U. Reislöhner, W. Witthuhn, Photoluminescence of epitaxial CuGaS2 on Si (111): model for intrinsic defect levels, Thin solid films, 451 (2004) 241-244.

[147] C. Bellabarba, J. Gonzalez, C. Rincon, Optical-absorption spectrum near the exciton band edge in CuGaS2 at 5 K, Phys Rev B Condens Matter, 53 (1996) 7792-7796.
[148] C. Guillen, J. Herrero, CuInS2 and CuGaS2 thin films grown by modulated flux deposition with various Cu contents, physica status solidi (a), 203 (2006) 2438-2443.
[149] C. Guillén, J. Herrero, Characteristics of stacked CuInS2 and CuGaS2 layers as determined by the growth sequence, Thin Solid Films, 515 (2007) 5917-5920.
[150] J. Binsma, L. Giling, J. Bloem, Luminescence of CuInS2: I. The broad band emission and its dependence on the defect chemistry, Journal of Luminescence, 27 (1982) 35-53.
[151] I.V. Bodnar, I.T. Bodnar, A.A. Vaipolin, Growth and morphology of the CuGaS2, CuAlSe2, CuGaSe2 and CuInS2 ternary compounds, Crystal Research and Technology, 19 (1984) 1553-1557.
[152] H. Matsushita, S.E.S. Endo, T.I.T. Irie, Thermodynamical properties of I-III-VI2-group chalcopyrite semiconductors, Japanese journal of applied physics, 30 (1991) 1181.
[153] C. Rincón, Deby temperature and melting point in AIBIIIC2VI and AIIBIVC2V chalcopyrite compounds, physica status solidi (a), 134 (1992) 383-389.
[154] M. Klenk, O. Schenker, V. Alberts, E. Bucher, Preparation of device quality chalcopyrite thin films by thermal evaporation of compound materials, Semiconductor science and technology, 17 (2002) 435.
[155] R. Caballero, C. Guillén, Comparative studies between Cu□ Ga□ Se and Cu□ In□ Se thin film systems, Thin Solid Films, 403 (2002) 107-111.
[156] S. Ishizuka, A. Yamada, P. Fons, S. Niki, Texture and morphology variations in (In,Ga)2Se3 and Cu(In,Ga)Se2 thin films grown with various Se source conditions, Progress in Photovoltaics: Research and Applications, 21 (2013) 544-553.
[157] G. Gdowski, R. Madix, The effect of sulfur on co adsorption/desorption on Pt (S)-[9 (111)×(100)], Surface Science, 115 (1982) 524-540.
[158] C. Guillen, J. Herrero, M. Gutierrez, F. Briones, Structure, morphology and optical properties of CuInS2 thin films prepared by modulated flux deposition, Thin solid films, 480 (2005) 19-23.
[159] R. Klenk, T. Walter, H.W. Schock, D. Cahen, A model for the successful growth of polycrystalline films of CuInSe2 by multisource physical vacuum evaporation, Advanced Materials, 5 (1993) 114-119.

[160] S. Siebentritt, L. Gütay, D. Regesch, Y. Aida, V. Deprédurand, Why do we make Cu (In, Ga) Se2 solar cells non-stoichiometric?, Solar Energy Materials and Solar Cells, 119 (2013) 18-25.
[161] J. Van der Ziel, A. Meixner, H. Kasper, J. Ditzenberger, Lattice vibrations of AgGa S 2, AgGa Se 2, and CuGa S 2, Physical Review B, 9 (1974) 4286.
[162] S. Sugai, Resonant raman scattering in CuGaS2, Journal of the Physical Society of Japan, 43 (1977) 592-599.
[163] C. Rincon, F. Ramirez, Lattice vibrations of CuInSe2 and CuGaSe2 by Raman microspectrometry, Journal of Applied Physics, 72 (1992) 4321-4324.
[164] K. Wakita, H. Hirooka, S. Yasuda, F. Fujita, N. Yamamoto, Resonant Raman scattering and luminescence in CuInS 2 crystals, Journal of applied physics, 83 (1998) 443-447.
[165] X. Li, J. Li, K. Wang, X. Wang, S. Wang, X. Chu, M. Xu, X. Fang, Z. Wei, Y. Zhai, Pressure and temperature-dependent Raman spectra of MoS2 film, Applied Physics Letters, 109 (2016) 242101.
[166] T. Schmidt, K. Lischka, W. Zulehner, Excitation-power dependence of the near-band-edge photoluminescence of semiconductors, Physical Review B, 45 (1992) 8989.
[167] C. Spindler, T. Galvani, L. Wirtz, G. Rey, S. Siebentritt, Excitation-intensity dependence of shallow and deep-level photoluminescence transitions in semiconductors, Journal of Applied Physics, 126 (2019) 175703.
[168] C. Spindler, Optical detection of deep defects in Cu (In, Ga) Se2, University of Luxembourg, Luxembourg, Luxembourg, 2018.
[169] J.J. Hopfield, D.G. Thomas, M. Gershenzon, Pair Spectra in GaP, Physical Review Letters, 10 (1963) 162-164.
[170] P.W. Yu, Excitation-dependent emission in Mg-, Be-, Cd-, and Zn-implanted GaAs, Journal of Applied Physics, 48 (1977) 5043-5051.
[171] P.W. Yu, D.L. Downing, Y.S. Park, Electrical properties of CuGaS2 single crystals, Journal of Applied Physics, 45 (1974) 5283-5288.
[172] C. Rincón, J. González, Acoustic deformation potentials in AIBIIICVI2 chalcopyrite semiconductors, Physical Review B, 40 (1989) 8552-8554.
[173] B. Tell, H.M. Kasper, Electrical properties of CuGaS2, Journal of Applied Physics, 44 (1973) 4988-4990.

[174] R. Sharma, S. Rodriguez, Theory of excitons bound to ionized impurities in semiconductors, Physical Review, 153 (1967) 823.
[175] J. Hopfield, The quantum chemistry of bound exciton complexes, Physics of Semiconductors, 7 (1964).
[176] J.R. Haynes, Experimental Observation of the Excitonic Molecule, Physical Review Letters, 17 (1966) 860-862.
[177] H. Atzmüller, F. Fröschl, U. Schröder, Theory of excitons bound to neutral impurities in polar semiconductors, Physical Review B, 19 (1979) 3118-3129.
[178] J. Botha, M. Branch, A. Chowles, A. Leitch, J. Weber, Photoluminescence of vacuum-deposited CuGaS2 thin films, Physica B: Condensed Matter, 308 (2001) 1065-1068.
[179] K. Huang, A. Rhys, N.F. Mott, Theory of light absorption and non-radiative transitions in F-centres, Proceedings of the Royal Society of London. Series A. Mathematical and Physical Sciences, 204 (1950) 406-423.
[180] M.A. Reshchikov, H. Morkoç, Luminescence properties of defects in GaN, Journal of applied physics, 97 (2005) 5-19.
[181] A. Alkauskas, M.D. McCluskey, C.G. Van de Walle, Tutorial: Defects in semiconductors—Combining experiment and theory, Journal of Applied Physics, 119 (2016) 181101.
[182] C. Spindler, D. Regesch, S. Siebentritt, Revisiting radiative deep-level transitions in CuGaSe2 by photoluminescence, Applied Physics Letters, 109 (2016) 032105.
[183] J. Gonzalez, E. Moya, J. Chervin, Anharmonic effects in light scattering due to optical phonons in CuGaS 2, Physical Review B, 54 (1996) 4707.
[184] E. Zacks, A. Halperin, Dependence of the peak energy of the pair-photoluminescence band on excitation intensity, Physical Review B, 6 (1972) 3072.
[185] M. Sood, A. Urbaniak, C. Kameni Boumenou, T.P. Weiss, H. Elanzeery, F. Babbe, F. Werner, M. Melchiorre, S. Siebentritt, Near surface defects: Cause of deficit between internal and external open-circuit voltage in solar cells, Prog. Photovolt., 30 (2021) 263-275.
[186] M. Sood, A. Lomuscio, F. Werner, A. Nikolaeva, P.J. Dale, M. Melchiorre, J. Guillot, D. Abou-Ras, S. Siebentritt, Passivating Surface Defects and Reducing Interface Recombination in CuInS2 Solar Cells by a Facile Solution Treatment, Sol. RRL., 5 (2021) 2100078.

[187] M.A. Contreras, J. Tuttle, A. Gabor, A. Tennant, K. Ramanathan, S. Asher, A. Franz, J. Keane, L. Wang, J. Scofield, High efficiency Cu (In, Ga) Se/sub 2/-based solar cells: Processing of novel absorber structures, Proceedings of 1994 IEEE 1st World Conference on Photovoltaic Energy Conversion-WCPEC (A Joint Conference of PVSC, PVSEC and PSEC), IEEE, 1994, pp. 68-75.
[188] S.H. Wei, A. Zunger, Band offsets and optical bowings of chalcopyrites and Zn-based II-VI alloys, Journal of Applied Physics, 78 (1995) 3846-3856.
[189] L.C. Hirst, N.J. Ekins-Daukes, Fundamental losses in solar cells, Progress in Photovoltaics: Research and Applications, 19 (2011) 286-293.
[190] D. Adeleye, M. Sood, M. Melchiorre, S. Siebentritt, Composition dependence of electronic defects in CuGaS2, DOI (in preparation).
[191] M. Sood, A. Urbaniak, C. Kameni Boumenou, T.P. Weiss, H. Elanzeery, F. Babbe, F. Werner, M. Melchiorre, S. Siebentritt, Near surface defects: Cause of deficit between internal and external open-circuit voltage in solar cells, Progress in Photovoltaics: Research and Applications, 30 (2022) 263-275.
[192] H. Lewerenz, H. Goslowsky, K.-D. Husemann, S. Fiechter, Efficient solar energy conversion with CuInS2, Nature, 321 (1986) 687-688.
[193] H. Hiroi, Y. Iwata, H. Sugimoto, A. Yamada, Progress Toward 1000-mV Open-Circuit Voltage on Chalcopyrite Solar Cells, IEEE Journal of Photovoltaics, 6 (2016) 1630-1634.
[194] S. Merdes, R. Mainz, J. Klaer, A. Meeder, H. Rodriguez-Alvarez, H. Schock, M.C. Lux-Steiner, R. Klenk, 12.6% efficient CdS/Cu (In, Ga) S2-based solar cell with an open circuit voltage of 879 mV prepared by a rapid thermal process, Solar Energy Materials and Solar Cells, 95 (2011) 864-869.
[195] N. Barange, V.B. Chu, M. Nam, I.H. Ahn, Y.D. Kim, I.K. Han, B.K. Min, D.H. Ko, Ordered Nanoscale Heterojunction Architecture for Enhanced Solution-Based CuInGaS2 Thin Film Solar Cell Performance, Advanced Energy Materials, 6 (2016) 1601114.
[196] G. He, C. Yan, J. Li, X. Yuan, K. Sun, J. Huang, H. Sun, M. He, Y. Zhang, J.A. Stride, 11.6% efficient pure sulfide Cu (In, Ga) S2 solar cell through a Cu-deficient and KCN-free process, ACS Applied Energy Materials, 3 (2020) 11974-11980.

[197] S. Merdes, R. Sáez-Araoz, A. Ennaoui, J. Klaer, M.C. Lux-Steiner, R. Klenk, Recombination mechanisms in highly efficient thin film Zn (S, O)/Cu (In, Ga) S 2 based solar cells, Applied Physics Letters, 95 (2009) 213502.
[198] R. Scheer, M. Alt, I. Luck, H. Lewerenz, Electrical properties of coevaporated CuInS2 thin films, Solar energy materials and solar cells, 49 (1997) 423-430.
[199] T. Walter, D. Braunger, H. Dittrich, C. Köble, R. Herberholz, H. Schock, Sequential processes for the deposition of polycrystalline Cu (In, Ga)(S, Se) 2 thin films: Growth mechanism and devices, Solar Energy Materials and Solar Cells, 41 (1996) 355-372.
[200] R. Klenk, U. Blieske, V. Dieterle, K. Ellmer, S. Fiechter, I. Hengel, A. Jäger-Waldau, T. Kampschulte, C. Kaufmann, J. Klaer, Properties of CuInS2 thin films grown by a two-step process without H2S, Solar Energy Materials and Solar Cells, 49 (1997) 349-356.
[201] K. Siemer, J. Klaer, I. Luck, J. Bruns, R. Klenk, D. Bräunig, Efficient CuInS2 solar cells from a rapid thermal process (RTP), Solar energy materials and solar cells, 67 (2001) 159-166.
[202] T. Watanabe, H. Nakazawa, M. Matsui, Improvement of the electrical properties of Cu-poor CuInS2 thin films by sodium incorporation, Japanese Journal of Applied Physics, 37 (1998) L1370.
[203] T. Ohashi, Y. Hashimoto, K. Ito, Cu (In1-xGax) S2 thin-film solar cells with efficiency above 12%, fabricated by sulfurization, Japanese journal of applied physics, 38 (1999) L748.
[204] R. Mainz, F. Streicher, D. Abou-Ras, S. Sadewasser, R. Klenk, M.C. Lux-Steiner, Combined analysis of spatially resolved electronic structure and composition on a cross-section of a thin film Cu (In1–x Gax) S2 solar cell, physica status solidi (a), 206 (2009) 1017-1020.
[205] R. Klenk, J. Klaer, C. Köble, R. Mainz, S. Merdes, H. Rodriguez-Alvarez, R. Scheer, H. Schock, Development of CuInS2-based solar cells and modules, Solar energy materials and solar cells, 95 (2011) 1441-1445.
[206] T. Dullweber, U. Rau, M.A. Contreras, R. Noufi, H.-W. Schock, Photogeneration and carrier recombination in graded gap Cu (In, Ga) Se/sub 2/solar cells, IEEE Transactions on Electron Devices, 47 (2000) 2249-2254.
[207] Y. Ando, S. Ishizuka, S. Wang, J. Chen, M.M. Islam, H. Shibata, K. Akimoto, T. Sakurai, Relationship between bandgap grading and carrier recombination for Cu (In, Ga) Se2-based solar cells, Japanese Journal of Applied Physics, 57 (2018) 08RC08.

[208] J.I. Goldstein, D.E. Newbury, J.R. Michael, N.W. Ritchie, J.H.J. Scott, D.C. Joy, Scanning electron microscopy and X-ray microanalysis, Springer2017.
[209] D. Drouin, A. Couture, R. Gauvin, P. Hovington, P. Horny, H. Demers, monte CArlo SImulation of electroN trajectory in sOlids, Casino Version 3.3, DOI (2001).
[210] M.H. Wolter, B. Bissig, E. Avancini, R. Carron, S. Buecheler, P. Jackson, S. Siebentritt, Influence of sodium and rubidium postdeposition treatment on the quasi-fermi level splitting of Cu (In, Ga) Se 2 thin films, IEEE Journal of Photovoltaics, 8 (2018) 1320-1325.
[211] E.G. Vajda, J.G. Skedros, R.D. Bloebaum, Errors in quantitative backscattered electron analysis of bone standardized by energy-dispersive x-ray spectrometry, Scanning: The Journal of Scanning Microscopies, 20 (1998) 527-535.
[212] M. Topič, F. Smole, J. Furlan, Band-gap engineering in CdS/Cu (In, Ga) Se2 solar cells, Journal of applied physics, 79 (1996) 8537-8540.
[213] T. Higuchi, N. Usami, T. Minemoto, Effect of Ga content and growth temperature on Cu (In, Ga) Se2 thin film deposited on heat-resistant glass substrates, physica status solidi c, 10 (2013) 1035-1037.
[214] B. Peace, J. Claypoole, N. Sun, D. Dwyer, M.D. Eisaman, P. Haldar, H. Efstathiadis, Characterization of Cu (In, Ga) Se2 (CIGS) films with varying gallium ratios, Journal of Alloys and Compounds, 657 (2016) 873-877.
[215] F. Larsson, N.S. Nilsson, J. Keller, C. Frisk, V. Kosyak, M. Edoff, T. Törndahl, Record 1.0 V open-circuit voltage in wide band gap chalcopyrite solar cells, Progress in Photovoltaics: Research and Applications, 25 (2017) 755-763.
[216] S. Bremner, M. Levy, C.B. Honsberg, Analysis of tandem solar cell efficiencies under AM1. 5G spectrum using a rapid flux calculation method, Progress in photovoltaics: Research and Applications, 16 (2008) 225-233.
[217] A. Onno, N. Rodkey, A. Asgharzadeh, S. Manzoor, J.Y. Zhengshan, F. Toor, Z.C. Holman, Predicted power output of silicon-based bifacial tandem photovoltaic systems, Joule, 4 (2020) 580-596.
[218] A.M. Gabor, J.R. Tuttle, D.S. Albin, M.A. Contreras, R. Noufi, A.M. Hermann, High-efficiency CuIn x Ga1− x Se2 solar cells made from (In x, Ga1− x) 2Se3 precursor films, Applied physics letters, 65 (1994) 198-200.

[219] W.N. Shafarman, S. Siebentritt, L. Stolt, Cu (InGa) Se2 Solar Cells, Handbook of photovoltaic science and engineering, DOI (2010) 546-599.
[220] T. Kirchartz, K. Ding, U. Rau, Fundamental electrical characterization of thin-film solar cells, Advanced Characterization Techniques for Thin Film Solar Cells, 1 (2016) 41-69.
[221] C.M. Pelicano, H. Yanagi, Effect of rubrene:P3HT bilayer on photovoltaic performance of perovskite solar cells with electrodeposited ZnO nanorods, Journal of Energy Chemistry, 27 (2018) 455-462.
[222] R. Carron, C. Andres, E. Avancini, T. Feurer, S. Nishiwaki, S. Pisoni, F. Fu, M. Lingg, Y.E. Romanyuk, S. Buecheler, Bandgap of thin film solar cell absorbers: A comparison of various determination methods, Thin Solid Films, 669 (2019) 482-486.
[223] U. Rau, B. Blank, T.C. Müller, T. Kirchartz, Efficiency potential of photovoltaic materials and devices unveiled by detailed-balance analysis, Physical review applied, 7 (2017) 044016.
[224] O. Almora, C.I. Cabrera, J. Garcia-Cerrillo, T. Kirchartz, U. Rau, C.J. Brabec, Quantifying the absorption onset in the quantum efficiency of emerging photovoltaic devices, Advanced energy materials, 11 (2021) 2100022.
[225] S. Abrahams, J. Bernstein, Piezoelectric nonlinear optic CuGaS2 and CuInS2 crystal structure: Sublattice distortion in AIB III C 2 VI and A II B IV C 2 V type chalcopyrites, The Journal of Chemical Physics, 59 (1973) 5415-5422.
[226] S. Ishizuka, CuGaSe2 thin film solar cells: challenges for developing highly efficient wide-gap chalcopyrite photovoltaics, physica status solidi (a), 216 (2019) 1800873.
[227] C. Iatosti, M. Moret, A. Tiberj, O. Briot, Analysis of the gallium gradient in Cu (In1-xGax) Se2 absorbers by X-ray diffraction, Solar Energy Materials and Solar Cells, 220 (2021) 110847.
[228] A.R. Denton, N.W. Ashcroft, Vegard's law, Physical review A, 43 (1991) 3161.
[229] T. Klinkert, M. Jubault, F. Donsanti, D. Lincot, J.-F. Guillemoles, Ga gradients in Cu (In, Ga) Se2: formation, characterization, and consequences, Journal of Renewable and Sustainable Energy, 6 (2014) 011403.
[230] C. Frisk, C. Platzer-Björkman, J. Olsson, P. Szaniawski, J. Wätjen, V. Fjällström, P. Salomé, M. Edoff, Optimizing Ga-profiles for highly efficient Cu (In, Ga) Se2 thin film solar cells in simple and complex defect models, Journal of Physics D: Applied Physics, 47 (2014) 485104.

[231] O. Lundberg, J. Lu, A. Rockett, M. Edoff, L. Stolt, Diffusion of indium and gallium in Cu (In, Ga) Se2 thin film solar cells, Journal of Physics and Chemistry of Solids, 64 (2003) 1499-1504.
[232] A. Neisser, R. Klenk, M.C. Lux-Steiner, Diffusion of Ga and In in sequentially prepared Cu (In, Ga) S2 thin films for photovoltaic applications, MRS Online Proceedings Library (OPL), 763 (2003).
[233] A. Neisser, I. Hengel, R. Klenk, T.W. Matthes, J. Alvarez-Garcıa, A. Pérez-Rodrıguez, A. Romano-Rodrıguez, M.-C. Lux-Steiner, Effect of Ga incorporation in sequentially prepared CuInS2 thin film absorbers, Solar energy materials and solar cells, 67 (2001) 97-104.
[234] H. Rau, T. Kutty, J.G. De Carvalho, Thermodynamics of sulphur vapour, The Journal of Chemical Thermodynamics, 5 (1973) 833-844.
[235] R. Steudel, B. Eckert, Elemental sulfur and sulfur-rich compounds II, Springer Science & Business Media2003.
[236] D.-H. Cho, W.-J. Lee, S.-W. Park, J.-H. Wi, W.S. Han, J. Kim, M.-H. Cho, D. Kim, Y.-D. Chung, Non-toxically enhanced sulfur reaction for formation of chalcogenide thin films using a thermal cracker, Journal of Materials Chemistry A, 2 (2014) 14593-14599.
[237] P. Jackson, D. Hariskos, R. Wuerz, O. Kiowski, A. Bauer, T.M. Friedlmeier, M. Powalla, Properties of Cu (In, Ga) Se2 solar cells with new record efficiencies up to 21.7%, physica status solidi (RRL)–Rapid Research Letters, 9 (2015) 28-31.
[238] W.N. Shafarman, J. Zhu, Effect of substrate temperature and depostion profile on evaporated Cu (InGa) Se2 films and devices, Thin Solid Films, 361 (2000) 473-477.
[239] R. Carron, S. Nishiwaki, T. Feurer, R. Hertwig, E. Avancini, J. Löckinger, S.C. Yang, S. Buecheler, A.N. Tiwari, Advanced alkali treatments for high-efficiency Cu (In, Ga) Se2 solar cells on flexible substrates, Advanced Energy Materials, 9 (2019) 1900408.
[240] M. Sood, D. Adeleye, S. Shukla, T. Törndahl, A. Hultqvist, S. Siebentritt, Low temperature (Zn, Sn) O deposition for reducing interface open-circuit voltage deficit to achieve highly efficient Se-free Cu (In, Ga) S 2 solar cells, Faraday Discussions, DOI (2022).
[241] M. Edoff, T. Jarmar, N.S. Nilsson, E. Wallin, D. Högström, O. Stolt, O. Lundberg, W. Shafarman, L. Stolt, High V oc in (Cu, Ag)(In, Ga) Se 2 Solar Cells, IEEE Journal of Photovoltaics, 7 (2017) 1789-1794.

[242] S.-C. Yang, T.-Y. Lin, M. Ochoa, H. Lai, R. Kothandaraman, F. Fu, A.N. Tiwari, R. Carron, Efficiency boost of bifacial Cu (In, Ga) Se2 thin-film solar cells for flexible and tandem applications with silver-assisted low-temperature process, Nature Energy, DOI (2022) 1-12.
[243] C. Wang, D. Zhuang, M. Zhao, Y. Li, L. Dong, H. Wang, J. Wei, Q. Gong, Effects of silver-doping on properties of Cu(In,Ga)Se2 films prepared by CuInGa precursors, Journal of Energy Chemistry, 66 (2022) 218-225.
[244] G. Kim, W.M. Kim, J.-K. Park, D. Kim, H. Yu, J.-h. Jeong, Thin Ag precursor layer-assisted co-evaporation process for low-temperature growth of Cu (In, Ga) Se2 thin film, ACS applied materials & interfaces, 11 (2019) 31923-31933.
[245] L. Chen, J. Lee, W.N. Shafarman, The Comparison of (Ag,Cu)(In,Ga)Se and Cu(In,Ga)Se Thin Films Deposited by Three-Stage Coevaporation, IEEE Journal of Photovoltaics, 4 (2013) 447-451.
[246] J. Hwang, Y. Cho, D. Shin, I. Jeong, J.H. Park, J.-S. Cho, J. Gwak, J.H. Yun, K. Han, H.S. Chang, Improved carrier transport in CIGS solar cells induced by Ag treatment, Journal of Alloys and Compounds, 886 (2021) 161193.
[247] S. Siebentritt, E. Avancini, M. Bär, J. Bombsch, E. Bourgeois, S. Buecheler, R. Carron, C. Castro, S. Duguay, R. Félix, Heavy alkali treatment of Cu (In, Ga) Se2 solar cells: surface versus bulk effects, Advanced Energy Materials, 10 (2020) 1903752.
[248] J. Kessler, C. Chityuttakan, J. Lu, J. Schöldström, L. Stolt, Cu (In, Ga) Se2 thin films grown with a Cu-poor/rich/poor sequence: growth model and structural considerations, Progress in Photovoltaics: Research and Applications, 11 (2003) 319-331.